



TOR VERGATA
UNIVERSITÀ DEGLI STUDI DI ROMA



SAPIENZA
UNIVERSITÀ DI ROMA



INAF
ISTITUTO NAZIONALE
DI ASTROFISICA

Deriving Cosmological Parameters from the *Euclid* mission

Sapienza Università di Roma

PhD program in Astronomy, Astrophysics and Space Science (XXXVI cycle)

Davide Sciotti

ID number 1570331

Advisors

Prof. Roberto Maoli

Prof. Roberto Scaramella

Dr. Vincenzo Fabrizio Cardone

Coordinator:

Prof. Francesco Piacentini

Academic Year 2023/2024

Thesis not yet defended

Deriving Cosmological Parameters from the *Euclid* mission
Sapienza University of Rome and University of Rome Tor Vergata

© 2023 Davide Sciotti. All rights reserved

This thesis has been typeset by L^AT_EX and the Sapthesis class.

Author's email: davide.sciotti@uniroma1.it

Acknowledgements

I would like to express my deep gratitude to all the people who kindly assisted me in this work, through their comments, suggestions, encouragement, and fruitful discussion. In particular, I would like to thank Sylvain Gouyou Beauchamps, Marco Bonici, Santiago Casas, Guadalupe Cañas Herrera, Vincenzo Cardone, Matteo Martinelli, Roberto Maoli, Roberto Scaramella, Stefano Camera, Isaac Tutusauus, Fabien Lacasa, Alex Barreira, Peter Taylor, Martin Croce, Alkistis Pourtsidou, Carlo Giocoli, Robin Upham, Louis Legrand, Massimiliano Lattanzi, Riccardo La Placa, and the many others who made this journey possible.

*“A Giò, ancora e sempre.
E a Guido, Fabrizio, Milo, Cecilia, Francesco, Andrea, Yari, e Simona.*

Contents

Introduction	1
1 Cosmology	3
1.1 The Cosmological Principle	3
1.2 Hubble's law and Friedmann equations	4
1.3 Distances in Cosmology	9
1.4 Inhomogeneities	10
1.4.1 The Boltzmann equation	11
1.4.2 Initial conditions	13
1.4.3 Linear structure formation	14
1.4.4 Nonlinear scales	17
1.5 Neutrinos	21
1.6 Constraints on cosmological parameters from current experiments . .	24
2 Statistics	25
2.1 Bayes' Theorem	25
2.2 Fisher Information Matrix	29
2.3 Monte Carlo Markov Chain	33
2.4 Two-point statistics	34
2.4.1 Power Spectrum	34
2.4.2 Angular power spectrum	36
3 Galaxy Clustering and Gravitational Lensing	41
3.1 Galaxy Clustering	41
3.1.1 Spectroscopic Galaxy Clustering	42
3.1.2 Photometric galaxy clustering	43
3.1.3 Redshift distribution	46
3.1.4 Linear galaxy bias	48
3.1.5 Magnification bias	50
3.2 Weak Lensing	51
3.2.1 Theory	53
3.2.2 Lens equation	55
3.2.3 Lensing potential, shear and convergence matrices	56
3.2.4 Ellipticity and shear	57
3.2.5 Shear power spectrum	58
3.2.6 Intrinsic alignment	60

3.2.7	Multiplicative shear bias	62
3.2.8	Putting it all together: the 3×2 pt analysis	62
3.3	<i>Euclid</i>	65
3.3.1	Satellite	65
3.3.2	Survey strategy and data releases	67
3.3.3	Data processing	69
4	Super-sample covariance	71
4.1	Introduction	71
4.2	Theory and approximations	74
4.2.1	Power spectrum estimator and covariance in the presence of a survey window	74
4.2.2	Response functions	79
4.3	SSC for projected observables	85
4.3.1	Multi-probe, tomographic case	87
4.4	SSC approximations	90
5	Super-sample covariance for the <i>Euclid</i> photometric survey	93
5.1	Forecast specifics	93
5.1.1	Cosmological model and matter power spectrum	93
5.1.2	Radial kernels	94
5.1.3	Multi-probe response	95
5.1.4	Higher-order bias	96
5.1.5	Gaussian covariance	97
5.1.6	Data vectors and Fisher matrix	99
5.2	Forecast code validation	101
5.3	SSC impact on forecasts	102
5.3.1	Reference scenario	103
5.3.2	Non-flat cosmologies	107
5.3.3	Role of nuisance parameters	108
5.3.4	Dependence on redshift binning	110
5.3.5	Requirements on prior information	112
5.4	Summary	115
6	Scale Cuts	119
6.1	Scale cuts and the BNT transform	119
6.2	Angular scale cuts	123
6.3	k -cut forecasts	126
6.4	Summary	131
	Postface	133
	A High order bias from halo model	135
	B Appendix B: Details of the code validation	137
	C Slowly varying response approximation for broad kernels	141

D Multipole binning

143

Bibliography

145

Introduction

THE cosmological parameters are fundamental quantities of the cosmological model, the theoretical framework that tries to predict and explain the dynamics, geometry, and evolutionary course of the Universe. From the rate of expansion, encapsulated by the Hubble constant, to the density parameters, describing the relative proportions of the different cosmic species, these quantities allow us, amongst other things, to reconstruct the Universe's evolution from a homogeneous, hot, and dense early state to the complex and beautiful structures we observe at low redshift.

We are now living in the epoch of precision cosmology, characterized by unprecedented amounts of high-resolution data. Amongst the most important milestones in the direction of this new era of Cosmology is the accurate measurement of the anisotropies in Cosmic Microwave Background (CMB) by the *Planck* Satellite, giving us a wealth of information about the early Universe. However, the quest for unravelling the cosmic mysteries calls for independent and complementary routes to improve the precision of the parameters' estimates, hence opening the possibility of selecting between competing cosmological models.

In this regard, the *Euclid* mission, a project undertaken by the European Space Agency (ESA), emerges as a promising tool to probe the low-redshift Universe, and hence study its expansion history and geometry. By surveying the position and morphology of billions of galaxies, *Euclid* will construct the largest and most accurate map of the large-scale structure (LSS) of the Universe, allowing for unique insights into the nature of dark matter and dark energy.

This thesis revolves around the central theme of quantifying the constraining power of the upcoming *Euclid* photometric survey, by taking into account several factors which have been neglected to this date in the official forecasts, especially more subtle sources of uncertainty which need to be included in the forecast (and data) analysis due to the precision of the observations.

The present work is organized as follows: Chapter 1 will introduce the current concordance cosmological model and the aspects that will be best investigated by *Euclid*. Chapters 2 and 3 will illustrate the statistical framework and cosmological probes used in our forecasts (and often in the literature). Chapters 4 and 5 will discuss super-sample covariance, its analytical treatment, the approximations used to study it in this context and the results obtained for the photometric survey; this is the result of one of the Key Papers of the Galaxy Clustering Science Working Group

(GC SWG), [Euclid Collaboration: Sciotti et al. \(2023\)](#), submitted to Astronomy & Astrophysics after having successfully undergone the internal review of the Euclid Collaboration. Finally, Chapter 6 will give some details about the work done in the context of the latest Science Performance Verification (SPV) of the survey, the last before the first data release, regarding the inclusion of scale cuts in the forecast analysis through the use of the Bernardeau-Nishimichi-Taruya (BNT) transform.

Chapter 1

Cosmology

Cosmology is the domain of physics that investigates the global characteristics of the Universe. This includes an exploration of the types, densities, and distributions of matter-energy components within the cosmos, along with its age, expansion history and geometric properties. Such a study, as with all physics, is based on the continuous feedback loop between data and model: we formulate a model based on key insights and existing observations, which motivates further experiments, which corroborate or conforte the existing models, and so on. This Chapter will introduce the key principles and models at the heart of modern cosmological analyses, laying the foundation for the concepts presented in the rest of the work.

1.1 The Cosmological Principle

At the basis of our current understanding of the Universe is the cosmological principle, the observation that on sufficiently large scales ($\gtrsim 10^2 \text{Mpc}$, [Peebles 1993](#)) the Universe manifests as homogeneous and isotropic. Mathematically, this means that on sufficiently large scales the cosmological fields – and the metric tensor, describing the geometry of spacetime – possess translational and rotational symmetry. This principle has in turn its roots in the Copernican principle, stating that we are not special observers of the Universe: there is no privileged point or direction. It is interesting to note that these two assumptions are not independent: if the Universe appears the same in every direction, and if this is true for any observer - as a natural consequence of the Copernican principle - it must also be homogeneous. Isotropy for every observer is the stronger condition:

$$\begin{aligned} \text{isotropy for every observer} &\Rightarrow \text{homogeneity} \\ \text{homogeneity} &\not\Rightarrow \text{isotropy for every observer.} \end{aligned}$$

Such a principle implies the following general form for the metric tensor, the mathematical object which allows defining distances and angles on a manifold, expressed through the line element ds^2

$$ds^2 = -c^2 dt^2 + a(t)^2 [dr^2 + S_k^2(r) d\Omega^2] \quad (1.1)$$

in spherical coordinates (r, θ, ϕ) , with $d\Omega^2 = d\theta^2 + \sin^2 \theta d\phi^2$. This is called the Friedmann-Lemaître-Robertson-Walker (FLRW) metric. The isotropy condition

forces the mixed terms $g_{0i} = g_{i0}$ to vanish. The homogeneity condition primarily governs the spatial part of the metric tensor g_{ij} , making the spatial components maximally symmetric. This is expressed by the fact that g_{ij} can be written as a function of a single spatial coordinate r and a time-dependent scale factor $a(t)$, along with $S_k(r)$ to account for possible (Gaussian) curvature k , which has to be constant due to, again, homogeneity and isotropy. This constant curvature can be positive, negative or null, and has units of $[L^{-2}]$:

$$S_k(r) = \begin{cases} \frac{\sin(r\sqrt{k})}{\sqrt{k}} & (k > 0) \\ r & (k = 0) \\ \frac{\sinh(r\sqrt{|k|})}{\sqrt{|k|}} & (k < 0) \end{cases}, \quad (1.2)$$

where r is the radial coordinate. The dimensionless quantity $a(t)$ is called the *scale factor*. It encodes the time dependence of the spatial degrees of freedom, therefore allowing the possibility of an expanding or contracting space (again, an isotropic model needs just one such quantity - all spatial directions scale at the same rate). It is defined as

$$a(t) = d_{\text{pr}}(t)/d_{\text{pr},0}, \quad (1.3)$$

where $d_{\text{pr}}(t)$ is the *proper distance* at some time t , compared to the proper distance at some reference time $d_{\text{pr}}(t_0) = d_{\text{pr},0}$. This definition ensures that $a(t_0) = a_0 = 1$. It is customary to take as a reference time the present epoch, so $a = 1$ today. The time coordinate is called *cosmic time*, and it represents the time measured by a clock moving along (*comoving*) with the expanding Universe (with the so-called “Hubble flow”).

An expanding Universe naturally leads to define different types of distance indicators. Two points whose distance changes in time only due to the expansion of space are said to be at a constant comoving distance χ . This is the distance measured in a coordinate system which follows the expansion of space. The proper distance, as seen above, is measured instead with a coordinate system that does not track the space expansion, hence the distance between the two points will change just by virtue of the scale factor variation. Proper distance is therefore the distance between two regions of space at a constant cosmological time. It is not directly observable, but can be calculated by factoring in the scale factor: $d_{\text{pr}}(t) = a(t)\chi$. Since $a(t_0) = 1$, today the two distances correspond.

1.2 Hubble’s law and Friedmann equations

One of the first direct observations of the expansion of the Universe was performed by Edwin Hubble in the late 1920s. In the law that now carries his name, he stated that distant galaxies tend to recede from us, with a velocity directly proportional to their distance:

$$v = H_0 d. \quad (1.4)$$

H_0 is called Hubble (more recently¹ Hubble-Lemaître) constant, and is often expressed in $\text{km s}^{-1} \text{Mpc}^{-1}$. Its measurement constitutes one of the most important

¹<https://www.iau.org/news/pressreleases/detail/iau1812/>

open problems in Cosmology, since observations from early-time and late-time probes give statistically incompatible results (the so-called “Hubble tension”: see [Di Valentino et al. 2021](#) for a recent comprehensive review). Cosmologists often use the reduced dimensionless Hubble constant $h = H_0/(100 \text{ km s}^{-1} \text{ Mpc}^{-1})$. In this work we will set $h = 0.67$, following results from the *Planck* mission [Planck Collaboration et al. \(2020a\)](#).

Hubble's law can be recast in terms of the scale factor by introducing one of the most important quantities in Astrophysics: the *redshift* z , defined as

$$z = \frac{\lambda_{\text{obs}} - \lambda_{\text{em}}}{\lambda_{\text{em}}}. \quad (1.5)$$

which is the relative differential shift between the observed and emitted wavelength of the radiation source. This can be caused by different factors, such as the relative peculiar velocity of the source, or the presence of a gravitational potential. In the context of Cosmology, we are mainly interested in the redshift caused by the expansion of the Universe, which increases the radiation wavelength (hence decreasing its energy) as it follows its geodesic. For small values of v/c - or small distances d - we have, from special relativity (see e.g. [Hogg 1999](#)):

$$z = \sqrt{\frac{1 + v/c}{1 - v/c}} \simeq v/c, \quad (1.6)$$

from which

$$z \simeq \frac{H_0 d}{c}. \quad (1.7)$$

We can connect the redshift to the scale factor via the following equation:

$$\frac{a_{\text{obs}}}{a_{\text{em}}} = \frac{1}{a} = \frac{\lambda_{\text{obs}}}{\lambda_{\text{em}}} = 1 + z. \quad (1.8)$$

This makes redshift, which is directly observable, a key quantity in our analysis: light coming from distant galaxies carries an imprint of the value of the scale factor at the time of the signal emission. This allows reconstructing the expansion history $a(t)$ of the Universe, one of its most fundamental properties. We can predict the functional form of $a(t)$ and connect it to other fundamental quantities by using the Friedmann equations. These can be derived by using the metric (1.1) and assuming General Relativity (GR) to be the correct theory of gravity on cosmological scales.

We begin by introducing the Einstein field equations, a set of differential equations relating the Einstein tensor $G_{\mu\nu}$ to the stress-energy tensor $T_{\mu\nu}$:

$$G_{\mu\nu} + \Lambda g_{\mu\nu} = \frac{8\pi G}{c^4} T_{\mu\nu}, \quad (1.9)$$

where G is the gravitational constant, Λ is the cosmological constant (with a positive value) and the second term on the l.h.s. was originally introduced to achieve a static Universe, which was thought to be the correct model at the beginning of the 20th century – before the observations by Hubble. The Einstein tensor encodes the geometric properties (i.e., the curvature) of spacetime, while the stress-energy tensor

characterizes the distribution and flow of energy-momentum in that spacetime. The stress-energy tensor $T_{\mu\nu}$ acts as the source term in Eq. (1.9), dictating how energy and momentum contribute to the curvature. The Einstein tensor, in turn, governs the geodesic motion of particles and radiation in the curved spacetime. Hence, this equation captures the dynamical interplay between the distribution of matter-energy in the Universe and the geometry of spacetime.

The Einstein tensor can be expressed as a combination of the Ricci tensor $R_{\mu\nu}$, the Ricci scalar $R = g^{\mu\nu} R_{\mu\nu}$ and the metric tensor $g_{\mu\nu}$:

$$G_{\mu\nu} = R_{\mu\nu} - \frac{1}{2} R g_{\mu\nu} . \quad (1.10)$$

Since the Ricci tensor only depends on the metric tensor and its derivatives, the l.h.s. is purely geometrical. Evaluating it for the FLRW metric (1.1), we get for the time-time component G_{00} :

$$G_{00} = 3 \left(\frac{\dot{a}}{a} \right)^2 , \quad (1.11)$$

with the dot denoting the time derivative; we note that \dot{a}/a , the relative rate of change of the scale factor, is just the Hubble parameter $H(t)$. We can then move the cosmological constant term to the r.h.s. of Eq. (1.9), interpreting it as a matter-energy component (*dark energy*) rather than a property of space, which makes it easier to generalize it to dynamical forms. Considering the different components of the Universe as non-interacting perfect fluids with no anisotropic stresses (as implied by the requirement of homogeneity and isotropy), the stress-energy tensor will be $\text{diag}(\rho_i, P_i, P_i, P_i)$ where ρ_i is the density and P_i the pressure of the i -th component and the “diag” notation indicates a diagonal matrix with entries specified by the arguments. The Λ component has a stress-energy tensor

$$T_{(\Lambda)\nu}^{\mu} = -\frac{\Lambda}{8\pi G} \delta^{\mu}_{\nu} = \text{diag}(-\rho_{\Lambda}, -\rho_{\Lambda}, -\rho_{\Lambda}, -\rho_{\Lambda}) ; \rho_{\Lambda} = \frac{\Lambda}{8\pi G} \quad (1.12)$$

with a time- and position-independent energy density (hence the name *cosmological constant*). We can now write the first Friedmann equation, describing the evolution of the homogeneous Universe, in the form of a differential equation for the scale factor:

$$H^2 = \left(\frac{\dot{a}}{a} \right)^2 = \frac{8\pi G}{3} \rho = \frac{8\pi G}{3} \sum_i \rho_i \quad (1.13)$$

where i runs over the different (non-interacting) energy components and $\rho(t)$ is the total energy density. This derivation holds for a flat universe; in the most general case, there is an additional term accounting for curvature:

$$H^2 = \left(\frac{\dot{a}}{a} \right)^2 = \frac{8\pi G}{3} \rho - \frac{kc^2}{a^2} \quad (1.14)$$

which makes it natural to define the *critical density* ρ_{cr} as the density which makes the curvature vanish: its value today is $\rho_{\text{cr}} = 3H_0^2/8\pi G$.

Taking the time derivative of Eq. (1.14), we get

$$2H\dot{H} = \frac{8\pi G}{3} \dot{\rho} + \frac{2kc^2}{a^3} \dot{a} . \quad (1.15)$$

We now need to relate $\dot{\rho}$ to other known quantities. The continuity equation for perfect fluids in an expanding universe fluid is given by the conservation equation $T^{\mu\nu}_{;\nu} = 0$ (more specifically, from the $\mu = 0$ term), where the semicolon indicates the covariant derivative :

$$\dot{\rho} + 3H(\rho + \frac{P}{c^2}) = 0 . \quad (1.16)$$

Solving for $\dot{\rho}$ and substituting into Eq. (1.15), we arrive at the second Friedmann equation:

$$\frac{\ddot{a}}{a} = \dot{H} + H^2 = -\frac{4\pi G}{3} \left(\rho + \frac{3P}{c^2} \right) . \quad (1.17)$$

To solve the two Friedmann equations (Eqs. 1.14 and 1.17) we need an equation relating the density and pressure of the perfect fluids involved, i.e., an equation of state (EoS): we assume cosmological fluids to be described by a simple EoS, in the form

$$P = w\rho c^2 , \quad (1.18)$$

parameterized by w . Combining this with the continuity equation (1.16), we get

$$\rho \propto a^{-3(1+w)} \quad (1.19)$$

which gives the evolution of the density as a function of the scale factor under the assumption of constant w .

The perfect fluids which make up the Universe described by our model are essentially of three types: matter (baryonic matter, cold dark matter, non-relativistic neutrinos), radiation, and cosmological constant. Concerning its impact on the time evolution of the scale factor, curvature can be treated as a further matter-energy component; the EoS parameter and scale factor dependence of these different species are given in Table 1.1. The energy densities ρ_i can be normalized by the critical den-

Table 1.1. The equation of state parameters and the dependence of the energy densities with the scale factor for the different cosmic species.

radiation	$w = 1/3$	$\rho_r \propto a^{-4}$
matter	$w = 0$	$\rho_m \propto a^{-3}$
curvature	$w = -1/3$	$\rho_k \propto a^{-2}$
Λ	$w = -1$	$\rho_\Lambda = \text{const}$

sity to obtain the *density parameters* $\Omega_i = \rho_i/\rho_{\text{cr}}$. Curvature and Λ will respectively have $\Omega_{\Lambda,0} = \Omega_\Lambda = \Lambda c^2/3H_0^2$ and $\Omega_{k,0} = -k/H_0^2$. As usual, the 0 subscript indicates the value today. The different scaling with a shows how different components were prevalent at different times, allowing distinguishing between *epochs* when they were dominant over the others. These different components will now be briefly introduced.

Recent observations (Perlmutter et al., 1999; Riess et al., 1998) have shown that the Universe is currently accelerating its expansion ($\ddot{a} > 0$); in the current concordance model, this means that we now live in the Λ -dominated epoch. Explaining the cause of this accelerated expansion is arguably the central problem in modern Cosmology. After being rejected by Einstein because of the rise of the expanding

Universe model, the cosmological constant was reintroduced after this discovery; in fact, from the second Friedmann equation:

$$\frac{\ddot{a}}{a} = -\frac{4\pi G}{3} \left(\rho_m + \rho_\Lambda + \frac{3P_m}{c^2} + \frac{3P_\Lambda}{c^2} \right) = -\frac{4\pi G}{3} (\rho_m - 2\rho_\Lambda) , \quad (1.20)$$

from which we get $\ddot{a} > 0$ if $\rho_\Lambda > \rho_m/2$. As mentioned earlier, the Λ term in Eq. (1.9) can be interpreted as an additional component, a form of a yet-to-be-understood type of energy (Dark Energy, DE, or as the energy of vacuum), or as a property of space itself, depending on whether we choose to include it in right- or left-hand side (l.h.s.) of the Einstein equations. In the first case, the DE EoS can be allowed to have time dependence by letting $w = w(t)$; one of the simplest time-dependent parameterizations of the DE EoS is the Chevallier-Polarski-Linder (CPL) parametrization (Chevallier and Polarski, 2001; Linder, 2005):

$$w_{\text{DE}}(z) = w_0 + w_a \frac{z}{1+z} = w_0 + w_a(1-a). \quad (1.21)$$

where w_0 is the current time value and w_a controls the time dependence of w_{DE} . Any observation of $w_a \neq 0$ would allow discriminating between different DE theories; a key goal of the *Euclid* mission is to place tight bounds on w_0 and w_a , hence selecting between the cosmological constant and dynamical DE models with high statistical power (Laureijs et al., 2011). Of course, another possibility to explain the accelerated expansion is that GR is not the correct theory of gravity (not on all scales, at least) and must be modified: this class of solutions is referred to as *Modified Gravity* (MG) models.

The second component is matter, which is pressureless; it is composed of baryonic (protons, neutrons and electrons; in Cosmology, the term “baryons” is used more loosely than in particle physics) and Dark matter (DM). This second type is of unknown nature and origin and exhibits very low electromagnetic interaction (hence the name “dark”) but does interact gravitationally. It makes up $\sim 27\%$ of the total matter-energy content, and its existence has been proposed to explain several observations, such as the statistical properties of the large-scale matter distribution (Sect. 2.4.2), Baryon Acoustic Oscillations (Sect. 3.1.1), galaxy rotation curves (Rubin et al., 1982) and the Bullet Cluster (Clowe et al., 2006). In the concordance model, this form of matter is cold – i.e., has $v_{\text{DM}}/c \ll 1$; a possible DM candidate are Weakly Interacting Massive Particles (WIMPs, Jungman et al. 1996), with masses ranging from a few GeV to several TeV. Massive neutrinos are another potential form of Dark Matter, although their large velocity dispersion makes them a kind of *hot* DM: they too are weakly interacting particles, but their energy density is far too low to be the only actor at play in the DM sector. They are treated as radiation at early times and matter when they become non-relativistic, so their equation of state varies as well.

Our current standard cosmological model is called Lambda - Cold Dark Matter (Λ CDM), reflecting our current most accepted hypotheses on the nature of the dark components.

We can recast the first Friedmann equation as a function of the different density parameters:

$$H^2 = H_0^2(\Omega_r + \Omega_m + \Omega_k + \Omega_\Lambda) , \quad (1.22)$$

or:

$$H^2 = H_0^2 \left(\frac{\Omega_{r,0}}{a^4} + \frac{\Omega_{m,0}}{a^3} + \frac{\Omega_{k,0}}{a^2} + \Omega_{DE} a^{-3(1+w_{DE})} \right) , \quad (1.23)$$

The sum of the density parameters gives information about the curvature:

$$\Omega_k = 0 \rightarrow \Omega_{tot} = 1 \rightarrow \text{flat geometry} \quad (1.24)$$

$$\Omega_k > 0 \rightarrow \Omega_{tot} < 1 \rightarrow \text{open geometry} \quad (1.25)$$

$$\Omega_k < 0 \rightarrow \Omega_{tot} > 1 \rightarrow \text{closed geometry} , \quad (1.26)$$

having defined $\Omega_{tot} = 1 - \Omega_{k,0} = \Omega_{m,0} + \Omega_{r,0} + \Omega_\Lambda$. Current observations and theoretical models (in particular, inflation: [Starobinsky 1980](#), [Guth 1981](#)) tend to favour a flat geometry, with $\Omega_k = 0$.

In this work we will mainly deal with low-redshift probes; because of this, we can consider the contribution from the radiation component as negligible (setting $\Omega_{r,0} = 0$) and the massive neutrinos as non-relativistic, splitting $\Omega_{m,0}$ in

$$\Omega_{m,0} = \Omega_{b,0} + \Omega_{c,0} + \Omega_{\nu,0} \quad (1.27)$$

with subscripts ν for neutrinos, b for baryons and c for Cold Dark Matter.

1.3 Distances in Cosmology

Until now, we have encountered two possible distance measures in Cosmology, the proper and comoving distance. A distinction between the two was made necessary by the dynamic nature of space. Other distance indicators are needed to connect the comoving distance to other observable quantities, such as the angular scale or luminosity of an object. This section will briefly introduce these.

To begin with, the comoving distance can be expressed as a function of the cosmological fluids by integrating the first Friedmann equation:

$$\chi(z) = \frac{c}{H_0} \int_0^z \frac{dz}{E(z)} , \quad (1.28)$$

with $H(z) = H_0 E(z)$ and $E(z) = \sqrt{\Omega_{m,0}(1+z)^3 + \Omega_{k,0}(1+z)^2 + \Omega_{0\Lambda}}$ (for a Λ CDM model, having set $\Omega_{r,0} = 0$).

This can be used to compute another useful quantity, the *comoving volume*, used for example to get the volume of a region subtending a solid angle Ω between two redshifts z_1 and z_2 :

$$V(z_1, z_2) = \Omega \int_{\chi(z_1)}^{\chi(z_2)} \chi^2 d\chi = \frac{\Omega}{3} [\chi^3(z_2) - \chi^3(z_1)] \quad (1.29)$$

Another important distance indicator is the *angular diameter distance*, defined as the ratio of an object's physical transverse size to its angular size in radians (Hogg, 1999):

$$D_A(z) = \frac{c}{(1+z)H_0\sqrt{|\Omega_{k0}|}} S_k \left[\sqrt{|\Omega_{k0}|} \int_0^z \frac{dz'}{E(z')} \right], \quad (1.30)$$

or, writing explicitly the different cases of Eq. (1.2):

$$D_A(z) = \begin{cases} (1+z)^{-1} \frac{c}{H_0} \frac{1}{\sqrt{|\Omega_{k,0}|}} \sin \left(\sqrt{|\Omega_{k,0}|} \frac{H_0}{c} \chi(z) \right) & \Omega_{k,0} < 0 \\ (1+z)^{-1} \chi(z) & \Omega_{k,0} = 0 \\ (1+z)^{-1} \frac{c}{H_0} \frac{1}{\sqrt{\Omega_{k,0}}} \sinh \left(\sqrt{\Omega_{k,0}} \frac{H_0}{c} \chi(z) \right) & \Omega_{k,0} > 0 \end{cases} \quad (1.31)$$

which depends on the density parameters through $\chi(z)$.

Finally, the *luminosity distance* D_L is given by the bolometric (i.e., integrated over all frequencies) luminosity L and the bolometric flux S :

$$D_L = \sqrt{\frac{L}{4\pi S}} \quad (1.32)$$

and it is related to the angular diameter distance by

$$D_L = (1+z)^2 D_A \quad (1.33)$$

1.4 Inhomogeneities

While the Cosmological principle posits the homogeneity and isotropy of the Universe at large scales, observations clearly show this not to be the case when restricting our field of view (FoV) to smaller regions. Large-scale galaxy surveys have uncovered a rich and complex structure of galaxies and matter, organized in clusters, voids and filaments (the *cosmic web*), and which act as a proxy for the underlying dark matter distribution. Hence, the large-scale matter distribution breaks the assumptions of homogeneity and isotropy, creating the need to go beyond the treatment seen so far to describe the evolution of such inhomogeneities.

Our starting point in this treatment, leading to the equations of the (linear) growth of perturbations in an expanding Universe for the different species, is the perturbed FLRW metric. In the following, we will rely on the approximation of small perturbations around the smooth background, and rewrite the metric as:

$$\begin{aligned} g_{00}(\mathbf{x}, t) &= -1 - 2\Psi(\mathbf{x}, t) \\ g_{0i}(\mathbf{x}, t) &= 0 \\ g_{ij}(\mathbf{x}, t) &= a^2(t) \delta_{ij} [1 + 2\Phi(\mathbf{x}, t)], \end{aligned} \quad (1.34)$$

where the space- and time-dependent metric perturbations Ψ and Φ parameterize deviation from the FLRW metric, and describe the gravitational (or temporal)

potential and the curvature (or spatial) potential. Since they are small ($\mathcal{O}(10^{-4})$, [Dodelson and Schmidt 2020](#)), we can treat them at linear order to a good approximation. We note that Eq. (1.34) describes only scalar perturbations, the most relevant to structure formation, whereas tensor perturbations capture gravitational waves; moreover, the above expression is in the *conformal Newtonian* gauge ([Mukhanov et al., 1992](#)), a choice which does not influence our results since GR possesses gauge freedom.

The framework for the perturbative description of inhomogeneities in the Universe was laid out in [Lifshitz \(1946\)](#), and used to study photon and baryon perturbations in [Peebles and Yu \(1970\)](#); neutrinos were added to the picture in [Bond and Szalay \(1983\)](#), and a complete treatment including dark energy, CDM and massive and massless neutrinos in a flat universe was presented in [Ma and Bertschinger \(1995\)](#), which solved numerically the linearized Boltzmann, Einstein, and fluid equations for the evolution of the metric perturbations in both the synchronous and the conformal Newtonian gauges. A gauge-invariant approach to perturbation theory, on the other hand, was introduced in [Bardeen \(1980\)](#); one of the advantages of the conformal Newtonian gauge is precisely that the fields Ψ and Φ are equal (modulo a -1 factor) to the gauge-invariant variables thereby identified.

1.4.1 The Boltzmann equation

Until this point, we have derived the equations governing the evolution, or expansion history, of the smooth background, as a function of its various components. Now we turn our attention to the evolution of the species inhabiting the Universe; in the context of Cosmology, a statistical, average description of the collective behaviour of such species (luckily) suffices. This evolution is regulated by the central equation in statistical mechanics, the Boltzmann equation. These differential equations describe the time evolution of the phase-space distribution function $f(\mathbf{x}, \mathbf{p}, t)$ of a given set of particles, also taking into account their couplings to other species. The conjugate variables \mathbf{x} and \mathbf{p} , respectively the position and momentum of the particles, completely characterize the system. This distribution is defined by:

$$N(\mathbf{x}, \mathbf{p}, t) = f(\mathbf{x}, \mathbf{p}, t) \left(\frac{\Delta x \Delta p}{2\pi} \right)^3, \quad (1.35)$$

where $N(\mathbf{x}, \mathbf{p}, t)$ is the number of particles in the phase-space volume around (\mathbf{x}, \mathbf{p}) . The Boltzmann equation essentially expresses the conservation of phase space volume, which implies a null total derivative (d/dt) of the distribution function:

$$\frac{df}{dt} = 0 \quad \text{with} \quad \frac{d}{dt} = \frac{\partial}{\partial t} + \dot{\mathbf{x}} \nabla_{\mathbf{x}} + \dot{\mathbf{p}} \nabla_{\mathbf{p}}, \quad (1.36)$$

where ∇ is the gradient. We can account for particle-particle interactions, including particle annihilation and creation, by including a source term on the r.h.s., the *collision term*:

$$\frac{df}{dt} = C[f]. \quad (1.37)$$

Having obtained the distribution function for a given species by solving the Boltzmann equation, we can derive macroscopic quantities such as the stress-energy tensor

$$T^\mu{}_\nu(\mathbf{x}, t) = \frac{g_s}{\sqrt{-\det[g_{\alpha\beta}]}} \int \frac{dP_1 dP_2 dP_3}{(2\pi)^3} \frac{P^\mu P_\nu}{P^0} f(\mathbf{x}, \mathbf{p}, t) \quad (1.38)$$

where g_s represents the quantum degeneracy factor of the species considered, counting the number of particle states described by f , typically given by the number of spin (or helicity) states. We will not delve into the details of the solution of the Boltzmann equation for the different species here.

As seen above, the connection between the perturbed metric (1.34) and the stress-energy tensor derived through the Boltzmann equations can be made via the Einstein equations (1.9). Inserting the perturbed metric into the Einstein tensor (1.10) we get a 0-order term (the Friedmann equations) and a first-order term, which we are interested in in the context of the present discussion. The time-time component of the perturbation to the Einstein tensor is

$$\delta G^0{}_0 = 8\pi G \delta T^0{}_0 \quad (1.39)$$

$$\delta G^0{}_0 = -6H\Phi_{,0} + 6\Psi H^2 - 2\frac{k^2\Phi}{a^2}, \quad (1.40)$$

where the first line comes from Eq. (1.9) and the second from plugging the perturbed metric into Eq. (1.10), at linear order in Fourier-space (with k indicating the wavenumber) and the comma stands for the partial derivative: $_{,\alpha} \equiv \partial/\partial x^\alpha$.

The Boltzmann equation then gives us the form of the $\delta T^0{}_0$, allowing us to couple the gravitational potentials Φ and Ψ to the various components of matter and energy in the Universe. Here, we consider cold dark matter (CDM), baryons, photons, and neutrinos:

$$k^2\Phi + 3\frac{a'}{a} \left(\Phi' - \Psi \frac{a'}{a} \right) = 4\pi G a^2 [\rho_c \delta_c + \rho_b \delta_b + 4\rho_\gamma \Theta_0 + 4\rho_\nu \mathcal{N}_0], \quad (1.41)$$

where the derivative w.r.t. the conformal time, defined as

$$\eta(t) = \int_0^t \frac{dt'}{a(t')}, \quad (1.42)$$

is denoted by the prime symbol ($'$), a'/a represents the Hubble parameter in terms of conformal time, and we have defined the *density contrast* for species i as the relative difference between the local and average density at a given redshift z :

$$\delta_i(\mathbf{x}, z) = \frac{\rho_i(\mathbf{x}, z) - \bar{\rho}_i(z)}{\bar{\rho}_i(z)} \in [-1, \infty], \quad (1.43)$$

where \mathbf{x} is the comoving coordinate vector and $\bar{\rho}_i$ the average density. The meaning of the different contributions on the r.h.s. is listed below:

- $\rho_c \delta_c$ represents the contribution from cold dark matter, where ρ_c is its energy density.

- $\rho_b \delta_b$ is the analogous for baryonic matter.
- $4\rho_\gamma \Theta_0$ represents the contribution from photons. ρ_γ is the photon energy density and Θ_0 is the monopole term of the photon temperature perturbation in a multipole expansion.
- $4\rho_\nu \mathcal{N}_0$ is the analogous for massless neutrinos, with \mathcal{N}_0 the monopole term of the neutrino distribution function perturbation. In principle, one such term would be required for each mass eigenstate; neutrino masses can however be neglected at least until recombination (Dodelson and Schmidt, 2020).

The second equation, from the spatial part of the Einstein equations, gives instead

$$k^2(\Phi + \Psi) = -32\pi G a^2 [\rho_\gamma \Theta_2 + \rho_\nu \mathcal{N}_2] , \quad (1.44)$$

which tells us that the two gravitational potentials Φ and Ψ are equal and opposite unless the photons or neutrinos exhibit a non-negligible quadrupole moment, which is true only for collisionless neutrinos during radiation domination.

To solve this system of equations, we need some initial conditions; these will be discussed in the next section.

1.4.2 Initial conditions

In order to solve the system of equations for the evolution of perturbations, the initial conditions for all fields should be set in principle; we will see how, under specific assumptions, the initial conditions for just one field will suffice. At early times, such that $k\eta \ll 1$, the Boltzmann equations for radiation and cold dark matter become:

$$\begin{aligned} \Theta'_0 + \Phi' &= 0, \\ \mathcal{N}'_0 + \Phi' &= 0, \\ \delta'_b &= -3\Phi', \\ \delta'_c &= -3\Phi' . \end{aligned}$$

In this epoch radiation is the dominant energy component, so we can neglect the matter terms in the r.h.s. of Eq. (1.41) to get:

$$3\frac{a'}{a} \left(\Phi' - \frac{a'}{a} \Psi \right) = 16\pi G a^2 (\rho_\gamma \Theta_0 + \rho_\nu \mathcal{N}_0) . \quad (1.45)$$

Combining this with the above early-time equations for photons and neutrinos and (1.44) and setting $\Phi \simeq -\Psi$ (i.e. neglecting the neutrinos and photons quadrupole moment) we obtain:

$$\Phi''\eta + 4\Phi' = 0 . \quad (1.46)$$

To set the initial conditions, we just need to specify the properties of the perturbations. Inflationary models predict that at early times the Universe contains a stochastic background of Gaussian, adiabatic, and nearly scale-invariant perturbations. The adiabatic perturbation hypothesis has been tested with great accuracy by CMB experiments, such as *Planck* (Planck Collaboration et al., 2020c). For such

perturbations, different points of the Universe have different overdensities, but the relative density perturbations are the same for all species:

$$\frac{\delta\rho_i}{\rho_i} = \frac{\delta\rho}{\rho}, \quad (1.47)$$

for i running over the different components. With this choice, the evolution equations become:

$$\Phi(\mathbf{k}, \eta_i) = 2\Theta_0(\mathbf{k}, \eta_i) = 2\mathcal{N}_0(\mathbf{k}, \eta_i) \quad (1.48)$$

$$\delta_c(\mathbf{k}, \eta_i) = \delta_b(\mathbf{k}, \eta_i) = 3\Theta_0(\mathbf{k}, \eta_i) = \frac{3}{2}\Phi(\mathbf{k}, \eta_i) \quad (1.49)$$

where η_i is the conformal time (Eq. 1.42) of the initial conditions. The last two equations have a profound consequence: it is sufficient to set the initial conditions just for one field, for example, the metric perturbation Φ .

It is commonly assumed that the primordial fluctuations of the field Φ_p are Gaussian with zero mean $\langle\Phi_p(k)\rangle = 0$ and with a two-point function given in Fourier space by

$$\langle\Phi_p(\mathbf{k})\Phi_p^*(\mathbf{k}')\rangle = P_{\Phi_p}(k)(2\pi)^3\delta_D^3(\mathbf{k}-\mathbf{k}'). \quad (1.50)$$

where $P_{\Phi_p}(k)$ is the power spectrum (PS) of the field Φ_p , which gives its variance as a function of scale (see Sect. 2.4 for a formal introduction of two-point statistics and the PS), and δ_D^3 the three-dimensional Dirac delta. The initial perturbation power spectrum is usually set to a power law with the Harrison-Zel'dovich-Peebles parametrization:

$$P_{\Phi}(k) = A_s \left(\frac{k}{k_p}\right)^{n_s-1} k^{-3} \quad (1.51)$$

where the dimensionless parameter A_s sets the amplitude of the initial perturbations, n_s , the *scalar spectral index*, their scale dependence, and k_p is the pivot scale, which has to be fixed conventionally. Inflationary models predict $n_s \simeq 1$, i.e., nearly scale-invariant perturbations. Given the A_s and n_s parameters, the initial conditions are completely characterized.

1.4.3 Linear structure formation

In this section, we want to find a form for the PS of the matter density contrast field δ_m (the *matter* PS) as a function of scale and time (expressed by z or a). In linear theory, density modes with different wavenumbers k evolve independently, since the governing evolution equations for each k are decoupled.

This linear evolution can be divided into different phases, or regimes, based on the scale of the perturbation (k) relative to the scale of the horizon (which equals η in natural units): the super-horizon regime, horizon crossing, and sub-horizon regime. The horizon grows with time, becoming larger than a broader and broader range of scales k . In particular, modes evolve in different ways depending on the dominant species at the epoch they “cross the horizon” – whether it is during radiation ($a \ll a_{\text{eq}}$) or matter ($a \gg a_{\text{eq}}$) domination. This scale-dependent behavior

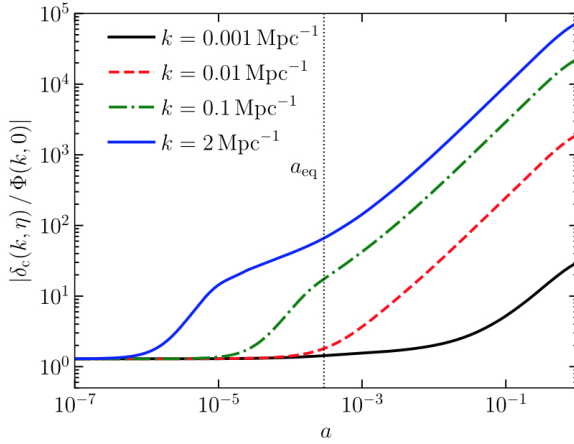


Figure 1.1. Evolution of CDM perturbations in the concordance cosmological model, normalized by the potential at early times. During matter domination, all scales evolve identically, proportionally to a . At very late times, Λ domination starts suppressing the growth again. Source: [Dodelson and Schmidt 2020](#)

can be factorized as a function of k and a in the potential Φ : the *transfer function* $T(k)$ and the *growth function* $D(a)$:

$$\Phi(\mathbf{k}, a) = \frac{3}{5} \Phi_p(\mathbf{k}) T(k) \frac{D(a)}{a}. \quad (1.52)$$

During the radiation-dominated era, smaller-scale modes of Φ decay as they enter the horizon, and the growth of perturbations is suppressed. Conversely, larger scale modes remain constant, entering the horizon during the matter-dominated epoch. Intermediate scales exhibit modest decay as they cross the horizon near the matter-radiation equality.

Analytical models for the transfer function exist in the literature (e.g. [Eisenstein and Hu 1998](#)), but are nowadays less relevant thanks to the accuracy and speed reached by numerical solvers of the coupled Boltzmann equations such as **CLASS**² ([Blas et al., 2011](#)) and **CAMB**³ ([Lewis et al., 2000](#)). Additionally, these codes can go beyond the linear perturbative treatment expounded in this section and compute the power spectrum even with nonlinear effects, for example using N -body simulation-based fitting formulas like **halofit** ([Smith et al., 2003](#); [Takahashi et al., 2012](#)), introduced in the next section.

The dark matter overdensity evolves with Φ as illustrated in Fig. 1.1. Applying the late-time, no-radiation constraint of Eq. (1.41) yields:

$$k^2 \Phi(\mathbf{k}, a) = 4\pi G \rho_m(a) a^2 \delta_m(\mathbf{k}, a) \quad (k \gg aH), \quad (1.53)$$

and substituting the zeroth-order Friedmann equation provides an expression for δ_m :

$$\delta_m(\mathbf{k}, a) = \frac{2}{5} \frac{k^2}{\Omega_{m,0} H_0^2} \Phi_p(\mathbf{k}) T(k) D(a). \quad (1.54)$$

The parameterization of the linear power spectrum of matter density fluctuations is then given by:

$$P_{\delta\delta}^L(k, a) = \frac{8\pi^2}{25} \frac{A_s}{\Omega_{m,0}^2} D^2(a) T^2(k) \frac{k^{n_s}}{H_0^4 k_p^{n_s-1}}. \quad (1.55)$$

²https://lesgourg.github.io/class_public/class.html

³<https://camb.info/>

Traditionally, σ_8 , the standard deviation of cold matter perturbations at scale $8h^{-1}\text{Mpc}$, is used instead of the scalar amplitude A_s . The relationship between them is:

$$\sigma_8^2 = \int \frac{dk}{k} \frac{k^3 P_L(k)}{2\pi^2} |W_{\text{TH}}(kR_8)|^2, \quad (1.56)$$

where

$$W_{\text{TH}}(x) = \frac{3(\sin x - x \cos x)}{x^3} \quad (1.57)$$

is the Fourier-transformed top-hat filter. The evolution equation for the growth function $D(a)$ can now be derived:

$$\frac{d^2 \delta_m}{da^2} + \frac{\partial \ln(a^3 H)}{\partial a} \frac{\partial \delta_m}{\partial a} - \frac{3\Omega_{m,0} H_0^2}{2a^5 H^2} \delta_m = 0. \quad (1.58)$$

In the late Universe, this equation simplifies to an integral form:

$$D(a) = \frac{5\Omega_{m,0}}{2} \frac{H(a)}{H_0} \int_0^a \frac{da'}{(a' H(a')/H_0)^3}. \quad (1.59)$$

A useful empirical fit exists for the logarithmic growth rate $f(a)$ (Lahav et al., 1991; Linder, 2005):

$$f(a) = \frac{d \ln D(a)}{d \ln a} \approx [\Omega_{m,0}(a)]^\gamma, \quad (1.60)$$

where γ is the *growth parameter*, approximately 0.55 in ΛCDM . This parameterization is useful to detect deviations from GR, which would result in a different observed value for the γ parameter. In fact, placing tight constraints on γ is one of the main aims of the *Euclid* mission (Laureijs et al., 2011).

A more complete description of the growth of structures, allowing, for example, a scale-dependent growth function, can be obtained by introducing the μ_{MG} and Σ_{MG} free functions (Planck Collaboration et al., 2016):

$$k^2 \Psi = -\mu_{\text{MG}}(a, k) 4\pi G a^2 \sum_i [\rho_i \delta_i + 3(\rho_i + p_i) \sigma_i] \quad (1.61)$$

$$k^2 (\Psi + \Phi) = -\Sigma_{\text{MG}}(a, k) 4\pi G a^2 \sum_i [2\rho_i \delta_i - 3(\rho_i + p_i) \sigma_i]. \quad (1.62)$$

μ_{MG} and Σ_{MG} parametrize respectively the deviations of the growth of structures and light deflection from the GR case. σ_i is the anisotropic stress, non-vanishing for relativistic species; it is negligible at low redshifts. In the $(\mu_{\text{MG}}, \Sigma_{\text{MG}}) = (1, 1)$ case we re-obtain the ΛCDM model; deviations from these values can be due either to modified gravity or to the presence of extra relativistic species.

We can relate μ_{MG} to γ via (Euclid Collaboration: Blanchard et al., 2020) – hereafter EC20:

$$\mu_{\text{MG}}(a, \gamma) = \frac{2}{3} \Omega_m^{\gamma-1} \left[\Omega_m^\gamma + 2 + \frac{H'}{H} + \gamma \frac{\Omega_m'}{\Omega_m} + \gamma' \ln \Omega_m \right] \quad (1.63)$$

where $\Omega_m = \Omega_m(a)$ and the prime indicates differentiation with respect to $\ln a$. For a constant γ we still have to choose the form of the second free function, Σ_{MG} : we can pick $\Sigma_{\text{MG}} = 1$ to recover the same light deflection as in ΛCDM . In this way, a $\gamma \neq 0.55$ value would only affect the growth of structures through $\mu_{\text{MG}} \neq 1$, and the resultant different dependence of the matter PS from the growth rate (1.60).

1.4.4 Nonlinear scales

The unprecedented resolution of *Euclid* observations will allow probing the galaxy distribution and the weak lensing signal up to very small angular scales, where structure formation enters the nonlinear regime. This means that the linear treatment of perturbations seen so far, which allowed us to derive an analytical expression for the linear matter power spectrum, is no longer valid. Density perturbations are larger on smaller scales, hence structures collapse on small scales first; the large-scale structures are then built hierarchically (Dodelson and Schmidt, 2020). Therefore, to begin with, we can look for a more accurate description of the clustering of DM on small scales, which is much simpler to model being collisionless, with no baryonic effects such as radiative cooling of gas, AGN feedback and so forth, which become important only deeply in the nonlinear regime ($k \gtrsim 1 h \text{ Mpc}^{-1}$) anyways. The following discussion will introduce the perturbative and halo-model approach to the problem.

Perturbation theory

Perturbation theory is a possible (analytical) approach to the solution of this problem, at least up to scales at which the perturbative correction to the leading order term (the linear PS, in this case) is small ($k \lesssim 0.2 h \text{ Mpc}^{-1}$, Dodelson and Schmidt 2020). The starting point of this treatment is the collisionless Boltzmann (Vlasov) equation and the Poisson equation, governing the dynamics of the (dark) matter density and velocity fields. By taking and truncating moments of this equation we obtain the simpler fluid (continuity and Euler) equations (Bernardeau et al., 2002; Desjacques et al., 2018):

$$\begin{aligned} \frac{\partial}{\partial \eta} \delta(\mathbf{x}, \eta) + \nabla \cdot \{[1 + \delta(\mathbf{x}, \eta)] \mathbf{v}(\mathbf{x}, \eta)\} &= 0 \\ \frac{\partial}{\partial \eta} \mathbf{v}(\mathbf{x}, \eta) + [\mathbf{v}(\mathbf{x}, \eta) \cdot \nabla] \mathbf{v}(\mathbf{x}, \eta) + \mathcal{H}(\eta) \mathbf{v}(\mathbf{x}, \eta) &= -\nabla \Phi(\mathbf{x}, \eta) \\ \nabla^2 \Phi(\mathbf{x}, \eta) &= \frac{3}{2} \mathcal{H}^2 \Omega_m(\eta) \delta(\mathbf{x}, \eta) . \end{aligned}$$

Having introduced $\mathcal{H} = a'/a = aH$ and writing $\Omega_m(\eta)$ to highlight that we are referring to the density parameter as a function of (conformal) time. In Fourier space these equations become, introducing the velocity divergence $\theta \equiv \nabla \cdot \mathbf{v}(\mathbf{x}, \eta)$ and using the Fourier transform of the Poisson equation to eliminate Φ :

$$\frac{\partial \delta(\mathbf{k}, \eta)}{\partial \eta} + \theta(\mathbf{k}, \eta) = - \int_{\mathbf{k}_1} \int_{\mathbf{k}_2} (2\pi)^3 \delta_D(\mathbf{k} - \mathbf{k}_{12}) \alpha(\mathbf{k}_1, \mathbf{k}_2) \theta(\mathbf{k}_1, \eta) \delta(\mathbf{k}_2, \eta) \quad (1.64)$$

$$\begin{aligned} \frac{\partial \theta(\mathbf{k}, \eta)}{\partial \eta} + \mathcal{H}(\eta) \theta(\mathbf{k}, \eta) + \frac{3}{2} \mathcal{H}^2(\eta) \Omega_m(\eta) \delta(\mathbf{k}, \eta) &= \\ - \int_{\mathbf{k}_1} \int_{\mathbf{k}_2} (2\pi)^3 \delta_D(\mathbf{k} - \mathbf{k}_{12}) \beta(\mathbf{k}_1, \mathbf{k}_2) \theta(\mathbf{k}_1, \eta) \theta(\mathbf{k}_2, \eta) . \end{aligned} \quad (1.65)$$

with $\mathbf{k}_{ij\dots} \equiv \mathbf{k}_i + \mathbf{k}_j + \dots$, and

$$\alpha(\mathbf{k}_1, \mathbf{k}_2) = \frac{\mathbf{k}_{12} \cdot \mathbf{k}_1}{k_1^2}, \quad \beta(\mathbf{k}_1, \mathbf{k}_2) = \frac{k_{12}^2 (\mathbf{k}_1 \cdot \mathbf{k}_2)}{2k_1^2 k_2^2}, \quad (1.66)$$

These can be solved using a perturbative approach:

$$\delta(\mathbf{k}, \eta) = \sum_{n=1}^{\infty} \delta^{(n)}(\mathbf{k}, \eta), \quad \theta(\mathbf{k}, \eta) = \sum_{n=1}^{\infty} \theta^{(n)}(\mathbf{k}, \eta), \quad (1.67)$$

with n indicating the order of the perturbative expansion.

On large scales ($k \rightarrow 0, \delta^{(1)} \ll 1$), the quadratic source term on the right-hand side (r.h.s.) of Eqs. (1.64) and (1.65) can be neglected. This is equivalent to assuming that the interactions between different Fourier modes are negligible: we obtain then the differential equation for the evolution of the linear density contrast (which is Eq. 1.58):

$$\frac{\partial^2}{\partial \eta^2} \delta^{(1)}(\mathbf{k}, \eta) + \mathcal{H}(\eta) \frac{\partial}{\partial \eta} \delta^{(1)}(\mathbf{k}, \eta) - \frac{3}{2} \Omega_m(\eta) \mathcal{H}^2(\eta) \delta^{(1)}(\mathbf{k}, \eta) = 0 \quad (1.68)$$

The equations of motion (1.64) and (1.65) suggest the ansatz of writing the n -th order solution in Eq. (1.67) as:

$$\begin{aligned} \delta^{(n)}(\mathbf{k}, \eta) &= \int_{\mathbf{k}_1} \cdots \int_{\mathbf{k}_n} (2\pi)^3 \delta_D(\mathbf{k} - \mathbf{k}_{12\dots n}) \\ &\quad \times F_n(\mathbf{k}_1, \dots, \mathbf{k}_n, \eta) \delta^{(1)}(\mathbf{k}_1, \eta) \cdots \delta^{(1)}(\mathbf{k}_n, \eta) \end{aligned} \quad (1.69)$$

$$\begin{aligned} \theta^{(n)}(\mathbf{k}, \eta) &= -\mathcal{H}(\eta) f(\eta) \int_{\mathbf{k}_1} \cdots \int_{\mathbf{k}_n} (2\pi)^3 \delta_D(\mathbf{k} - \mathbf{k}_{12\dots n}) \\ &\quad \times G_n(\mathbf{k}_1, \dots, \mathbf{k}_n, \eta) \delta^{(1)}(\mathbf{k}_1, \eta) \cdots \delta^{(1)}(\mathbf{k}_n, \eta), \end{aligned} \quad (1.70)$$

with F_n and G_n being respectively the density and velocity divergence kernels, which are time-independent in Einstein-de Sitter cosmologies ($\Omega_{m,0} = 1$) – and to good approximation in Λ CDM –, where they take the form:

$$F_2(\mathbf{k}_1, \mathbf{k}_2) = \frac{5}{7} + \frac{2}{7} \frac{(\mathbf{k}_1 \cdot \mathbf{k}_2)^2}{k_1^2 k_2^2} + \frac{\mathbf{k}_1 \cdot \mathbf{k}_2}{2k_1 k_2} \left(\frac{k_1}{k_2} + \frac{k_2}{k_1} \right) \quad (1.71)$$

$$G_2(\mathbf{k}_1, \mathbf{k}_2) = \frac{3}{7} + \frac{4}{7} \frac{(\mathbf{k}_1 \cdot \mathbf{k}_2)^2}{k_1^2 k_2^2} + \frac{\mathbf{k}_1 \cdot \mathbf{k}_2}{2k_1 k_2} \left(\frac{k_1}{k_2} + \frac{k_2}{k_1} \right). \quad (1.72)$$

We finally arrive at the solution for the “next-to-leading order” (NLO) contribution to the matter PS (and velocity PS, which we do not write explicitly), which allows expressing the nonlinear PS as

$$P_{\text{mm}}(k) = P_L(k) + P_{\text{mm}}^{\text{NLO}}(k), \quad (1.73)$$

with

$$P_{\text{mm}}^{\text{NLO}}(k) = P_{\text{mm}}^{(22)}(k) + 2P_{\text{mm}}^{(13)}(k) \quad (1.74)$$

$$P_{\text{mm}}^{(22)}(k) \equiv \langle \delta^{(2)}(\mathbf{k}) \delta^{(2)}(\mathbf{k}') \rangle = 2 \int \frac{d^3 \mathbf{p}}{(2\pi)^3} [F_2(\mathbf{p}, \mathbf{k} - \mathbf{p})]^2 P_L(p) P_L(|\mathbf{k} - \mathbf{p}|) \quad (1.75)$$

$$P_{\text{mm}}^{(13)}(k) \equiv \langle \delta^{(1)}(\mathbf{k}) \delta^{(3)}(\mathbf{k}') \rangle = 3P_L(k) \int \frac{d^3 \mathbf{p}}{(2\pi)^3} F_3(\mathbf{p}, -\mathbf{p}, \mathbf{k}) P_L(p). \quad (1.76)$$

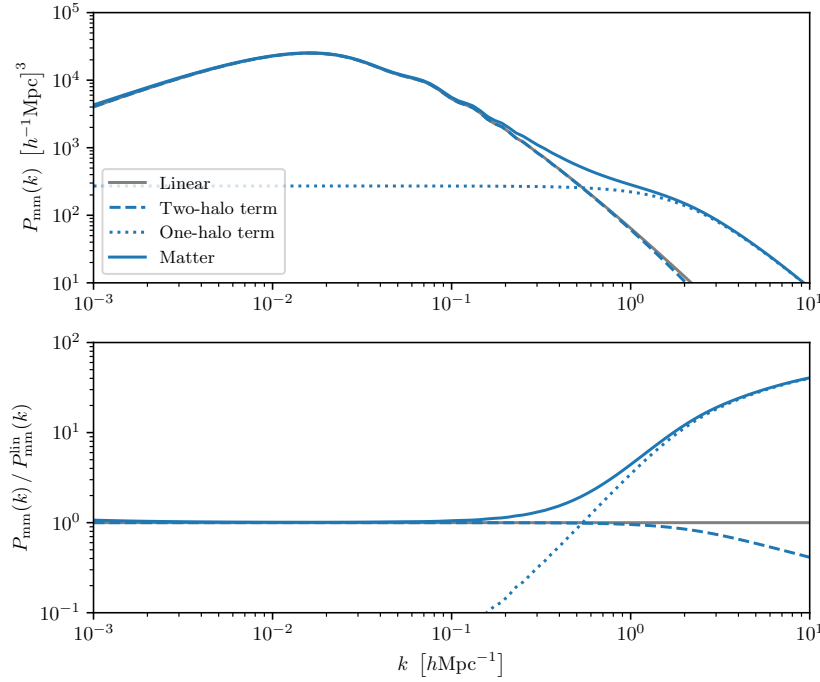


Figure 1.2. The one- and two-halo terms in the matter PS computed with the HM. The two-halo term dominates on large scales and captures well the linear PS (see bottom plot) up to $k \sim 1 h \text{ Mpc}^{-1}$, where the one-halo term is already dominant. The one-halo term acts as a shot-noise contribution on large scales – unphysical but of very little effect –, becoming important at the nonlinear threshold $k \sim 0.1 h \text{ Mpc}^{-1}$. Plot produced with the `pyhalomodel` code (Asgari et al., 2023), adapted from one of the notebooks available at <https://github.com/alexander-mead/pyhalomodel/tree/main>

In the above equation, we indicated with P_L the linear matter PS and introduced the third-order mode-coupling density kernel F_3 :

$$F_3(\mathbf{k}_1, \mathbf{k}_2, \mathbf{k}_3) \equiv \frac{7}{18} \frac{\mathbf{k}_{12} \cdot \mathbf{k}_1}{k_1^2} [F_2(\mathbf{k}_2, \mathbf{k}_3) + G_2(\mathbf{k}_1, \mathbf{k}_2)] + \frac{1}{18} \frac{k_{12}^2 (\mathbf{k}_1 \cdot \mathbf{k}_2)}{k_1^2 k_2^2} [G_2(\mathbf{k}_2, \mathbf{k}_3) + G_2(\mathbf{k}_1, \mathbf{k}_2)] . \quad (1.77)$$

Perturbation theory will also be used in Sect. 4.2.2 to derive some of the terms needed to compute the matter power spectrum response to a shift (perturbation) in the background density.

Halo Model

Another powerful framework to model the nonlinear clustering of matter is the halo model (HM, Seljak (2000); Ma and Fry (2000); Peacock and Smith (2000); see also Asgari et al. (2023) for a recent comprehensive review). This model relies on the main assumption that most of the matter in our Universe is concentrated in *halos*, regions with ~ 200 times the critical density (although different definitions

are possible). The power spectrum is then seen as the sum of two contributions:

$$P(k) = P_{1h}(k) + P_{2h}(k) , \quad (1.78)$$

where $P_{1h}(k)$ describes the two-point correlations amongst the same halo (“intra-halo”, or 1-halo), which become relevant at small (“sub-halo”) scales, and $P_{2h}(k)$ captures the correlations amongst two different halos (“inter-halo”, or 2-halo), which describe the large-scale PS. These are shown in Fig. 1.2. A key assumption of this approach is that the growth of halos should depend only on the local physics at the scale of the halo, and not on the large-scale distribution of matter (Bird et al., 2012). The expressions for these two terms are given by:

$$P_{1h}(k) = I_2^0(k, k) \quad (1.79)$$

$$P_{2h}(k) = \left[I_1^1(k) \right]^2 P_L(k) , \quad (1.80)$$

having defined the auxiliary halo model functions $I_\mu^\beta(k)$ (Cooray and Hu, 2001), consisting essentially of integrals over the halo mass:

$$I_\mu^\beta(k_1, \dots, k_\mu) \equiv \int dM \Phi_{MF} \left(\frac{M}{\bar{\rho}_m} \right)^\mu b_\beta^h \prod_{i=1}^\mu \tilde{u}(k_i | M) , \quad (1.81)$$

M being the halo mass, Φ_{MF} the halo mass function, $\bar{\rho}_m$ the background matter density, $b_0^h = 1$, $b_1^h = b^h(M)$ the linear halo bias, and $\tilde{u}_M(k|M)$ the Fourier transform of the halo density profile normalized so that $\tilde{u}(k=0|M) = 1$.

The halo mass M is usually defined as the mass enclosed within a sphere of radius R where the average density is Δ times the critical (or mean matter) density of the Universe, with e.g. $\Delta = 200$ (as mentioned above). The halo mass function $\Phi_{MF} = dn/dM$ describes the number density n of halos as a function of their mass, commonly described through the Press-Schechter formalism (Press and Schechter, 1974) and its extensions. Analogously to the linear galaxy bias, the linear halo bias $b^h(M)$ quantifies how the distribution of halos of a given mass M traces the underlying matter distribution. A bias of $b^h(M) = 1$ means that halos trace the matter distribution perfectly (that is, $\delta_{\text{halos}}(\mathbf{x}) = \delta_m(\mathbf{x})$), while $b^h(M) > 1$ or $b^h(M) < 1$ indicate that halos are respectively more or less clustered than the total matter. The halo density profile describes the density of matter as a function of radial distance from the center of a dark matter halo. This profile is crucial for understanding the internal structure of halos and is usually modelled using profiles like the Navarro-Frenk-White (NFW; Navarro et al. 1996):

$$\rho(r) = \frac{\rho_s}{\frac{r}{R_s} \left(1 + \frac{r}{R_s} \right)^2} , \quad (1.82)$$

with ρ_s and R_s the halo-dependent scaling density and scaling radius respectively, or the Einasto profile. The auxiliary halo model function I_μ^β allows integrating over all halos to get the total power spectrum (or correlation function), encapsulating the contributions from halos of all masses and sizes.

The halo model is at the core of commonly adopted semi-analytical models like *halofit* (Smith et al., 2003), which is based on empirical fitting formulas obtained from N -body DM simulations. Originally introduced for a CDM universe, it has been updated in Takada and Hu (2013) to use better simulation and to account for DE with a constant equation of state (reaching a quoted accuracy of 5% for $k \leq 1 h \text{ Mpc}^{-1}$ at $0 \leq z \leq 10$ and 10% for $1 h \text{ Mpc}^{-1} \leq k \leq 10 h \text{ Mpc}^{-1}$ at $0 \leq z \leq 3$) and in Bird et al. (2012) to account for massive neutrinos, which as seen in Sect. 1.5 suppress the nonlinear power spectrum. We will take this (dubbed **TakaBird**) as the reference model for the nonlinear clustering of matter, and discuss other possible options in Chap. 6.

We note that this model does *not* account for baryonic feedback, which has a non-negligible effect on very small scales (up to 15% suppression of power at $k \sim 10 h \text{ Mpc}^{-1}$ and $z = 0$, Chisari et al. 2018) and is even harder to model.

Lastly, we note that the Vlasov-Poisson system of equations can be solved numerically: this is the approach adopted in N -body simulations, where the phase-space is volume discretized and its evolution is solved (time-)step by step. DM halos can then be identified and populated with galaxies through, e.g., a halo occupation distribution (HOD) or the abundance matching technique. We will not explore the details of numerical simulations here, but we will rely on some results from the *Euclid* “Flagship” DM simulation (Potter et al., 2017) in the next chapters.

1.5 Neutrinos

Neutrinos are chargeless, weakly interacting leptons the existence of which was postulated in 1930 by Wolfgang Pauli to explain the apparent non-conservation of energy in beta decay processes, specifically in the context of neutron decay (see Ramond 1999 for a brief historical review):

$$n \rightarrow p + e^- + \bar{\nu}_e . \quad (1.83)$$

They can be categorised according to their type, or *flavor* (electronic, ν_e , muonic, ν_μ , or tauonic, ν_τ) or their mass (ν_1, ν_2, ν_3) eigenstates. Since they interact so little with matter, they are called a *free streaming* component, i.e. they can travel for enormous distances without interacting; this makes detecting them a very hard job. The free streaming length can reach cosmological scales, and is sometimes defined as the distance travelled in the Hubble time $t_H = H_0^{-1}$ (while they are relativistic).

Neutrinos - and photons - are usually assumed to be the only light (sub-KeV) relic particles still existing after Big Bang Nucleosynthesis (BBN). The study of these particles in Cosmology mainly revolves around the effect they leave on BBN, CMB anisotropies and large-scale clustering. This is because cosmological experiments are sensitive to the effective number of neutrino species N_{eff} - defined as the relativistic energy density beyond that of photons, in units of one neutrino, in the instantaneous decoupling limit (Verde, 2010) - and the sum of their masses Σm_ν .

The *effective* number of neutrino species is related to the ratio $\frac{\rho_\nu}{\rho_\gamma}$ via the relation

$$\frac{\rho_\nu}{\rho_\gamma} = \frac{7}{8} N_{\text{eff}} \left(\frac{4}{11} \right)^{4/3}. \quad (1.84)$$

If the three species decouple instantaneously from the primordial plasma (at a temperature $T \simeq 2\text{MeV}$), N_{eff} will indeed be equal to the number of neutrino species $N_\nu = 3$; in a more realistic treatment, accounting for non-instantaneity of the decoupling process, we can use the same formula with a slightly different value for N_{eff} (e.g., the Standard Model prediction $N_{\text{eff}} = 3.044$, see [Bennett et al. 2021](#)).

Neutrinos are characterised by being a relativistic component at early times, before switching to the non-relativistic regime (“nr”) at a redshift corresponding to the moment their average momentum equals their mass m_i , with i running over the different mass eigenstates:

$$z_i^{\text{nr}} = \frac{m_i}{0.53\text{meV}} - 1. \quad (1.85)$$

While relativistic, they contribute to the radiation component ($\Omega_r = \Omega_\gamma + \Omega_\nu$), then they become part of the matter component ($\Omega_m = \Omega_b + \Omega_c + \Omega_\nu$). This transition happens at $z \simeq 110$ for $m_\nu = 0.6\text{ eV}$, thus in the matter-dominated regime. As mentioned, when non-relativistic, neutrinos make a very good Dark Matter candidate, being so weakly interacting; however they have large thermal velocity, given by $v_i/c = 0.53(1+z)\text{meV}/m_i$. Mixed Dark Matter models treat them as a Hot DM fraction.

One of the most important properties of these particles is their mass; the phenomenon of neutrino oscillation - the variation of the flavour during their propagation - suggests that at least two mass eigenstates have non-zero mass. In particular, oscillation of solar and atmospheric neutrinos has allowed measuring the differences of squared neutrino masses, while remaining blind to the absolute mass scale. This allows for two possible mass orderings, or *hierarchies* ([Esteban et al., 2020](#); [de Salas et al., 2021](#); [Capozzi et al., 2021](#)):

$$\Delta m_{21}^2 = m_2^2 - m_1^2 = 7.37 \times 10^{-5} \text{ eV}^2 \quad (1.86)$$

$$\Delta m^2 = m_3^2 - (m_1^2 + m_2^2)/2 = 2.50 \times 10^{-3} \text{ eV}^2 \quad (\text{Normal Hierarchy}) \quad (1.87)$$

$$= -2.46 \times 10^{-3} \text{ eV}^2 \quad (\text{Inverted Hierarchy}) \quad (1.88)$$

Because of the small difference between m_1 and m_2 , we have $\Delta m^2 \simeq |\Delta m_{13}^2| \simeq |\Delta m_{23}^2|$. If the lightest neutrino (m_1 or m_3) is much heavier than the mass differences we deal with almost degenerate species, since the masses would be very close (see [Fig. 1.3](#)). If instead the lightest neutrino mass is close to zero, we can estimate the lower limits of $\Sigma m_\nu = m_1 + m_2 + m_3$ as:

$$\text{NH} : m_1 \simeq 0 \rightarrow \Sigma m_\nu \simeq \sqrt{\Delta m_{12}^2} + \sqrt{\Delta m_{23}^2} \simeq 0.06 \text{ eV} \quad (1.89)$$

$$\text{IH} : m_3 \simeq 0 \rightarrow \Sigma m_\nu \simeq \sqrt{\Delta m_{13}^2} + \sqrt{\Delta m_{23}^2} \simeq 2\sqrt{\Delta m_{13}^2} + \sqrt{\Delta m_{12}^2} \simeq 0.1 \text{ eV} \quad (1.90)$$

Since the neutrino temperature today is greater than $|\Delta m_{31}^2|^{1/2}$ and $|\Delta m_{21}^2|^{1/2}$, at least two mass eigenstates are non-relativistic. The best cosmology can do in this

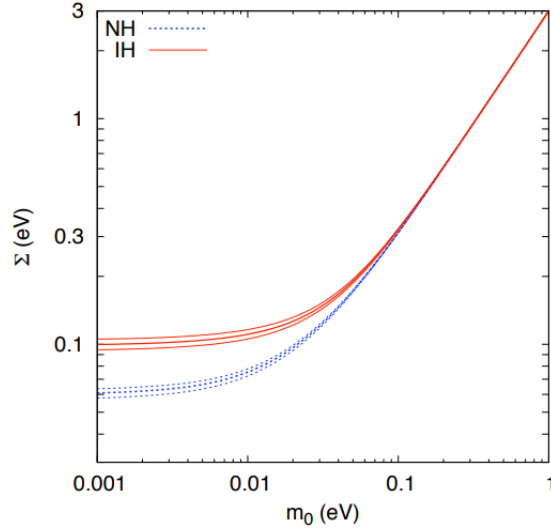


Figure 1.3. Total neutrino mass as a function of the lightest state m_0 within the 3σ regions. Blue dotted (red solid) lines correspond to normal (inverted) hierarchy for neutrino masses, where $m_0 = m_1$ ($m_0 = m_3$). Source: (Lesgourgues and Pastor, 2012)

sense, to this day, is to place an upper bound on the total mass $\Sigma m_\nu = m_1 + m_2 + m_3$. Improving this upper limit is one of the aims of *Euclid*.

The way to experimentally measure the neutrino mass is through its effect on the matter power spectrum. We can relate the neutrino energy density with their mass sum:

$$\Omega_\nu = \frac{\rho_\nu}{\rho_0} = \frac{\Sigma m_i}{93.14 h^2 \text{eV}} ; \quad (1.91)$$

we can define the neutrino density fraction f_ν as

$$f_\nu \equiv \frac{\rho_\nu}{\rho_c + \rho_b + \rho_\nu} = \frac{\Omega_\nu}{\Omega_m} . \quad (1.92)$$

Neutrinos do not cluster on scales smaller than their (comoving) free streaming length, which is related to their velocity (assumed to be the thermal velocity) via

$$\lambda_{\text{fs}} = \frac{2\pi a(t)}{k_{\text{fs}}} = 2\pi \sqrt{\frac{2}{3}} \frac{v_{\text{th}}(t)}{H(t)} \simeq 126 \text{ Mpc/h} \quad (1.93)$$

with the last value calculated at the current time. The thermal velocity equals c before the non-relativistic transition, and

$$v_{\text{th}} \simeq 158(1+z) \left(\frac{1 \text{eV}}{m} \right) \text{ km s}^{-1} \quad (1.94)$$

afterwards. On scales larger than λ_{fs} , neutrinos cluster like CDM: this means that the power spectrum of matter fluctuations, related to the matter density fluctuations $\delta_m = \delta_b + \delta_c + \delta_\nu$ is damped on small scales, because the velocity of neutrinos is

larger than the escape velocity of the gravitational potential wells on those scales; the larger the neutrino mass, the more damping occurs (Audren et al., 2013). The lack of clustering on scales $k > k_{\text{fs}} (\simeq 0.05 h \text{ Mpc}^{-1})$ at current time for $m_\nu = 0.06 \text{ eV}$ damps the matter power spectrum by a factor (Bird et al., 2012)

$$\frac{\delta P_{\text{m}}(k)}{P_{\text{m}}(k)} \simeq -8f_\nu \quad \text{for} \quad f_\nu < 0.07. \quad (1.95)$$

On scales $k < k_{\text{fs}}$ neutrinos could not free stream for the whole cosmic history, inducing a smaller suppression. The maximum scale at which neutrinos alter the PS is given by

$$k_{\text{nr}} \simeq 0.018 \sqrt{\Omega_{\text{m}} \left(\frac{\Sigma m_\nu}{1 \text{ eV}} \right)} \frac{h}{\text{Mpc}}, \quad (1.96)$$

for which they free-streamed only immediately after becoming non-relativistic.

1.6 Constraints on cosmological parameters from current experiments

As stated above, *Euclid*'s aim is to place tight constraints on the cosmological parameters, for a variety of different models; to better contextualize this statement, we briefly report the current state of the art in the measurement of such parameters. For CMB observations, the reference results are the ones from the *Planck* mission, which constitute our fiducial choice. Some constraints for key parameters from the temperature and polarization anisotropies, as well as their cross-correlation and CMB lensing, are (Planck Collaboration et al., 2014) $\Omega_{\text{m},0} = 0.3156 \pm 0.0091$ (3%), $\sigma_8 = 0.831 \pm 0.013$ (1%); for the time-varying DE EoS parameters, *Planck* alone has a low constraining power, and is combined with external LSS datasets and observations of Supernovae Ia to get (Planck Collaboration et al., 2020b) $w_0 = -0.957 \pm 0.080$ (8%) and $w_a = -0.29^{+0.32}_{-0.26}$ (100%).

Concerning LSS surveys, we quote the recent values from the Dark Energy Survey (DES: Crocce et al. 2019; Hoyle et al. 2018) Year 3 results (Abbott et al., 2022); we refer to the combination of weak lensing cosmic shear and photometric galaxy clustering, which will be formally introduced in Sect. 3, as well as the combination with datasets from previous LSS experiments, such as the Baryon Oscillation Spectroscopic Survey (BOSS, Dawson et al. 2016). For the baseline Λ CDM parameters, DES reports $\Omega_{\text{m},0} = 0.339^{+0.032}_{-0.031}$ (10%) and $\sigma_8 = 0.733^{+0.039}_{-0.049}$ (6%) uncertainties; and $w_0 \gtrsim -1.4$, $w_a = -0.9 \pm 1.2$, which improve to $w_0 = -0.95 \pm 0.08$ (8%), $w_a = -0.4 \pm 0.4$ (100%) when including other external LSS datasets. *Euclid*-only photometric forecast quote in the optimistic case a precision of 0.3% on $\Omega_{\text{m},0}$ and 0.1% on σ_8 , and 2% and 10% on w_0 and w_a respectively, suggesting the magnitude of the increase in precision. The forecast setup leading to these results will be illustrated in detail in the following Chapters.

Chapter 2

Statistics

One of the peculiarities of Cosmology is the fact that only one realization of the phenomenon to be characterized (the Universe itself) is accessible to the observer. Moreover, Cosmology has an inherently probabilistic nature: most of the processes we observe, especially in large-scale structure (LSS) studies, originate in the inflationary paradigm from quantum random fluctuations of the primordial Universe, which constitute its initial conditions. This makes the Bayesian approach to probability the most suited to analyze and interpret the data in the context of the different models under consideration.

This chapter will introduce the statistical framework and specific tools used in this work (and in general in Cosmology) to define meaningful physical observables, to forecast the expected constraints on the model parameters of interest and to perform inference on the actual data. We will mainly rely on Bayes' theorem, and introduce the Fisher Information Matrix (FM) as a powerful forecasting tool. We will then outline the two-point observables used in this work (following the *de facto* standard in cosmological analyses), in particular the power spectrum. These tools constitute the building blocks of modern cosmological analyses.

2.1 Bayes' Theorem

The pivotal idea in all of Statistics is arguably the concept of probability, around which two main schools of thought exist: the frequentist and the Bayesian. In the frequentist framework, probability is defined as

$$P(A) = \lim_{N \rightarrow \infty} \frac{n(A)}{N} \quad (2.1)$$

where $P(A)$ is the probability of event A occurring, and $n(A)$ is the number of times the event A occurs in N equiprobable trials. It is therefore defined as the relative frequency, in the limit of infinite trials.

This definition hinges on an asymptotic behaviour, therefore assuming that it is indeed possible to repeat the experiment – which we can think of as a random “draw”, or realization, of a physical process – an infinite (very large) number of times. Cosmology offers a perfect example of a situation in which this is not possible.

The Bayesian approach, by contrast, defines probability as the *degree of belief* in a hypothesis, which can be influenced by some prior knowledge about the said hypothesis. This makes probability not an inherent property of the process, but rather a subjective measure, contingent upon the available information to the observer. For two events, or hypotheses, A and B , we have:

$$P(A|B) = P(B \cap A)P(B) \quad (2.2)$$

where $P(A|B)$ is the *conditional probability*, the probability of the occurrence of A once B has occurred, i.e, conditioned to the occurrence of B ; $P(A \cap B)$ is the *joint probability*, the probability for both A and B to occur simultaneously. Finally, $P(B)$ is the *marginal probability* for B to occur, which can be obtained by summing or integrating over all possible outcomes of A that are compatible with B . From the commutative property of joint probability $P(A \cap B) = P(B \cap A)$ and Eq. (2.2) we easily obtain Bayes' theorem:

$$P(A|B) = \frac{P(B|A)P(A)}{P(B)}, \quad (2.3)$$

which holds also in the frequentist paradigm, being it a direct consequence of Eq. (2.2). This expression can be cast in a form more pertinent to our discussion if we let A and B be respectively the ensemble of model parameters, organised in a vector $\boldsymbol{\theta} = (\theta_1, \theta_2 \dots \theta_m)$, and the observed (or synthetic) data, $\mathbf{d} : d_i = (x_i, y_i)$, $i = 1, 2, \dots, n$; here, x_i is the independent variable, e.g., the values of the multipoles ℓ when measuring the angular power spectra $C(\ell)$ (see Sect. 2.4.2). In this way, we have:

$$P(\boldsymbol{\theta}|\mathbf{d}) = \frac{P(\mathbf{d}|\boldsymbol{\theta})P(\boldsymbol{\theta})}{P(\mathbf{d})}. \quad (2.4)$$

The meaning of the above probability density functions (PDFs) is as follows:

- $P(\boldsymbol{\theta}|\mathbf{d})$ is the *posterior*, the probability of the model parameters $\boldsymbol{\theta}$ being true given the measurement of the data \mathbf{d} . It is the quantity we want to compute, from which we can extract the expected values of the parameters, their uncertainties and their covariance. This interpretation is unique to the Bayesian approach, in which parameters are random variables themselves; the frequentist approach, on the other hand, does not assign probabilities to parameters, which are seen as unknown but fixed quantities inherent to the system under study.
- $P(\mathbf{d}|\boldsymbol{\theta})$ is the *likelihood*, the probability of the data \mathbf{d} given a model $\boldsymbol{\theta}$. It is often written as $\mathcal{L}(\boldsymbol{\theta})$, and treated as a function of the model parameters only (for a fixed data vector, the observations themselves). Parameter estimation aims at finding the particular vector $\boldsymbol{\theta}^*$ which maximizes \mathcal{L} (the “argmax” of \mathcal{L}); in our case of interest, this also means maximizing the posterior (see Eq. 2.6).
- $P(\boldsymbol{\theta})$ is the *prior*, and encodes any knowledge, or *prejudice* we may possess on the model parameters before performing the experiment; these can come from theoretical predictions or from other experiments. Such knowledge is

parameterized as a PDF for the different parameters θ_i . Broad, flat prior distributions are often used to let the posterior distribution be influenced almost exclusively by the data at hand, although flat priors can still carry information (for example, on the credible intervals of a parameter's values) and can be non-flat in a different parameter basis.

- $P(\mathbf{d})$ is the *evidence*. This is the probability of \mathbf{d} as determined by summing (or integrating) across all possible values of $\boldsymbol{\theta}$, weighted by the probability of $\boldsymbol{\theta}$, and it acts as a normalisation factor.

To find the analytical form of $P(\mathbf{d})$ we can integrate Eq. (2.4) in $d\boldsymbol{\theta}$ and solve for the evidence. Since $P(\mathbf{d})$ does not depend on $\boldsymbol{\theta}$ and the posterior is normalised to 1 (that is, $\int P(\boldsymbol{\theta}|\mathbf{d})d\boldsymbol{\theta} = 1$), we get

$$P(\mathbf{d}) = \int P(\boldsymbol{\theta})\mathcal{L}(\mathbf{d}|\boldsymbol{\theta})d\boldsymbol{\theta} \quad (2.5)$$

This operation is in general numerically expensive because the dimensionality of the problem is set by the number of model parameters (including the nuisance parameters, describing quantities which are not of direct interest, such as systematic effects). Luckily, the overall normalization of the posterior is not important in parameter inference, since we are only interested in finding the argument that maximises the distribution, and not the value of the maximum itself. This is not the case for model selection, which we will not treat here.

in the case of flat prior probability distributions, Bayes' theorem simplifies to

$$P(\boldsymbol{\theta}|\mathbf{d}) \propto \mathcal{L}(\mathbf{d}|\boldsymbol{\theta}) . \quad (2.6)$$

In order to construct the likelihood we need a model, which provides a function $f(\mathbf{x}, \boldsymbol{\theta})$ such that $f(x_i, \boldsymbol{\theta})$ approximates y_i well enough $\forall i$ (Kerscher and Weller, 2019). In our case, the function f is the theoretical modelling of the angular PS: $y_i = C(x_i = \ell_i, \boldsymbol{\theta})$. Moreover, an error model for the data is needed. It should be noted that in the context of this work, we will not test different models (say, $f(x, \boldsymbol{\theta})$ vs $g(x, \boldsymbol{\phi})$); we will focus instead on the standard Λ CDM concordance model, extending the parameter space when necessary (e.g., adding curvature as a free parameter or using the CPL parameterization for the Dark Energy equation of state as in Eq. 1.21). Thus f will be fixed throughout, and when incurring no risk of ambiguity the model parameter vector $\boldsymbol{\theta}$ itself will be referred to as the “model”.

If the measurements y_i are drawn from a normal distribution, or if the sample size is sufficiently large (by virtue of the central limit theorem), the likelihood takes the form of a multivariate Gaussian, or

$$\mathcal{L}(\boldsymbol{\theta}) = \prod_{j=1}^n \frac{1}{\sqrt{2\pi}\sigma_j} \exp\left(-\frac{(y_j - f(x_j, \boldsymbol{\theta}))^2}{2\sigma_j^2}\right) , \quad (2.7)$$

where we introduced the variance of the data σ_j^2 ; n is the number of data points. Here, we assumed the data to be independent and identically distributed (iid), which means that their covariance matrix is diagonal. If instead the data are correlated,

we define a covariance matrix with elements $\text{Cov}_{ij} = \langle (y_i - f(x_i, \boldsymbol{\theta}))(y_j - f(x_j, \boldsymbol{\theta})) \rangle$, and write \mathcal{L} as

$$\mathcal{L}(\boldsymbol{\theta}) = \frac{1}{[(2\pi)^n \det(\text{Cov})]^{1/2}} \exp \left(-\frac{1}{2} \boldsymbol{\Delta}^T \text{Cov}^{-1} \boldsymbol{\Delta} \right), \quad (2.8)$$

where $\boldsymbol{\Delta}$ is the residual vector between the observed data and the model prediction. The term $\boldsymbol{\Delta}^T \text{Cov}^{-1} \boldsymbol{\Delta}$ is commonly referred to as χ^2 . The χ^2 statistic follows a chi-squared distribution with n degrees of freedom under the null hypothesis that the model is an adequate description of the data. Minimizing the χ^2 is equivalent to maximizing the likelihood, thus providing the best-fit model parameters $\boldsymbol{\theta}^*$.

Note that the likelihood can take other functional forms beyond the (multivariate) Gaussian. This, however, has been found to be a good approximation for the *Euclid* photometric survey, producing a negligible effect on the best-fit parameters and their uncertainties, as discussed in Upham et al. (2021). We also stress the fact that, even if \mathcal{L} is Gaussian in the data, this is not necessarily the case for the model parameters: indeed, this is true only if f is a linear function. The likelihood is in general a complicated function of $\boldsymbol{\theta}$, which is one of the reasons why we need to sample (explore) it using numerical techniques. A “good” experiment (i.e., a constraining dataset), however, will allow exploring the likelihood function sufficiently close to the peak; in this region, the log-likelihood can be approximated well by a second-order expansion, the exponential of which yields precisely a normal distribution.

For multiple experiments that produce independent datasets D_j the total likelihood function is the product of the ones for each dataset:

$$\mathcal{L}_{\text{tot}} = \mathcal{L}(D_{\text{tot}}|\boldsymbol{\theta}) = \prod_{j=1}^n \mathcal{L}_j(D_j|\boldsymbol{\theta}). \quad (2.9)$$

This is because, for independent datasets, the joint probability distribution is simply the product of the individual PDFs, which, in the context of parameter estimation, translates to the product of individual likelihood functions.

In general, the cross-correlation of data from different cosmological probes offers an extremely powerful tool for improving the constraining power, by leveraging the different nature of the probes and of the different systematics affecting them. An example of this is the cross-correlation of weak lensing and galaxy clustering, which is able to mitigate the systematic uncertainty affecting the latter probe as a tracer of the dark matter distribution, parameterized by the galaxy bias parameters. These LSS probes, as in many other cases, are not statistically independent. The datasets exhibit covariance, either because they originate from overlapping regions of the sky, share common observational techniques, or are influenced by similar systematic effects. In such cases, the total likelihood function \mathcal{L}_{tot} becomes

$$\mathcal{L}_{\text{tot}}(D_{\text{tot}}|\boldsymbol{\theta}) = \exp \left[-\frac{1}{2} \boldsymbol{\Delta}^T \text{Cov}^{-1} \boldsymbol{\Delta} \right], \quad (2.10)$$

where $\boldsymbol{\Delta}$ is again the vector of residuals and Cov is the total covariance matrix, which encapsulates the covariance of each dataset as well as the “cross-covariance”

between them. As will be shown in Sect. 5.1.5, the covariance matrix is often decomposed into signal and noise terms, $\text{Cov} = \text{Cov}_{\text{signal}} + \text{Cov}_{\text{noise}}$, respectively due to the observed signal and observational noise or other systematics. An accurate covariance matrix, which can be derived from analytical models, simulations or bootstrap resampling techniques is crucial for unbiased parameter inference.

2.2 Fisher Information Matrix

In order to understand if an experiment will be able to improve significantly our knowledge of some physical quantities (i.e., to reduce the uncertainties on some model parameters) *before actually performing it*, we need a way to translate the information on the experimental setup into the predicted parameter uncertainties; in other words, we need a way to propagate the expected uncertainty on the data in the expected uncertainty on the parameters. In this way, we can optimize the survey design to achieve the best possible constraining power. This is possible through the Fisher Information Matrix (Fisher, 1935).

The Fisher Matrix describes the curvature of the likelihood function, which in turn encodes the sensitivity of the experiment on a given parameter (i.e., with respect to a given direction in parameter space), and hence the associated uncertainty. If the likelihood falls steeply from the maximum in some direction, the uncertainty on the corresponding parameter will be small, and vice-versa. To construct the FM, we need three ingredients (Dodelson and Schmidt, 2020):

- A model with its parameters. We choose some particular parameter values, dubbed *fiducial*, which we assume describe the real Universe. The argmax of the likelihood is therefore known by construction. The FM can indeed only provide information on the forecasted uncertainties, not on the best-fit values.
- The theory (model) prediction as a function of the model parameters
- The expected covariance of the data around the fiducial.

Note that in doing this we are assuming the true Universe to be described by the chosen fiducial cosmology; we assume the argmax of the likelihood function to be known, and we compute the curvature of the function around the maximum. This means that, in general, we cannot use the FM formalism to quantify the shift (bias) in the best-fit parameters from an incorrect modelling or from neglecting some systematic effects. Appendix A of Camera et al. (2017) shows an interesting approach to circumvent this limitation in the case of nested models (two models are “nested” if the parameter space of one is contained in the parameter space of the other).

We start by expanding the logarithmic form of Eq. (2.7) (the “log-likelihood”) as a function of $\boldsymbol{\theta}$, around the fiducial vector $\boldsymbol{\theta}_{\text{fid}}$ (Verde, 2010):

$$\ln\mathcal{L}(\boldsymbol{\theta}) = \ln\mathcal{L}(\boldsymbol{\theta}_{\text{fid}}) + \frac{1}{2} \sum_{ij} (\theta_i - \theta_{\text{fid},i}) \left. \frac{\partial^2 \ln\mathcal{L}(\boldsymbol{\theta})}{\partial\theta_i \partial\theta_j} \right|_{\boldsymbol{\theta}_{\text{fid}}} (\theta_j - \theta_{\text{fid},j}) + \dots \quad (2.11)$$

The first term vanishes by construction; the term containing the second derivatives,

$$\mathcal{H}_{ij} = - \left. \frac{\partial^2 \ln \mathcal{L}(\boldsymbol{\theta})}{\partial \theta_i \partial \theta_j} \right|_{\boldsymbol{\theta}_{\text{fid}}}, \quad (2.12)$$

is the Hessian matrix. It expresses the local curvature of a multi-variate function, describing how fast the function decreases from the maximum along different directions in the parameter space, and it is used to test whether a point from the domain corresponds to a local maximum, minimum or saddle. In this context, we use it to obtain the parameter covariance. A non-zero covariance between two parameters indicates that variations in the first result in variations in the other. It is a measure of the degree of the linear joint variability of the two parameters.

We can now define the Fisher Matrix as (minus) the expected value of Hessian of our model's log-likelihood. By virtue of the Schwarz theorem, it is symmetric, like \mathcal{H}_{ij} .

$$F_{\alpha\beta} \equiv \left\langle - \frac{\partial^2 \ln \mathcal{L}}{\partial \theta_\alpha \partial \theta_\beta} \right\rangle. \quad (2.13)$$

Again, the brackets indicate an ensemble average, which can be seen as the expected value for a stochastic process. We compute this average over the observed data that we would get if the Universe was indeed described by our fiducial model (Verde, 2010). This matrix encodes the information that the data vector \boldsymbol{d} carries about the model parameters $\boldsymbol{\theta}$, and can also be seen as the covariance of the score function:

$$s(\boldsymbol{\theta}) = \nabla_{\boldsymbol{\theta}} \ln \mathcal{L} \quad (2.14)$$

which is used to evaluate the goodness of our estimated model $\boldsymbol{\theta}$. Under the assumption that the log-likelihood can be approximated to second order as a function of the parameters, and therefore that it is Gaussian in $\boldsymbol{\theta}$, the FM allows computing (lower limits of the) parameter uncertainties from the knowledge of a fiducial model and the measurement uncertainties.

If \mathcal{L} is Gaussian, the log-likelihood is simply proportional to the χ^2 and F depends only on the expected mean and covariance of the data EC20:

$$F_{\alpha\beta} = \frac{1}{2} \text{tr} \left[\frac{\partial \text{Cov}}{\partial \theta_\alpha} \text{Cov}^{-1} \frac{\partial \text{Cov}}{\partial \theta_\beta} \text{Cov}^{-1} \right] + \sum_{pq} \frac{\partial \mu_p}{\partial \theta_\alpha} (\text{Cov}^{-1})_{pq} \frac{\partial \mu_q}{\partial \theta_\beta} \quad (2.15)$$

with $\boldsymbol{\mu}$ mean of the data $\boldsymbol{\mu} = (\mu_1(\boldsymbol{\theta}), \mu_2(\boldsymbol{\theta}), \dots, \mu_n(\boldsymbol{\theta}))$, $\boldsymbol{y} = (y_1, y_2, \dots, y_n)$ the data and $\text{Cov} = \langle (\boldsymbol{y} - \boldsymbol{\mu})(\boldsymbol{y} - \boldsymbol{\mu})^T \rangle$ is their expected covariance. p and q run over the data vector indices, from 1 to n .

Since the uncertainties of the actual data will not depend on the cosmological model (we assume the data covariance to be model-independent, a choice commonly adopted in the literature: see e.g. Joachimi et al. (2021); Friedrich et al. (2021)), we take the derivatives $\partial \text{Cov} / \partial \theta_\alpha = 0$, leaving only the second term; this is the final expression we will use in this work.

$$F_{\alpha\beta} = \sum_{pq} \frac{\partial \mu_p}{\partial \theta_\alpha} (\text{Cov}^{-1})_{pq} \frac{\partial \mu_q}{\partial \theta_\beta}. \quad (2.16)$$

It can be shown that the inverse FM is simply the covariance matrix of the model parameters, which is exactly what we want to compute:

$$C_{\alpha\beta} = (F^{-1})_{\alpha\beta} \quad (2.17)$$

where F^{-1} is the inverse FM and C is the parameter covariance matrix $C_{\alpha\beta} = \rho_{\alpha\beta}\sigma_\alpha\sigma_\beta$, with $\rho_{\alpha\beta}$ the correlation coefficient and σ_α the *marginalised* 1σ uncertainty on the parameter θ_α . It is important not to confuse the *data* covariance matrix, Cov_{pq} , with the *parameter* covariance matrix, $C_{\alpha\beta}$.

The marginalized (1σ) uncertainty on parameter θ_α is then trivially obtained as

$$\sigma_\alpha = \sqrt{C_{\alpha\alpha}} = (F^{-1})_{\alpha\alpha}^{1/2}. \quad (2.18)$$

The uncertainties derived in this way are actually lower bounds, or optimistic estimates, of the actual parameter uncertainties, as stated by the Cramér-Rao inequality; indeed, this estimate is exact only in the case of a Gaussian likelihood:

$$\sigma_\alpha^{\text{non-Gauss}} > (F^{-1})_{\alpha\alpha}^{1/2}. \quad (2.19)$$

Marginalised uncertainties on a given parameter are obtained by integrating out the other parameters, i.e. by integrating over their possible values within some intervals set by the chosen priors. To marginalise is then to find the distribution of one or more random variables by exhausting all the cases on the others:

$$p(x, y | \mathbf{d}) = \iint p(x, y, z, w | \mathbf{d}) dz dw. \quad (2.20)$$

The process is used, for example, to make inference over some physical parameters while correctly taking into account the uncertainty on the *nuisance* parameters (called in this example z and w), describing astrophysical or instrumental systematic uncertainties, and thus being able to provide rigorous confidence intervals on the parameters of interest. As seen above, the FM framework makes it easy to compute these uncertainties, avoiding the need to compute expensive multidimensional integrals of the posterior distribution.

Conditional uncertainty, on the other hand, is the uncertainty on a parameter conditioned to the specific value of another (see Sect. 2.1):

$$\sigma_\alpha^{\text{unmarg.}} = \sqrt{1/F_{\alpha\alpha}}. \quad (2.21)$$

Computing the conditional uncertainties of the cosmological parameters means assuming perfect knowledge of the nuisance ones, which are fixed at a given value. This is an often unrealistic approach, which is why conditional uncertainties are rarely used, but can be convenient in some situations: for example, we can produce forecasts for flat models by conditioning our uncertainties to $\Omega_{k,0} = 0$, without having to re-run the analysis. This can easily be achieved through the Fisher Matrix: it is sufficient to cut the parameter covariance matrix C by removing the rows and columns corresponding to the parameters we wish to fix to their fiducial value (to keep using our example, the row and column corresponding to $\Omega_{k,0}$), and then invert it again to obtain the new (reduced) FM.

To summarize, the algorithm we used to produce the forecasts is the following:

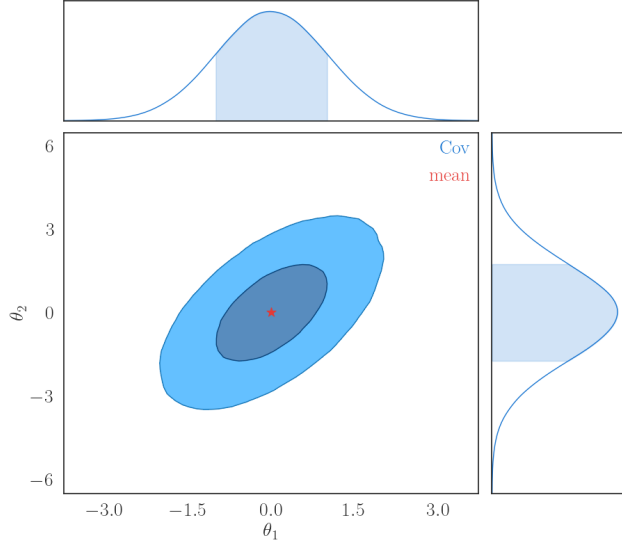


Figure 2.1. The 1σ and 2σ contours for the joint probability distribution for the two parameters θ_1 and θ_2 . On the top and right-hand side are the marginal distributions, obtained by integrating over all possible values of the other parameter. The conditional distribution would be instead obtained by slicing the joint PDF at the desired value of the parameter we condition over. Note that the 1σ contour of a multivariate 2D Gaussian distribution has a smaller probability content than in the 1D case ($\sim 39\%$ vs $\sim 68\%$): in this kind of contour plots, we will refer to the 68% intervals as “ 1σ ”, with a slight abuse of notation.

1. Choose a fiducial model f , and a fiducial (physical and nuisance) parameter vector θ
2. Compute the data covariance matrix
3. Compute the derivatives $\partial f / \partial \theta$ either numerically or analytically
4. Compute the FM

The numerical derivatives are computed through the algorithm proposed in Appendix B of Camera et al. (2017), in which the model is evaluated in 15 points in the neighbourhood of the fiducial value for added numerical stability.

One of the advantages of FM analysis is that Fisher matrices from independent data sets can be added up, because the log-likelihood of independent datasets is the sum of the individual log-likelihoods and by virtue of the sum rule of derivatives. We can leverage this property as a quick way to include (Gaussian) priors of a given variance in our forecast; to do this we construct a separate FM, with all entries set to 0 except the diagonal ones at the index of the parameter of interest. For example, if we want to add a prior on the first parameter, θ_1 , we can use

$$F^{\text{tot}} = F + F^{\text{pr}} = F + \begin{pmatrix} (\sigma_1^{\text{pr}})^{-2} & 0 & 0 & 0 \\ 0 & 0 & \dots & 0 \\ 0 & \vdots & \ddots & \vdots \\ 0 & 0 & \dots & 0 \end{pmatrix} \quad (2.22)$$

where F^{pr} is the priors FM and σ_1^{pr} is the standard deviation of the Gaussian prior on the parameter θ_1 . This method offers a very convenient way to gauge the impact of different priors on the analysis, and will be used in Sect. 5.3.5.

As a final note, we point out that the FM analysis suffers from some limitations, most notably the above-mentioned approximation of Gaussianity of the posterior distribution in the model parameters. This implies that the various 2D projections used to visualize the joint posterior contours over the different couples of parameters are ellipses by construction (see Fig. 2.1), and can only represent linear degeneracies between parameters. Some of the information present in the true multidimensional posterior volume is therefore lost in the FM representation. This is not always a good approximation, as discussed in Wolz et al. (2012); however, this depends on the probe considered and the precision of the experiment. One example of this is the forecasted constraint on n_s for the weak lensing probe in isolation, which is likely overly optimistic considering that the probe is not well-suited to constraint such a parameter (see Sect. 3.2.5). Euclid Collaboration: Casas et al. (2023), however, showed a very good agreement between forecasts obtained for the reference EC20 likelihood in the FM and Monte Carlo Markov Chain approach (see next section) when considering the full photometric survey. This is mainly due to the high precision of *Euclid*, which will, as mentioned above, allow the likelihood to be characterized in a tight neighbourhood of its mode.

2.3 Monte Carlo Markov Chain

A different approach to the problem of characterizing the likelihood function is the Monte Carlo Markov Chain (MCMC) technique. Contrary to the FM, this enables us to find the best-fit values of the parameters – albeit it is more effective in characterizing the distribution around its maximum, than in finding point estimates such as the mode – and in this way to also quantify the bias induced by discrepancies between different models. Moreover, this method is well-suited to treat non-Gaussian posterior distributions.

The core idea is to sample the target distribution (the posterior) through a random walk in parameter space. A simple method to construct a Markov Chain (a sequence in which each step only depends on the previous one) is the Metropolis-Hastings algorithm (Hastings, 1970). The procedure followed to choose the next step, $\boldsymbol{\theta}^{i+1}$, given the current position, $\boldsymbol{\theta}^i$ (with $\boldsymbol{\theta}^0$ being the initial point of the chain), is as follows: we define the *acceptance ratio* r as

$$r = \frac{p(\boldsymbol{\theta}^{i+1})q(\boldsymbol{\theta}^i|\boldsymbol{\theta}^{i+1})}{p(\boldsymbol{\theta}^i)q(\boldsymbol{\theta}^{i+1}|\boldsymbol{\theta}^i)}, \quad (2.23)$$

where p is the target distribution (the posterior) and q is the proposal distribution, the conditional probability of $\boldsymbol{\theta}^{i+1}$ given $\boldsymbol{\theta}^i$ (often taken as Gaussian). At each step, we sample $\boldsymbol{\theta}^{i+1}$ from q and a random number x from a uniform distribution. If $r > x$ we accept the new step, otherwise we reject it and set $\boldsymbol{\theta}^{i+1} = \boldsymbol{\theta}^i$; we then repeat the procedure. This simple algorithm allows the random walker to also explore areas of lower likelihood, for a complete sampling of the hypersurface. An advantage of this approach is the possibility to run many chains in parallel.

Ensuring convergence of the chains, especially in high-dimensional spaces, can be computationally intensive; a commonly adopted way to check this is the Gelman-Rubin convergence diagnostic (Gelman and Rubin, 1992). After a sufficient number

of steps, the different chains should all be close to the stationary distribution. To assess this, it is possible to compare the variance of the chain means, and the mean of chain variances. If all the chains have converged, then the between-chain variation should be close to zero.

Once the chains have been obtained, the posterior distribution is simply given by their histogram: the more often a walker has visited a position in parameter space, the higher the value of the posterior.

2.4 Two-point statistics

A key step in the process of parameter inference is the comparison (fit) of the theory to the data. The observations produced by the *Euclid* mission will allow us to build shear and density maps, characterizing the specific realization of the Universe we live in. It is impossible, and most likely unnecessary, to predict the totality of the features of such a specific realization; we can instead compress the information present in the maps into some summary statistics, for which our current theory is able to produce predictions. The following sections present the summary statistics used in the present work.

2.4.1 Power Spectrum

The most commonly used, and simple, summary statistic is the two-point correlation function (2PCF), and its Fourier transform, the power spectrum. Given two fields $f(\mathbf{x})$ and $g(\mathbf{x}')$, the 2PCF gives their (co)variance as a function of the positions \mathbf{x}, \mathbf{x}' :

$$\xi_{fg}(\mathbf{x}, \mathbf{x}') = \langle f(\mathbf{x})g(\mathbf{x} + \mathbf{x}') \rangle , \quad (2.24)$$

where the brackets indicate the expected value over some ensemble of realizations, or over the volume (see [Peacock 2003](#)). Under the hypotheses of homogeneity and isotropy, ξ becomes function of only the distance: $\xi_{fg}(\mathbf{x}, \mathbf{x}') = \xi_{fg}(|\mathbf{x}' - \mathbf{x}|) = \xi_{fg}(r)$. More specifically, for a homogeneous Poisson process, the probability (number) of points (e.g., galaxies) in two volumes V_1, V_2 is given by

$$dP_{12} = \bar{n}^2 dV_1 dV_2 , \quad (2.25)$$

where \bar{n} is the average number density of points. The 2PCF then quantifies the *excess* probability, with respect to the case of uniform random distribution, (which has a null 2PCF), of finding two points at a separation \mathbf{r} :

$$dP_{12} = \bar{n}^2 [1 + \xi_{12}(r)] dV_1 dV_2 . \quad (2.26)$$

If $f(\mathbf{x})$ is an integrable function we can perform the Fourier transform:

$$\mathcal{F}(f(\mathbf{x})) = \tilde{f}(\mathbf{k}) = \int_{-\infty}^{+\infty} d^3\mathbf{x} f(\mathbf{x}) e^{-i\mathbf{k}\cdot\mathbf{x}} \quad (2.27)$$

and its inverse:

$$\mathcal{F}^{-1}(\tilde{f}(\mathbf{k})) = f(\mathbf{x}) = \int_{-\infty}^{+\infty} \frac{d^3\mathbf{k}}{(2\pi)^3} \tilde{f}(\mathbf{k}) e^{i\mathbf{k}\cdot\mathbf{x}} . \quad (2.28)$$

Sometimes $\tilde{f}(\mathbf{k})$ is called the *spectrum* of $f(\mathbf{x})$. The \mathcal{F} operator allows going from the \mathbf{x} (in our example the spatial coordinates vectors) to the \mathbf{k} (wave vectors, conjugated to \mathbf{x}) spaces, allowing choosing the most convenient basis for the problem at hand. We can now consider the 2PCF function of $\tilde{f}(\mathbf{k})$ and $\tilde{g}(\mathbf{k})$:

$$\langle \tilde{f}(\mathbf{k}) \tilde{g}^*(\mathbf{k}') \rangle = \int d^3\mathbf{x} \int d^3\mathbf{x}' \langle f(\mathbf{x}) f(\mathbf{x}') \rangle e^{-i\mathbf{k}\cdot\mathbf{x}} e^{i\mathbf{k}'\cdot\mathbf{x}'} , \quad (2.29)$$

which under homogeneity assumption becomes

$$\langle \tilde{f}(\mathbf{k}) \tilde{g}^*(\mathbf{k}') \rangle = \int d^3\mathbf{x} \int d^3\mathbf{x}' \xi_{fg}(\mathbf{x}' - \mathbf{x}) e^{-i\mathbf{k}\cdot\mathbf{x}} e^{i\mathbf{k}'\cdot\mathbf{x}'} ; \quad (2.30)$$

performing the variable change $\mathbf{x}' \rightarrow \mathbf{z} = \mathbf{x}' - \mathbf{x}$, we have

$$\langle \tilde{f}(\mathbf{k}) \tilde{g}^*(\mathbf{k}') \rangle = \int d^3\mathbf{x} e^{-i(\mathbf{k}-\mathbf{k}')\cdot\mathbf{x}} \int d^3\mathbf{z} \xi_{fg}(\mathbf{z}) e^{i\mathbf{k}'\cdot\mathbf{z}} , \quad (2.31)$$

Remembering the definition of the Dirac delta $\delta_D^3(\mathbf{k}) = (2\pi)^{-3} \int d^3\mathbf{x} e^{i\mathbf{k}\cdot\mathbf{x}}$ we finally get

$$\langle \tilde{f}(\mathbf{k}) \tilde{g}^*(\mathbf{k}') \rangle = (2\pi)^3 \delta_D^3(\mathbf{k} - \mathbf{k}') P_{fg}(\mathbf{k}) \quad (2.32)$$

or equivalently

$$\langle \tilde{f}(\mathbf{k}) \tilde{g}(\mathbf{k}') \rangle = (2\pi)^3 \delta_D^3(\mathbf{k} + \mathbf{k}') P_{fg}(\mathbf{k}) \quad (2.33)$$

with $P_{fg}(\mathbf{k})$ the power spectrum (or the “cross-spectrum”):

$$P_{fg}(\mathbf{k}) = \int d^3\mathbf{x} \xi_{fg}(\mathbf{x}) e^{-i\mathbf{k}\cdot\mathbf{x}} = \mathcal{F}(\xi_{fg}(\mathbf{x})). \quad (2.34)$$

The PS of fg is therefore the Fourier transform of the two-point correlation function ξ_{fg} . The Dirac delta $\delta_D^3(\mathbf{k} \pm \mathbf{k}')$ ensures the power to be non-zero only when $\mathbf{k} = -\mathbf{k}'$. This comes from the isotropy of the Universe; the power spectrum should only depend on the magnitude of the wavevector \mathbf{k} and not its direction. The factor $(2\pi)^3$ arises from the normalization convention used in the Fourier transform.

In the case of spatial isotropy, $\xi_{fg}(r)$ and $P_f(k)$ are connected via the relation

$$P_{fg}(k) = 2\pi \int_0^\infty dr r^2 \xi_{fg}(r) \int_{-1}^1 du e^{-ikru} , \quad (2.35)$$

where u is the cosine of the angle between \mathbf{k} and \mathbf{x} . Performing the u integration, one finally gets:

$$P_{fg}(k) = 4\pi \int_0^\infty dr r^2 \xi_{fg}(r) \frac{\sin(kr)}{kr} . \quad (2.36)$$

Note that, since $\xi_{fg}(r)$ is dimensionless, $P_{fg}(k)$ has dimension of a volume. The PS is also often expressed in dimensionless form, $\Delta_{fg}^2(k) = k^3 P_{fg}(k) / 2\pi^2$

We can give a concrete example in the case of matter density fluctuations, introducing the time- and position-dependent density contrast:

$$\delta_m(\mathbf{x}, z) = \frac{\rho_m(\mathbf{x}, z) - \bar{\rho}_m(z)}{\bar{\rho}_m(z)} \quad (2.37)$$

which describes the density fluctuations around the mean $\bar{\rho}_m(z)$ as a function of position and redshift; we can construct similar fields for the different components, such as galaxies (in which case we will use the galaxy number density $n_g(\mathbf{x}, z)$ instead of ρ_m). Switching to the Fourier space (i.e., projecting δ_m on the plane-wave basis) and taking the expected value (cf. Eq. 2.33), we obtain the *matter* PS, which as we shall see plays a central role in LSS analyses:

$$\langle \tilde{\delta}_m(\mathbf{k}, z) \tilde{\delta}_m(\mathbf{k}', z) \rangle = (2\pi)^3 \delta_D^3(\mathbf{k} + \mathbf{k}') P_{mm}(\mathbf{k}, z) \quad (2.38)$$

under the homogeneity and isotropy assumptions we have the simplification $P_{mm}(\mathbf{k}, z) \rightarrow P_{mm}(|\mathbf{k}|, z) = P_{mm}(k, z)$. We will refer to the matter power spectrum as $P_{\delta\delta}$ or P_{mm} interchangeably, since unless specified otherwise δ will represent the matter density contrast field.

The $\delta(\mathbf{k}, z)$ fields are interpreted as random variables drawn from some probability density functions. In the case of Gaussian PDFs, all the information is contained in the variance (the density contrast fields have zero mean by construction), which is precisely the power spectrum (Piattella, 2018). In other words, if the perturbations are Gaussian all predictions can be derived from the power spectrum, which is therefore a complete statistic.

The PS encodes information on the amplitude of the matter fluctuations at a given scale (see Fig. 2.2), making it possible to see at a glance the magnitude of the density perturbations (or, in general, of the function we are computing the power spectrum of), and thus to understand the different physical processes at play. The power spectra of relevance in our analysis are the matter (matter-matter), galaxy-galaxy and matter-galaxy PS. The latter two can be derived from the former simply by defining a relation between the galaxy and matter statistics, the *galaxy bias* (see Sect. 3.1.4). The accurate characterization of galaxy bias is one of the most daunting challenges in the use of galaxy statistics for Cosmology and the reason why weak lensing cosmic shear is such a powerful probe, being it sensitive to the total matter distribution instead of just the baryonic part. Moreover, cross-correlating the galaxy and matter fields can greatly help lift the degeneracy between galaxy bias and other cosmological parameters.

2.4.2 Angular power spectrum

The *Euclid* satellite is equipped with a near-infrared spectrometer for accurate determination of redshifts of up to $\mathcal{O}(10^7)$ sources (EC20). Such observations will allow constructing the 3-dimensional power spectrum exploiting the high resolution in the radial direction, but are time-consuming. A different approach, widely used nowadays in galaxy surveys (see e.g. de Jong et al. 2013; The Dark Energy Survey Collaboration 2005), is to estimate redshifts through observations in different photometric bands, or filters. This yields a much larger number of redshift estimates ($\mathcal{O}(10^9)$), at the cost of lower precision (see Sect. 3.1.3), which translates into a large uncertainty over the radial dimension of the measured field. We then divide these observations into redshift bins, which will likely overlap because of photometric-redshift uncertainties (see Sect. 3.1.2).

To exploit this binned data, we need to define the 2-dimensional version of the

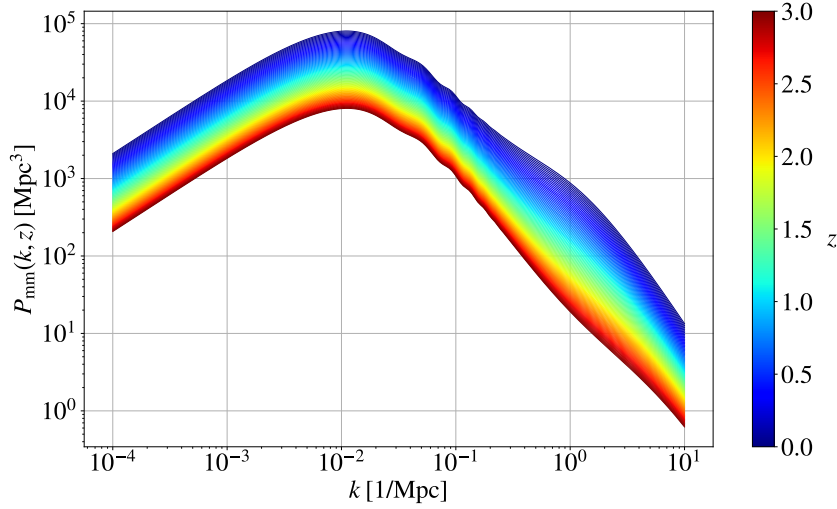


Figure 2.2. The nonlinear matter PS as a function of scale k and redshift (see color bar). The slope of the PS changes sign after the scale of matter-radiation equality $k_{\text{eq}} \sim 10^{-2} \text{Mpc}^{-1}$: large-scale perturbations enter the horizon after equality, when the Universe is matter-dominated, hence continuing their super-horizon growth. This is why they retain the primordial shape, which follows a power law form (see Eq. 1.51). Smaller scales, on the other hand, enter the horizon earlier – during radiation domination – and their growth is suppressed, giving rise to the relative lack of small-scale power at large k . Because structures at low z have had more time to grow, the power increases as z decreases.

3D observables introduced in the present section, that is, the angular power spectra. To do that, we need a formalism describing the projection of fields on the (celestial) sphere. Since two angles are required to specify each direction in the sky, we can use (θ, ϕ) as our coordinates. As mentioned, for each z bin a different map is constructed, which allows greatly enhancing the statistical power of the survey.

In the same way as we defined the two-point correlation function and its Fourier space version, the power spectrum, we can define the *angular* two-point correlation function and its Fourier transform on the sphere, the *angular power spectrum*. To illustrate this, we take as an example the above-mentioned matter density contrast, this time expressed as a function of the unit vector $\hat{\mathbf{n}} = (\cos \theta \sin \phi, \sin \theta \sin \phi, \cos \phi)$; we drop the subscript m to simplify the notation, without loss of generality. Since $\delta(\hat{\mathbf{n}})$ is now defined on a spherical (non-flat) surface, the basis functions of the decomposition are no longer sines and cosines (or complex exponentials), but *spherical harmonics* $Y_{\ell m}(\hat{\mathbf{n}})$:

$$Y_{\ell m}(\hat{\mathbf{n}}) = Y_{\ell m}(\theta, \phi) = \sqrt{\frac{2\ell + 1}{4\pi} \frac{(\ell - m)!}{(\ell + m)!}} e^{im\phi} \mathcal{P}_{\ell}^m(\cos \theta) \quad (2.39)$$

with ℓ and m integer numbers satisfying the condition $\ell \geq 0$, $-\ell \leq m \leq \ell$. Just like \mathbf{k} was the conjugate of \mathbf{x} in the Fourier transform, the subscripts ℓ and m are the conjugate of $\hat{\mathbf{n}}$ in the spherical harmonics transform. The “multipole” ℓ is related to the angular scale of the features described by the spherical harmonic decomposition.

Specifically, ℓ corresponds to the number of oscillations of the function along a meridian, with larger ℓ values representing smaller angular scales. The phase and number of oscillations of the function in the azimuthal direction ϕ is described instead by m . The value of m also dictates the symmetry properties of the spherical harmonic: for $m = 0$, the function is axisymmetric; for $m \neq 0$, the function will have a m -fold azimuthal symmetry. Finally, the terms $\mathcal{P}_\ell^m(\cos \theta)$ represent the *Legendre Polynomials*.

The $Y_{\ell m}$ functions satisfy the symmetry condition $Y_{\ell m}^* = (-1)^m Y_{\ell m}(\theta, \phi)$ and the orthonormality relation $\int Y_{\ell m} Y_{\ell' m'}^* d^2 n = \delta_{\ell \ell'}^K \delta_{m m'}^K$, which make them an appropriate basis choice to represent functions on a sphere and ensure that the $a_{\ell m}$ coefficients can be uniquely determined. In the last equation, δ^K is the Kronecker delta.

With these definitions, we can introduce the following expansion, where the $a_{\ell m}$ (*multipole moments*) terms play the role of expansion coefficients (Dodelson and Schmidt, 2020):

$$\delta(\hat{\mathbf{n}}) = \sum_{\ell=1}^{\infty} \sum_{m=-\ell}^{\ell} Y_{\ell m}(\hat{\mathbf{n}}) = \sum_{\ell m} a_{\ell m} Y_{\ell m}(\hat{\mathbf{n}}). \quad (2.40)$$

which can be inverted to obtain the $a_{\ell m}$ s using the orthonormality relation:

$$a_{\ell m} = \int d^2 \hat{\mathbf{n}} \delta(\hat{\mathbf{n}}) Y_{\ell m}^*. \quad (2.41)$$

The $a_{\ell m}$ (complex) coefficients provide information about the amplitude of the mode identified by ℓ and m (and no longer by the wave vector \mathbf{k}). We can connect the value of ℓ to the angular scale through the relation

$$\alpha \simeq \frac{\pi}{\ell}, \quad (2.42)$$

with α expressed in radians. If the field $\delta(\hat{\mathbf{n}})$ follows a Gaussian distribution, so will the $a_{\ell m}$ coefficients, with a null expectation value $\langle a_{\ell m} \rangle = 0$ (Poutanen et al., 2004). We can compute the variance of the multipole moments $\langle a_{\ell m} a_{\ell' m'}^* \rangle$ – the second moment of the field distribution around the mean, which again completely defines a Gaussian field – which under the hypothesis of symmetry under rotations (derived from the isotropy assumption of the Cosmological Principle) becomes

$$\langle a_{\ell m} a_{\ell' m'}^* \rangle = \delta_{\ell \ell'}^K \delta_{m m'}^K C_\ell, \quad (2.43)$$

where C_ℓ is the angular power spectrum. This harmonic space observable is the one employed in this work and many cosmological analyses. Eq. (2.43) tells us that the $a_{\ell m}$ variance does not depend on m , which means that for a fixed ℓ all the coefficients have the same variance. When we compute the C_ℓ s, then, we estimate the variance from a limited population, with $2\ell + 1$ samples (i.e., different values of m) at our disposal. If the observations cover the whole celestial sphere, we can define an unbiased estimator (an estimator the mean of which does not systematically under- or over-estimate the true value of the parameter under consideration) of the true C_ℓ s as (Montani et al., 2011):

$$\hat{C}_\ell = \frac{1}{2\ell + 1} \sum_m |a_{\ell m}|^2, \quad (2.44)$$

which is an average over m for every ℓ . There is an intrinsic limitation to the accuracy with which we can measure the C_ℓ s, which arises precisely from the limited number of large-scale modes. This is called *cosmic variance*. More specifically, the minimum variance of a measured C_ℓ is $2C_\ell^2/(2\ell + 1)$ so the relative uncertainty related to the cosmic variance is

$$\frac{\Delta C_\ell}{C_\ell} = \sqrt{\frac{2}{2\ell + 1}} C_\ell. \quad (2.45)$$

An additional common source of uncertainty in Cosmology is *sample variance*, which arises from the limitedness of the portion of sky observed (most likely even for full-sky observations, because of the necessity to mask out foreground sources). This term goes instead as $\propto 1/f_{\text{sky}}$, with $f_{\text{sky}} = \Omega_{\text{S}}/4\pi$ the fraction of the sky observed (Ω_{S} being the survey area in steradians).

Just as the 3D PS is related to the 2PFC, the angular PS can be related to the *angular* two-point correlation function:

$$w(\boldsymbol{\theta}) = \langle \delta(\hat{\mathbf{n}}) \delta^*(\hat{\mathbf{n}}') \rangle = \langle \delta(\hat{\mathbf{n}}) \delta(\hat{\mathbf{n}}') \rangle, \quad (2.46)$$

since the density contrast function is real-valued and the correlation function only depends on the amplitude of the angular separation, not its direction. Using Eq. (2.40) we have

$$w(\theta) = \left\langle \sum_{\ell m} a_{\ell m} Y_{\ell m}(\hat{\mathbf{n}}) \sum_{\ell' m'} a_{\ell' m'}^* Y_{\ell' m'}^*(\hat{\mathbf{n}}') \right\rangle \quad (2.47)$$

$$= \sum_{\ell m} \sum_{\ell' m'} \langle a_{\ell m} a_{\ell' m'}^* \rangle Y_{\ell m}(\hat{\mathbf{n}}) Y_{\ell' m'}^*(\hat{\mathbf{n}}') \quad (2.48)$$

which we can connect to the angular PS via (Dodelson and Schmidt, 2020):

$$w(\theta) = \frac{1}{4\pi} \sum_{\ell} \sum_{m=-\ell}^{\ell} |a_{\ell m}|^2 \mathcal{P}_{\ell}(\cos \theta) = \frac{1}{4\pi} \sum_{\ell} C_{\ell} (2\ell + 1) \mathcal{P}_{\ell}(\cos \theta) \quad (2.49)$$

having performed the sum over m and having used Eq. (2.43).

Chapter 3

Galaxy Clustering and Gravitational Lensing

In the present Chapter, we will discuss the main observables used by the *Euclid* mission to explore the fundamental properties of the Universe: the large-scale clustering of galaxies and the weak gravitational lensing of light. In fact, *Euclid*’s main aim is to construct the most accurate and complete catalogue of galaxy positions and shapes, to “map the dark Universe”. These two highly complementary probes are amongst the most promising ways to explore the low-redshift Universe, with the potential to increase the precision in the measurement of key cosmological quantities by more than one order of magnitude (Laureijs et al., 2011; Amendola et al., 2018). The following discussion will introduce the theory behind galaxy number counts and weak lensing cosmic shear, as well as the modelling chosen and systematics included to produce the fiducial spectra used in the subsequent forecasts.

3.1 Galaxy Clustering

The main observable studied in the context of galaxy clustering surveys is the degree of spatial correlation between galaxies’ positions. This correlation is the result of the interplay between many different factors, the main one being the “tug of war” between gravity and the expansion of the Universe, accelerated by Dark Energy (in the concordance cosmological model) at early times. The initial shape and amplitude of the matter power spectrum, the epoch of matter-radiation equality and the contribution of massive neutrinos and baryonic physics further contribute to determining the large-scale distribution of the *tracer* of matter under consideration, galaxies. The uncertainty over the bias affecting this tracer, the *galaxy bias*, further complicates the picture. On the other hand, the dependence on such a rich set of phenomena hints at the large amount of information which can potentially be extracted from this probe. This section will introduce the main theoretical and practical aspects allowing its use to estimate the parameters of the cosmological model.

3.1.1 Spectroscopic Galaxy Clustering

As detailed in Sect. 3.3.1, *Euclid* will be equipped with a slitless near-infrared spectrometer for accurate measurement of galaxies' spectra, which allows a very accurate measure of redshift – the requirement on the redshift uncertainty is, in fact, $\sigma_z^{\text{sp}} < 0.001(1+z)$ (Laureijs et al., 2011). The primary target of the spectroscopic survey will be H α emitters, because of the strength of the spectral line and its being associated with star-forming regions. The resulting galaxy map will have a high radial resolution, allowing the reconstruction of the 3D galaxy power spectrum, which is not possible with the photometric survey. This can then be related to the PS of matter by detailing the above-mentioned relation between galaxies and matter, the galaxy bias. In its simplest form, this relation is simply linear (Peacock and Dodds, 1994); we refer to this modelling as “linear galaxy bias”:

$$\delta_g(k, z) = b(z) \delta_m(k, z) \implies P_{gg}(k, z) = b^2(z) P_{mm}(k, z). \quad (3.1)$$

This of course can be made more complex (and realistic) by allowing $b(z)$ to acquire scale dependence, and/or by including higher-order bias terms. An extensive review of galaxy bias is given in Desjacques et al. (2018).

Another probe which is possible to investigate thanks to the precision of the spectroscopic survey is the Baryon Acoustic Oscillations (BAO) signal. This is the imprint left by the acoustic density wave oscillations in the photon-baryon plasma – coupled by Compton scattering – in the early Universe, created by the interplay of radiation pressure and the DM-sourced gravitational pull. This plasma has a high sound speed ($\sim 170\,000\text{ km s}^{-1}$), since the photons provide the dominant pressure contribution. At recombination ($\sim 400\,000$ yrs after the Big Bang) the photons become free to travel unbounded to the newly formed hydrogen atoms, thus depriving the baryonic matter of the radiation pressure and leaving it “frozen” on the shell of the propagation sphere at that time. The maximum radius of this sphere, i.e. the maximum distance travelled by the acoustic waves before recombination (the sound horizon), is the BAO scale. The $\sim 127\text{ kPc}$ ($400\,000$ light years, ly) travelled before recombination corresponds to roughly $\sim 150\text{ Mpc}$ (500 million ly) today, due to the Universe expansion. This is a powerful standard ruler, measured to high precision in CMB experiments, which we can observe at different redshifts in the angular and radial direction to constrain the expansion history of the Universe. Surveys that aim at detecting this signal must cover an area wider than this typical scale; moreover, since the peak in the two-point correlation function (Fig. 3.1) corresponding to this characteristic separation distance is quite small, a large number of objects must be observed to reach the statistical power needed to measure it. The *Euclid* survey is optimized to capture the BAO signal, because of the large sample size and wide survey area, which can accommodate the BAO scale.

Finally, spectroscopic GC allows studying the so-called *redshift space distortions* (Kaiser, 1987). Galaxies move relative to us both because they follow the Hubble flow and because of their peculiar velocities, induced by the local gravitational potential. Consequently, when one maps the galaxy distribution in redshift space, an anisotropy is observed, manifesting as elongations along the line of sight in the galaxy distribution, commonly referred to as the “Fingers of God”, and squashing

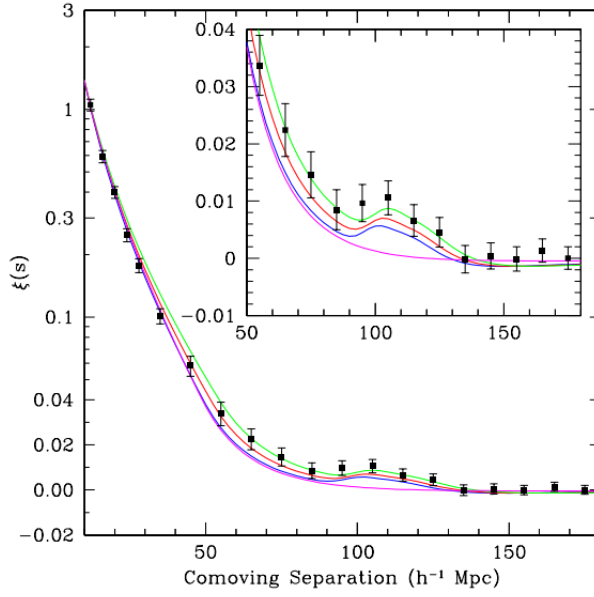


Figure 3.1. Redshift-space correlation function of the SDSS LRG sample (Sloan Digital Sky Survey - Luminous Red Galaxies), showing the excess of pairs at separation s . The BAO peak is clearly visible. The green, red and blue lines represent $\Omega_m h^2 = (0.12, 0.13, 1.14)$ respectively, while the magenta line is the CDM model with $\Omega_b = 0$, highlighting the statistical significance of the peak. Source: (Eisenstein et al., 2005)

in the perpendicular direction. This anisotropy can be measured to constrain the growth rate (Eq. 1.60).

3.1.2 Photometric galaxy clustering

In addition to the spectroscopic survey, *Euclid* will build the largest photometric galaxy catalogue to date, characterizing the position and morphology of billions ($\sim 1.5 \times 10^9$) of sources. This work revolves primarily around the photometric survey.

While with spectroscopy the redshift is determined by measuring the shift of a particular spectral line (such as the $H\alpha$ emission line), or set of lines, between the rest-frame wavelength and the observed one, the photometric survey lacks the spectral resolution to do this. In fact, the light is measured in (i.e., integrated over) different filters, or bands, which cover a broad range of frequencies (Fig. 3.2). The redshift can then be obtained by color-color diagrams, machine learning approaches or template fitting, comparing the observed, low-resolution spectral energy distribution (SED) to a set of model SED templates at different redshifts, obtained through more accurate techniques (Bolzonella et al., 2000). A comparison of the performance of different methods for the *Euclid* survey is presented in Euclid Collaboration: Desprez et al. (2020). The redshift estimates obtained in this way suffer significant uncertainty (see Sect. 3.1.3), with a requirement of $\sigma_z^{\text{ph}} < 0.05(1+z)$ but are much quicker to obtain, hence allowing a larger number of estimates w.r.t. the spectroscopic case.

The consequence of the poor radial resolution of the photometric survey is the

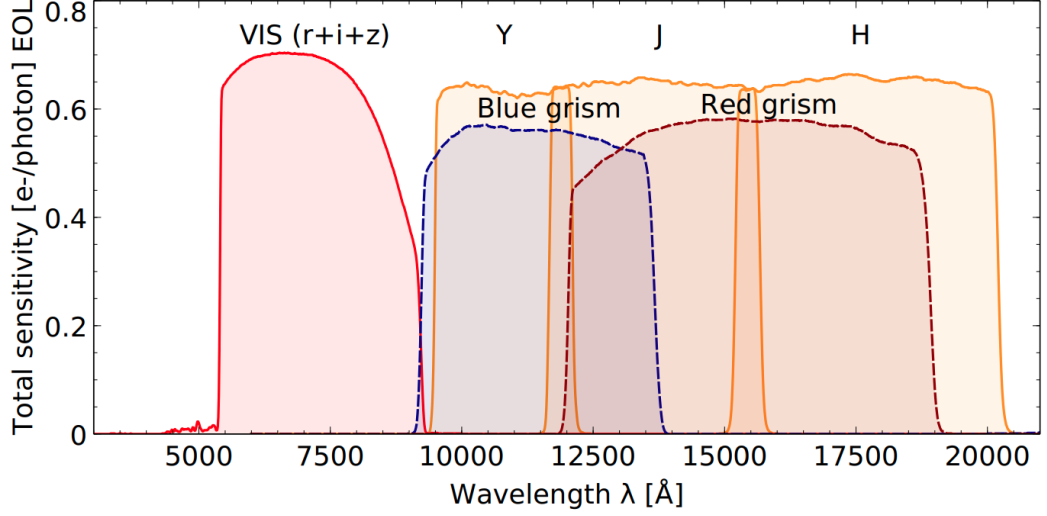


Figure 3.2. Forecasted sensitivity of the different bands of the VIS and NISP instrument, in units of electron per photon, at the end of the nominal life (6 yrs) of the instruments. The significant width of the photometric filters affects the precision of photometric redshift estimates. One of the advantages of space-based observations is the possibility to cover wavelength ranges poorly transmitted by the atmosphere. Source: (Euclid Collaboration: Scaramella et al., 2022)

need to bin our observations into redshift slices, inside of which we study 2D-projected statistics of the galaxy field instead of the three-dimensional one. Having introduced the formalism used to describe 2D-projected fields on a sphere in Sect. 2.4.2, we can derive the expression for the angular photometric galaxy clustering (GCph) PS which will be used in the rest of the work.

The uncertain source distances are described for GCph by a distribution $\mathcal{K}(\chi)$, defined as

$$\mathcal{K}(\chi) = \frac{1}{N_g} \frac{dN_g}{d\chi}, \quad (3.2)$$

with N_g the total number of galaxies. This distribution allows projecting the galaxy density contrast field in the radial direction, acting as a *projection kernel*:

$$\Delta_g(\hat{\mathbf{n}}) = \int_0^\infty d\chi \mathcal{K}(\chi) \delta_g(\mathbf{x} = \hat{\mathbf{n}}\chi, \eta(\chi)), \quad (3.3)$$

where $\eta(\chi) = \eta_0 - \chi$ and Δ_g is the projected density contrast field. Inserting the Fourier transform of δ_g (indicated without a tilde) and expanding in spherical harmonics, we get (Dodelson and Schmidt, 2020):

$$\begin{aligned} \Delta_g(\hat{\mathbf{n}}) &= \int_0^\infty d\chi \mathcal{K}(\chi) \int \frac{d^3\mathbf{k}}{(2\pi)^3} e^{i\mathbf{k} \cdot \hat{\mathbf{n}}\chi} \delta_g(\mathbf{k}, \eta(\chi)) \\ &= 4\pi \int \frac{d^3\mathbf{k}}{(2\pi)^3} \sum_{\ell m} i^\ell Y_{\ell m}(\hat{\mathbf{n}}) Y_{\ell m}^*(\hat{\mathbf{k}}) \int_0^\infty d\chi \mathcal{K}(\chi) j_\ell(k\chi) \delta_g(\mathbf{k}, \eta(\chi)) \end{aligned} \quad (3.4)$$

where the coefficients of the expansion are

$$\Delta_{g,\ell m} = 4\pi i^\ell \int \frac{d^3\mathbf{k}}{(2\pi)^3} Y_{\ell m}^*(\hat{\mathbf{k}}) \int_0^\infty d\chi \mathcal{K}(\chi) j_\ell(k\chi) \delta_g(\mathbf{k}, \eta(\chi)). \quad (3.5)$$

As seen in Eq. (2.43), the angular power spectrum is simply given in terms of the expectation value of the product of these coefficients:

$$\begin{aligned} \langle \Delta_{g,\ell m} \Delta_{g,\ell' m'}^* \rangle &= (4\pi)^2 i^{\ell-\ell'} \int \frac{d^3 \mathbf{k}}{(2\pi)^3} \int \frac{d^3 \mathbf{k}'}{(2\pi)^3} Y_{\ell m}^*(\hat{\mathbf{k}}) Y_{\ell' m'}(\hat{\mathbf{k}}') \int_0^\infty d\chi \mathcal{K}(\chi) j_\ell(k\chi) \\ &\quad \times \int_0^\infty d\chi' \mathcal{K}(\chi') j_{\ell'}(k'\chi') \langle \delta_g(\mathbf{k}, \eta(\chi)) \delta_g^*(\mathbf{k}', \eta(\chi')) \rangle. \\ &= \delta_{\ell\ell'}^K \delta_{mm'}^K C_{gg}(\ell), \end{aligned} \quad (3.6)$$

where the angular power spectrum is defined as

$$\begin{aligned} C_{gg}(\ell) &= \frac{2}{\pi} \int k^2 dk \int_0^\infty d\chi \mathcal{K}(\chi) j_\ell(k\chi) \int_0^\infty d\chi' \mathcal{K}(\chi') j_\ell(k\chi') \\ &\quad \times P_{gg}(k, \eta(\chi), \eta(\chi')). \end{aligned} \quad (3.7)$$

Which involves the unequal-time power spectrum $P_{gg}(k, \eta(\chi), \eta(\chi'))$, because the radial projection spans different times. Next section will show how, on small scales, the contribution from this PS at $\chi' \neq \chi$ can be neglected.

Limber approximation

The general form of the angular PS (Eq. 3.7) involves a double integral over the comoving distance and an integral over the scale k . This is extremely expensive numerically because the integrand is modulated by the highly oscillatory spherical Bessel functions, and hence has to be evaluated in a large number of points. To reduce the numerical burden to a level appropriate for the many thousands of evaluations required for accurately sampling the likelihood in parameter space, we make use of the Limber approximation (Limber, 1953; Kaiser, 1998).

This approximation is based on the consideration that, on small angular scales ($\ell \gtrsim 20$) the product of spherical Bessel functions $j_\ell(x = k\chi)$ is sharply peaked around $k\chi = \nu$, with $\nu = \ell + 1/2$ (Dodelson and Schmidt, 2020). Thus, we can approximate $j_\ell(k\chi)$ with a scaled delta function:

$$j_\ell(k\chi) \rightarrow \sqrt{\frac{\pi}{2\nu}} \delta_D(\nu - k\chi) \quad (3.8)$$

This approximation is valid if the PS varies slowly in the interval $\Delta k \sim 1/(\ell\chi)$ over which the Bessel functions are non-null; in this case, it can be approximated as constant and pulled out of the integral. Under this approximation, then, the expression for the angular PS becomes much simpler:

$$C_{gg}(\ell) \simeq \int d\chi \frac{\mathcal{K}^2(\chi)}{\chi^2} P_{gg} \left[k_\ell = \frac{\ell + 1/2}{\chi}, \eta(\chi) \right] \quad (3.9)$$

where, as mentioned in the last paragraph, we are only left with the equal-time PS and k_ℓ is the Limber wavenumber.

The combined effect of the Limber and flat-sky approximations is negligible except for very large angular scales ($\ell \lesssim 10$, see e.g. Lemos et al. 2017). This approximation works best when the kernels cover much larger support in radial distance χ than the physical scale being probed, and when they have significant overlap (Leonard et al., 2023). This is indeed the case for the cosmic shear signal, for which we will also use the Limber and flat-sky approximations.

Tomography

Photometric LSS surveys rely on the large sample size to make up for their low radial resolution. Their statistical power can be largely enhanced by repeating the observations in different redshift slices (bins), and constructing the angular PS for each of these. This is necessary, for example, to achieve high-precision dark energy measurements (EC20). Beyond increasing the number of spectra to the number of bins, this makes it also possible to study the cross-correlation between redshift bins. Furthermore, we can use the tomographic approach both for the auto- and for the cross-spectra, which correlate different fields to break the parameter degeneracies affecting the individual probes and to maximize the constraining power from a multi-probe survey such as *Euclid*.

To facilitate comparison against other codes (and to follow the recipe and notation outlined in EC20, the main official reference for the *Euclid* forecasts), we choose z as our radial coordinate, so the general form of the tomographic $C_{ij}^{AB}(\ell)$ between observables A and B in redshift bins i and j (both of which can of course coincide), in the context of the Limber approximation, is

$$C_{ij}^{AB}(\ell) = \frac{c}{H_0} \int dz \frac{\mathcal{K}_i^A(z) \mathcal{K}_j^B(z)}{E(z) \chi^2(z)} P_{AB} \left[\frac{\ell + 1/2}{\chi(z)}, z \right]. \quad (3.10)$$

This equation is symmetric under the exchange of redshift bin indices ($i \leftrightarrow j$) only if $A = B$, that is, for the auto-spectra. Tomography is used for both the photometric probes, as well as their cross-correlation; the number of spectra for weak lensing ($A = B = L$) and photometric galaxy clustering ($A = B = G$) is $N(N + 1)/2$, while for the cross-correlation it is N^2 .

The different angular power spectra studied in this work are obtained by plugging the appropriate radial kernel and power spectra in Eq. (3.10). For the photometric galaxy clustering case, we express the radial kernel (3.2) as a function of redshift as

$$\mathcal{K}_i^G(z) = \frac{H_0}{c} \frac{n_i(z)}{\bar{n}} E(z). \quad (3.11)$$

and the galaxy-galaxy power spectrum as indicated in Eq. (3.1). In the last equation, $n_i(z)$ represents the distribution of galaxies in the i -th redshift bin and \bar{n} the total number density.

In general, the redshift distributions used for galaxy number counts and weak lensing may differ. In this case, with a slightly confusing notation, the literature refers to the redshift distribution entering the galaxy kernel as the *lens* distribution, $n_i^L(z)$, and to the one entering the lensing kernel as the *source* redshift distribution, $n_i^S(z)$. The next section will discuss the modelling of these distributions, which are a key ingredient in our analysis.

3.1.3 Redshift distribution

First, we assume that the same galaxy population is used to probe both the weak lensing cosmic shear and the GCph PS. This assumption is likely to be relaxed in

case, for example, the data are complemented by ground-based photometry, covering different sky regions (e.g., northern or southern hemispheres): in fact, for *Euclid*, a strong interaction with existing and future surveys, such as the Vera C. Rubin Observatory Legacy Survey of Space and Time (LSST, Ivezić et al., 2019) is planned. We therefore set:

$$n_i^L(z) = n_i^S(z) = n_i(z) , \quad (3.12)$$

The same equality applies of course for the total source and lens number density, \bar{n}^L and \bar{n}^S .

In (EC20), the intrinsic or “true” number density redshift distribution is modelled analytically as a function of redshift as (Smail et al., 1994):

$$n(z) \propto \left(\frac{z}{z_0} \right)^2 e^{-(z/z_0)^{3/2}} , \quad (3.13)$$

where z_m is the median redshift of the sample and $z_0 = z_m/\sqrt{2}$. This distribution then needs to be mapped into the one actually measured in each redshift bin, taking into account the unavoidable uncertainties due to the less precise and less accurate estimate of the redshifts obtained through photometry (compared to spectroscopy). The number density $n_i(z)$ for each redshift bin is then formally defined through a convolution with some function $p_{\text{ph}}(z_p|z)$, which is the conditional probability distribution function that describes the likelihood of a galaxy with a true redshift z being observed at a photometric redshift (“photo- z ”) z_p :

$$n_i(z) = \frac{\int_{z_i^-}^{z_i^+} dz_p n(z) p_{\text{ph}}(z_p|z)}{\int_{z_{\text{min}}}^{z_{\text{max}}} dz \int_{z_i^-}^{z_i^+} dz_p n(z) p_{\text{ph}}(z_p|z)} . \quad (3.14)$$

where the interval boundaries z_i^- and z_i^+ are the left and right edges of each redshift bin. These boundaries can be selected to yield \mathcal{N}_b equipopulated or equidistant bins; in the former case, which is the reference choice in EC20, 10 equipopulated bins with a number density $\bar{n}/\mathcal{N}_b = 3 \text{ gal/arcmin}^2$ and $\bar{n} = 30$ are chosen.

The photometric redshift PDF $p_{\text{ph}}(z_p|z)$ can be parametrized by a bimodal Gaussian model:

$$p_{\text{ph}}(z_p|z) = (1 - f_{\text{out}}) p_{\text{ph}}^{\text{in}}(z_p|z) + (f_{\text{out}}) p_{\text{ph}}^{\text{out}}(z_p|z) \\ = \frac{1 - f_{\text{out}}}{\sqrt{2\pi}\sigma_{\text{in}}(1+z)} \exp \left[-\frac{1}{2} \left(\frac{z - c_{\text{in}}z_p - z_{\text{in}}}{\sigma_{\text{in}}(1+z)} \right)^2 \right] \quad (3.15)$$

$$+ \frac{f_{\text{out}}}{\sqrt{2\pi}\sigma_{\text{out}}(1+z)} \exp \left[-\frac{1}{2} \left(\frac{z - c_{\text{out}}z_p - z_{\text{out}}}{\sigma_{\text{out}}(1+z)} \right)^2 \right] . \quad (3.16)$$

Here, f_{out} is the fraction of “catastrophic outliers”, i.e., sources with substantially erroneous redshift measurements. Consequently, $1 - f_{\text{out}}$ is the fraction of galaxies with accurately measured redshifts. As can be seen in the equation, the standard deviation of the distributions $\tilde{\sigma}$, is an increasing function of z : $\tilde{\sigma}_i = \sigma_i(1+z)$, with $i = \text{in, out}$. The model incorporates a set of tunable parameters ($c_{\text{in}}, z_{\text{in}}, \sigma_{\text{in}}, c_{\text{out}}, z_{\text{out}}, \sigma_{\text{out}}, f_{\text{out}}$) to investigate various observational scenarios. In (EC20), these are fixed in the analysis to their fiducial values:

c_{in}	z_{in}	σ_{in}	c_{out}	z_{out}	σ_{out}	f_{out}
1.0	0.0	0.05	1.0	0.1	0.05	0.1

Note that the actual data analysis will allow accounting for uncertainties in the mean of the redshift distribution (i.e., its first moment), by introducing additional nuisance parameters, the shifts in the source redshift distribution Δz_i in the i -th bin: $n_i(z) \rightarrow n_i(z + \Delta z_i)$. This is in line with the standard approach used in the recent literature – see e.g. the DES Year 3 results: [Abbott et al. 2022](#) –, and is motivated by the fact that the uncertainty on mean of the source redshift distribution is the one, amongst the different moments of the distribution, to have the greatest impact on the final constraints (see [Reischke 2023](#)).

A more realistic galaxy redshift distribution than the analytical one assumed in Eq. (3.13) can be obtained from simulations. In our forecasts, we will use the results from [Euclid Collaboration: Pocino et al. \(2021\)](#), in which the $n(z)$ is constructed from photometric redshift estimates in a 400 deg^2 patch of the Flagship 1 N -body dark matter simulation ([Potter et al., 2017](#)), using the training-based directional neighbourhood fitting algorithm (DNF, [De Vicente et al., 2016](#)).

The training set is a random subsample of objects with true (spectroscopic) redshifts known from the Flagship 1 simulation. We choose the fiducial case presented in [Euclid Collaboration: Pocino et al. \(2021\)](#), which takes into account a drop in completeness of the spectroscopic training sample with increasing magnitude. A cut in magnitude $I_E < 24.5$ is applied, isotropic and equal for all photometric bands, corresponding to the optimistic *Euclid* setting. The DNF algorithm then produces a first estimate of the photo- z , z_{mean} , using as a metric the objects' closeness in colour and magnitude space to the training samples. A second estimate of the redshift, z_{mc} , is computed from a Monte Carlo draw from the nearest neighbour in the DNF metric. The final distributions for the different redshift bins, $n_i(z)$, are obtained by assigning the sources to the respective bins using their z_{mean} , and then taking the histogram of the z_{mc} values in each of the bins – following what has been done in real surveys such as DES. This redshift distribution is shown in Fig. 3.3. The total galaxy number density measured from the simulation is $\bar{n} = 28.73 \text{ arcmin}^{-2}$.

As a reference setting, we choose to bin the galaxy distribution into $\mathcal{N}_b = 10$ equipopulated redshift bins, with edges

$$z_{\text{edges}} = \{0.001, 0.301, 0.471, 0.608, 0.731, 0.851, 0.980, 1.131, 1.335, 1.667, 2.501\} . \quad (3.17)$$

This choice of redshift binning will be discussed and varied in Sect. 5.3.4.

3.1.4 Linear galaxy bias

As mentioned, one of the main systematic uncertainties affecting GCph measurements is the modelling of galaxy bias. Several different approaches have been presented in the literature to compute it. Simulations are a viable option, but it is much more difficult to simulate a realistic galaxy field than a dark matter field,

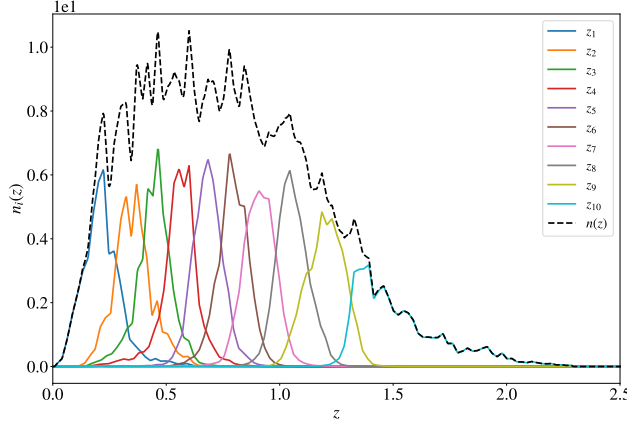


Figure 3.3. Sources (and lenses) redshift distribution per redshift bin, as well as their sum, obtained from the Flagship 1 simulation as described in Sect. 3.1.3

being baryonic effects and the physics of galaxy formation and evolution of utmost importance in the former case.

In this work, we choose to model the galaxy bias as linear and scale-independent (Eq. 3.1). We note that, at the same time, we are using the nonlinear recipe for the matter power spectrum $P_{\text{mm}}(k, z)$. This is reminiscent of the hybrid 1-loop perturbation theory (PT) model adopted by, e.g., the DES Collaboration in the analysis of the latest data release (Krause et al., 2021; Pandey et al., 2022), but we drop the higher-order bias terms; it has been referred to as “minimal bias model” in recent publications (e.g. Sugiyama et al., 2023). This simplified model has been chosen in order to be consistent with EC20 forecasts, against which we will validate some of our results. However, we move on from the simple analytical prescription of EC20:

$$b(z) = \sqrt{1+z} \quad (3.18)$$

and use the fitting function presented in Euclid Collaboration: Pocino et al. (2021), obtained from direct measurements from the *Euclid* Flagship galaxy catalogue, based in turn on the Flagship 1 simulation:

$$b(z) = \frac{Az^B}{1+z} + C, \quad (3.19)$$

with $(A, B, C) = (0.81, 2.80, 1.02)$.

The galaxy bias is modelled to be constant in each bin with the fiducial value obtained by evaluating Eq. (3.19) at effective values z_i^{eff} computed as the median of the redshift distribution (cf. Fig. 3.3) considering only the part of the distribution at least larger than 10% of its maximum. The z_i^{eff} values obtained in this way are

$$z^{\text{eff}} = \{0.233, 0.373, 0.455, 0.571, 0.686, 0.796, 0.913, 1.070, 1.195, 1.628\}. \quad (3.20)$$

We therefore have \mathcal{N}_b additional nuisance parameters

$$\theta_{\text{gal. bias}} = \{b_1, b_2, \dots, b_{\mathcal{N}_b}\}, \quad (3.21)$$

with fiducial values

$$\theta_{\text{gal. bias}}^{\text{fid}} = \{1.031, 1.057, 1.081, 1.128, 1.187, 1.258, 1.348, 1.493, 1.628, 2.227\} . \quad (3.22)$$

Although we choose to work with a linear galaxy bias for the power spectra, higher-order terms are relevant in other ingredients of our forecasts; their modelling will be introduced in Sect. 5.1.4.

3.1.5 Magnification bias

Another systematic affecting GCph is *magnification bias*. The effect is caused by foreground lensing magnification (see Sect. 3.2.3 for a formal introduction), which modulates the observed number of sources in a magnitude-limited survey. This effect has been found to significantly bias best-fit cosmological parameters for *Euclid* in [Euclid Collaboration: Lepori et al. 2022](#).

Magnification bias can be accounted for as an additional contribution to the galaxy number counts angular power spectrum, in a similar way to the intrinsic alignment term in weak lensing cosmic shear (see Sect. 3.2.6):

$$C_{ij}^{\mathcal{GG}}(\ell) = C_{ij}^{\text{gg}}(\ell) + C_{ij}^{\text{g}\mu}(\ell) + C_{ij}^{\mu\mu}(\ell) \quad (3.23)$$

expressing these contributions in the general form of Eq. (3.10), we have:

$$C_{ij}^{\text{gg}}(\ell) = \frac{c}{H_0} \int \frac{\mathcal{K}_i^g(z) \mathcal{K}_j^g(z)}{\chi^2(z) E(z)} P_{\text{gg}}(k_\ell, z) dz \quad (3.24)$$

$$C_{ij}^{\text{g}\mu}(\ell) = \frac{c}{H_0} \int \frac{\mathcal{K}_i^g(z) \mathcal{K}_j^\mu(z) + \mathcal{K}_i^\mu(z) \mathcal{K}_j^g(z)}{\chi^2(z) E(z)} P_{\text{gm}}(k_\ell, z) dz \quad (3.25)$$

$$C_{ij}^{\mu\mu}(\ell) = \frac{c}{H_0} \int \frac{\mathcal{K}_i^\mu(z) \mathcal{K}_j^\mu(z)}{\chi^2(z) E(z)} P_{\text{mm}}(k_\ell, z) dz . \quad (3.26)$$

We used the superscript \mathcal{GG} and gg to indicate respectively the galaxy clustering PS including or neglecting magnification bias, denoted with μ . The magnification bias radial kernel is given by:

$$\mathcal{K}_i^\mu(z) = \frac{3}{2} \frac{H_0}{c} \Omega_{\text{m},0} (1+z) \tilde{\chi}(z) \int_z^{z_{\text{max}}} dz' b_{\mu,i}(z') \frac{n_i(z')}{\bar{n}} \left[1 - \frac{\tilde{\chi}(z)}{\tilde{\chi}(z')} \right] \quad (3.27)$$

z_{max} being the maximum redshift reached by the survey for the source distribution and $\tilde{\chi}(z) = \chi(z)/(c/H_0)$ the dimensionless comoving distance; $b_{\mu,i}(z) = 2[\beta_i(z) - 1]$, with $\beta_i(z)$ the magnification bias in redshift bin i , which can be estimated as $\beta_i(z) = (5/2)s_i(z)$. Finally, $s_i(z)$ the logarithmic slope¹ of the cumulative number density N as a function of the limiting magnitude, which can be measured directly from the luminosity function of the galaxy sample ([Euclid Collaboration: Lepori et al., 2022](#)):

$$\frac{2}{5} s(z, F_{\text{lim}}) \equiv - \frac{\partial \log_{10} N(z, F > F_{\text{lim}})}{\partial \log_{10} F_{\text{lim}}} , \quad (3.28)$$

¹In the literature, sometimes $s(z)$ itself is referred to as magnification bias.

where F is the measured flux and F_{lim} is the survey flux limit. The magnification kernel (Eq. 3.27) is very similar to the lensing kernel (Eq. 3.77), being magnification a lensing effect. It should be noted that the $n_i(z)$ and \bar{n} terms entering the expression for the magnification kernel refer to *lens* redshift distribution. Magnification bias will be included in our forecasts in Chap. 6; unless otherwise specified, when left free to vary, we will not impose priors either on these or on the galaxy bias parameters.

3.2 Weak Lensing

A key insight of General relativity is that mass-energy (and momentum) distort the curvature of the spacetime manifold, hence changing the geodesic path of particles travelling along their worldline. In particular, photons' trajectories are distorted by the presence of matter (*lenses*) between the source and the observer, resulting in the shear, magnification and multiplication of the images of distant objects. Such effect is called *gravitational lensing*, and constitutes one of the main ways in which we are able to infer the global geometry and map the matter distribution of our Universe. A spectacular example of this phenomenon can be found in Fig. 3.4, showcasing the galaxies' shape distortion caused by the gravitational field of a massive cluster in the foreground.

With galaxy clustering we map the 3D distribution of galaxies, which needs galaxy bias as an additional ingredient (suffering significant uncertainty) to allow the reconstruction of the total (baryonic + dark) matter distribution. Being dependent on the overall gravitational potential, on the other hand, weak lensing (WL) gives us the possibility to map the distribution of *all* gravitationally interacting kinds of matter, whether of baryonic nature or not.

In the context of the *Euclid* survey we are interested in particular in one sub-category of this phenomenon: *weak lensing cosmic shear*, which is the distortion of a galaxy's shape (ellipticity) caused not by one specific massive object, but by the large-scale structures of the Universe. Being this a very small effect (order 1% deviation from the intrinsic ellipticity, Weinberg et al. 2013), requiring high-resolution imaging and exquisite control over the many systematics involved, it is best measured from space (although ground-based observations have made significant progress in recent years, see e.g. the DES, KiDS and HSC surveys: The Dark Energy Survey Collaboration 2005; de Jong et al. 2013; Aihara et al. 2018). The point spread function (PSF) is an example of one such systematic which space-based observations help mitigate. The observed galaxy shape is smeared by the convolution of the real image with the PSF, which is caused by astronomical seeing and instrumental effects. The PSF anisotropy and dependence on the source redshift and brightness complicate the job of removing this effect. Space experiments are unaffected by the atmospheric component of this effect but not by the instrumental ones, which can however be measured in the laboratory or modelled mathematically.

Weak gravitational lensing affects the image of the source in two ways: *shear* and *magnification*. Whereas the first results in a distortion of the galaxies' shape, the second affects their observed size. Of the two, the former effect is easier to



Figure 3.4. An example of *strong* gravitational lensing in one of the first public images by the James Webb Space Telescope: around the centre are visible galaxies belonging to the galaxy cluster SMACS 0723, whose strong gravitational field warps the shape of background galaxies, making them appear in the form of long arcs and multiplying their number. Source: nasa.gov/webbfirstimages/

observe and the most used in cosmology. In fact, although we do not have access to the information about the real image of the source (the image on the *source plane*), the ellipticity cancels out when averaged over a large number of sources (there is no preferred ellipticity direction); this is not true for the galaxies' sizes. From this recognition, statistical observations about the observed shape distortions can be made, such as their degree of correlation as a function of angular scale. In order to increase the sample size (hence statistical power) as much as possible, $\sim 90\%$ of *Euclid*'s observational time will be dedicated to the wide survey, covering about $14\,700\text{ deg}^2$ ($\sim 36\%$ of the entire sky). The main observable studied here is the *cosmic shear angular power spectrum*, which is the Fourier transform on a sphere of the shear angular correlation function (see Sect. 2.4.2 for a mathematical introduction). This function is related to the projection of the matter power spectrum over the line of sight, and thus it is sensitive to the cosmological parameters (more specifically, as we will see, to $\Omega_{m,0}$ and σ_8). To further enhance the survey constraining power it is possible to engage in a tomographic analysis, which as explained in 3.1.2 introduces the information on the auto- and cross-correlation between the different redshift bins.

The following pages will give a brief theoretical description of weak lensing.

3.2.1 Theory

The presence of mass-energy deflects light by virtue of the effect it has on the geometry of spacetime, which is the 4-dimensional space in which the photons' trajectories, the geodesics, are defined. These are the solutions to the *geodesic equation*:

$$\frac{d^2 x^\mu}{d\lambda^2} + \Gamma_{\alpha\beta}^\mu \frac{dx^\alpha}{d\lambda} \frac{dx^\beta}{d\lambda} = 0 \quad (3.29)$$

where λ is the affine parameter and

$$\Gamma_{\alpha\beta}^\mu = \frac{1}{2} g^{\mu\gamma} \left(\frac{dg_{\gamma\alpha}}{dx^\beta} + \frac{dg_{\gamma\beta}}{dx^\alpha} - \frac{dg_{\alpha\beta}}{dx^\gamma} \right) \quad (3.30)$$

are the *Christoffel symbols*, which account for the change in the basis vectors in curved space when taking the x^μ derivatives, and only depend on the metric and its derivatives. As discussed in the introduction, the Einstein field equations (Eq. 1.9) tell us how to build the metric tensor once in possess of the information about the mass-energy density distribution, and Eqs. (3.30) and (3.29) allow computing the resulting particle trajectories.

The following analysis of the WL effect is based on the following assumptions (Dodelson and Schmidt, 2020):

- Background spacetime is described by the FLRW metric
- Deflection angles are small
- The time evolution of the perturbations is slow: $d\Phi/dt \ll d\Phi/dx_i$
- Perturbations are small, so that a first-order theory provides a good enough description
- The lenses are thin, i.e. with a linear scale much smaller than the curvature scale of the Universe.

To make quantitative considerations about light deflection in the weak regime, we can make use of simple but powerful concepts from geometrical optics, such as *Fermat's principle*: the path followed by light is the one which minimizes the travel time

$$t = \int_A^B \frac{dl}{v[\mathbf{x}(l)]} = \int_A^B \frac{n}{c} dl, \quad (3.31)$$

which is the path $\mathbf{x}(l)$ for which the variation

$$\delta \int_A^B n[\mathbf{x}(l)] dl \quad (3.32)$$

is null. Here the curvature acts as a medium with refraction index $n(\mathbf{x}(l)) = c/v(\mathbf{x}(l))$ in which the light travels at speed $v(\mathbf{x}(l))$; l is the geodesic parameter.

Calling Φ the gravitational potential of the massive structure which distorts the light path (the *lens*), we can write the line element as

$$ds^2 = \left(1 + \frac{2\Phi}{c^2}\right) c^2 dt^2 - \left(1 - \frac{2\Phi}{c^2}\right) d\mathbf{x}^2, \quad (3.33)$$

Using the null geodesic condition $ds = 0$ we can then compute the new travel speed c' :

$$c' = \frac{|d\mathbf{x}|}{dt} = c \left(1 + \frac{2\Phi}{c^2}\right)^{1/2} \left(1 - \frac{2\Phi}{c^2}\right)^{-1/2} \simeq c \left(1 + \frac{2\Phi}{c^2}\right) \quad (3.34)$$

having used the fact that the weak regime is defined by the condition $\Phi/c^2 \ll 1$. Now we have an expression for the refraction index with which to compute the integral (3.31): using again the weak potential approximation, we have in fact

$$n \equiv \frac{c}{c'} = \frac{1}{1 + \frac{2\Phi}{c^2}} \simeq 1 - \frac{2\Phi}{c^2} . \quad (3.35)$$

We can now make use of the Euler-Lagrange equation:

$$\frac{\partial}{\partial \lambda} \frac{\partial L}{\partial \dot{\mathbf{x}}} - \frac{\partial L}{\partial \mathbf{x}} = 0 \quad \text{with} \quad \dot{\mathbf{x}} \equiv \frac{d\mathbf{x}}{d\lambda} , \quad (3.36)$$

in which the Lagrangian is $L = n(\mathbf{x}(\lambda)) \left| \frac{d\mathbf{x}}{d\lambda} \right|$, having used λ to re-parametrise the light path: $dl = \left| \frac{d\mathbf{x}}{d\lambda} \right| d\lambda$.

Choosing λ such that $|\dot{\mathbf{x}}| = 1$, way we obtain a set of normal vectors tangent to the curve, $\dot{\mathbf{x}} = \mathbf{e}$. With this notation, the Euler-Lagrange equation yields the result [Meneghetti \(2022\)](#):

$$\frac{d}{d\lambda}(n\mathbf{e}) - \nabla n = 0 \quad \rightarrow \quad n\dot{\mathbf{e}} = \nabla n - \mathbf{e}(\nabla n \cdot \mathbf{e}) , \quad (3.37)$$

the right-hand side being the gradient ∇n minus its projection along the direction tangential to the geodesic \mathbf{e} . We can then interpret such difference as the gradient of n in the direction perpendicular to the light path, $\nabla_{\perp} n$:

$$\dot{\mathbf{e}} = \frac{1}{n} \nabla_{\perp} n = \nabla_{\perp} \ln n \quad (3.38)$$

and, since $n = 1 - 2\Phi/c^2$, $\ln n \simeq -2\Phi/c^2$, so the last expression becomes

$$\dot{\mathbf{e}} \simeq -\frac{2}{c^2} \nabla_{\perp} \Phi . \quad (3.39)$$

This equation relates the angle of the vector tangent to the geodesic curve to the gravitational potential experienced by the photon along its path. Integrating $-\dot{\mathbf{e}}$ along the whole path we obtain the total deflection angle $\hat{\alpha}$:

$$\hat{\alpha} = \frac{2}{c^2} \int_{\lambda_A}^{\lambda_B} \nabla_{\perp} \Phi d\lambda . \quad (3.40)$$

Exploiting the fact that this angle is small - that is, the actual path is not very different from the one induced by the gravitational pull of the lens - we can use the *Born approximation*, integrating Eq. (3.40) over the unperturbed path.

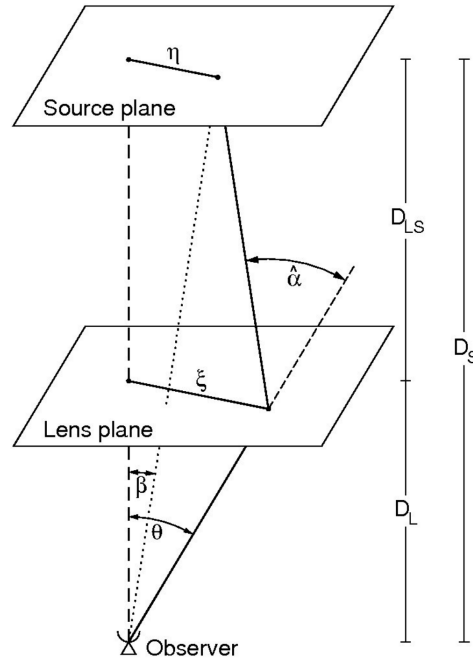


Figure 3.5. The photon path gets distorted by a small angle $\hat{\alpha}$ due to the presence of intervening overdensity. The description of the angles and distances is in the text. Adapted in Meneghetti (2022) from Bartelmann and Schneider (2001)

3.2.2 Lens equation

The main quantities at play are depicted in Fig. 3.5. D_S is the angular diameter distance (ADD, see Sect. 1.3) of the source, placed at redshift z_S ; D_L is the ADD of the lens, placed at redshift z_L , and D_{LS} is the ADD from the lens to the source. In curved space such distances are not necessarily additive, so the relation $D_S = D_{LS} + D_L$ is not true in general. $\boldsymbol{\eta} = D_S \boldsymbol{\beta}$ is the actual position of the source on the source plane, $\boldsymbol{\xi} = D_L \boldsymbol{\theta}$ is the impact parameter (the distance of the geodesic from the lens once the photon reaches the lens plane) and $\hat{\alpha}$ is the above-mentioned deflection angle. At all times, the photon position can be characterized by a 2D vector specifying its angular distance from the perpendicular to the lens and source plane (the optical axis). The photon starts with angular vector $\boldsymbol{\beta}$, but appears to us to be coming from $\boldsymbol{\theta}$.

If the angles $(\hat{\alpha}, \boldsymbol{\beta}, \boldsymbol{\theta})$ are small, the distances are related via the *lens equation*:

$$\boldsymbol{\theta} D_S = \boldsymbol{\beta} D_S + \hat{\alpha} D_{LS} \quad (3.41)$$

which can be rewritten introducing the *reduced deflection angle* $\boldsymbol{\alpha}(\boldsymbol{\theta})$ as

$$\boldsymbol{\theta} = \boldsymbol{\alpha} + \boldsymbol{\beta} \quad \text{with} \quad \boldsymbol{\alpha} = \boldsymbol{\alpha}(\boldsymbol{\theta}) \equiv \frac{D_{LS}}{D_S} \hat{\alpha}(\boldsymbol{\theta}) . \quad (3.42)$$

As a final remark, we can introduce the quantities ξ and $\eta = \xi D_S/D_L$ as typical scales of the problem, with the aim of defining the dimensionless vectors

$$\mathbf{x} = \frac{\boldsymbol{\xi}}{\xi} \quad \text{and} \quad \mathbf{y} = \frac{\boldsymbol{\eta}}{\eta} \quad (3.43)$$

and to scale the deflection angle:

$$\boldsymbol{\alpha}(\mathbf{x}) \equiv \frac{D_L D_{LS}}{\xi D_S} \hat{\boldsymbol{\alpha}}(\xi \mathbf{x}). \quad (3.44)$$

Thanks to these we can rewrite the lens equation as

$$\mathbf{y} = \mathbf{x} - \boldsymbol{\alpha}(\mathbf{x}) \quad (3.45)$$

3.2.3 Lensing potential, shear and convergence matrices

In many cases of interest - including the one under examination - the lens is an extended matter distribution. In these situations it is useful to define a function of the gravitational potential, the *effective lensing potential*:

$$\hat{\Psi}(\boldsymbol{\theta}) \equiv \frac{D_{LS}}{D_L D_S} \frac{2}{c^2} \int dz \Phi(D_L \boldsymbol{\theta}, z), \quad (3.46)$$

which is the rescaled three-dimensional gravitational potential, projected on the lens plane. Its dimensionless version $\Psi = \frac{D_L^2}{\xi_0^2} \hat{\Psi}$ has the useful properties:

1. $\nabla_x \Psi(\mathbf{x}) = \boldsymbol{\alpha}(\mathbf{x})$: the gradient along the \mathbf{x} vector (therefore in the direction perpendicular to the geodesic) gives the scaled deflection angle.
2. $\Delta_x \Psi(\mathbf{x}) = 2\kappa(\mathbf{x})$: the laplacian along the \mathbf{x} vector gives twice the *convergence*, which we will define below.

The image distortion caused by weak lensing can be conveniently described through the Jacobian matrix:

$$A_{ij} \equiv \frac{\partial y_i}{\partial x_j} = \left(\delta_{ij}^K - \frac{\partial \alpha_i(\mathbf{x})}{\partial x_j} \right) = \left(\delta_{ij}^K - \frac{\partial^2 \Psi(\mathbf{x})}{\partial x_i \partial x_j} \right). \quad (3.47)$$

The first equality comes from the lens equation (3.45) and the second one from the first of the two points above. Defining the *distortion tensor* $\Psi_{ij} = \partial^2 \Psi / \partial x_i \partial x_j$ and I the identity matrix we can consider the isotropic, traceless part of A_{ij} :

$$\left(A - \frac{1}{2} \text{tr} A \cdot I \right)_{ij} = \delta_{ij} - \Psi_{ij} - \frac{1}{2} (1 - \Psi_{11} + 1 - \Psi_{22}) \delta_{ij}^K \quad (3.48)$$

$$= \begin{pmatrix} -\frac{1}{2}(\Psi_{11} - \Psi_{22}) & -\Psi_{12} \\ -\Psi_{12} & \frac{1}{2}(\Psi_{11} - \Psi_{22}) \end{pmatrix}. \quad (3.49)$$

This matrix is called *shear matrix*. This can be rewritten introducing the shear pseudo-vector $\boldsymbol{\gamma} = (\gamma_1, \gamma_2)$:

$$\gamma_1(\mathbf{x}) = \frac{1}{2}(\Psi_{11} - \Psi_{22}) \quad (3.50)$$

$$\gamma_2(\mathbf{x}) = \Psi_{12} = \Psi_{21}, \quad (3.51)$$

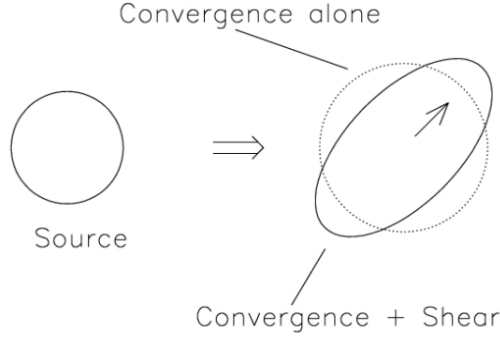


Figure 3.6. The effect of convergence and shear. Source: (Meneghetti, 2022)

so that Eq. (3.49) can be recast in the form:

$$\left(A - \frac{1}{2} \text{tr} A \cdot I \right)_{ij} = \begin{pmatrix} \gamma_1 & \gamma_2 \\ \gamma_2 & -\gamma_1 \end{pmatrix}. \quad (3.52)$$

The remaining part of A_{ij} is

$$\frac{1}{2} \text{tr} A \cdot I = \left(1 - \frac{1}{2} (\Psi_{11} + \Psi_{22}) \right) \delta_{ij} \quad (3.53)$$

$$= \left(1 - \frac{1}{2} \Delta_x \Psi \right) \delta_{ij} = \begin{pmatrix} 1 - \kappa & 0 \\ 0 & 1 - \kappa \end{pmatrix}; \quad (3.54)$$

this is the *convergence matrix*. Putting together equations (3.52) and (3.54), we obtain a new expression for the Jacobian:

$$A_{ij} = \begin{pmatrix} 1 - \kappa - \gamma_1 & -\gamma_2 \\ -\gamma_2 & 1 - \kappa + \gamma_1 \end{pmatrix}, \quad (3.55)$$

where two key quantities appear: the *convergence* κ , quantifying the (isotropic) magnification, and the *shear* γ , whose components govern the image distortion (see Fig. 3.6). The former will not be discussed in detail since this work will focus on weak lensing cosmic shear as a cosmological probe.

3.2.4 Ellipticity and shear

The last step is to relate the shear to some observable quantity. The case of interest is that of weak lensing cosmic shear by large-scale structures.

A circular shape is mapped into an elliptical one via the matrix A_{ij} , with the semi-major and semi-minor axes a and b functions of the distortion parameters γ and κ :

$$a = \frac{r}{1 - \kappa - \gamma} \quad \text{and} \quad b = \frac{r}{1 - \kappa + \gamma} \quad (3.56)$$

where $\pm\gamma = \pm\sqrt{\gamma_1^2 + \gamma_2^2}$ are the eigenvalues of the shear matrix and r is the circular source radius. The *ellipticity* ϵ is defined as

$$\epsilon = \frac{a - b}{a + b} = \frac{2\gamma}{2(1 - \kappa)} = \frac{\gamma}{1 - \kappa} \simeq \gamma \quad (3.57)$$

assuming $\kappa, \gamma \ll 1$. The observed ellipticity is the sum of the source's intrinsic ellipticity and the shear

$$\epsilon_i = \epsilon_i^I + \gamma_i ; \quad (3.58)$$

if we average over a large number of sources:

$$\langle \epsilon \rangle = \langle \epsilon^I \rangle + \langle \gamma \rangle = \langle \gamma \rangle . \quad (3.59)$$

The last equality assumes that the distribution of galaxy shapes and orientations is completely random - which is not exactly the case, due to, e.g., intrinsic alignment, as we shall discuss. In this case, the average over the intrinsic ellipticity cancels out: this means that in the WL limit the ellipticity is a direct measure of the shear. The statistical description of errors associated with the intrinsic variation in galaxy shapes, uncorrelated with the lensing signal, is commonly referred to as “shape noise”, and it is by far the largest source of uncertainty in WL surveys (Gurri et al., 2021).

3.2.5 Shear power spectrum

From the shear field, two main statistics can be extracted: the two-point shear correlation function and its spherical harmonic transform, the cosmic shear angular power spectrum. In the context of *Euclid*, the preferred quantity is the latter. Both choices have advantages and disadvantages; the covariance matrix terms, for example, have a simpler expression in angular space. A large number of additional higher-order statistics can also be constructed (see *Euclid Collaboration: Ajani et al. 2023* for a recent application to the *Euclid* survey), maximizing the information extracted from the shear field, but these will not be discussed in the present work. To derive the cosmic shear angular PS in the flat-sky approximation, we take the Fourier transform (instead of the spherical harmonics transform) of the shear field (Weinberg et al., 2013):

$$\tilde{\gamma}_{1,2}(\boldsymbol{\ell}) = \int d^2 \boldsymbol{\theta} \gamma_{1,2}(\boldsymbol{\theta}) e^{-i\boldsymbol{\ell} \cdot \boldsymbol{\theta}} \quad \leftrightarrow \quad \gamma_{1,2}(\boldsymbol{\theta}) = \int \frac{d^2 \boldsymbol{\ell}}{(2\pi)^2} \tilde{\gamma}_{1,2}(\boldsymbol{\ell}) e^{i\boldsymbol{\ell} \cdot \boldsymbol{\theta}} . \quad (3.60)$$

We can simplify the problem by rotating the basis of the Fourier space to align them with the direction of the wavevector describing the plane-wave perturbation (Crittenden et al., 2002). We call these rotated components *E* and *B* modes; they are generated by galaxies which are respectively stretched in the direction of the wave vector and squashed perpendicular to it, or at 45° angles.

$$\tilde{\gamma}_E(\boldsymbol{\ell}) = \cos(2\phi_\ell) \tilde{\gamma}_1(\boldsymbol{\ell}) + \sin(2\phi_\ell) \tilde{\gamma}_2(\boldsymbol{\ell}) \quad (3.61)$$

$$\tilde{\gamma}_B(\boldsymbol{\ell}) = \cos(2\phi_\ell) \tilde{\gamma}_2(\boldsymbol{\ell}) - \sin(2\phi_\ell) \tilde{\gamma}_1(\boldsymbol{\ell}) , \quad (3.62)$$

where $\tan \phi_1 = \ell_2/\ell_1$, and ℓ_1 and ℓ_2 being the components of $\boldsymbol{\ell}$ in the old coordinate system. The angular PS are then defined as (see Sect. 2.4.2):

$$\langle \tilde{\gamma}_E^*(\boldsymbol{\ell}) \tilde{\gamma}_E(\boldsymbol{\ell}') \rangle = (2\pi)^2 C_{EE}(\ell) \delta_D^2(\boldsymbol{\ell} - \boldsymbol{\ell}') \quad (3.63)$$

$$\langle \tilde{\gamma}_B^*(\boldsymbol{\ell}) \tilde{\gamma}_E(\boldsymbol{\ell}') \rangle = (2\pi)^2 C_{BE}(\ell) \delta_D^2(\boldsymbol{\ell} - \boldsymbol{\ell}') \quad (3.64)$$

$$\langle \tilde{\gamma}_B^*(\boldsymbol{\ell}) \tilde{\gamma}_B(\boldsymbol{\ell}') \rangle = (2\pi)^2 C_{BB}(\ell) \delta_D^2(\boldsymbol{\ell} - \boldsymbol{\ell}') . \quad (3.65)$$

Isotropy makes these PS depend only on the magnitude of ℓ and not its direction, and reflection symmetry guarantees that $C_{EB}(\ell) = 0$. We now need to connect these to the lensing potential Ψ ; this can be done by leveraging Eqs. (3.50) and (3.51), which we rewrite in angular coordinates:

$$\gamma_1(\theta) = \frac{1}{2} \left(\frac{\partial^2 \Psi}{\partial \theta_1^2} - \frac{\partial^2 \Psi}{\partial \theta_2^2} \right) \quad (3.66)$$

$$\gamma_2(\theta) = \frac{\partial^2 \Psi}{\partial \theta_1 \partial \theta_2}. \quad (3.67)$$

Using the replacement $\partial/\partial\theta_i \rightarrow i\ell_i$, we find in Fourier space

$$\tilde{\gamma}_1(\ell) = \frac{1}{2} (\ell_1^2 - \ell_2^2) \tilde{\Psi}(\ell) = \frac{1}{2} \ell^2 \cos(2\phi_1) \tilde{\Psi}(\ell) \quad (3.68)$$

$$\tilde{\gamma}_2(\ell) = \ell_1 \ell_2 \tilde{\Psi}(\ell) = \frac{1}{2} \ell^2 \sin(2\phi_\ell) \tilde{\Psi}(\ell). \quad (3.69)$$

Substitution back into equations (3.61) and (3.62) we get the important results that cosmic shear possesses only E modes, in other words, it has no curl component:

$$\tilde{\gamma}_E(\ell) = \frac{\ell^2}{2} \tilde{\Psi}(\ell) \rightarrow C_{EE}(\ell) = \frac{\ell^4}{4} C_{\Psi\Psi}(\ell) \quad (3.70)$$

$$\tilde{\gamma}_B(\ell) = 0. \quad (3.71)$$

One potential source of spurious B modes is shape noise, which is a priori equally distributed among these and E modes. Equation (3.70) connects the E mode, shear PS to the PS of the lensing potential Ψ , $C_{\Psi\Psi}(\ell)$. This potential is related to the gravitational one by the weighted projection (3.46), and the gravitational potential is related in turn to the matter overdensity by the Poisson equation (in an expanding background), which in Fourier space is given by:

$$\Phi(k) = \left[\frac{3}{2} \Omega_{m,0} \frac{H_0^2}{c^2} (1+z) \right] k^{-2} \delta_m(k) \implies P_\Phi(k) = \left[\frac{3}{2} \Omega_{m,0} \frac{H_0^2}{c^2} (1+z) \right]^2 k^{-4} P_{\delta\delta}(k). \quad (3.72)$$

Where $P_{\delta\delta} = P_{\delta_m\delta_m} = P_{mm}$ is the matter PS; this allows to obtain the the analogous of Eq. (3.9):

$$C_{EE}(\ell) = \int_0^\chi d\chi' \frac{\mathcal{K}^2(\chi', \chi)}{\chi'^2} P_{\delta\delta} \left(k_\ell = \frac{(\ell + 1/2)}{\chi'} \right), \quad (3.73)$$

with

$$\mathcal{K}(\chi', \chi) = \frac{3}{2} \Omega_{m,0} \frac{H_0^2}{c^2} (1+z') \frac{\chi'(\chi - \chi')}{\chi} \quad (3.74)$$

the lensing weight function, describing the contributions to lensing of sources at comoving distance χ from lens structures at distance χ' . Note that this vanishes as the lens approaches the source ($\chi' \rightarrow \chi$). This result is valid in the flat case and in the Limber, flat-sky approximation used throughout this work. This weight function

has to be re-weighted taking into consideration the lens redshift distribution, i.e., the probability distribution of their distance $n(\chi)$:

$$\mathcal{K}_{\text{eff}} = \int_0^{\chi_{\text{max}}} n(\chi) \mathcal{K}(\chi', \chi) d\chi \quad (3.75)$$

As can be seen from Eqs. (3.73) and (3.74), the shear signal will be primarily sensitive to the square of the matter density parameter and the integral of the matter PS, which in the linear regime goes as $\sim \sigma_8^2$ and in the nonlinear one close to $\sim \sigma_8^3$ (Weinberg et al., 2013). It will therefore best constrain the degenerate combination $\Omega_{\text{m},0}^2 \sigma_8^3$, with the bulk of the information coming from the small-scale regime. This is why often analyses report constraints on some combination of the two parameters (in particular, $S_8 = \sigma_8 \Omega_{\text{m},0}^{0.5}$, see Hall 2021).

Recasting the expression to the general form given in Eq. (3.10), we get:

$$C_{ij}^{\gamma\gamma}(\ell) \simeq \frac{c}{H_0} \int dz \frac{\mathcal{K}_i^\gamma(z) \mathcal{K}_j^\gamma(z)}{E(z) \chi^2(z)} P_{\delta\delta} \left[\frac{\ell + 1/2}{\chi(z)}, z \right]. \quad (3.76)$$

and²

$$\mathcal{K}_i^\gamma(z) = \frac{3}{2} \frac{H_0}{c} \Omega_{\text{m},0} (1+z) \tilde{\chi}(z) \int_z^{z_{\text{max}}} dz' \frac{n_i(z')}{\bar{n}} \left[1 - \frac{\tilde{\chi}(z)}{\tilde{\chi}(z')} \right]. \quad (3.77)$$

The present discussion has been devoted to the modelling of the cosmic shear signal. Real observations are affected by many different systematic effects, some of which we proceed to describe in the following sections.

3.2.6 Intrinsic alignment

Amongst the most challenging and significant systematic effects for upcoming WL surveys is the intrinsic alignment (IA) of galaxies. Intrinsic alignment refers to the tendency of galaxies to have shapes or orientations that are correlated, independently of any lensing effects. These alignments can be broadly classified into two categories: (i) intrinsic-intrinsic alignments (II), where the shapes of two galaxies are directly correlated, and (ii) intrinsic-shear alignments ($I\gamma$), where the shape of a foreground galaxy is correlated with the background (Troxel and Ishak, 2015). IA mimics the cosmological shear signal, introducing a spurious contribution to the measured power.

As seen in Sect. 3.2.4, we can consider the observed ellipticity as the contribution of two terms

$$\epsilon = \epsilon^{\text{I}} + \gamma \quad (3.78)$$

where ϵ^{I} is the intrinsic, or unlensed, ellipticity. Taking the two-point correlation function of Eq. (3.78) we have:

$$C_{ij}^{\epsilon\epsilon}(\ell) = C_{ij}^{\gamma\gamma}(\ell) + C_{ij}^{I\gamma}(\ell) + C_{ij}^{\gamma I}(\ell) + C_{ij}^{\text{II}}(\ell). \quad (3.79)$$

The cross terms $C_{ij}^{I\gamma}(\ell)$ and $C_{ij}^{\gamma I}(\ell)$ represent respectively the correlation between background shear and foreground intrinsic alignment and the correlation between

²We remind that Eq. (3.77) assumes a spatially flat Universe. For the general case, one must replace the term in brackets with $S_k(\chi' - \chi)/S_k(\chi')$, with $S_k(\chi)$ given in Eq. (1.2)

foreground shear and background ellipticity; $P_{\delta I}$ and $P_{I\delta}$ are the corresponding power spectra. Since foreground shear and background ellipticity should not be correlated the $C_{ij}^{\gamma I}(\ell)$ term vanishes. For the $C_{ij}^{I\gamma}(\ell)$ and $C_{ij}^{II}(\ell)$ the *linear alignment* model can be used:

$$C_{ij}^{I\gamma}(\ell) = \frac{c}{H_0} \int dz \frac{\mathcal{K}_i^\gamma(z) \mathcal{K}_j^{IA}(z) + \mathcal{K}_i^{IA}(z) \mathcal{K}_j^\gamma(z)}{E(z) \chi^2(z)} P_{\delta I}(k_\ell, z) \quad (3.80)$$

$$C_{ij}^{II}(\ell) = \frac{c}{H_0} \int dz \frac{\mathcal{K}_i^{IA}(z) \mathcal{K}_j^{IA}(z)}{E(z) \chi^2(z)} P_{II}(k_\ell, z) . \quad (3.81)$$

The IA weight function is equal to the GCph one, as long as the source and lens redshift distributions coincide:

$$\mathcal{K}_i^{IA}(z) = \mathcal{K}_i^G(z) = \frac{H_0}{c} \frac{n_i(z)}{\bar{n}} E(z). \quad (3.82)$$

$P_{\delta I}(k, z)$ and $P_{II}(k, z)$ can be related to the matter power spectrum thanks to models such as the *extended nonlinear alignment* model (eNLA); with respect to the nonlinear alignment model (NLA, [Bridle and King 2007](#)) this accounts for the luminosity dependence of the IA:

$$P_{\delta I}(k, z) = -\mathcal{A}_{IA} \mathcal{C}_{IA} \Omega_{m,0} \frac{\mathcal{F}_{IA}(z)}{D(z)} P_{\delta\delta}(k, z) \quad (3.83)$$

$$P_{II}(k, z) = \left[-\mathcal{A}_{IA} \mathcal{C}_{IA} \Omega_{m,0} \frac{\mathcal{F}_{IA}(z)}{D(z)} \right]^2 P_{\delta\delta}(k, z) . \quad (3.84)$$

In these equations, the parameters of the eNLA model appear: \mathcal{A}_{IA} is the overall IA amplitude, \mathcal{C}_{IA} a constant (whose value is fixed at 0.0134, [EC20](#)), $D(z)$ is the linear growth factor, and $\mathcal{F}_{IA}(z)$ a function modulating the dependence on redshift:

$$\mathcal{F}_{IA}(z) = (1+z)^{\eta_{IA}} [\langle L \rangle(z)/L_\star(z)]^{\beta_{IA}} , \quad (3.85)$$

where $\langle L \rangle(z)/L_\star(z)$ is the redshift-dependent ratio of the mean luminosity $\langle L \rangle(z)$ over the characteristic luminosity of WL sources $L_\star(z)$ as estimated from an average luminosity function (see e.g. [Joachimi et al., 2015](#), and references therein). The IA nuisance parameters vector is then:

$$\boldsymbol{\theta}_{IA} = \{\mathcal{A}_{IA}, \eta_{IA}, \beta_{IA}\} , \quad (3.86)$$

with fiducial values set using numerical simulations or fitting of the data ([EC20](#))

$$\boldsymbol{\theta}_{IA}^{\text{fid}} = \{1.72, -0.41, 2.17\} . \quad (3.87)$$

All of the IA parameters, except for \mathcal{C}_{IA} , will be varied in the analysis.

We can finally define a total lensing kernel as (see e.g. [Kitching et al., 2017](#); [Kilbinger et al., 2017](#); [Taylor et al., 2018b](#))

$$\mathcal{K}_i^L(z) = \mathcal{K}_i^\gamma(z) - \frac{\mathcal{A}_{IA} \mathcal{C}_{IA} \Omega_{m,0} \mathcal{F}_{IA}(z)}{D(z)} \mathcal{K}_{IA}(z) , \quad (3.88)$$

so that the total lensing PS takes the form of Eq. (3.76):

$$C_{ij}^{LL}(\ell) \simeq \frac{c}{H_0} \int dz \frac{\mathcal{K}_i^L(z) \mathcal{K}_j^L(z)}{E(z) \chi^2(z)} P_{\delta\delta} \left[\frac{\ell + 1/2}{\chi(z)}, z \right] . \quad (3.89)$$

The lensing kernel constructed in this way, along with the galaxy one, is shown in [Fig. 3.7](#).

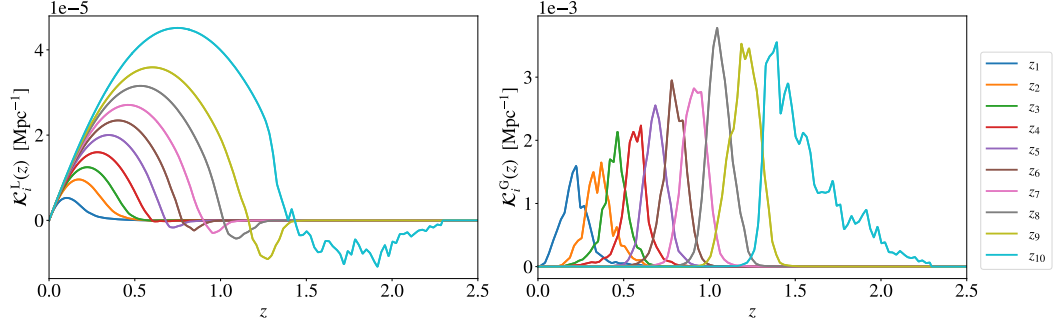


Figure 3.7. Weight functions, or radial kernels $\mathcal{K}_i^A(z)$, for the two photometric probes. The analytic expressions for these are, respectively, Eq. (3.88) (left, WL) and Eq. (3.11) (right, GCph). At high redshifts the IA term dominates over the shear term in the lensing kernels, making them negative. Moreover, the wiggly behaviour of the source redshift distribution $n_i(z)$ is smoothed out in the integration (Eq. 3.88), but this is only true for the shear kernel $\mathcal{K}_i^G(z)$, not for the IA one; this means that, in the z region where latter term dominates over the former, the total lensing kernel ceases to be smooth.

3.2.7 Multiplicative shear bias

An additional ingredient which we include to mimic as closely as possible the analysis of the actual data is the multiplicative shear bias, m , defined as the multiplicative coefficient of the linear bias expansion of the shear field γ , see e.g. Cragg et al. (2023) for a recent study for stage-IV surveys:

$$\hat{\gamma} = (1 + \mathbf{m}) \gamma + \mathbf{c} \quad (3.90)$$

with $\hat{\gamma}$ the measured shear field, γ the true one, \mathbf{m} the multiplicative and \mathbf{c} the additive shear bias parameters (which we will fix to 0 in the present analysis). The latter two are, in principle, complex numbers, albeit they are often assumed to be real. The multiplicative shear bias can come from astrophysical or instrumental systematics (such as the effect of the point spread function), which affect the measurement of galaxy shapes. We take the m_i parameters (one for each redshift bin) as constant and with a fiducial value of 0 in all bins. To include this further nuisance parameter, which is mathematically equivalent to linear galaxy bias insofar it appears as a multiplicative factor to the $C(\ell)$ s, one just has to update the shear angular PS as:

$$C_{ij}^{LL}(\ell) \rightarrow (1 + m_i)(1 + m_j)C_{ij}^{LL}(\ell) \quad (3.91)$$

where m_i is the i -th bin multiplicative bias. We will then have:

$$\boldsymbol{\theta}_{\text{shear bias}} = \{m_1, m_2, \dots, m_{N_b}\}, \quad (3.92)$$

with fiducial values

$$\boldsymbol{\theta}_{\text{shear bias}}^{\text{fid}} = \{0, 0, \dots, 0\}. \quad (3.93)$$

3.2.8 Putting it all together: the 3×2pt analysis

Despite the unprecedented accuracy and control over systematics of the WL and GCph surveys, the true power of *Euclid* will come from the capability of adding

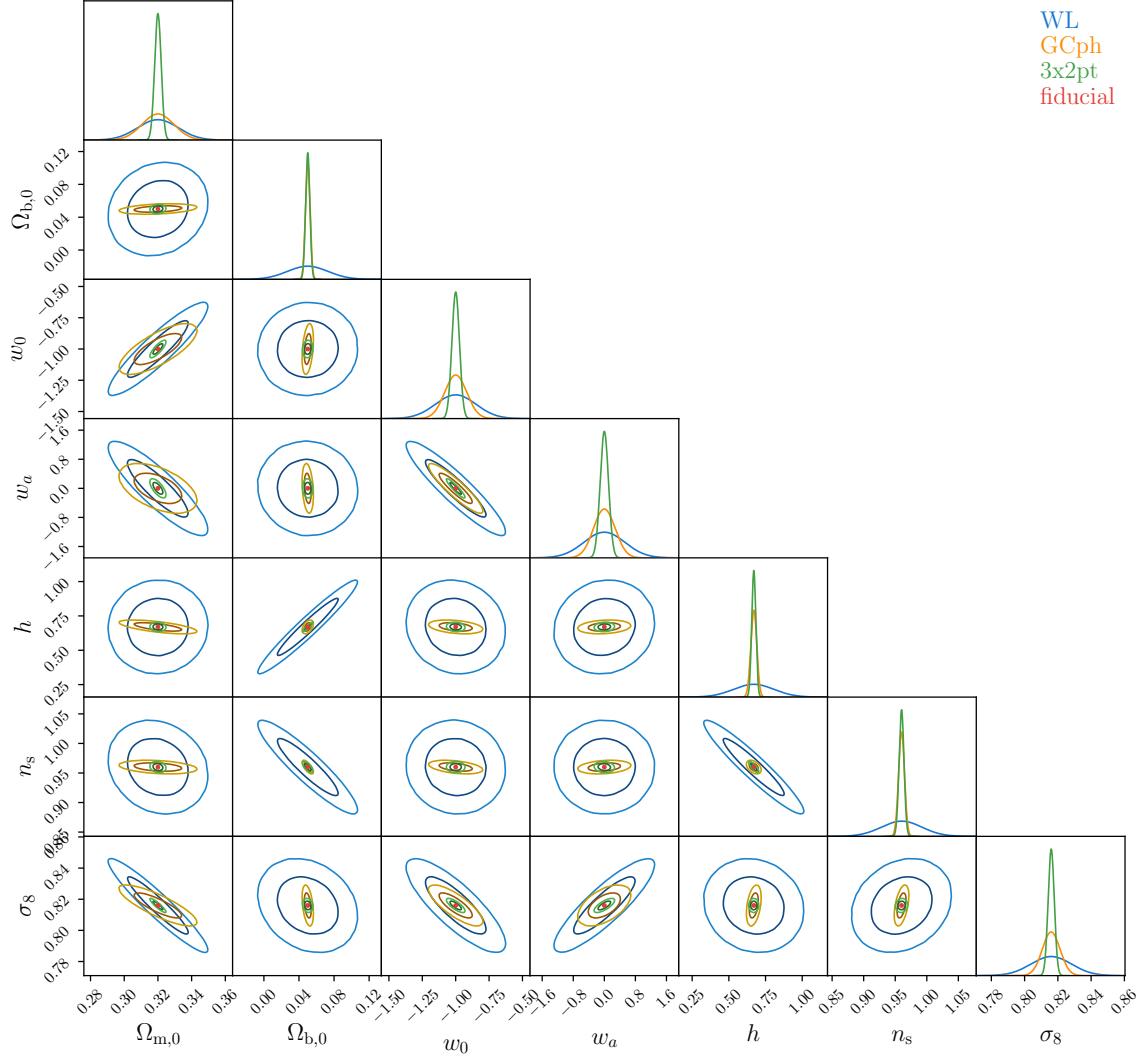


Figure 3.8. Fisher analysis 68% and 95% confidence contours for the photometric probes: WL, GCph and 3x2pt. The fiducial cosmology is indicated in red. As discussed, WL best constrains $\Omega_{m,0}$ and σ_8 (rather, a degenerate combination of the two), but significantly improves the GCph constraints when added in the 3x2pt analysis, by for example, reducing the correlation between the DE EoS parameters and the standard parameters n_s , h , and $\Omega_{b,0}$, as also found in (EC20). Plot produced with the `ChainConsumer` package (Hinton, 2016).

together and cross-correlating these two probes. This approach is nowadays the state of the art in multi-probe cosmological surveys (Joachimi et al., 2021; Abbott et al., 2022) because it combines the strengths of multiple data sets. Different observables have in fact different parameter degeneracies, are affected by different systematics, and constrain different sets of parameters. Just to give an example, the combined use of cosmic shear and galaxy clustering is able to break the degeneracy between galaxy bias and cosmological parameters, which significantly degrades the constraints from GCph when marginalizing over the former set of parameters. The addition of WL and/or the cross-spectra adds information which is unaffected by galaxy bias, improving the constraints on the cosmological parameters while at the same time providing information on $b(z)$ (Tutusaus et al., 2020). Some example confidence contours from a EC20-like Fisher analysis are shown in Fig. 3.8. The different degeneracy directions are visible, for example in the $\Omega_{m,0}$ - σ_8 plane.

The cross-correlation of WL and GCph can be referred to as “XC” (for “cross-correlation”), “GGL” (for “galaxy-galaxy lensing”) or as “GL”, which will be our preferred choice, following the convention defined in Sect. 3.1.2: G for GCph, L for WL. We consider this notation more convenient, because for two-point statistics it allows writing, e.g., $C_{ij}^{LL}(\ell)$ instead of the more cumbersome $C_{ij}^{WLWL}(\ell)$; this is even more true for four-point functions, such as the covariance matrix, which correlates four tracers.

The 3×2 pt data vector is then constructed by concatenating the LL, GL and GG angular PS, derived by plugging the appropriate radial kernel (Eq. 3.11 for galaxy clustering, Eq. 3.88 for weak lensing) in Eq. (3.10). These angular PS are shown in Fig. 3.9. As anticipated, the corresponding power spectra are given by the following expressions:

$$P_{AB}(k, z) = \begin{cases} P_{mm}(k, z) & A = B = L \\ b(z)P_{mm}(k, z) & (A, B) = (L, G) \text{ or } (G, L) \\ b^2(z)P_{mm}(k, z) & A = B = G, \end{cases} \quad (3.94)$$

with $P_{mm}(k, z)$ the *nonlinear* matter-matter PS and $b(z)$ the linear, scale-independent and deterministic first-order galaxy bias, described in Sect. 3.1.4.

We note that the 3×2 pt analysis can be further enhanced by combining it with the spectroscopic galaxy clustering (GCsp) probe. As mentioned in Sect. 2.2, the log-likelihoods for independent datasets can be simply added up. This is what is often done for surveys which cover different parts of the sky, come from different experiments or study uncorrelated probes. The combination of the photometric and spectroscopic probes is a notable example; recent works (Taylor and Markovič, 2022) suggest that these can be treated as independent even in case the observed region overlaps, because the probes correlate significantly only on large scales, where cosmic variance dominates. This greatly simplifies the analysis, since modelling the covariance between 3D and 2D observables is not a trivial task.

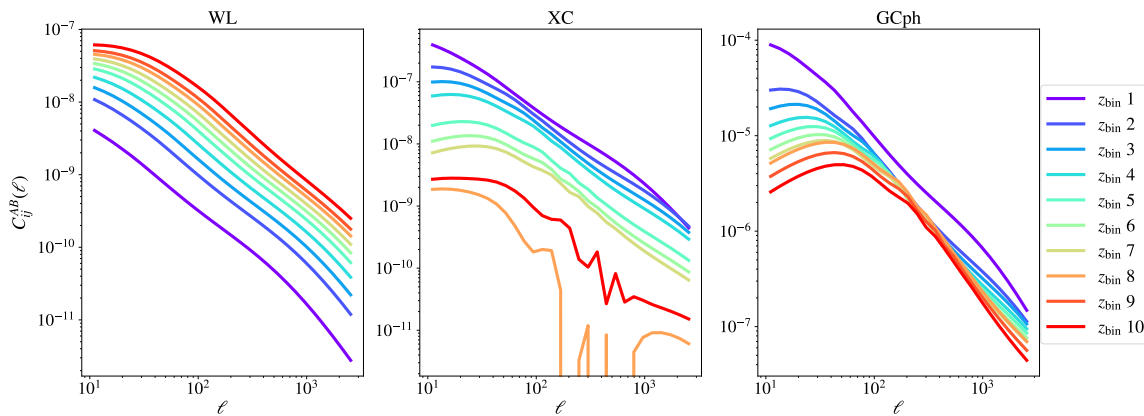


Figure 3.9. Angular PS for the photometric probes and their cross-correlation, for the different z_i, z_j redshift bins (with bin $i = j$). The BAO wiggles, visible in the GCph spectra, are smoothed out in the rather featureless (and low-amplitude) lensing signal.

The preceding sections illustrated galaxy clustering and weak lensing cosmic shear as main probes for *Euclid*. Having established the theoretical framework for these observables, we now transition to detailing the mission in charge of their measurement.

3.3 *Euclid*

Euclid is a medium-class ESA mission, born from the union of the DUNE and SPACE proposals in the ESA Cosmic Vision 2015-2025 program. The satellite was launched on the 1st of July, 2023 on a SpaceX Falcon 9 rocket from Cape Canaveral, Florida, USA; after about one month of travel, it reached the second Sun-Earth Lagrangian point (L2), at a distance of approximately 1.5×10^6 km. From there, during the course of the designed six years of nominal survey operations, it will produce the most advanced catalogue of galaxies' shapes and morphology to date, advancing our understanding of Cosmology and producing a wealth of data for legacy science studies. This section will introduce the main technical aspects of the survey.

3.3.1 Satellite

Euclid is placed in a Lissajous-type orbit around the L2 point, where the gravitational pull of the Sun and the Earth balances the centrifugal force experienced by the satellite. The halo orbit is quite large (10^6 km), and the satellite does not experience Earth eclipses, which would affect the thermal stability of the system.

The satellite is equipped with an axial Korsh telescope measuring 1.2 m in diameter, composed of three curved silicon carbide mirrors operating below 130 K. The light is directed through the exit pupil and split with the use of a dichroic plate; the transmitted fraction is sent to the Near Infrared Spectrometer and Photometer (NISP), and the reflected fraction to the visible (VIS) instrument. The telescope and instruments are part of the Payload Module (PLM); the Service Module (SVM),

Visible instrument, VIS

- detector array: 36 4x4k pixel CCD273-84, produced by Teledyne E2V; detectors read from each corner, 144 read channels
- 16-bit digitisation, 3.4 e-/ADU; <4.4 electrons internal noise in VIS detection chain
- pixel scale: 0.1 arcsec (slightly undersampling diffraction limit)
- effective angular resolution: 0.18 arcsec (through multiple exposures)
- field of view: 0.57 deg²
- single passband: I_E=530-920nm, defined by dichroic reflection and combined effect of mirror coatings
- shutter unit
- calibration source (VIS-CU), for flat-fields and other calibration purposes: using LEDs at 6 wavelengths

Near Infrared Spectrometer and Photometer, NISP

- detector array: 16 2x2k H2RG detectors, produced by Teledyne
- pixel scale: 0.3 arcsec (undersampling the PSF)
- radius of 50%/80% encircled energy (note: these are requirements; actual value will differ and be known only after launch):
 - rEE50: <0.4 arcsec
 - rEE80: <0.7 arcsec
- spectral elements: in filter wheel (FWA) and grism wheel (GWA)
- photometry passbands (50% cut-on to 50% cut-off, from [Euclid Consortium: Schirmer+ 2022](#), Tab. 3):
 - Y_E: 949.6nm-1212.3nm
 - J_E: 1167.6nm-1567.0nm
 - H_E: 1521.5nm-2021.4nm
- grism passbands (50% cut-on to 50% cut-off):
 - BG_E (from grism BGS000, orientation 0°): 926nm-1366nm, R~400
 - RG_E (from grisms RGS000/RGS180, orientations 0°, 180° [RGS270 is unused]): 1206nm-1892nm, R~480
- calibration unit (NI-CU), for flat-fields and other calibration purposes:
 - 5 LEDs from ~920 to ~2000 nm

Figure 3.10. VIS and NISP specifics, from the [Euclid Consortium website](#)

on the other hand, houses the spacecraft’s essential subsystems, including power distribution, propulsion, and communication systems. The whole satellite has a size of $4,5 \times 3 \times 3$ m and a mass of 2200 kg. VIS and NISP are its two main scientific instruments; their characteristics are summarized in Fig. 3.10.

The main aim of the VIS instrument is to provide high-resolution images to characterize the morphology of the sources to the accuracy needed for the study of cosmic shear. The focal plane is composed of 6×6 4096×4132 CCDs with 12-micron pixels (609 million pixels in total) and a spectral range from 550 to 950 nm (Cropper et al., 2016), covering a wide instantaneous field of view of 0.57 deg^2 , which is almost three times the solid angle of the full Moon. This high-quality panoramic imager reaches a resolution of 0.18 arcsec, achieving a signal-to-noise ratio of 10 or more for 1.5 billion galaxies down to magnitude $I_E = 24.5$ in 4200 seconds exposures³. Data from the Gaia mission (Gaia Collaboration et al., 2016) will be used to remove bright stars contaminating the field of view.

The main aim of the NISP instrument is to provide galaxies’ redshift, either through photometry or spectroscopy. The focal plane is composed of 4×4 , 2040×2040 18 micron pixels (64 million pixels in total), covering the 950 to 2020 nm range (Euclid Collaboration: Schirmer et al., 2022), and can operate as a photometer (NISP-P) and a spectrometer (NISP-S) – although not simultaneously. It shares the same 0.57 deg^2 FoV of the VIS instrument. The incoming light is sent through two wheels, one containing the three photometry filters (Y, J, and H; see Fig. 3.2), and the other four spectrometry grism, which splits light from every star and galaxy by wavelength directly on the image (a technique called “slitless spectroscopy”). This allows measuring all the spectra in each exposure, at the cost of a more laborious analysis to disentangle them, for which the different orientations of the grisms are essential.

Some early commissioning test images, amongst the first ever captured by the satellite, are shown in Fig. 3.11

3.3.2 Survey strategy and data releases

The observational strategy will consist of both wide and deep surveys. The wide survey (Euclid Collaboration: Scaramella et al., 2022) will explore the darkest sky (free from the contaminating light of the sun and the galaxy) over an area of $14\,700 \text{ deg}^2$, which corresponds to more than one-third of the whole celestial sphere. This is the main part of the survey operation, to which *Euclid* will devote the most time (about $\sim 90\%$ of the total observational time). It will cover patches of 400 deg^2 per month, and the orientation of the telescope will be changed every six months to explore the other hemisphere.

The wide survey will be complemented by three deep field surveys covering 40 deg^2 , reaching 2 magnitudes deeper than the wide survey in order to calibrate the instruments and provide data for the secondary scientific objectives (the so-called

³<https://www.euclid-ec.org>

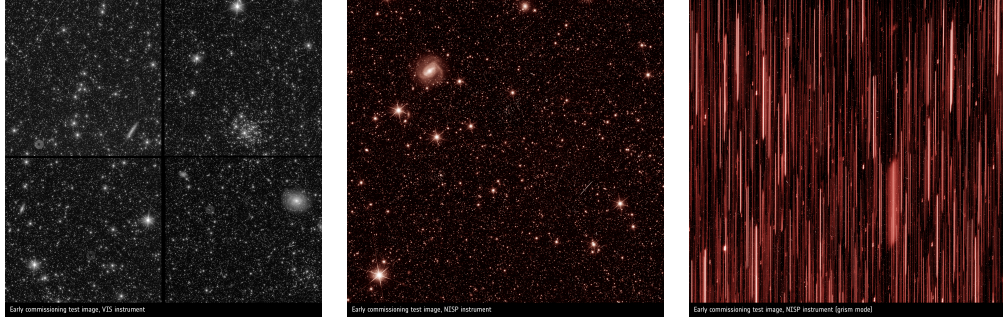


Figure 3.11. Early commissioning test images, the first publicly released by the Euclid Consortium. Left: 566 s exposure from the VIS instrument, showing 4 out of the 36 available CCDs. Some cosmic rays and optical artefacts are present in the largely unprocessed image. Center: NISP-P instrument, 100 s exposure, Y band, zoomed in from one of the 16 detectors. Right: NISP-S instrument. The light from stars and galaxies is spread by the grism into its different wavelengths, allowing measurement of the spectra of all the different sources in the image. Source: [Euclid Consortium website](#).

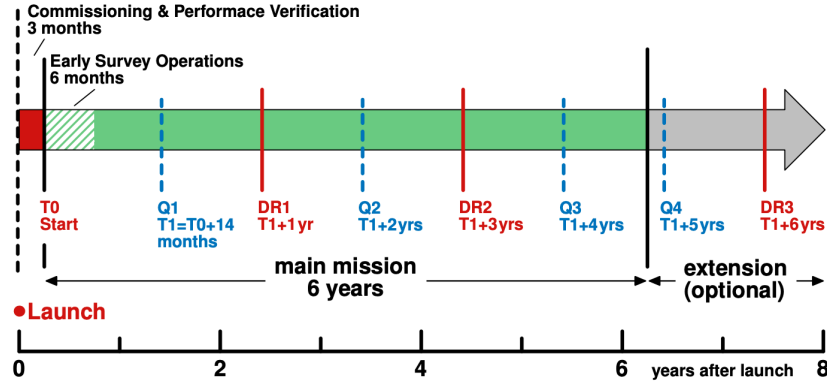


Figure 3.12. The expected survey timeline for the *Euclid* mission. Source: (Euclid Collaboration: Scaramella et al., 2022).

“legacy science”, such as the detection of faint high-redshift galaxies, AGNs and supernovae). Furthermore, the deep surveys will be used to assess the purity and completeness of the wide surveys. Purity is a measure of how well a sample isolates a particular type of object or phenomenon of interest: in this case, a high-purity sample would predominantly contain galaxies that genuinely belong to the category under investigation ($H\alpha$ emitters), with minimal contamination from interlopers or artefacts. Completeness, conversely, quantifies the fraction of the total objects of interest that are successfully identified and included in the sample, i.e., it measures how exhaustive the survey is in capturing the galaxies that meet the selection criteria.

The timeline for the survey operations is sketched in Fig. 3.12. The main Data Releases (DR) will cover respectively 2500, 7500 and 14700 deg^2 . In addition, four Quick Data Releases (Q) are foreseen, each of $\sim 50 \text{ deg}^2$ (Euclid Collaboration: Scaramella et al., 2022). The Euclid Consortium will publicly release the data after a proprietary period of about one year (Laureijs et al., 2011).

3.3.3 Data processing

Over the mission’s six-year span, *Euclid* will collect over 500,000 visible and near-infrared images, which will be relayed to Earth on a daily cadence.

The analysis and processing of this massive volume of data, expected to reach tens of petabytes, are under the responsibility of the Science Ground Segment (SGS). The SGS is divided into two core sections: the ESA Science Operations Centre (SOC), and the Euclid Consortium Science Ground Segment (EC SGS). Among the SOC’s responsibilities are survey planning, managing the downlinked data and daily quality reports, whereas the EC SGS is in charge of the reduction of the data from (real or simulated) images to observables (such as the $C(\ell)$ described in Sect. 2.4.2), as well as the integration of photometric data from other ground-based surveys, which will provide data for the missing g, r, i and z bands.

Chapter 4

Super-sample covariance

As mentioned in the previous chapters, we are entering the era of precision cosmology, characterized by a large amount of high-quality data. This wealth of information will allow us to constrain the cosmological parameters with unprecedented accuracy and precision, thus making it possible to select between competing cosmological models and advance in this way our understanding of the dark and visible Universe. However, these new and exciting possibilities come with their own unique set of challenges, mainly the need to tame the systematic effect that could bias the parameters' estimates at this level of precision. Indeed, upcoming Stage IV surveys such as the Vera C. Rubin Observatory Legacy Survey of Space and Time (LSST, [Ivezić et al., 2019](#)), the Nancy Grace Roman Space Telescope ([Spergel et al., 2015](#)), and the *Euclid* mission ([Laureijs et al., 2011](#)) will have stringent requirements on the accuracy of the modelling of both the theory and the covariance of the observables under study. The covariance matrix is in fact one of the crucial ingredients in a likelihood analysis, as the measurement of a physical quantity is meaningless without an estimate of the associated uncertainty. The following two chapters focus on the description of super-sample covariance, an important contribution to sample variance for upcoming high-resolution LSS surveys, and the computation of its impact on the *Euclid* photometric survey, which is the aim of one of the Key Project papers ([Euclid Collaboration: Sciotti et al., 2023](#)) of the Photometric Galaxy Clustering Work Package within the GC SWG of the Euclid Collaboration.

4.1 Introduction

As illustrated in Chap. 2, the covariance matrix is a measure of the joint variability of two quantities, allowing to quantify their correlation or anti-correlation; its diagonal elements describe the covariance of the variable with itself, which is the variance, i.e., the square of its uncertainty. The likelihood analysis allows translating data into (cosmological) parameters, and the covariance of the data into the covariance of the parameters. This can be accomplished through a FM or MCMC approach.

The covariance matrix of the two-point harmonic space observables gets contributions from the measurement noise (e.g., the shot and shape noise), and the sample variance due to the incomplete sampling of Fourier modes caused by the

finiteness of the survey volume (in the radial and angular direction). In harmonic space, it is composed of three terms: the Gaussian (G), super-sample (SSC) and connected non-Gaussian (cNG) covariance. The first represents the covariance of the observables if the statistical distribution of the corresponding underlying field (e.g., the galaxy number density field $\delta_g(\mathbf{x}, a)$ in the case of GCph) was perfectly Gaussian. The second and third arise because of the non-Gaussian coupling of the different Fourier modes of the fields.

As seen in Sect. 1.4.3, the time evolution of the density contrast field $\delta(\mathbf{x}, a)$ at linear order, encapsulated in Eq. (1.58), is scale-independent, which means that all Fourier modes evolve at the same rate. Linear theory holds for small density perturbations around the mean, i.e., $\rho(\mathbf{x}) \sim \bar{\rho} \rightarrow \delta(\mathbf{x}) \sim 0$. However, contrary to the temperature perturbations in the CMB, which show a level of anisotropy of order 10^{-4} , the density contrast field δ can take much more extreme values: from -1 for the emptiest regions, to ~ 200 for the dark matter halos. Moreover, nonlinear clustering becomes increasingly more important at smaller scales, which contain most of the cosmological information (especially for WL). This makes the linear treatment inadequate for the investigation of the small scales of LSS. A more appropriate description involves the inclusion (at least) of the second-order terms when solving the differential equations describing the time evolution of the density and velocity fields as a function of time (Eqs. 1.64 and 1.65), which involve mode-coupling terms.

This coupling of modes is captured in the covariance matrix by the cNG and SSC terms. The first of these, also referred to as the “non-Gaussian covariance in the absence of survey window effects” Krause and Eifler (2017), describes mode coupling within the survey volume. Recent works have shown this term to be subdominant with respect to the SSC for upcoming Stage IV surveys (the parameter constraints obtained with a G + SSC + cNG covariance are $\lesssim 5\%$ larger than the ones obtained with a G + SSC covariance for a *Euclid*-like cosmic shear survey, see Barreira et al. 2018b), and will not be treated in the present work.

The second term, instead, describes the effects of the coupling of modes respectively larger and smaller than the survey typical linear size $L = V_W^{1/3}$ (or the smallest survey dimension, V_W being the survey volume). SSC has been first introduced for cluster counts in Hu and Kravtsov (2003) – sometimes being referred to as ‘beat coupling’, see Rimes and Hamilton (2006); Hamilton et al. (2006) – and has garnered a lot of attention in recent years (Takada and Hu, 2013; Li et al., 2014; Barreira et al., 2018b; Digman et al., 2019; Bayer et al., 2022; Yao et al., 2023); see also Linke et al. (2023) for an insightful discussion on SSC in real space.

The above-mentioned length L sets a natural scale for the maximum wavelength λ (minimum wavenumber k) which can be sampled by any real survey. In fact, Fourier modes with $k < 1/L$ simply cannot be accommodated by the survey volume; moreover, the nonlinear mode coupling described above intertwines the evolution of these “super-survey”, or “soft” modes with the evolution of “sub-survey”, or “hard” modes. The net result of these two factors is a modulation of the observables within the survey volume by an unobservable background perturbation, called δ_b , which

biases our measurement. This is the fundamental quantity characterizing the SSC effect, and is defined by

$$\delta_b \equiv \frac{\bar{\rho}_{mW}}{\bar{\rho}_m} - 1, \quad (4.1)$$

where $\bar{\rho}_{mW}$ is the matter density averaged *within the survey volume* and $\bar{\rho}_m$ is the matter density averaged over the whole Universe (Lacasa et al., 2018). In other words, δ_b is the spatial average (denoted by the brackets) of the density contrast $\delta_m(\mathbf{x}, z)$, or mean density fluctuation, over the survey volume (window):

$$\langle \delta_m(\mathbf{x}, z) \rangle_{\text{universe}} = 0, \quad (4.2)$$

$$\langle \delta_m(\mathbf{x}, z) \rangle_W = \delta_b(z). \quad (4.3)$$

The modulation induced by the super-survey modes is therefore equivalent to a change in the background density of the observed region, which affects and correlates all LSS probes – see Fig. 4.1. This is accounted for as an additional term in the

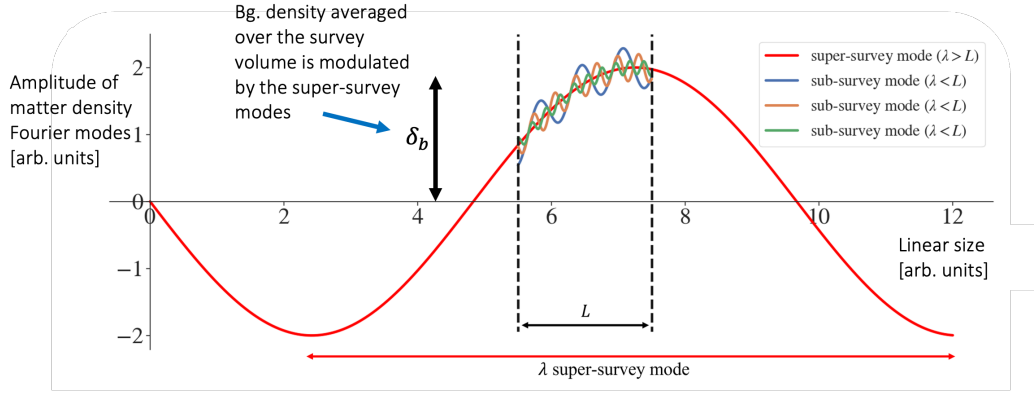


Figure 4.1. A sketch of the mode modulation induced by a long-wavelength background density perturbation δ_b , or super-survey mode, in red. The blue, orange and green curves represent the sub-survey (or hard) modes, which have $\lambda < L$ and can thus be sampled. The net effect is a shift of the observed modes, which biases the measurement of the density perturbations.

data covariance matrix, which becomes non-diagonal in (ℓ_1, ℓ_2) – or in (k_1, k_2) – again because the different modes do not evolve independently. Being the most affected by nonlinear dynamics, the smaller scales are heavily impacted by SSC, where the effect is expected to be the dominant source of statistical uncertainty for the two-point statistics of WL: it has in fact been found to increase unmarginalised uncertainties on cosmological parameters up to a factor of about 2 (for a *Euclid*-like survey, see Barreira et al., 2018a; Gouyou Beauchamps et al., 2022). In the case of photometric galaxy clustering (again, for a *Euclid*-like survey), Lacasa and Grain (2019) – hereafter LG19 – found the cumulative signal-to-noise to be decreased by a factor of ~ 5.7 at $\ell_{\text{max}} = 2000$. These works, however, either do not take into account marginalised uncertainties or the variability of the probe responses, do not include cross-correlations between probes, or do not follow the full specifics of the *Euclid* photometric survey described below.

In the following two Chapters, we detail the theory, approximations, survey settings, assumptions and numerical pipelines underlying the present treatment of SSC for the WL, GCph and 3×2 pt probes in *Euclid*. We first validate the forecast constraints on the cosmological parameters both including and neglecting the SSC term; these are produced using two independent codes, whose only shared feature is their use of the public Python module PySSC¹² (LG19) to compute the fundamental elements needed to build the SSC matrix. Secondly, we investigate the impact of SSC on the marginalised uncertainties and on the dark energy Figure of Merit (FoM), both obtained through a Fisher forecast of the constraining power of *Euclid*'s photometric observables.

These Chapters are organized as follows: Sect. 4.2 presents a general overview of the theoretical framework underpinning SSC, with the application to the projected observables relevant for this work discussed in Sect. 4.3 and the approximations used in presented in Sect. 4.4. In Sect. 5.1 we outline the theoretical model and specifics used to produce the forecasts, while Sect. 5.2 provides technical details on the codes' implementation and validation. Then, we study in Sect. 5.3 the impact of SSC on *Euclid* constraints, for different binning schemes and choices of systematic errors and priors. Finally, we present our conclusions in Sect. 5.4.

4.2 Theory and approximations

The starting point to obtain an analytical model for SSC is, due to the nature of the effect, a formalism describing the observables in the presence of a finite window function, which as we shall see is sufficient in itself to introduce mode couplings. Furthermore, the reaction, or response, of the observables to a shift in background density must be quantified, using semi-analytical models or simulations. The present section will introduce these.

4.2.1 Power spectrum estimator and covariance in the presence of a survey window

We begin by introducing the different terms in the covariance matrix of the matter power spectrum in the presence of a finite window function $W(\mathbf{x})$ describing the survey volume (e.g., with a value of 1 for \mathbf{x} in the observed region and 0 outside), mainly following the discussion presented in Scoccimarro et al. (1999); Takada and Hu (2013); Li et al. (2014). In the following, we assume the mean density of the field to be known, which is appropriate for WL (in this case, we probe the matter density directly, whose background value is fixed by the cosmological parameters); we will then generalize the result to the case of a density contrast field measured w.r.t. the mean of the survey region, as in the case of GCph.

The observed field in the presence of a window function is, in real space, $\delta_W(\mathbf{x}) =$

¹<https://github.com/fabienlacasa/PySSC>

²<https://pyssc.readthedocs.io/en/latest/index.html>

$\delta(\mathbf{x})W(\mathbf{x})$. This product becomes a convolution in Fourier space:

$$\tilde{\delta}_W(\mathbf{k}) = \int \frac{d^3\mathbf{q}}{(2\pi)^3} \tilde{W}(\mathbf{q}) \tilde{\delta}(\mathbf{k} - \mathbf{q}) , \quad (4.4)$$

where the tilde denotes Fourier-transformed quantities. We define a binned estimator (or “band-power” estimator) $\hat{P}(k_i)$ of the true underlying power spectrum $P(k)$, which as seen in Sect. 2.4 is defined by the relation

$$\langle \tilde{\delta}(\mathbf{k}) \tilde{\delta}(\mathbf{k}') \rangle = (2\pi)^3 \delta_D^3(\mathbf{k} + \mathbf{k}') P(k) , \quad (4.5)$$

as

$$\hat{P}(k_i) \equiv \frac{1}{V_W} \int_{|\mathbf{k}| \in k_i} \frac{d^3\mathbf{k}}{V_{k_i}} \tilde{\delta}_W(\mathbf{k}) \tilde{\delta}_W(-\mathbf{k}) \quad (4.6)$$

where $V_W = \int d^3\mathbf{x} W(\mathbf{x})$ is the survey volume and the integral is computed over a thin spherical shell of width Δk , with volume $V_{k_i} \approx 4\pi k_i^2 \Delta k$ for $\Delta k \ll k_i$. Its ensemble average is

$$\langle \hat{P}(k_i) \rangle = \frac{1}{V_W} \int_{|\mathbf{k}| \in k_i} \frac{d^3\mathbf{k}}{V_{k_i}} \int \frac{d^3\mathbf{q}}{(2\pi)^3} |\tilde{W}(\mathbf{q})|^2 P(\mathbf{k} - \mathbf{q}) , \quad (4.7)$$

having used Eqs. (4.4), (4.5), and (4.6). The observed power spectrum is then a convolution of the underlying power spectrum with the Fourier transform of the window function. Such convolution has the effect of combining (or “smearing”) the density modes that are separated by less than the Fourier width of the window, which in this case is $1/L$. The Fourier transform of the window function acts in fact as a filter in Fourier space, with its width determining the range of modes that are combined. This is a general property of convolutions: they combine the information from the input function (in this case, the true power spectrum) over the range determined by the other function (in this case, the Fourier transform of the window function).

The estimator $\hat{P}(k_i)$ is biased low for modes outside the window function support, i.e., for $k < 1/L$, whereas the bias becomes progressively smaller for shorter-wavelength modes within the survey volume, $k \gg 1/L$. In this limit, we have in fact an unbiased estimator:

$$\begin{aligned} \langle \hat{P}(k_i) \rangle &\simeq \frac{1}{V_W} \int_{|\mathbf{k}| \in k_i} \frac{d^3\mathbf{k}}{V_{k_i}} P(k) \int \frac{d^3\mathbf{q}}{(2\pi)^3} |\tilde{W}(\mathbf{q})|^2 \\ &\simeq P(k_i) \frac{1}{V_W} \int \frac{d^3\mathbf{q}}{(2\pi)^3} |\tilde{W}(\mathbf{q})|^2 = P(k_i) . \end{aligned} \quad (4.8)$$

Having used $P(|\mathbf{k} - \mathbf{q}|) \simeq P(k)$ over the integration range of $d^3\mathbf{q}$ which the window function supports (first line); indeed, for $q \gg 1/L$ the above integral is suppressed by the window function $|\tilde{W}(\mathbf{q})|$, which means that the result is only non-negligible if $k \gg q$ (Barreira et al., 2018b). We have also assumed that $P(k)$ varies slowly within the k bin (second line); the last equality relies on the general identity of the window function:

$$V_W = \int d^3\mathbf{x} W^n(\mathbf{x}) = \int \left[\prod_{a=1}^n \frac{d^3\mathbf{q}_a}{(2\pi)^3} \tilde{W}(\mathbf{q}_a) \right] (2\pi)^3 \delta_D^3(\mathbf{q}_{1\dots n}) , \quad (4.9)$$

having adopted the notation $\mathbf{q}_{1\dots n} = \mathbf{q}_1 + \dots + \mathbf{q}_n$.

Having constructed our unbiased power spectrum estimator, we can now proceed to study its statistical properties, namely its covariance matrix. In the following discussion, we will neglect measurement noise contributions such as shape and shot noise (that is, we will consider only sample variance). The covariance matrix is then defined as:

$$\text{Cov}_{ij} \equiv \text{Cov} [P(k_i), P(k_j)] = \langle \hat{P}(k_i) \hat{P}(k_j) \rangle - \langle \hat{P}(k_i) \rangle \langle \hat{P}(k_j) \rangle \quad (4.10)$$

$$\simeq \frac{1}{V_W} \left[\frac{(2\pi)^3}{V_{k_i}} 2P(k_i)^2 \delta_{ij}^K + \bar{T}^W(k_i, k_j) \right] \quad (4.11)$$

where the third equality holds in the same $k \gg 1/L$ limit. The Kronecker delta function enforces the first term of the covariance, the Gaussian (or “disconnected”) term, to be diagonal in k_i, k_j (but not necessarily in other quantities, such as the different redshift bins for a tomographic analysis). This is because, in the Gaussian limit, each Fourier mode is an independent Gaussian random variable. Hence, the Gaussian covariance is simply proportional to the number of independent k modes (Gaussian random variables) in the shell i :

$$\text{Cov}_{ij}^G = \frac{1}{N_{\text{modes}}(k_i)} P^2(k_i) \delta_{ij}^K, \quad (4.12)$$

with

$$N_{\text{modes}}(k_i) = \frac{V_{k_i} V_W}{2(2\pi)^3} \simeq \frac{2\pi k_i^2 \Delta k V_W}{(2\pi)^3} \quad (4.13)$$

The factor 2 in the denominator of Eq. (4.13) arises from the reality condition of the density field $\tilde{\delta}_W^*(\mathbf{k}) = \tilde{\delta}_W(-\mathbf{k})$.

The second term is the non-Gaussian contribution and is described by the trispectrum, the Fourier transform of the connected 4-point correlation function:

$$\langle \tilde{\delta}(\mathbf{k}_1) \tilde{\delta}(\mathbf{k}_2) \tilde{\delta}(\mathbf{k}_3) \tilde{\delta}(\mathbf{k}_4) \rangle_c = (2\pi)^3 \delta_D^3(\mathbf{k}_{1234}) T(\mathbf{k}_1, \mathbf{k}_2, \mathbf{k}_3, \mathbf{k}_4) \quad (4.14)$$

where the Dirac delta once again enforces momentum conservation: $\mathbf{k}_1 + \mathbf{k}_2 + \mathbf{k}_3 + \mathbf{k}_4 = 0$. The 4-point function appears naturally from the definition of covariance itself, which involves the (expectation value of the) product of two two-point functions. We note that both terms in Eq. (4.11) scale as the inverse of the survey volume, but the non-Gaussian term does not scale as $1/V_{k_i}$, the volume of the shell. This means that, contrary to the Gaussian contribution, we cannot average over more Fourier modes k_i (i.e., use finer band-powers) to decrease the non-Gaussian covariance; the only way to reduce this term is to increase the survey volume.

The trispectrum itself is then convolved with the window function, analogously to Eq. (4.7):

$$\begin{aligned} \bar{T}^W(k_i, k_j) &= \frac{1}{V_W} \int_{|\mathbf{k}| \in k_i} \frac{d^3 \mathbf{k}}{V_{k_i}} \int_{|\mathbf{k}'| \in k_j} \frac{d^3 \mathbf{k}'}{V_{k_j}} \int \left[\prod_{a=1}^4 \frac{d^3 \mathbf{q}_a}{(2\pi)^3} \tilde{W}(\mathbf{q}_a) \right] (2\pi)^3 \delta_D^3(\mathbf{q}_{1234}) \\ &\quad \times T(\mathbf{k} + \mathbf{q}_1, -\mathbf{k} + \mathbf{q}_2, \mathbf{k}' + \mathbf{q}_3, -\mathbf{k}' + \mathbf{q}_4) . \end{aligned} \quad (4.15)$$

This convolution with the window function means that different 4-point configurations separated by less than the Fourier width of the window function $1/L$ and involving contributions from super-survey modes contribute to the covariance.

If, as assumed for the PS, the trispectrum is slowly varying as a function of scale, it can be pulled out of the innermost integral; moreover, we can again use Eq. (4.9) to eliminate one $1/V_W$ factor, leaving us with

$$\text{Cov}_{ij} \approx \text{Cov}_{ij}^G + \text{Cov}_{ij}^{T0} \quad (4.16)$$

$$\approx \frac{1}{V_W} \frac{(2\pi)^3}{V_{k_i}} 2P^2(k_i) \delta_{ij}^K + \text{Cov}_{ij}^{T0}, \quad (4.17)$$

being

$$\text{Cov}_{ij}^{T0} = \frac{1}{V_W} \int_{|\mathbf{k}| \in k_i} \frac{d^3 \mathbf{k}}{V_{k_i}} \int_{|\mathbf{k}'| \in k_j} \frac{d^3 \mathbf{k}'}{V_{k_j}} T(\mathbf{k}, -\mathbf{k}, \mathbf{k}', -\mathbf{k}'). \quad (4.18)$$

This equation implies that only parallelogram configurations of the trispectrum contribute to the non-Gaussian covariance of the band-power estimates.

If, on the other hand, the small-scale ($k \gg 1/L$) trispectrum exhibits significant variations or features within a range of wavenumbers $\Delta k \lesssim 1/L$ (i.e., comparable to the inverse of the survey size), additional effects arise in the non-Gaussian term of the covariance matrix. These are described in the pioneering work of [Takada and Hu \(2013\)](#) by the so-called *squeezed quadrilaterals* configurations of the trispectrum (see Fig. 4.2), which have pairs of sides nearly equal and opposite. Reminding the condition $\mathbf{q}_{1234} = \mathbf{0}$, we can perform a change of variables to rewrite the trispectrum term of Eq. (4.16):

$$\mathbf{k} + \mathbf{q}_1 \rightarrow \mathbf{k} \quad (4.19)$$

$$\mathbf{k}' + \mathbf{q}_3 \rightarrow \mathbf{k}' \quad (4.20)$$

$$\mathbf{q}_1 + \mathbf{q}_2 \rightarrow \mathbf{q}_{12}. \quad (4.21)$$

which gives $T(\mathbf{k} + \mathbf{q}_1, -\mathbf{k} + \mathbf{q}_2, \mathbf{k}' + \mathbf{q}_3, -\mathbf{k}' + \mathbf{q}_4) \leftrightarrow T(\mathbf{k}, -\mathbf{k} + \mathbf{q}_{12}, \mathbf{k}', -\mathbf{k}' - \mathbf{q}_{12})$. The configurations of interest can then be expressed as

$$\lim_{q_{12} \rightarrow 0} T(\mathbf{k}, -\mathbf{k} + \mathbf{q}_{12}, \mathbf{k}', -\mathbf{k}' - \mathbf{q}_{12}), \quad (4.22)$$

always under the approximation $q_{12} \ll k, k'$. Again, k, k' are hard modes and q_{12} is a soft mode that approaches zero in the squeezed limit; this limit therefore captures the correlation between the PS at k and k' that is induced by a shared long- (infinite-) wavelength mode q_{12} .

The key ansatz introduced in the above-mentioned paper is that these particular configurations in the trispectrum are determined by the response of the PS to a change in the background density δ_b , given by the infinite-wavelength mode q_{12} . This is called the *trispectrum consistency relation*:

$$\bar{T}(\mathbf{k}, -\mathbf{k} + \mathbf{q}_{12}, \mathbf{k}', -\mathbf{k}' - \mathbf{q}_{12}) \approx T(\mathbf{k}, -\mathbf{k}, \mathbf{k}', -\mathbf{k}') + \frac{\partial P(k)}{\partial \delta_b} \frac{\partial P(k')}{\partial \delta_b} P_L(q_{12}), \quad (4.23)$$

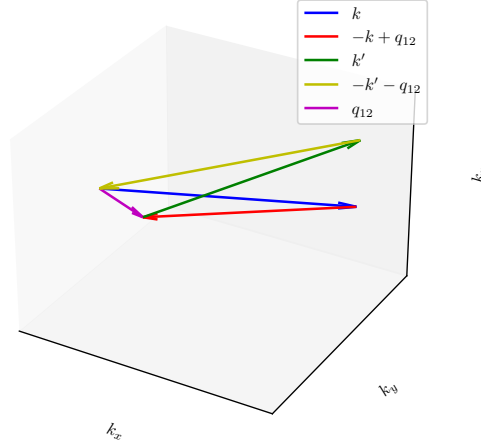


Figure 4.2. A sketch of a possible squeezed quadrilateral configuration. The magnitude of the long-wavelength mode q_{12} has been exaggerated for clarity. The units are arbitrary.

where the overbar indicates an angle average over \mathbf{q}_{12} , because a constant mode δ_b cannot quantify a directional dependence. In the last equation the *linear* matter power spectrum appears: the perturbation δ_b must be a mode in the linear regime. The complete covariance matrix becomes therefore :

$$\text{Cov}_{ij} = \text{Cov}_{ij}^G + \text{Cov}_{ij}^{T0} + \sigma^2 \frac{\partial P(k_i)}{\partial \delta_b} \frac{\partial P(k_j)}{\partial \delta_b} \quad (4.24)$$

$$= \text{Cov}_{ij}^G + \text{Cov}_{ij}^{\text{cNG}} + \text{Cov}_{ij}^{\text{SSC}}. \quad (4.25)$$

The second term, Cov_{ij}^{T0} , is given again in Eq. (4.18) and can be interpreted as the nonlinear correlations which are not mediated by a long-wavelength (super-survey), constant mode. This is the connected non-Gaussian term, although the term “connected” is slightly deceptive, being the SSC also related to connected configurations of the trispectrum.

The last term, the SSC, quantifies the correlation between the PS in bins k_i and k_j induced by the shared background fluctuation δ_b , whose variance is given by

$$\sigma^2 \equiv \frac{1}{V_W^2} \int \frac{d^3 \mathbf{q}}{(2\pi)^3} |\tilde{W}(\mathbf{q})|^2 P_L(q); \quad (4.26)$$

Combining the two expressions above, we can give the explicit form of the SSC:

$$\text{Cov}^{\text{SSC}}(k_i, k_j) = \frac{1}{V_W^2} \frac{\partial P(k_i)}{\partial \delta_b} \frac{\partial P(k_j)}{\partial \delta_b} \int \frac{d^3 \mathbf{q}}{(2\pi)^3} |\tilde{W}(\mathbf{q})|^2 P_L(q). \quad (4.27)$$

This term is composed of two main ingredients: the (co)variance of the background density mode δ_b , given by Eq. (4.26), and the *response functions* $\partial P(k_i) / \partial \delta_b$, which quantify the reaction of a given statistics (in this case, the matter power spectrum) to a coherent change in background density. Of these two terms, the latter is less straightforward to compute; different methods will be presented in the following section.

We conclude this section by noting that, contrary to the Gaussian and connected non-Gaussian terms, the SSC dependence on the survey volume is non-trivial, and encoded within the σ^2 term: $\text{Cov}_{ij}^{\text{SSC}} \propto \sigma^2(V_W)$, while $\text{Cov}_{ij}^{\text{G,cNG}} \propto 1/V_W$.

4.2.2 Response functions

As stated in the introduction and shown formally in the previous section, super-sample covariance parameterizes our ignorance on the effect of large-scale density modes on the observables of interest. This effect arises precisely because of the sensitivity of these to a coherent change in background density, which is a common characteristic of all LSS probes. Quantifying this sensitivity is the aim of the present section.

In the literature, two main approaches are used to solve this problem. The first is to compute the responses using the halo model (Takada and Hu, 2013; Krause and Eifler, 2017; Rizzato et al., 2019; Lacasa and Grain, 2019); this semi-analytical treatment offers the advantage of a more profound physical intuition of the mechanisms at play and the different contributions to the responses but tends to fail on small, highly nonlinear scales (Wagner et al., 2015a). The second possible approach is the so-called *separate universe* technique (Wagner et al., 2015a,b; Li et al., 2016; Barreira et al., 2019), which is based on the ansatz that a constant background density perturbation is akin to a separate universe with different cosmological parameters. The next two sections will explain these two different methods.

Halo model response

The trispectrum consistency relation (Eq. 4.23) tells us that it is possible to compute the responses from the squeezed configurations of the matter trispectrum. In the halo model approach, the trispectrum can be described in a similar way to the PS, but including contributions from up to four halos: T_{nh} are the n -halo terms, describing the correlations between *four* points distributed in n halos (1 for the intra-halo term and 2, 3 or 4 for the inter-halo terms).

$$T = T_{1h} + (T_{2h}^{22} + T_{2h}^{13}) + T_{3h} + T_{4h}. \quad (4.28)$$

The superscripts in the 2-halo terms indicate the number of points in the first and second halos: T_{2h}^{22} will have two points in the first and two points in the second, while T_{2h}^{13} will have one point in the first and three in the second.

These terms are in turn given by the halo model auxiliary functions (1.81) and perturbation theory expressions:

$$\begin{aligned} T_{1h}(\mathbf{k}_1, \mathbf{k}_2, \mathbf{k}_3, \mathbf{k}_4) &= I_4^0(k_1, k_2, k_3, k_4), \\ T_{2h}^{22}(\mathbf{k}_1, \mathbf{k}_2, \mathbf{k}_3, \mathbf{k}_4) &= P_L(k_{12}) I_2^1(k_1, k_2) I_2^1(k_3, k_4) + 2 \text{ perm.} \\ T_{2h}^{13}(\mathbf{k}_1, \mathbf{k}_2, \mathbf{k}_3, \mathbf{k}_4) &= P_L(k_1) I_1^1(k_1) I_3^1(k_2, k_3, k_4) + 3 \text{ perm.} \\ T_{3h}(\mathbf{k}_1, \mathbf{k}_2, \mathbf{k}_3, \mathbf{k}_4) &= B_{\text{PT}}(\mathbf{k}_1, \mathbf{k}_2, \mathbf{k}_3, \mathbf{k}_4) I_1^1(k_1) I_1^1(k_2) I_2^1(k_3, k_4) + 5 \text{ perm.}, \\ T_{4h}(\mathbf{k}_1, \mathbf{k}_2, \mathbf{k}_3, \mathbf{k}_4) &= T_{\text{PT}}(\mathbf{k}_1, \mathbf{k}_2, \mathbf{k}_3, \mathbf{k}_4) I_1^1(k_1) I_1^1(k_2) I_1^1(k_3) I_1^1(k_4), \end{aligned} \quad (4.29)$$

where “perm.” refers to cyclic permutations, obtained by rotating the k_i indices: $k_1 \rightarrow k_2, k_2 \rightarrow k_3, k_3 \rightarrow k_4$ and $k_4 \rightarrow k_1$. B_{PT} and T_{PT} are the bispectrum and

trispectrum computed from perturbation theory, defined as

$$B_{\text{PT}}(\mathbf{k}_1, \mathbf{k}_2, \mathbf{k}_3) = 2F_2(\mathbf{k}_1, \mathbf{k}_2) P_L(k_1) P_L(k_2) + 2 \text{ perm.} \quad (4.30)$$

$$\begin{aligned} T_{\text{PT}}(\mathbf{k}_1, \mathbf{k}_2, \mathbf{k}_3, \mathbf{k}_4) = & 4[F_2(\mathbf{k}_{13}, -\mathbf{k}_1) F_2(\mathbf{k}_{13}, \mathbf{k}_2) P_L(k_{13}) P_L(k_1) P_L(k_2) \\ & + 11 \text{ perm.}] \\ & + 6[F_3(\mathbf{k}_1, \mathbf{k}_2, \mathbf{k}_3) P_L(k_1) P_L(k_2) P_L(k_3) + 3 \text{ perm.}] , \end{aligned} \quad (4.31)$$

where the mode-coupling kernels F_2 , G_2 and F_3 are given respectively in Eqs. (1.71), (1.72) and (1.77). We remind that these are only exact for Einstein-de Sitter cosmologies, but are approximately valid for other cosmological models by virtue of their weak dependence on $\Omega_{\text{m},0}$.

To obtain an expression for the response functions, we compare the SSC term from the consistency relation (Eq. 4.23):

$$\begin{aligned} \delta T & \simeq T(\mathbf{k}, -\mathbf{k} + \mathbf{q}_{12}, \mathbf{k}', -\mathbf{k}' - \mathbf{q}_{12}) - T(\mathbf{k}, -\mathbf{k}, \mathbf{k}', -\mathbf{k}') \\ & \simeq \frac{\partial P(k)}{\partial \delta_{\text{b}}} \frac{\partial P(k')}{\partial \delta_{\text{b}}} P_L(q_{12}) \end{aligned} \quad (4.32)$$

with the expression of δT from the halo model; to leading order in q_{12}/k , the variation in the trispectrum induced by the long-wavelength mode \mathbf{q}_{12} can be expressed by plugging the different terms of Eq. (4.29) for the connected configurations of interest in Eq. (4.28):

$$\begin{aligned} \delta T_{1\text{h}} & \approx 0 \\ \delta T_{2\text{h}}^{22} & \approx P_L(q_{12}) I_2^1(k, k) I_2^1(k', k') \\ \delta T_{2\text{h}}^{13} & \approx 0 \\ \delta T_{3\text{h}} & \approx 2P_L(q_{12}) I_2^1(k', k') \mathcal{F}(\mathbf{k}, \mathbf{q}_{12}) + 2P_L(q_{12}) I_2^1(k, k) \mathcal{F}(\mathbf{k}', -\mathbf{q}_{12}) \\ \delta T_{4\text{h}} & \approx 4P_L(q_{12}) \mathcal{F}(\mathbf{k}, \mathbf{q}_{12}) \mathcal{F}(\mathbf{k}', -\mathbf{q}_{12}) \end{aligned} \quad (4.33)$$

having again used the approximation $|\mathbf{k} + \mathbf{q}_1| \sim k$, and in which we defined

$$\mathcal{F}(\mathbf{k}, \mathbf{q}) \equiv [P_L(k) F_2(\mathbf{q}, -\mathbf{k}) + P_L(|\mathbf{k} - \mathbf{q}|) F_2(\mathbf{q}, \mathbf{k} - \mathbf{q})] I_1^1(k) I_1^1(|\mathbf{k} - \mathbf{q}|) , \quad (4.34)$$

We can factor out the terms in $P_L(q_{12})$ and write δT as

$$\begin{aligned} \delta T & \approx P_L(q_{12}) \left[I_2^1(k, k) I_2^1(k', k') + 2I_2^1(k', k') \mathcal{F}(\mathbf{k}, \mathbf{q}_{12}) \right. \\ & \quad \left. + 2I_2^1(k, k) \mathcal{F}(\mathbf{k}', -\mathbf{q}_{12}) + 4\mathcal{F}(\mathbf{k}, \mathbf{q}_{12}) \mathcal{F}(\mathbf{k}', -\mathbf{q}_{12}) \right] \\ & = P_L(q_{12}) \left[\left(I_2^1(k, k) + 2\mathcal{F}(\mathbf{k}, \mathbf{q}_{12}) \right) \times \left(I_2^1(k', k') + 2\mathcal{F}(\mathbf{k}', -\mathbf{q}_{12}) \right) \right] \end{aligned} \quad (4.35)$$

We now integrate \mathcal{F} over the cosine μ_k of the angle θ between \mathbf{k} and \mathbf{q} to average over all possible directions, or orientations of \mathbf{k} with respect to \mathbf{q} :

$$\int_{-1}^1 \frac{d\mu_k}{2} \mathcal{F}(\mathbf{k}, \mathbf{q}) \approx \frac{1}{2} \left(\frac{68}{21} - \frac{1}{3} \frac{d \ln k^3 P_{2h}}{d \ln k} \right) P_{2h} \quad \mu_k = \cos(\theta) = \frac{\mathbf{k} \cdot \mathbf{q}}{|\mathbf{k}| |\mathbf{q}|} , \quad (4.36)$$

1/2 being a normalization factor.

In Eqs. (4.33) recognise how only the trispectrum terms involving $P_L(k)$ contribute to the SSC. Comparing the last line of Eq. (4.35) with Eq. (4.32), it's immediately apparent that the matter power spectrum responses take the form

$$\frac{\partial P(k)}{\partial \delta_b} \approx \left(\frac{68}{21} - \frac{1}{3} \frac{d \ln k^3 P_{2h}(k)}{d \ln k} \right) P_{2h}(k) + I_2^1(k, k) \quad (4.37)$$

$$= \left(\frac{68}{21} - \frac{1}{3} \frac{d \ln k^3 [I_1^1(k)]^2 P_L(k)}{d \ln k} \right) [I_1^1(k)]^2 P_L(k) + I_2^1(k, k) . \quad (4.38)$$

This is the final expression for the SSC responses in the halo model formalism. It allows isolating the different terms to the covariance and to understand their physical meaning (Li et al., 2014):

1. The first addendum is called “beat coupling”, and represents the intuitive fact that the growth of a sub-survey, short-wavelength perturbation is enhanced in a large-scale overdensity.
2. The second is the “linear dilation” effect; it arises because the long-wavelength perturbation changes the scale factor a locally, and therefore the physical size of small-scale modes. This corresponds to a rescaling of the argument of the matter power spectrum.
3. The last term is the “halo sample variance”, which accounts for the increase in the *halo* number density caused by the large-scale overdensity.

We conclude this section by noting that this treatment assumes that the density contrast used to compute the matter power spectrum is defined with respect to the *global* mean density, as opposed to the *in-survey* mean density. This is appropriate for statistics such as weak lensing, which probes the matter density field directly; in the case of galaxy number counts, on the other hand, the mean (reference) density is computed from the survey and hence is itself affected by the background perturbation δ_b . In this case, we need to rescale the power spectrum as:

$$P_W(k) = P(k) / (1 + \delta_b)^2 . \quad (4.39)$$

so the response rescales as

$$\frac{\partial P(k)}{\partial \delta_b} \rightarrow \frac{\partial P_W(k)}{\partial \delta_b} \approx \frac{\partial P(k)}{\partial \delta_b} - 2P(k) . \quad (4.40)$$

Separate universe response

A different method to compute the probe response is through the so-called “separate universe” technique, which takes advantage of the above-mentioned correspondence between a local constant background density perturbation and a separate universe with different background density. This method is better suited to characterize the response functions in the nonlinear regime, where the validity of the halo model and perturbation theory breaks down (Wagner et al., 2015b).

The key idea of this approach can be expressed by the definition of the background density perturbation itself (see Eq. 4.1, but with the subscript W now indicating the quantities of the separate universe), relating the mean densities averaged over the universe and over the survey (which is now the separate universe):

$$\bar{\rho}_m (1 + \delta_b) = \bar{\rho}_{mW} . \quad (4.41)$$

from which follows the relation between the density parameters in the two universes:

$$\frac{\Omega_m h^2}{a^3} (1 + \delta_b) = \frac{\Omega_{mW} h_W^2}{a_W^3} . \quad (4.42)$$

We also have

$$\lim_{a \rightarrow 0} \delta_b(a) = 0 \quad \rightarrow \quad \lim_{a \rightarrow 0} a_W(a, \delta_b) = a \quad (4.43)$$

from the fact that there is no SSC effect at early times. This means that the scale factors of the two different cosmologies agree at high redshift ($a \rightarrow 0$). From this, it follows that the *physical* densities of the two universes match:

$$\Omega_{mW} h_W^2 = \Omega_m h^2 . \quad (4.44)$$

from which we obtain a mapping for the scale factors:

$$a_W = \frac{a}{(1 + \delta_b)^{1/3}} \approx a \left(1 - \frac{\delta_b}{3} \right) . \quad (4.45)$$

or equivalently, defining $\delta_a(t)$ such that $a_W(t) = [1 + \delta_a(t)] a(t)$:

$$1 + \delta_b(t) = [1 + \delta_a(t)]^{-3} . \quad (4.46)$$

These equations allow writing the Friedmann equations in the two cosmologies to obtain the different expansion rates:

$$\delta H^2 = H_W^2 - H^2 \approx -\frac{2}{3} H \dot{\delta}_b ; \quad (4.47)$$

with the growth rate given by

$$H \dot{\delta}_b = \frac{\Omega_m H_0^2}{2a^2} \left[\frac{5}{D} - \frac{3}{a} - \frac{2\Omega_k}{\Omega_m} \right] \delta_b , \quad (4.48)$$

using the normalization for the linear growth function $\delta_b = (D/D_0) \delta_{b0}$:

$$\lim_{a \rightarrow 0} D = a . \quad (4.49)$$

we can then expand H_W^2 on the l.h.s., using the Friedmann equation for the separate universe:

$$\begin{aligned} H_W^2 &= H_{0W}^2 \left[\frac{\Omega_{mW}}{a_W^3} + \Omega_{\Lambda W} + \frac{\Omega_{kW}}{a_W^2} \right] \\ &\approx H^2 + \frac{H_{0W}^2 - H_0^2}{a^2} + H_0^2 \delta_b \left[\frac{\Omega_m}{a^3} + \frac{2}{3} \frac{\Omega_k}{a^2} \right] . \end{aligned} \quad (4.50)$$

We can plug this term in Eq. (4.47) to get the change in the Hubble constant:

$$\frac{\delta h}{h} \equiv \frac{H_{0W} - H_0}{H_0} \approx -\frac{5\Omega_m}{6} \frac{\delta_b}{D}. \quad (4.51)$$

The other density parameters are then given by

$$\frac{\delta\Omega_m}{\Omega_m} = \frac{\delta\Omega_\Lambda}{\Omega_\Lambda} \approx -2 \frac{\delta h}{h}. \quad (4.52)$$

having used Eq. (4.44); the separate universe will also have a different curvature (e.g., finally, a closed universe for $\delta_b > 0$):

$$\begin{aligned} \Omega_{kW} &= 1 - \Omega_{mW} - \Omega_{\Lambda W} \\ &= 1 - (\Omega_m + \Omega_\Lambda) \left(1 + \frac{5\Omega_m}{3} \frac{\delta_b}{D} \right). \end{aligned} \quad (4.53)$$

Having expressed the separate universe parameters as a function of the reference ones, it is possible to set up a simulation for different (small) variations of δ_b around 0 to numerically measure the power spectrum response.

In particular, we use the results presented in [Wagner et al. \(2015b\)](#), which use the separate universe technique to measure a specific term amongst the three different contributions to the responses presented in the previous section. In this work, the n -th order response functions are defined as the coefficients of the expansion of the power spectrum in the linearly extrapolated (Lagrangian) overdensity δ_L :

$$P(k, t | \delta_{L0}) = \sum_{n=0}^{\infty} \frac{1}{n!} R_n(k, t) [\delta_L]^n P(k, t), \quad (4.54)$$

with $\delta_L = \delta_{L0} \hat{D} = D(t)/D(t_0)\delta_{L0}$ and $\delta_{L0} = \delta_L(t=0)$ is the initial overdensity. Equivalently, the response coefficients $R_n(k, t)$ can be defined as the n -th derivative of the power spectrum with respect to δ_L (computed in $\delta_L = 0$), normalized by the power spectrum:

$$R_n(k, t) = \frac{1}{P(k)} \left. \frac{d^n P(k, t | \delta_L)}{d(\delta_L(t))^n} \right|_{\delta_L=0}. \quad (4.55)$$

For the first-order response coefficient $R_1(k, t)$, which we are interested in in the context of this work, the response to δ_L coincides with the response to the evolved nonlinear (Eulerian) overdensity δ_b . Note that, where no confusion arises, we will refer to $R_n(k, t)$ interchangeably as probe response coefficient or probe response (the only difference between the two being the normalization by the PS, as shown in the equation above).

As mentioned, $R_n(k, t)$ is composed of different terms, the first being the “reference density” effect (analogous to the halo sample variance), which rescales the power spectrum as:

$$P(k) = [1 + \delta_b]^2 P_W(k), \quad (4.56)$$

The second effect (the linear dilation) comes from a change in the comoving coordinates \mathbf{x} caused by the rescaling of the scale factor:

$$\mathbf{x} = \frac{a_W(t)}{a(t)} \mathbf{x}_W = [1 + \delta_a(t)] \mathbf{x}_W \quad \rightarrow \quad k_W = (1 + \delta_a) k, \quad (4.57)$$

and changes the power spectrum as

$$P(k) = [1 + \delta_a]^3 P_W([1 + \delta_a] k) . \quad (4.58)$$

Putting the two together and using Eq. (4.46) then gives

$$P(k) = [1 + \delta_b] P_W([1 + \delta_a] k) . \quad (4.59)$$

The δ_a and δ_b terms can be expanded in series as a function of δ_{L0} . The coefficients of these expansions can be derived analytically for an Einstein-de Sitter fiducial cosmology, which approximates very well the Λ CDM case (see Appendix B.1 of [Wagner et al. 2015b](#)):

$$\begin{aligned} \delta_a(t) &= \sum_{n=1}^{\infty} e_n [\delta_{L0} \hat{D}(t)]^n \\ \delta_b(t) &= \sum_{n=1}^{\infty} f_n [\delta_{L0} \hat{D}(t)]^n . \end{aligned} \quad (4.60)$$

The final contribution, which we referred to as “beat coupling”, is related to the modification in the growth of small-scale perturbations embedded in the local, large-scale overdensity (or underdensity). This is captured by the *growth-only* responses:

$$G_n(k) = \frac{1}{P(k)} \left. \frac{d^n P_W(k)}{d\delta_L^n} \right|_{\delta_L=0} . \quad (4.61)$$

We finally have, from the above expressions:

$$P(k | \delta_L) = [1 + \delta_\rho] \left[\left(1 + \sum_{n=1}^{\infty} \frac{1}{n!} G_n(k_W) \delta_L^n \right) P(k_W) \right]_{k_W=[1+\delta_a]k} \quad (4.62)$$

and, for the first-order response $R_1(k, t)$:

$$R_1(k, t) = f_1 + e_1 \frac{d \ln P(k, t)}{d \ln k} + G_1(k, t) = 1 - \frac{1}{3} \frac{d \ln P(k, t)}{d \ln k} + G_1(k, t) . \quad (4.63)$$

The G_1 term can be computed analytically in the linear regime, where the growth is scale-independent:

$$G_1^{\text{lin}} = \frac{1}{D^2} \left. \frac{d(D_W^2)}{d\delta_L} \right|_{\delta_L=0} \quad (4.64)$$

where D_W is the growth factor in the modified cosmology, which can again be expressed as a series expansion:

$$D_W(t) = D(t) \left\{ 1 + \sum_{n=1}^{\infty} g_n [\delta_{L0} \hat{D}(t)]^n \right\} . \quad (4.65)$$

For an Einstein-de Sitter cosmology, the first coefficients are

$$g_{1,2} = \left\{ \frac{13}{21}, \frac{71}{189} \right\} , \quad (4.66)$$

giving finally

$$G_1^{\text{lin}} = \frac{26}{21} . \quad (4.67)$$

We note that $R_1(k, t)$ is the response function of isotropic large-scale *density* perturbations; we neglect the contribution from the anisotropic *tidal-field* perturbations to the total response of the power spectrum (and consequently to the SSC), which has been shown in Barreira et al. (2018b) to be subdominant for WL with respect to the first contribution (about 5% of the total covariance matrix at $\ell \gtrsim 300$).

The $G_1(k)$ term is measured in the nonlinear regime, using the definition (Eq. 4.61). The separate universe simulations have linearly evolved, present-day overdensity of

$$\delta_{L0} = \{0, \pm 0.01, \pm 0.02, \pm 0.05, \pm 0.07, \pm 0.1, \pm 0.2, \pm 0.5, \pm 0.7, \pm 1\} . \quad (4.68)$$

The cosmological parameters of the separate universe are mapped from the ones of the reference cosmology using Eqs. (4.51, 4.52, 4.53). The simulations used in this work, presented in (Wagner et al., 2015a), have been run with **Gadget-2** (Springel, 2005) and have the following setup: simulation box with size $L_{\text{box}} = 500 h^{-1} \text{ Mpc}$ and $N_p = 512^3$ particles; starting redshift $z = 49$ and a flat, ΛCDM fiducial cosmology with parameters $\Omega_m = 0.27$, $h = 0.7$, $\Omega_b h^2 = 0.023$, $n_s = 0.95$, $\sigma_8 = 0.8$. This setup allows measuring the growth-only response in a limited range $k \in [k_{\text{fund}}, k_{\text{max}}]$, where $k_{\text{fund}} = 2\pi/L_{\text{box}} \approx 0.012 h \text{ Mpc}^{-1}$ and $k_{\text{max}} = k_{\text{Nyquist}} = N_p^{1/3} \pi/L_{\text{box}} \approx 3.2 h \text{ Mpc}^{-1}$. Outside of this range, we take, following (Barreira et al., 2018b):

$$k < k_{\text{fund}} : G_1(k) = \frac{26}{21} \quad (4.69)$$

$$k > k_{\text{max}} : G_1(k) = B_1 + [G_1(k = k_{\text{max}}) - B_1] \left(\frac{k}{k_{\text{max}}} \right)^{-1/2} . \quad (4.70)$$

In the last equation above we set $B_1 \approx 0.75$, which gives $R_1(k \rightarrow \infty) = 1$: on small scales, the (isotropic) density perturbations response contributes only via the density effect, while the other two vanish. The specific exponent (in this case, $-1/2$) does not have a significant impact on the final results and has been chosen to have a continuous and smooth transition between the different regimes. The response functions obtained in this way are shown in Fig. 4.3.

Having introduced the different ingredients entering the SSC term and their origin, we move on to the specific treatment for 2D-projected observables relevant to the *Euclid* photometric survey.

4.3 SSC for projected observables

To apply the SSC theory introduced in this chapter to our case scenario, we need to translate our formalism from the three-dimensional k space to the two-dimensional harmonic, or ℓ , space. This mapping is introduced again in the seminal paper of Takada and Hu (2013) and adapted to the multi-probe, tomographic case in

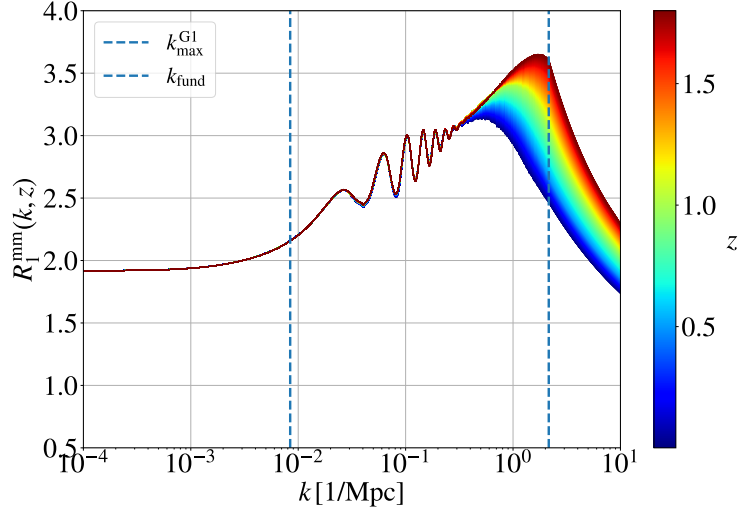


Figure 4.3. Scale and redshift dependence of the 3D first-order matter (“mm”) response coefficient. The minimum and maximum wavenumbers (k_{fund} and $k_{\text{max}}^{\text{G1}}$, respectively the left and right vertical dashed lines) used to compute the growth-only response from the [Wagner et al. 2015b](#) simulations are also shown. An analogous plot is shown in Fig. 1 of [Barreira et al. 2018b](#), which uses the same G_1^{mm} .

e.g. [Krause and Eifler \(2017\)](#); [Lacasa and Rosenfeld \(2016\)](#); [Barreira et al. \(2018a\)](#); [Upham et al. \(2022\)](#) (the latter for pseudo- $C(\ell)$).

We begin by considering the general expression for 2D-projected observables; considering a general field $\delta(\chi\boldsymbol{\theta}, \chi)$, we can project it on the sphere by means of a simple radial integration weighted by some radial kernel $\mathcal{K}(\chi)$, as seen in Sect. 3.1.2:

$$\Sigma(\boldsymbol{\theta}) = \int d\chi \mathcal{K}(\chi) \delta(\chi\boldsymbol{\theta}, \chi) . \quad (4.71)$$

We can equivalently use the redshift as our radial coordinate, hence integrating in dz , by leveraging the distance-redshift relation:

$$\frac{d\chi(z)}{dz} = \frac{c}{H(z)} = \frac{c}{H_0 E(z)} \quad \rightarrow \quad d\chi = \frac{c}{H_0 E(z)} dz \quad (4.72)$$

which is the choice commonly adopted in *Euclid* publications (and in the official *Euclid* code, CLOE (“Cosmology Likelihood for Observables in Euclid”).

Just as $\delta_W(\mathbf{x}) = \delta(\mathbf{x})W(\mathbf{x})$, the masked projected field $\Sigma_W(\boldsymbol{\theta})$ is given by a product in real (angular) space:

$$\Sigma_W(\boldsymbol{\theta}) = \Sigma(\boldsymbol{\theta})\mathcal{W}(\boldsymbol{\theta}) , \quad (4.73)$$

with $\mathcal{W}(\boldsymbol{\theta})$ the *angular* window function and $\boldsymbol{\theta}$ the angular coordinate. As seen in Eq. (4.4), this product becomes a convolution in harmonic space; using the flat-sky approximation, we can then express the Fourier transform of the projected field as a function of the multipole ℓ (see Sect. 2.4.2) as:

$$\tilde{\Sigma}_W(\ell) = \int \frac{d^2\ell'}{(2\pi)^2} \tilde{\mathcal{W}}(\ell - \ell') \tilde{\Sigma}(\ell') , \quad (4.74)$$

and its binned estimator, in analogy as Eq. (4.6), with

$$\hat{C}(\ell_i) \equiv \frac{1}{\Omega_{\mathcal{W}}} \int_{|\ell| \in \ell_i} \frac{d^2 \ell}{\Omega_{\ell_i}} \tilde{\Sigma}_{\mathcal{W}}(\ell) \tilde{\Sigma}_{\mathcal{W}}(-\ell), \quad (4.75)$$

where we have introduced the *angular* survey area $\Omega_{\mathcal{W}} \equiv \int d^2 \theta \mathcal{W}(\theta)$ and $\Omega_{\ell_i} = \int_{|\ell| \in \ell_i} d^2 \ell \simeq 2\pi \ell_i \Delta \ell$ when $\Delta \ell / \ell_i \ll 1$. In the same way as $\hat{P}(k_i)$ was an unbiased estimator for $k \gg 1/L$, for angular modes much larger than the angular width of the window function we have $\langle \hat{C}(\ell_i) \rangle = C(\ell_i)$. The covariance of this estimator is then defined similarly to what was done above:

$$\begin{aligned} \text{Cov}_{ij} &\equiv \langle \hat{C}(\ell_i) \hat{C}(\ell_j) \rangle - C(\ell_i) C(\ell_j) \\ &= \frac{1}{\Omega_{\mathcal{W}}} \left[\frac{(2\pi)^2}{\Omega_{\ell_i}} C(\ell_i) \delta_{ij}^{\text{K}} + \bar{\mathcal{T}}^{\mathcal{W}}(\ell_i, \ell_j) \right], \end{aligned} \quad (4.76)$$

with the trispectrum $\bar{\mathcal{T}}^{\mathcal{W}}$ now given by

$$\begin{aligned} \bar{\mathcal{T}}^{\mathcal{W}}(\ell_i, \ell_j) &= \frac{1}{\Omega_{\mathcal{W}}} \int_{|\ell| \in \ell_i} \frac{d^2 \ell}{\Omega_{\ell_i}} \int_{|\ell'| \in \ell_j} \frac{d^2 \ell'}{\Omega_{\ell_j}} \int \left[\prod_{a=1}^4 \frac{d^2 \mathbf{q}_a}{(2\pi)^2} \tilde{W}(\mathbf{q}_a) \right] (2\pi)^2 \delta_{\text{D}}^2(\mathbf{q}_{1234}) \\ &\quad \times \mathcal{T}(\ell + \mathbf{q}_1, -\ell + \mathbf{q}_2, \ell' + \mathbf{q}_3, -\ell' + \mathbf{q}_4). \end{aligned} \quad (4.77)$$

In the Limber approximation (Sect. 3.1.2), the angular power spectra and the trispectrum can be related to their 3D counterparts in terms of the Limber wavenumber \mathbf{k}_{ℓ} : this gives us, for the projected power spectrum and trispectrum,

$$C(\ell) \approx \int d\chi \frac{\mathcal{K}^2(\chi)}{\chi^2} P(\mathbf{k}_{\ell}; \chi), \quad (4.78)$$

$$\mathcal{T}(\ell_1, \ell_2, \ell_3, \ell_4) \approx \int d\chi \frac{\mathcal{K}^4(\chi)}{\chi^6} T(\mathbf{k}_{\ell_1}, \mathbf{k}_{\ell_2}, \mathbf{k}_{\ell_3}, \mathbf{k}_{\ell_4}; \chi), \quad (4.79)$$

so we finally get, using again the trispectrum consistency relation:

$$\text{Cov}_{ij}^{\text{G}} = \frac{1}{\Omega_{\mathcal{W}}} \frac{(2\pi)^2}{\Omega_{\ell_i}} C(\ell_i) \delta_{ij}^{\text{K}}, \quad (4.80)$$

$$\text{Cov}_{ij}^{\text{T0}} = \frac{1}{\Omega_{\mathcal{W}}} \int_{|\ell| \in \ell_i} \frac{d^2 \ell}{\Omega_{\ell_i}} \int_{|\ell'| \in \ell_j} \frac{d^2 \ell'}{\Omega_{\ell_j}} \mathcal{T}(\ell, -\ell, \ell', -\ell'), \quad (4.81)$$

$$\text{Cov}_{ij}^{\text{SSC}} = \frac{1}{\Omega_{\mathcal{W}}^2} \int d\chi \frac{\mathcal{K}^4(\chi)}{\chi^6} \frac{\partial P(k_{\ell_i}; \chi)}{\partial \delta_{\text{b}}} \frac{\partial P(k_{\ell_j}; \chi)}{\partial \delta_{\text{b}}} \int \frac{d^2 \ell}{(2\pi)^2} P_{\text{L}}(k_{\ell}; \chi) |\tilde{W}(\ell)|^2. \quad (4.82)$$

Let us now manipulate the third expression (which is essentially a “projected version” of Eq. 4.27) further to arrive at the final form used in our work.

4.3.1 Multi-probe, tomographic case

We now proceed to generalize Eq. (4.82), which allows computing the angular PS covariance between different ℓ bins (or, in its 3D version, between different k -bins) to take into account:

- multiple probes,
- multiple redshift bins,
- the covariance between δ_b at different redshifts.

This will indeed be necessary for the full 3×2 pt tomographic *Euclid* analysis.

We begin with the σ^2 term, generalizing the definition (4.26) by taking into account the covariance of the background density at different redshifts z_1, z_2 (Lacasa and Rosenfeld, 2016):

$$\sigma^2(z_1, z_2) \equiv \langle \delta_b(z_1) \delta_b(z_2) \rangle = \frac{1}{\Omega_{\mathcal{V}}^2} \int \frac{d^3 \mathbf{k}}{(2\pi)^3} \tilde{W}(\mathbf{k}, z_1) \tilde{W}(\mathbf{k}, z_2) P_L(k, z_{12}) . \quad (4.83)$$

Note that we are now expressing the radial dependence in terms of z instead of the comoving distance χ . This function can also take into account disjoint patches, as long as they are captured by the survey window function and we want to account for the (super-sample) covariance between them. We also introduced the linear matter cross-spectrum between z_1 and z_2 , $P_L(k, z_{12}) \equiv P_L(k, z=0) D(z_1) D(z_2)$. In the full-sky case ($\Omega_{\mathcal{V}} = 4\pi$), the harmonic space transform of W becomes a Kronecker delta $\delta_{\ell 0}^K$, reflecting the fact that only the monopole ($\ell = 0$) term contributes, and the projected background covariance, again in the Limber approximation, becomes:

$$\sigma^2(z_1, z_2) = \frac{1}{(4\pi)^2} \int \frac{d^3 \mathbf{k}}{(2\pi)^3} j_0(k\chi_1) j_0(k\chi_2) P_L(k, z_{12}) \quad (4.84)$$

$$= \frac{1}{(4\pi)^2} \frac{1}{2\pi^2} \int dk k^2 j_0(k\chi_1) j_0(k\chi_2) P_L(k, z_{12}) , \quad (4.85)$$

indicating with $j_0(k\chi) = j_{\ell=0}(k\chi)$ the 0-th order Bessel function and $\chi_i = \chi(z_i)$, and having integrated over the angular \mathbf{k} coordinates.

As for the remainder of the SSC expression, first of all, we can rewrite Eq. (4.78) as

$$\frac{\partial C(\ell)}{\partial \chi} = \frac{\mathcal{K}^2(\chi)}{\chi^2} P(\mathbf{k}_\ell; \chi) ; \quad (4.86)$$

and, assuming that the radial kernels $\mathcal{K}(\chi)$ vary slowly in δ_b , we can plug this expression in Eq. (4.82) to get

$$\text{Cov}_{ij}^{\text{SSC}} = \frac{1}{\Omega_{\mathcal{V}}^2} \int \frac{d\chi}{\chi^2} \frac{\partial^2 C(\ell_i)}{\partial \delta_b \partial \chi} \frac{\partial^2 C(\ell_j)}{\partial \delta_b \partial \chi} \int \frac{d^2 \ell}{(2\pi)^2} P_L(k; \chi) |\tilde{W}(\ell)|^2 . \quad (4.87)$$

We then use the expression for the volume element per steradian $dV = \chi^2 d\chi$ and generalize Eq. (4.82) following Lacasa and Rosenfeld 2016, i.e., considering the redshift width (and asymmetry) of the σ^2 term (see Fig. 4.4) and not treating it as a Dirac delta function of redshifts. In this way the SSC is expressed by a *double* integral over redshift (or distance, or volume), and the general expression becomes:

$$\text{Cov}_{ij}^{\text{SSC}} = \iint dV_1 dV_2 \frac{\partial^2 C(\ell_i)}{\partial \delta_b \partial V_1} \frac{\partial^2 C(\ell_j)}{\partial \delta_b \partial V_2} \sigma^2(z_1, z_2) . \quad (4.88)$$

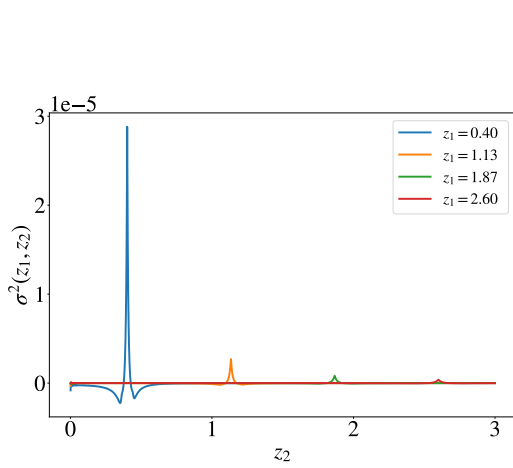


Figure 4.4. The dimensionless $\sigma^2(z_1, z_2)$, for four different values of z_1 . The $(4\pi)^{-2}$ factor has not been included, since it is absorbed in the volume element definition as described in the text.

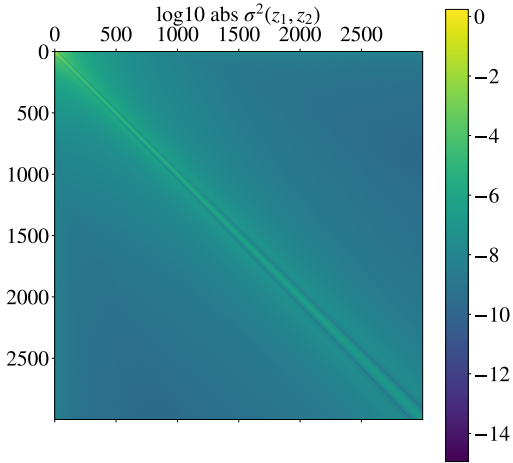


Figure 4.5. The same $\sigma^2(z_1, z_2)$, but displayed in matrix form. We take the absolute value to be able to plot in logarithmic scale also the negative values around the spikes, caused by the oscillatory nature of the Bessel functions in the integral. The larger values at $z_1 \sim z_2$ are clearly visible, and so is the increase of the function at lower z (indicating larger covariance).

Note the slight abuse of notation, having absorbed the $\Omega_{\mathcal{W}}^{-2}$ factors in $\sigma^2(z_1, z_2)$ (cf. Eq. 4.83) in the volume element per steradian dV . This expression can be further generalized for the multi-probe case as (Lacasa and Rosenfeld, 2016):

$$\text{Cov}^{\text{SSC}}(\mathcal{O}_1, \mathcal{O}_2) = \iint dV_1 dV_2 \frac{\partial o_1}{\partial \delta_b}(z_1) \frac{\partial o_2}{\partial \delta_b}(z_2) \sigma^2(z_1, z_2), \quad (4.89)$$

where o_i , $i = 1, 2$ is the *comoving density* of a generic LSS observable \mathcal{O}_i defined as $\mathcal{O}_i \equiv \int dV o_i$.

Taking into account the correlations of different probes in different redshift bins necessary for a full 3×2 pt tomographic analysis, we can rewrite the Limber angular PS (4.78) as

$$C_{ij}^{AB}(\ell) = \int d\chi \frac{\mathcal{K}_i^A(z) \mathcal{K}_j^B(z)}{\chi^2} P_{AB}(k_\ell, z) \quad (4.90)$$

$$= \int dV K_i^A(z) K_j^B(z) P_{AB}(k_\ell, z), \quad (4.91)$$

with $K_i^A(z) = \mathcal{K}_i^A(z) \chi^{-2}$, making it apparent that, for the case under study, $o_i = K_i^A(z) \mathcal{K}_j^B(z) P_{AB}(k_\ell, z) = \partial C_{ij}^{AB}(\ell) / \partial V$.

The general for SSC (4.89) is expensive to compute, involving a double integral over the volume and an integral of two Bessel functions over k . Moreover, the $\sigma^2(z_1, z_2)$ function is sharply peaked around $z_1 = z_2$, making it necessary to compute it for a large number of values even in the full-sky case. Having derived the general expression for the SSC between two 2D-projected observables in different redshift bins,

we can introduce the approximations used to speed up its computation, following the work of [Lacasa and Grain \(2019\)](#).

4.4 SSC approximations

As mentioned in the introduction of this Chapter, the code used to compute the SSC term is `PySSC`, a public `Python` module written by F. Lacasa et al., and presented alongside the paper [Lacasa and Grain 2019](#). To speed up the expensive computation of the SSC integrals, we start from the general form of Eq. (4.89) which, for the case of interest, becomes

$$\begin{aligned} \text{Cov}^{\text{SSC}} [C_{ij}^{AB}(\ell), C_{kl}^{CD}(\ell')] &= \iint dV_1 dV_2 K_i^A(z_1) K_j^B(z_1) K_k^C(z_2) K_l^D(z_2) \\ &\times \frac{\partial P_{AB}(k_\ell, z_1)}{\partial \delta_b} \frac{\partial P_{CD}(k_{\ell'}, z_2)}{\partial \delta_b} \sigma^2(z_1, z_2), \end{aligned} \quad (4.92)$$

and assume *the responses to vary slowly in redshift with respect to $\sigma^2(z_1, z_2)$* . This is the main approximation adopted, tested in the above-mentioned paper. This approximation hinges on the sharp redshift variability of $\sigma^2(z_1, z_2)$, which can be seen from Fig. 4.4. We can then approximate the responses with their weighted average over the $K_i^A(z)$ kernels, indicated with an overbar:

$$\begin{aligned} \frac{\partial \bar{P}^{AB}(k_\ell, z)}{\partial \delta_b} &= \frac{\int dV K_i^A(z) K_j^B(z) \partial P_{AB}(k_\ell, z) / \partial \delta_b}{\int dV K_i^A(z) K_j^B(z)} \\ &= \frac{1}{I_{ij}^{AB}} \int dV K_i^A(z) K_j^B(z) \frac{\partial P_{AB}(k_\ell, z)}{\partial \delta_b}; \end{aligned} \quad (4.93)$$

the denominator on the right-hand side of the first equation acts as a normalization term, which we call I_{ij}^{AB} . We then pull the average responses out of the dV integral:

$$\begin{aligned} \text{Cov}^{\text{SSC}} [C_{ij}^{AB}(\ell), C_{kl}^{CD}(\ell')] &\simeq \frac{\partial \bar{P}^{AB}(k_\ell, z_1)}{\partial \delta_b} \frac{\partial \bar{P}^{CD}(k_{\ell'}, z_2)}{\partial \delta_b} \\ &\times \iint dV_1 dV_2 K_i^A(z_1) K_j^B(z_1) K_k^C(z_2) K_l^D(z_2) \sigma^2(z_1, z_2). \end{aligned} \quad (4.94)$$

Additionally, we can further manipulate Eq. (4.93) by factorising the probe response as

$$\frac{\partial P_{AB}(k_\ell, z)}{\partial \delta_b} = R^{AB}(k_\ell, z) P_{AB}(k_\ell, z), \quad (4.95)$$

where $R^{AB}(k_\ell, z)$ is the first-order response coefficient defined in Eq. (4.55), which is given, for the matter-matter case, by Eq. (4.63). We can introduce the probe response coefficients of the *angular* power spectra $\mathcal{R}_{ij}^{AB}(\ell)$ in a similar way, using

Eq. (4.91):

$$\begin{aligned}
\frac{\partial}{\partial \delta_b} C_{ij}^{AB}(\ell) &= \frac{\partial}{\partial \delta_b} \int dV K_i^A(z) K_j^B(z) P_{AB}(k_\ell, z) \\
&= \int dV K_i^A(z) K_j^B(z) \frac{\partial P_{AB}(k_\ell, z)}{\partial \delta_b} \\
&= \int dV K_i^A(z) K_j^B(z) R^{AB}(k_\ell, z) P_{AB}(k_\ell, z) \\
&\equiv \mathcal{R}_{ij}^{AB}(\ell) C_{ij}^{AB}(\ell).
\end{aligned} \tag{4.96}$$

We can now substitute Eq. (4.96) into the r.h.s. of Eq. (4.93) and adopt the full-sky approximation by dividing the SSC by f_{sky} , to get the expression which will be used throughout this work:

$$\text{Cov}^{\text{SSC}} [C_{ij}^{AB}(\ell), C_{kl}^{CD}(\ell')] \simeq \frac{\mathcal{R}_{ij}^{AB}(\ell) C_{ij}^{AB}(\ell) \mathcal{R}_{kl}^{CD}(\ell') C_{kl}^{CD}(\ell') S_{i,j;k,l}^{A,B;C,D}}{f_{\text{sky}}}. \tag{4.97}$$

In the above equation, we have defined

$$S_{i,j;k,l}^{A,B;C,D} \equiv \int dV_1 dV_2 \frac{K_i^A(z_1) K_j^B(z_1)}{I_{ij}^{AB}} \frac{K_k^C(z_2) K_l^D(z_2)}{I_{kl}^{CD}} \sigma^2(z_1, z_2). \tag{4.98}$$

The $S_{i,j;k,l}^{A,B;C,D}$ matrix (referred to as S_{ijkl} from here on) is the volume average of $\sigma^2(z_1, z_2)$, and is a dimensionless quantity; it is the actual output of PySSC – we therefore need the additional ingredients appearing in Eq. (4.97) to compute the full SSC term. A description of the way this code has been used, and some comments on the inputs to provide and the outputs it produces, can be found in Sect. 5.2. Once the S_{ijkl} matrix has been computed, then, Eq. (4.97) makes the computation of the SSC have the same numerical cost as the computation of the angular PS themselves.

The validity of Eq. (4.97), commented in Appendix C, has been tested in LG19 in the case of GCph and found to reproduce the Fisher matrix (Tegmark et al., 1997) elements and signal-to-noise ratio from the original expression (Eq. 4.89):

- within 10% discrepancy up to $\ell \simeq 1000$ for $R_{ij}^{AB}(k_\ell, z) = \text{const}$;
- within 5% discrepancy up to $\ell \simeq 2000$ when using the linear approximation in scale for $R^{AB}(k_\ell, z)$ provided in Appendix C of the same work.

The necessity to push the analysis to smaller scales, as well as to investigate the SSC impact not only for GCph but also for WL and their cross-correlation, has motivated a more exhaustive characterization of the probe response functions, which will be detailed in the next section.

Lastly, we note that in Eq. (4.97) we account for the sky coverage of the survey through the full-sky approximation: $\text{Cov}_{\text{part. sky}}^{\text{SSC}} \simeq \text{Cov}_{\text{full sky}}^{\text{SSC}} / f_{\text{sky}}$. The validity of this approximation has been discussed in Gouyou Beauchamps et al. (2022), and found to agree at the percent level on the marginalized parameter constraints with the more rigorous treatment accounting for the exact survey geometry when

considering large survey areas. For this test, the authors considered an area of $15\,000\text{ deg}^2$ and a survey geometry very close to what *Euclid* will have, i.e. the full sky with the ecliptic and galactic plane removed. Intuitively, the severity of the SSC decays as f_{sky}^{-1} because larger survey volumes are able to accommodate more Fourier modes, although as mentioned in Sect. 4.2.1 the SSC term has a non-trivial scaling with the survey volume.

Having presented the theoretical framework and approximations used in our study, we can proceed to quantify the impact of this additional systematic effect on the *Euclid* photometric survey. To do this, we will introduce the additional ingredients and methodology used in the forecast analysis.

Chapter 5

Super-sample covariance for the *Euclid* photometric survey

This chapter will delve into the specifics and results obtained for the computation of the SSC term, computed with the formalism and approximation introduced in the last chapter, to the 3×2 pt survey for the *Euclid* mission.

5.1 Forecast specifics

The forecast analysis presented below has been performed with the goal of improving the work of the inter-science taskforce for forecasting (“IST:F”: EC20, based in turn on the *Euclid* Red Book Laureijs et al. 2011), mainly by considering SSC as an additional source of uncertainty beyond the already considered sample variance, shot and shape noise. We will take into account some updates to the EC20 prescriptions based on more recent results by the Euclid Collaboration. In particular, the updates concern the fiducial value of the linear bias, redshift distribution $n(z)$ and multipole binning, as detailed below.

5.1.1 Cosmological model and matter power spectrum

The baseline fiducial cosmological model adopted in this work is the flat w_0w_a CDM model, i.e., we model the dark energy equation of state with a CPL parameterization (Eq. 1.21). We also include the contribution from massive neutrinos with total mass set to the *Planck* preferred value (consistent with oscillation experiments) $\sum m_\nu = 0.06$ eV, which we keep fixed in the FM analysis. The cosmological parameters’ vector is then

$$\boldsymbol{\theta}_{\text{cosmo}} = \{\Omega_{\text{m},0}, \Omega_{\text{b},0}, w_0, w_a, h, n_s, \sigma_8\} ; \quad (5.1)$$

we will expand this parameter basis in the variations explored later on, e.g. considering non-flat models. The parameters’ fiducial values are set to the latest *Planck* results (Planck Collaboration et al. 2020a, EC20); for w_0 and w_a , we choose $(-1, 0)$ respectively, which describe a time-independent equation of state:

$$\boldsymbol{\theta}_{\text{cosmo}}^{\text{fid}} = \{0.32, 0.05, -1.0, 0.0, 0.67, 0.96, 0.816\} . \quad (5.2)$$

These are used as input for the evaluation of the fiducial linear and nonlinear matter PS, which is obtained using the **TakaBird** recipe. This is implemented in both **CAMB** and **CLASS**.

5.1.2 Radial kernels

Fig. 3.7 shows the redshift dependence of the radial kernels defined in Eqs. (3.88) and (3.11), for the different redshift bins. The two sets of kernels have very different shapes, because of the different nature of the probes they represent. In particular, the left panel shows the very large support in z of the lensing kernels, due to the integrated nature of the effect: the shear signal originating from the sources in the furthest bins is created by the lenses spanning the *whole* radial distance from said sources to the observer. This means that the sources from all bins receive a non-negligible contribution from the low- z region, a fact of great importance in the impact of SSC, as explained in Sect. 5.3.1. This also means that, contrary to GCph, the off-diagonal tomographic correlations $i \neq j$, quantified by the angular PS $C_{ij}^{AB}(\ell)$, will never be null, because the overlap between the kernels is non-zero even for distant redshift bins.

The large support in z also means that, when performing the integral of Eq. (5.5) (or equivalent forms), the signal at a single angular scale ℓ will receive contributions from the PS computed in a large set of k values: $k_\ell = (\ell + 1/2)\chi^{-1}(z)|_{z \in z_{\text{int}}}$ with z_{int} the z range of the $C_{ij}^{AB}(\ell)$ integral. This implies a non-univocal correspondence between angular and three-dimensional scales, which in turn complicates the process of imposing scale cuts. A potential solution to this problem will be discussed in Chap. 6.

For GCph, we choose to include the galaxy bias term $b_i(z)$ in the PS (see Eq. 3.94) rather than in the galaxy kernel, as opposed to what has been done in EC20. This is done to compute the galaxy response as described in Sect. 5.1.3. Since the galaxy bias is assumed constant in each bin, however, in this case the question is of no practical relevance when computing the S_{ijkl} matrix, since the constant bias cancels out.

We remind the reader once again that the above definitions of the lensing and galaxy kernels ($\mathcal{K}_i^A(z)$, $A = \text{L, G}$) differ from the ones used in LG19 – for which we used the notation $K_i^A(z)$. This is simply because of a different definition of the $C_{ij}^{AB}(\ell)$ Limber integral, which is performed in dV in LG19 (i.e., using Eq. 4.91) and in dz in EC20. The mapping between the two conventions is simply given by the expression for the volume element:

$$dV = \chi^2(z) \frac{d\chi}{dz} dz = \frac{c}{H_0} \frac{\chi^2(z)}{E(z)} dz, \quad (5.3)$$

and

$$K_i^A(z) = \mathcal{K}_i^A(z) / \chi^2(z), \quad (5.4)$$

so that the *Euclid* form of the $C_{ij}^{AB}(\ell)$ integral is simply

$$C_{ij}^{AB}(\ell) = \frac{c}{H_0} \int dz \frac{\mathcal{K}_i^A(z) \mathcal{K}_j^B(z)}{E(z) \chi^2(z)} P_{AB}(k_\ell, z) \quad (5.5)$$

with $A = \text{L, G}$. In Fig. 3.7 we plot the values of $\mathcal{K}_i^A(z)$ to facilitate the comparison with EC20. As outlined in Appendix B, when computing the S_{ijkl} matrix through PySSC, the user can either pass the kernels in the form used in LG19 (K_i^A), or the one used in EC20 (\mathcal{K}_i^A) while specifying a non-default `convention` parameter.

5.1.3 Multi-probe response

The responses for the different probes can be obtained in terms¹ of $R^{\text{mm}}(k, z)$ by plugging the relations between matter and galaxy PS (Eq. 3.94) into Eq. (4.95) – see also Krause and Eifler (2017) for a similar derivation of the multi-probe case, using the halo model responses².

We note that the linear modelling for the galaxy bias is not rigorous at high ℓ and scale cuts should be performed in order to avoid biasing the constraints, but in the present context, we are more interested in the relative impact of SSC on the constraints than the constraints themselves. Any systematic error due to this approximate modelling should roughly cancel out in the ratio we will compute later on.

We also note that we choose to include a perfectly Poissonian shot noise term in the covariance matrix, rather than in the galaxy PS of Eq. (3.94), as can be seen in Eq. (5.12). Again, we restrict our study to the first-order isotropic response $R_1(k, z)$, so we drop the subscript “1” from hereon:

$$R^{\text{gg}}(k, z) = \frac{\partial \ln P_{\text{gg}}(k, z)}{\partial \delta_{\text{b}}} = R^{\text{mm}}(k, z) + 2b_{(1)}^{-1}(z) [b_{(2)}(z) - b_{(1)}^2(z)], \quad (5.6)$$

and similarly for R^{gm} :

$$R^{\text{gm}}(k, z) = \frac{\partial \ln P_{\text{gm}}(k, z)}{\partial \delta_{\text{b}}} = R^{\text{mm}}(k, z) + b_{(1)}^{-1}(z) [b_{(2)}(z) - b_{(1)}^2(z)]. \quad (5.7)$$

Having used the definitions of the first and second-order galaxy bias, i.e., $b_{(1)}(z) = (\partial n_{\text{g}} / \partial \delta_{\text{b}}) / n_{\text{g}}$ and $b_{(2)}(z) = (\partial^2 n_{\text{g}} / \partial \delta_{\text{b}}^2) / n_{\text{g}}$, with n_{g} the total angular galaxy number density, in arcmin^{-2} . In the following, where there is no risk of ambiguity, we will also drop the subscript in parenthesis when referring to the first-order galaxy bias – i.e., $b(z) = b_{(1)}(z)$ – to shorten the notation, and we will indicate the value of the first-order galaxy bias in the i -th redshift bin with $b_i(z)$. Equations (5.6)–(5.7) are obtained by differentiating a PS model for a galaxy density contrast defined with respect to the *observed* galaxy number density, and so they already account for the fact that the latter also “responds” to the large scale perturbation δ_{b} – hence no rescaling of the response, shown in Eq. (4.40) is required. This is also the reason why $R_{ij}^{\text{GG}}(\ell)$ can have negative values: for galaxy clustering, the (number) density contrast δ_{gal} is measured w.r.t. the observed, local number density \bar{n}_{gal} : $\delta_{\text{gal}} = n_{\text{gal}} / \bar{n}_{\text{gal}} - 1$. The latter also responds to a background density perturbation δ_{b} , and it can indeed happen that \bar{n}_{gal} grows with δ_{b} faster than n_{gal} , which leads to δ_{gal} decreasing with increasing δ_{b} (which also implies $\partial C_{ij}^{\text{GG}}(\ell) / \partial \delta_{\text{b}} < 0$). We also

¹Since we are using the nonlinear matter power spectrum $P_{\text{mm}}(k, z)$, we do not force $R^{\text{mm}}(k, z)$ to reduce to its linear expression, that is to say, we do not set $G_1^{\text{mm}} = 26/21$ in Eq. (4.63).

²Note that, as of the time of writing, there is a typo in Eq. (A11) of the aforementioned paper: the factor in front of the logarithmic derivative of the PS should be $-1/3$ instead of $-1/2$.

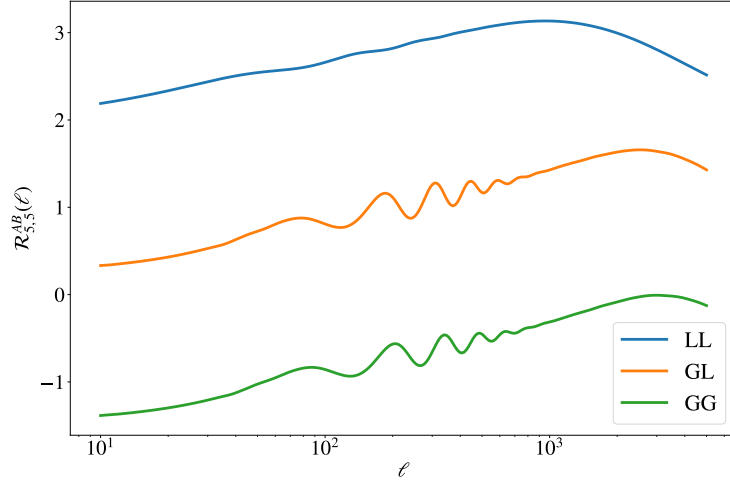


Figure 5.1. Projected response coefficients for the WL and GCph probes and their cross-correlation, for the central redshift bin considered ($0.8 \lesssim z \lesssim 0.9$; see Sect. 3.1.3) – the shape and amplitude of the functions for different redshift pairs are analogous. For WL, the baryon acoustic oscillation wiggles are smoothed out by the projection, due to the kernels being larger than the GCph ones. The different amplitude of the response is one of the main factors governing the severity of SSC.

stress the fact that the second-order galaxy bias appearing in the galaxy-galaxy and galaxy-lensing response coefficients is not included in the signal, following EC20. Once computed in this way, the response coefficients can be projected in harmonic space using Eq. (4.96), and inserted in Eq. (4.97) to compute the SSC in the LG19 approximation. The projected $\mathcal{R}_{ij}^{AB}(\ell)$ functions are shown in Fig. 5.1 for all the probes combinations considered.

5.1.4 Higher-order bias

To compute the galaxy-galaxy and galaxy-galaxy lensing probe response terms (Eqs. 5.6 and 5.7) we need the second-order galaxy bias $b_{(2)}(z)$. This can be estimated through the halo model³ as (Voivodic and Barreira 2021; Barreira et al. 2021; see also Appendix C of LG19):

$$b_{(i)}(z) = \int dM \Phi_{\text{MF}}(M, z) b_{(i)}^{\text{h}}(M, z) \langle N|M \rangle / n_{\text{g}}(z) , \quad (5.8)$$

with

$$n_{\text{g}}(z) = \int dM \Phi_{\text{MF}}(M, z) \langle N|M \rangle . \quad (5.9)$$

We remind the meaning of the different terms entering the last two equations, some of which have been introduced in Sect. 1.4.4; n_{g} is the galaxy number density, $\Phi_{\text{MF}}(M, z)$ the halo mass function (HMF), $b_{(i)}^{\text{h}}(M, z)$ the i -th order *halo* bias, and $\langle N|M \rangle$ the average number of galaxies hosted by a halo of mass M at redshift z (given by the HOD). These are integrated over the mass range $\log_{10} M \in [9, 16]$, with the mass expressed in units of solar masses. The expression for the i -th order

³We neglect here the response of $\langle N|M \rangle$ to a perturbation δ_{b} in the background density.

galaxy bias (Eq. 5.8) is the same as Eq. (C.2) of LG19, but here we are neglecting the scale dependence of the bias evaluating it at $k = 0$ so that $\tilde{u}(k | M = 0, z) = 1$, $\tilde{u}(k | M, z)$ being the Fourier Transform of the halo profile. Strictly speaking, this gives us the large-scale bias, but it is easy to check that the dependence on k is negligible over the range of interest.

Although Eq. (5.8) allows the computation of both the first and second-order galaxy bias, we prefer to use the values of $b_{(1)}(z)$ measured from the Flagship simulation for the selected galaxy sample; this is to maintain consistency with the choices presented in Sect. 3.1.4. For each redshift bin, we vary (some of) the HOD parameters to fit the measured $b_{(1)}(z)$, thus getting a model for $b_{(1)}^h(z)$. We then compute $b_{(2)}^h(z)$ using as an additional ingredient the following relation between the first and second-order halo bias, which approximates the results from separate universe simulations (Lazeyras et al., 2016) within the fitting range $1 \lesssim b_{(1)}^h \lesssim 10$:

$$b_{(2)}^h(M, z) = 0.412 - 2.143 b_{(1)}^h(M, z) + 0.929 \left[b_{(1)}^h(M, z) \right]^2 + 0.008 \left[b_{(1)}^h(M, z) \right]^3. \quad (5.10)$$

Finally, we plug the $b_{(2)}^h$ values obtained in this way back into Eq. (5.8) to get the second-order galaxy bias. The details of the HMF and HOD used and of the fitting procedure are given in Appendix A.

5.1.5 Gaussian covariance

As mentioned in Sect. 4.1, the Gaussian part of the covariance matrix encapsulates the sample variance (and, from hereon, the measurement noise) for perfectly Gaussian-distributed fields. For a multi-probe tomographic harmonic analysis, Eq. (4.12) generalizes to the following expression (EC20):

$$\begin{aligned} \text{Cov}^G \left[C_{ij}^{AB}(\ell), C_{kl}^{CD}(\ell') \right] &= [(2\ell + 1) f_{\text{sky}} \Delta\ell]^{-1} \delta_{\ell\ell'}^K \\ &\times \left\{ \left[C_{ik}^{AC}(\ell) + N_{ik}^{AC}(\ell) \right] \left[C_{jl}^{BD}(\ell') + N_{jl}^{BD}(\ell') \right] \right. \\ &\quad \left. + \left[C_{il}^{AD}(\ell) + N_{il}^{AD}(\ell) \right] \left[C_{jk}^{BC}(\ell') + N_{jk}^{BC}(\ell') \right] \right\}, \end{aligned} \quad (5.11)$$

where the noise PS $N_{ij}^{AB}(\ell)$, which were lacking in Eq. (4.12), are, for the different probe combinations:

$$N_{ij}^{AB}(\ell) = \begin{cases} (\sigma_\epsilon^2 / \bar{n}_i^G) \delta_{ij}^K & A = B = \text{L (WL)} \\ 0 & A \neq B \\ (1 / \bar{n}_i^L) \delta_{ij}^K & A = B = \text{G (GCph)}. \end{cases} \quad (5.12)$$

In the above equations σ_ϵ^2 is the variance of the total intrinsic ellipticity dispersion of WL sources – where $\sigma_\epsilon = \sqrt{2} \sigma_\epsilon^{(i)}$, $\sigma_\epsilon^{(i)}$ being the ellipticity dispersion per component of the galaxy ellipse. We assume no correlation between shot and shape

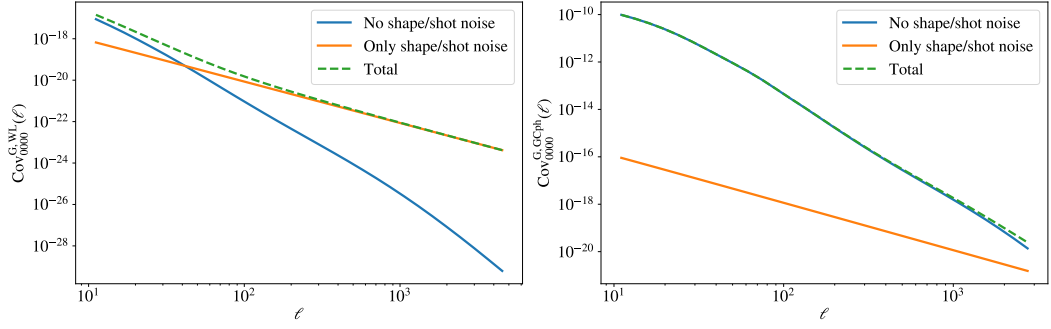


Figure 5.2. Gaussian covariance with and without the noise terms $N_{ij}^{AB}(\ell)$ (cf. Eq. 5.11), for the first redshift bin: $z_i, z_j, z_k, z_l = 0, 0, 0, 0$. The shape noise is more important for WL than the shot noise for GCph, becoming dominant before $\ell \sim 100$.

noise, resulting in $N_{ij}^{GL}(\ell) = N_{ij}^{LG}(\ell) = 0$, and no inter-bin noise, as enforced by the Kronecker delta δ_{ij}^K . The noise spectra are scale-independent, which makes them the dominant contribution at large ℓ , where the sample variance term goes to zero because of the larger number of modes available (see Eq. 4.12 and Fig. 5.2). We note that the average densities used in Eq. (5.12) are not the total number densities, but rather those in the i -th redshift bin. In the case of \mathcal{N}_b equipopulated redshift bins, they can be simply written as $\bar{n}_i^A = \bar{n}^A / \mathcal{N}_b$ for both $A = (L, G)$. Finally, we recall that f_{sky} is the fraction of the total sky area covered by the survey, while $\Delta\ell$ is the width of the multipole bin centered on a given ℓ . From Sect. 3.1.3 we have that $\bar{n} = 28.73 \text{ arcmin}^{-2}$, while we set $\sigma_\epsilon = 0.37$ (from the value $\sigma_\epsilon^{(i)} = 0.26$ reported in *Euclid Collaboration: Martinet et al., 2019*) and $f_{\text{sky}} = 0.356$ (corresponding to $\Omega_S = 14\,700 \text{ deg}^2$).

To make the computation of this covariance term, key to any likelihood analysis, quick and straightforward, I have prepared an optimized `Python` module, `Spaceborne_covg`⁴, available as a public repository. It only requires as inputs the signal, the noise, and the convention of choice for the ordering of the resulting two-dimensional covariance matrix, and it is currently being used by other groups within the *Euclid* Collaboration (for example, in the validation of the `CLOE` code and in the Key Paper “Cosmological constraints on non-standard cosmologies from simulated *Euclid* probes” (D’Amico et al, in prep)).

In the context of the present work, we do not consider the other non-Gaussian contribution to the total covariance matrix, the so-called connected non-Gaussian (cNG) term. This additional non-Gaussian term has been shown to be sub-dominant with respect to the Gaussian and SSC terms for WL both in *Barreira et al. (2018a)* and in *Upham et al. (2022)*. For what concerns galaxy clustering, *Wadekar et al. (2020)* showed that the cNG term was subdominant, but this was for a spectroscopic sample so (i) they had a much larger contribution from shot-noise-related terms compared to what is considered here for the *Euclid* photometric sample, and (ii) they considered larger and more linear scales than in the present study. *Lacasa (2020)* showed that the cNG term in the covariance matrix of GCph only impacts

⁴https://github.com/davidesciotti/Spaceborne_covg

the spectral index n_s and HOD parameters, but there are a few differences between that analysis and the present work, such as the modelling of galaxy bias. Thus it is still unclear whether the cNG term has a strong impact on cosmological constraints obtained with GCph. Quantifying the impact of this term for the 3×2 pt analysis with *Euclid* settings is left for future work.

5.1.6 Data vectors and Fisher matrix

We can now proceed to set some data-related specifications.

First, we assume to measure $C_{ij}^{AB}(\ell)$ in 10 equipopulated redshift bins over the redshift range (0.001, 2.5). When integrating Eq. (5.5) in dz , z_{\max} must be larger than the upper limit of the last redshift bin to account for the broadening of the bin redshift distribution due to photo- z uncertainties. We have found that the $C_{ij}^{AB}(\ell)$ stop varying for $z_{\max} \gtrsim 4$, which is what we take as the upper limit in the integrals over z . This also means that we need to extrapolate the bias beyond the upper limit of the last redshift bin; we then take its value as constant and equal to the one in the last redshift bin, that is, $b(z > 2.501) = b_{10}$.

Second, we assume the same multipole limits as in EC20, hence examining two cases, namely

- *pessimistic*:

$$(\ell_{\min}, \ell_{\max}) = \begin{cases} (10, 1500) & \text{for WL} \\ (10, 750) & \text{for GCph and XC} \end{cases},$$

- *optimistic*:

$$(\ell_{\min}, \ell_{\max}) = \begin{cases} (10, 5000) & \text{for WL} \\ (10, 3000) & \text{for GCph and XC} \end{cases}.$$

These limits were set in EC20 by a preliminary study of the impact of non-Gaussian contributions to the covariance matrix, whose characterization is precisely the aim of the present Chapter. For WL, a 30% signal-to-noise decrease was found when including non-Gaussian covariance, corresponding to an effective ℓ cut at $\ell_{\max} = 1420$, leading to the pessimistic choice of $\ell_{\max}^{\text{WL}} = 1500$. Similarly, for GCph, the signal-to-noise saturation above $\ell_{\max} \gtrsim 500$ – a similar value being found also in LG19 – is quoted as the main reason for the pessimistic cut at $\ell_{\max}^{\text{GCph}} = 750$; however, as acknowledged by the authors and as shown in Sect. 5.3, the signal-to-noise is not necessarily a faithful indicator of the impact of the additional covariance on parameter constraints. In the rest of the Chapter we keep using these as upper limits on the multipole, to facilitate comparison with the original results of EC20; these scale cuts will have to be updated by more nuanced analyses, accounting for, amongst other things, the SSC impact on marginalized uncertainties and the additional considerations introduced in Chapter 6.

As for the multipole binning, instead of dividing these ranges into \mathcal{N}_ℓ (logarithmically equispaced) bins in all cases as is done in EC20, we follow the most recent prescriptions of the EC and proceed as follows:

- we fix the centers and edges of 32 bins (as opposed to 30) in the ℓ range $[10, 5000]$ following the procedure described in Appendix D. This will be the ℓ configuration of the optimistic WL case.
- The bins for the cases with $\ell_{\max} < 5000$, i.e., WL pessimistic, GCph and XC, are obtained by cutting the bins of the optimistic WL case with $\ell_{\text{center}} > \ell_{\max}$. This means that instead of fixing the number of bins and having different bins' centers and edges as done in EC20, we fix the bins' centers and edges and use a different number of bins, resulting in, e.g., $\mathcal{N}_\ell^{\text{WL, opt}} > \mathcal{N}_\ell^{\text{GCph, opt}}$.

The number of multipole bins is then $\mathcal{N}_\ell^{\text{WL}} = 26$ and $\mathcal{N}_\ell^{\text{GCph}} = \mathcal{N}_\ell^{\text{XC}} = 22$ in the pessimistic case and $\mathcal{N}_\ell^{\text{WL}} = 32$ and $\mathcal{N}_\ell^{\text{GCph}} = \mathcal{N}_\ell^{\text{XC}} = 29$ in the optimistic case. In all these cases, the angular PS are computed at the center of the ℓ bin. We will both consider the different probes in isolation and combine them in the $3 \times 2\text{pt}$ analysis, for which the ℓ binning will be the same as for the GCph one.

The one-dimensional data vector \mathbf{C} is constructed by simply compressing the redshift and multipole indices (and, in the $3 \times 2\text{pt}$ case, the probe indices) into a single one, which we call p (or q). For Gaussian-distributed data with a parameter-independent covariance, the FM is given by Eq. (2.16):

$$F_{\alpha\beta} = \frac{\partial \mathbf{C}}{\partial \theta_\alpha} \text{Cov}^{-1} \frac{\partial \mathbf{C}}{\partial \theta_\beta} = \sum_{pq} \frac{\partial C_p}{\partial \theta_\alpha} \text{Cov}_{pq}^{-1} \frac{\partial C_q}{\partial \theta_\beta}. \quad (5.13)$$

We note that the size of the $3 \times 2\text{pt}$ covariance matrix quickly becomes large. For a standard setting with $\mathcal{N}_b = 10$ redshift bins there are respectively (55, 100, 55) independent redshift bin pairs for (WL, XC, GCph), to be multiplied by the different \mathcal{N}_ℓ . In general, the covariance will be a $\mathcal{N}_C \times \mathcal{N}_C$ matrix with

$$\begin{aligned} \mathcal{N}_C &= \left[\mathcal{N}_b(\mathcal{N}_b + 1)/2 \right] \left[\mathcal{N}_\ell^{\text{WL}} + \mathcal{N}_\ell^{\text{GCph}} \right] + \mathcal{N}_b^2 \mathcal{N}_\ell^{\text{XC}} \\ &= \left[\mathcal{N}_b(\mathcal{N}_b + 1) + \mathcal{N}_b^2 \right] \mathcal{N}_\ell^{3 \times 2\text{pt}}, \end{aligned} \quad (5.14)$$

for the $3 \times 2\text{pt}$ – where the second line represents the case with the same number of ℓ bins for all probes, which is the one under study – and

$$\mathcal{N}_C = [\mathcal{N}_b(\mathcal{N}_b + 1)/2] \mathcal{N}_\ell^{\text{WL/GCph}}. \quad (5.15)$$

for the WL and GCph cases. As an example, we will have $\mathcal{N}_C^{3 \times 2\text{pt, opt}} = 6090$.

Being diagonal in ℓ , most elements of this matrix will be null in the Gaussian case (see Fig. 5.3, displaying the G and GS correlation matrices⁵). This is no longer true with the inclusion of the SSC contribution, which makes the matrix computation – and the subsequent inversion, to implement Eq. (5.13) – much more resource-intensive.

Given the highly non-diagonal nature of the GS covariance, we can wonder whether the inversion of this matrix needed to obtain the FM is stable. To investigate this, we compute the condition number of the covariance, which is defined as the ratio between

⁵Where the correlation matrix is defined as $\text{Corr}_{ij} = \text{Cov}_{ij} / \sqrt{\text{Cov}_{ii} \text{Cov}_{jj}}$

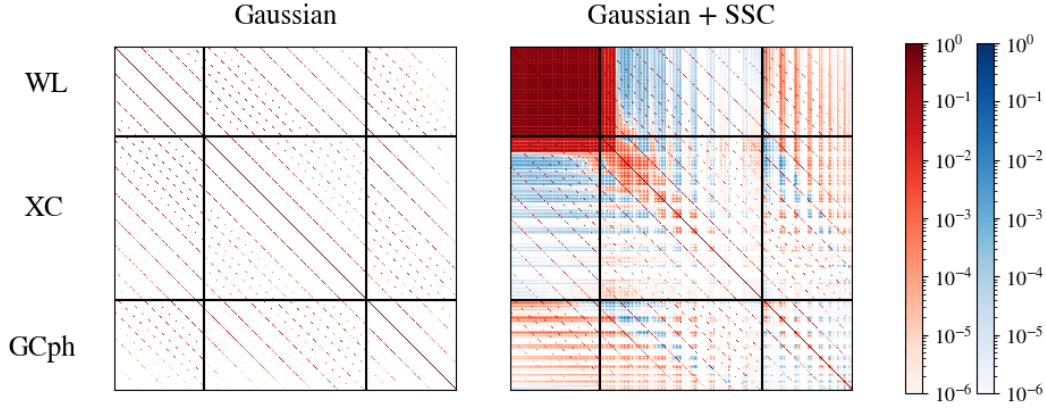


Figure 5.3. Correlation matrix in log scale for all the statistics of the 3×2 pt data-vector in the G and GS cases. The positive and negative elements are shown in red and blue, respectively. The Gaussian covariance is block diagonal (i.e., it is diagonal in the multipole indices, but not in the redshift ones; the different diagonals appearing in the plot correspond to the different redshift pair indices, for $\ell_1 = \ell_2$). The overlap in the WL kernels makes the WL block in the Gaussian + SSC covariance matrix much more dense than the GCph one.

its largest and smallest eigenvalues and in this case of order 10^{13} . This condition number, multiplied by the standard `numpy float64` resolution (2.22×10^{-16}), gives us the minimum precision that we have on the inversion of the matrix, of about 10^{-3} . This means that numerical noise in the matrix inversion can cause, at most, errors of order 10^{-3} on the inverse matrix. Hence, we consider the inversion to be stable for the purpose of this work.

5.2 Forecast code validation

In order to validate the SSC computation with `PySSC`, we compare the 1σ forecast uncertainties (which correspond to a 68.3% probability, due to the assumptions of the FM analysis) obtained using two different codes independently developed by two groups, which we call A and B. To produce the FM and the elements needed for its computation (the observables, their derivatives and the covariance matrix), group A uses a private⁶ code fully written in `Python` and group B uses `CosmoSIS`⁷ (Jennings et al., 2016). The only shared feature of the two pipelines is the use of `PySSC` (to compute the S_{ijkl} matrix). For this reason, and because the SSC is not considered in isolation but added to the Gaussian covariance, we compare the forecast results of the two groups both in the Gaussian and Gaussian + SSC cases.

Following EC20, we consider the results to be in agreement if the discrepancy of each group's results with respect to the median – which in our case equals the mean – is smaller than 10%. This simply means that the A and B pipelines' outputs are

⁶Available upon request to the author, Davide Sciotti

⁷<https://bitbucket.org/joezuntz/cosmosis/wiki/Home>

considered validated against each other if

$$\left| \frac{\sigma_\alpha^i}{\sigma_\alpha^m} - 1 \right| < 0.1 \quad \text{for } i = A, B; \quad \sigma_\alpha^m = \frac{\sigma_\alpha^A + \sigma_\alpha^B}{2}, \quad (5.16)$$

with σ_α^A the 1σ uncertainty on the parameter α for group A. The above discrepancies are equal and opposite in sign for A and B.

The *marginalised* uncertainties are extracted from the FM $F_{\alpha\beta}$, which is the inverse of the covariance matrix $C_{\alpha\beta}$ of the parameters, as described in Sect. 2.2: $(F^{-1})_{\alpha\beta} = C_{\alpha\beta}$. We do not consider unmarginalised, or conditional, uncertainties in this work. We then have

$$\sigma_\alpha = \sigma_\alpha^{\text{marg.}} = (F^{-1})_{\alpha\alpha}^{1/2}. \quad (5.17)$$

We remind that the uncertainties found in the FM formalism constitute lower bounds, or optimistic estimates, on the actual parameters' uncertainties, as stated by the Cramér-Rao inequality.

In the following, we normalize σ_α by the fiducial value of the parameter θ_α , in order to work with relative uncertainties: $\bar{\sigma}_\alpha^i = \sigma_\alpha^i / \theta_\alpha^{\text{fid}}$; $\bar{\sigma}_\alpha^m = \sigma_\alpha^m / \theta_\alpha^{\text{fid}}$, again with $i = A, B$. If a given parameter has a fiducial value of 0, such as w_a , we simply take the absolute uncertainty. The different cases under examination are dubbed ‘G’, or ‘Gaussian’, and ‘GS’, or ‘Gaussian + SSC’. The computation of the parameters constraints differs between these two cases only by the covariance matrix used in Eq. (5.13) to compute the FM

$$\text{Cov} = \begin{cases} \text{Cov}_G & \text{Gaussian} \\ \text{Cov}_{GS} = \text{Cov}_G + \text{Cov}_{SSC} & \text{Gaussian + SSC} \end{cases}. \quad (5.18)$$

For the reader wishing to validate their own code, we describe the validation process in Appendix B. Here we sketch the results of the code validation: in Fig. 5.4, we show the percent discrepancy as defined in Eq. (5.16) for the 3×2pt case. Similar results have been obtained for the GCph and WL cases, both for the optimistic and pessimistic settings specified in Sect. 5.1.6. The constraints are all found to satisfy the required agreement level (less than 10% discrepancy with respect to the mean). In light of these results, we consider the two forecasting pipelines validated against each other.

5.3 SSC impact on forecasts

We can now finally investigate how the inclusion of SSC degrades the constraints with respect to the Gaussian case. To this end, we will look in the following at the quantity

$$\mathcal{R}(\theta) = \sigma_{GS}(\theta) / \sigma_G(\theta), \quad (5.19)$$

where $\sigma_G(\theta)$ and $\sigma_{GS}(\theta)$ are the usual marginalised uncertainties on the parameter θ computed, as detailed above, with Gaussian or Gaussian + SSC covariance matrix. We run θ over the set of cosmological parameters listed in Eq. (5.1), i.e., $\theta \in \{\Omega_{m,0}, \Omega_{b,0}, w_0, w_a, h, n_s, \sigma_8\}$.

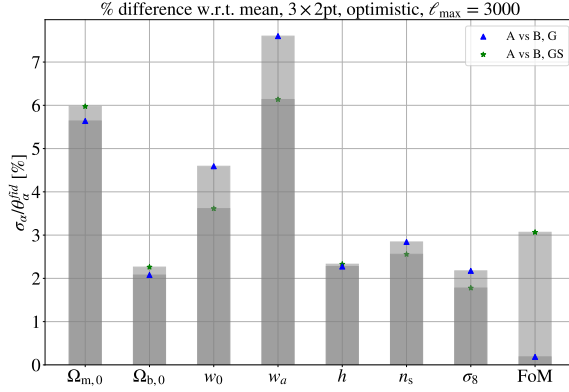


Figure 5.4. Percent discrepancy of the normalized 1σ uncertainties with respect to the mean for the WL probe, both in the G and GS cases (optimistic settings). The index $i = A, B$ indicates the two pipelines, whilst α indexes the cosmological parameter. The desired agreement level is reached in all cases (WL, GCph probes and pessimistic case not shown).

In addition, we examine the Figure of Merit (FoM) as defined in [Albrecht et al. \(2006\)](#), a useful way to quantify the joint uncertainty on several parameters. We parameterize the FoM following [EC20](#) to focus on the joint uncertainty on the dark energy equation of state parameters w_0 and w_a , such that

$$\text{FoM} = \sqrt{\det(\tilde{F}_{w_0 w_a})}. \quad (5.20)$$

This quantity is inversely proportional to the area of the 2σ confidence ellipse in the plane spanned by the parameters (w_0, w_a) . $\tilde{F}_{w_0 w_a}$ is the Fisher sub-matrix obtained by marginalising over all the parameters but w_0 and w_a , and is computed by inverting $F_{\alpha\beta}$ (that is, taking the parameters' covariance matrix), removing all the rows and columns but the ones corresponding to w_0 and w_a and re-inverting the resulting 2×2 matrix.

We will also use the notation $\mathcal{R}(\text{FoM})$ as a shorthand for $\text{FoM}_{\text{GS}}/\text{FoM}_{\text{G}}$. We note that, since we expect the uncertainties to be larger for the GS case, we will have $\mathcal{R}(\theta) > 1$, and the FoM being inversely proportional to the area of the uncertainty ellipse, $\mathcal{R}(\text{FoM}) < 1$.

5.3.1 Reference scenario

Let us start by considering the case with $\mathcal{N}_b = 10$ equipopulated redshift bins, which we will take in the following as a reference. Table 5.1 gives the values of the \mathcal{R} ratios for the different parameters and the FoM in both the pessimistic and optimistic scenarios, for the single or combined probes.

In accordance with previous results in the literature (see e.g. [Barreira et al., 2018a; Upham et al., 2022](#)), we find that the WL constraints are dramatically affected by the inclusion of SSC. The impact is so severe that the FoM is reduced by a factor of about 2 in both the pessimistic and optimistic scenarios. The marginalised uncertainties worsen by a large factor for those parameters which correlate the most with the amplitude of the signal: indeed, the largest $\mathcal{R}(\theta)$ values are obtained for $(\Omega_{m,0}, \sigma_8)$, while $\mathcal{R}(\theta)$ does not meaningfully deviate from unity for $\theta = (w_a, h, n_s)$, and w_0 sits in between the two extreme cases. This is because the SSC effect is essentially an unknown shift, or perturbation, in the background density, with which

Table 5.1. Ratio between the GS and G constraints for all cosmological parameters and the FoM in the reference scenario, for both pessimistic (P) and optimistic (O) assumptions. We remind the reader that in the reference case, we marginalize over the galaxy bias nuisance parameters while holding the multiplicative shear bias ones fixed.

$\mathcal{R}(x)$	$\Omega_{m,0}$	$\Omega_{b,0}$	w_0	w_a	h	n_s	σ_8	FoM
WL, P	1.998	1.001	1.471	1.069	1.052	1.003	1.610	0.475
WL, O	1.574	1.013	1.242	1.035	1.064	1.001	1.280	0.451
GCph, P	1.002	1.002	1.003	1.003	1.001	1.001	1.001	0.996
GCph, O	1.069	1.016	1.147	1.096	1.004	1.028	1.226	0.833
3×2pt, P	1.442	1.034	1.378	1.207	1.028	1.009	1.273	0.599
3×2pt, O	1.369	1.004	1.226	1.205	1.018	1.030	1.242	0.622

$\Omega_{m,0}$ and σ_8 are highly degenerate.

The results in Table 5.1 also show that GCph is not as strongly affected by SSC. This is an expected result, being the GCph probe response coefficients lower (in absolute value) than the WL ones, as can be seen in Fig. 5.1. This is due to the additional terms that account for the response of the galaxy number density n_g (see Eq. 5.6), which is itself affected by the super-survey modes. Moreover, the constraints from GCph alone are obtained by marginalising over a larger number of nuisance parameters than WL – the galaxy bias parameters, which are strongly degenerate with the amplitude of the signal. This works as a sort of effective systematic covariance which makes the SSC less dominant than in the WL case. Lastly, as can be seen from Fig. 3.7, all WL kernels have non-zero values for $z \rightarrow 0$, contrary to the GCph ones. In this limit, the effective volume probed by the survey tends to 0, hence making the variance of the background modes σ^2 tend to infinity. We thus have a larger S_{ijkl} matrix, which is one of the main factors driving the amplitude of the SSC. We nevertheless note, for GCph, a 17% decrease of the FoM in the optimistic case, which is related to the inclusion of nonlinear modes that are more sensitive to the SSC, as we discuss later.

The full 3×2pt case sits in between the two extremes as a consequence of the data vector containing the strongly affected WL probe, and the less affected GCph one. The contribution from the XC probe is again an intermediate case because of its lower response coefficient, so the final impact on the FM elements will be intermediate between the WL and GCph cases, as the $\mathcal{R}(\theta)$ values in Table 5.1 indeed show. Comparing the optimistic and the pessimistic cases for the two individual probes, we can see that there is a different behaviour of the SSC as a function of the maximum multipole. Indeed, for WL the $\mathcal{R}(\theta)$ ratio for the most affected⁸ parameters is larger in the pessimistic than in the optimistic case. This is consistent with the results of Upham et al. (2022) showing that the diagonal elements of the WL total covariance matrix are more and more dominated by the Gaussian term as we move to higher ℓ . This is because of the presence of the scale-independent shape noise in the Gaussian

⁸This is not the case for the unconstrained parameters, but the small difference is likely related to numerical artifacts.

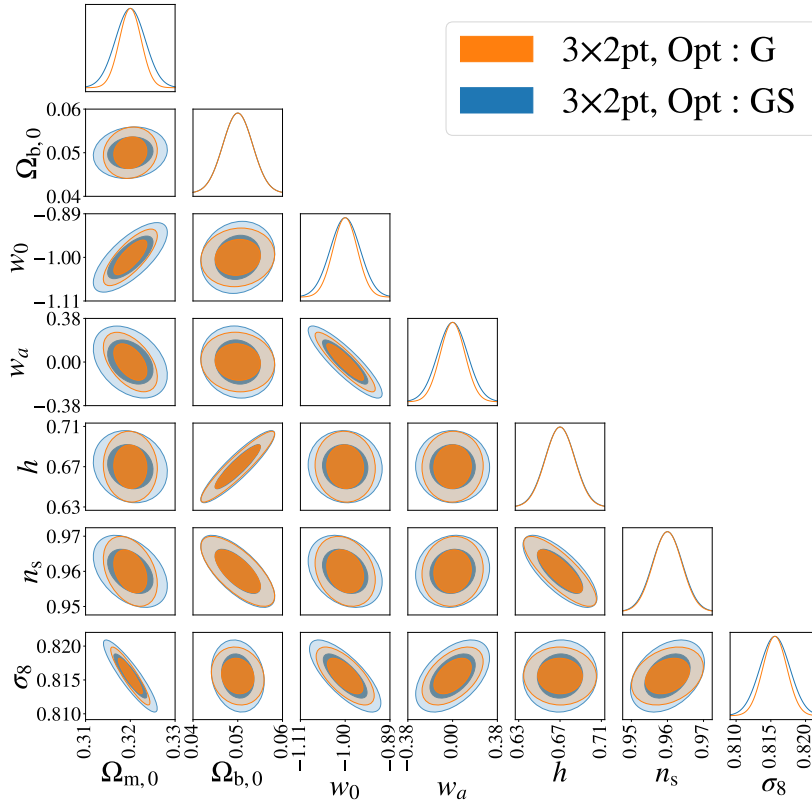


Figure 5.5. Contour plot for the G and GS constraints, considering the full 3x2pt analysis in the optimistic case, in the reference scenario. The addition of SSC does not seem to substantially modify the correlations between cosmological parameters. For clarity, the nuisance parameters are shown separately in Fig. 5.6.

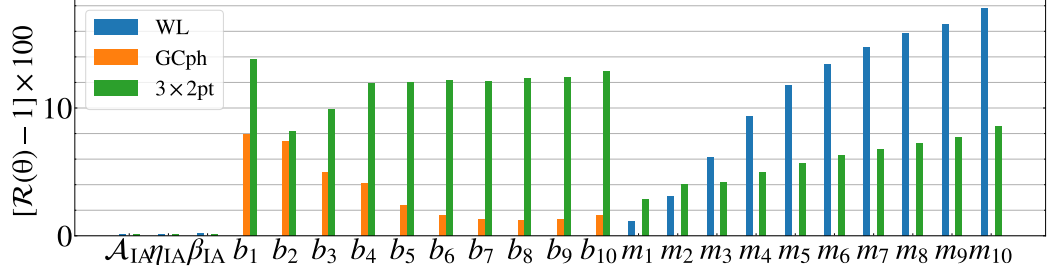


Figure 5.6. Percent increase of the marginalised 1σ uncertainty of the nuisance parameters, for all probe choices, in the optimistic case and for the reference scenario.

covariance (see Eq. 5.11 for $A = B = L$), which largely dominates over the SSC on small scales. As such, the relative importance of off-diagonal correlations decreases at large ℓ which is precisely what happens when moving from the pessimistic to the optimistic case. This causes the SSC impact to be smaller in the optimistic case, although we note that the $\mathcal{R}(\theta)$ are still remarkably large. Indeed, the \mathcal{R} values for the FoM are roughly the same, pointing to the importance of SSC in both scenarios.

As also seen in Lacasa (2020), we observe the opposite behaviour for the GCph probe, which is more impacted by the SSC in the optimistic case. This is because the impact of the shot noise at these scales is lower than the shape noise for WL, so the SSC still dominates in that multipole range.

In Fig. 5.5 we show the comparison of the 2D contours for all cosmological parameters between G and GS in the case of the 3×2 pt analysis, in the optimistic case. Again, we can clearly see that the most impacted parameters are $\theta = (\Omega_{m,0}, w_0, \sigma_8)$. In addition, this shows that SSC does not seem to strongly affect the degeneracy between cosmological parameters; however, we note that, in general, the Gaussian contours are more elliptical (more degenerate) than the GS ones. This is because, as noted in Lacasa 2020, in the former case we attribute artificially small uncertainties to the small scales (because of the very small cosmic variance), which consequently hold the majority of the constraining power, leading to parameter degeneracies. In the GS case, on the other hand, the constraining power is more evenly distributed between the different scales.

To conclude this section, it is also worth looking at the impact of SSC on the astrophysical nuisance parameters. Indeed, although an issue to be marginalised over when looking at cosmological ones, the IA and the galaxy bias parameters are of astrophysical interest. We show the impact of SSC on the constraints on these quantities in Fig. 5.6, and, as an anticipation of the next section, we also show the constraints for other WL-related nuisance parameters, the multiplicative shear bias parameters m_i . For IA-related nuisance parameters, the uncertainty increase due to SSC is lower than 0.5%. The uncertainty on b_i and m_i in each of the ten redshift bins is however significantly affected by SSC, showing an increase between 1 and 14% for b_i and between 1 and 18% for m_i , depending on the probe combination choice. This is because both of these nuisance parameters simply act as a multiplicative factor on the power spectrum and are thus highly degenerated with the effect of SSC. Again, this is because the first-order effect of SSC is to modulate

Table 5.2. Same as Table 5.1 but removing the flatness prior.

$\mathcal{R}(x)$	$\Omega_{m,0}$	$\Omega_{DE,0}$	$\Omega_{b,0}$	w_0	w_a	h	n_s	σ_8	FoM
WL, P	2.561	1.358	1.013	1.940	1.422	1.064	1.021	1.433	0.514
WL, O	2.113	1.362	1.004	1.583	1.299	1.109	1.038	1.559	0.631
GCph, P	1.002	1.001	1.002	1.002	1.003	1.001	1.000	1.001	0.996
GCph, O	1.013	1.020	1.006	1.153	1.089	1.004	1.039	1.063	0.831
3×2pt, P	1.360	1.087	1.043	1.408	1.179	1.021	1.009	1.040	0.677
3×2pt, O	1.572	1.206	1.013	1.282	1.191	1.013	1.008	1.156	0.756

the overall clustering amplitude because of a shift in the background density δ_b . As mentioned, this cross-talk between SSC and linear galaxy bias could also explain why the GCph probe seems less affected by SSC: some of the difference between G and GS is absorbed by the b_i in the marginalisation. This will be also confirmed for WL in the next section, showing a reduced relative impact of SSC in the presence of multiplicative shear bias. Note that going beyond the linear approximation for the modelling of the galaxy bias will add more nuisance parameters, thus degrading the overall constraints on cosmological parameters and further reducing the relative degradation of constraints due to SSC.

Finally, comparing how uncertainties on b_i and m_i react to the addition of SSC, we can see that surprisingly the b_i are more affected in the 3×2pt case than in the GCph case, while it is the contrary for m_i , the uncertainty increase is larger for WL than for 3×2pt. This difference in the behaviour of the uncertainty increase might come from the numerous degeneracies existing between these nuisance parameters and the most constrained cosmological parameters in each case. Though it is not easy to exactly understand this behaviour, we note that in all cases the $\mathcal{R}(\theta)$ for these parameters are of the same order of magnitude and are never completely negligible.

5.3.2 Non-flat cosmologies

In the previous section, we investigated the SSC on the cosmological parameters under the assumption of a flat model. Actually, the requirement on the FoM assessed in the *Euclid* Red Book refers to the case with the curvature as an additional free parameter to be constrained, i.e., the non-flat w_0w_a CDM model. This is why in EC20 are also reported the marginalised uncertainties for the parameter $\Omega_{DE,0}$, with a fiducial value $\Omega_{DE,0}^{\text{fid}} = 1 - \Omega_{m,0}^{\text{fid}}$ to be consistent with a flat Universe. It is worth wondering what the impact of SSC is in this case too. This is summarised in Table 5.2, where we now also include the impact on $\Omega_{DE,0}$.

A comparison with the results in Table 5.1 is quite hard if we look at the single parameters. Indeed, opening up the parameter space by removing the flatness assumption introduces additional degeneracy among the parameters controlling the background expansion, which are thus less constrained whether SSC is included or not. We can nevertheless note again that WL is still the most impacted probe, while GCph is less affected, and the 3×2pt sits in between. The difference between pessimistic and optimistic scenarios is now less evident with $\mathcal{R}(\theta)$ increasing or

Table 5.3. Same as Table 5.2 but adding multiplicative shear bias nuisance parameters.

$\mathcal{R}(x)$	$\Omega_{m,0}$	$\Omega_{DE,0}$	$\Omega_{b,0}$	w_0	w_a	h	n_s	σ_8	FoM
WL, P	1.082	1.049	1.000	1.057	1.084	1.034	1.025	1.003	0.917
WL, O	1.110	1.002	1.026	1.022	1.023	1.175	1.129	1.009	0.976
3×2pt, P	1.297	1.087	1.060	1.418	1.196	1.021	1.030	1.035	0.674
3×2pt, O	1.222	1.136	1.010	1.300	1.206	1.013	1.009	1.164	0.745

decreasing depending on the parameter and the probe.

Once more, the most affected parameters for WL are $(\Omega_{m,0}, \sigma_8)$, the uncertainties on which are now further degraded by the fact that they correlate with the parameter $\Omega_{DE,0}$ which is also affected. Although (w_0, w_a) are also degraded by the SSC, a sort of compensation is at work, so that the overall decrease in the FoM is similar to the case with the flatness prior. The motivations that make GCph much less affected still hold when dropping the flatness prior, explaining the corresponding $\mathcal{R}(\theta)$ values.

We also note an increase of $\mathcal{R}(\text{FoM})$ in the 3×2pt case, meaning a smaller degradation of the FoM due to SSC. The FoM indeed degrades by 24% (32%) in the non-flat case vs. 38% (40%) for the flat case in the optimistic (pessimistic) scenario. This can be qualitatively explained by noting that the decrease of both FoM(G) and FoM(GS) is related to a geometrical degeneracy which is the same on all scales, whether or not they are affected by the increase in uncertainty due to the SSC inclusion.

5.3.3 Role of nuisance parameters

We can now open up the parameter space by letting the shear bias parameters introduced in Sect. 3.2.7 free to vary. We expand the FM by adding these additional parameters and recompute the ratios of uncertainties with and without SSC obtaining the results shown⁹ in Table 5.3. We remind the reader that the number of nuisance parameters depends on which probe (WL or 3×2pt) one is considering. For the WL case, the \mathcal{N}_b multiplicative shear bias parameters add up to the 3 IA ones leading to the result that the SSC has a very minor impact on the constraints and on the FoM. The values in Table 5.3 are actually easily explained. We recall that $\mathcal{R}(\theta)$ is a ratio between the constraints with and without the SSC. Adding m_i to the cosmological parameters introduces a degeneracy between m_i itself and the parameters $(\Omega_{m,0}, \sigma_8)$ which set the overall amplitude of $C_{ij}^{LL}(\ell)$. Such a degeneracy is a mathematical one present on the whole ℓ range, similar to the galaxy bias parameters for GCph. As a consequence, the constraints on all the parameters and the FoM are strongly degraded in a way that is independent of the presence of SSC. This is shown in Fig. 5.7 and 5.8, which exhibits the relative uncertainty $\bar{\sigma}$ and the dark energy FoMs in the G and GS cases for each parameter, if we marginalise or not on over nuisance parameters. Letting the nuisance parameters free to vary, i.e. marginalising over them, tends to increase the uncertainty on cosmological parameters way more than

⁹We do not report here the results for GCph since they are the same as the ones shown in Table 5.1, given that $C_{ij}^{GG}(\ell)$ is unaffected by multiplicative shear bias.

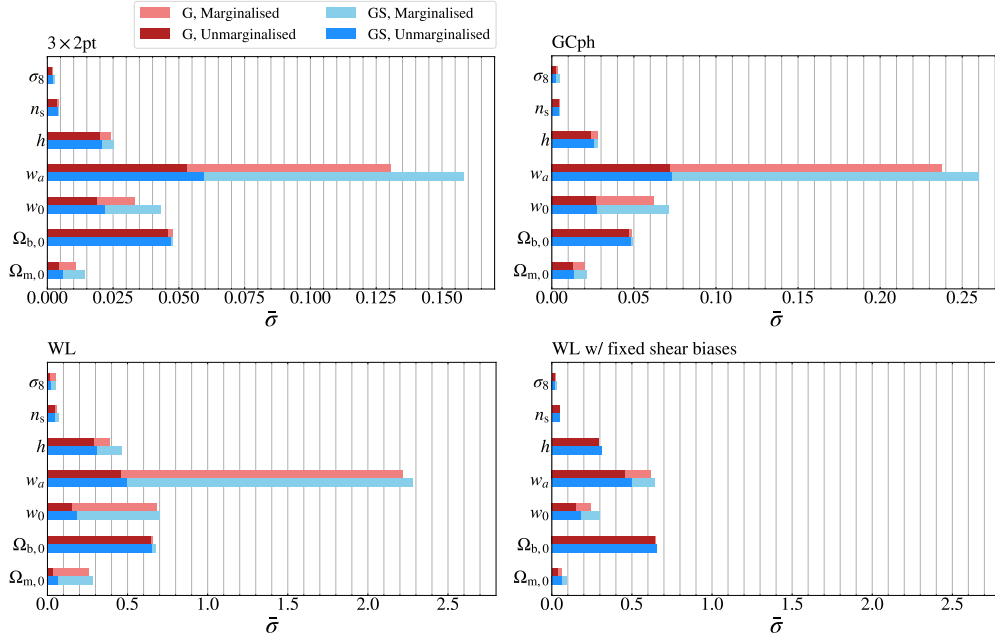


Figure 5.7. Marginalised and unmarginalised 1σ uncertainties on the cosmological parameters, relative to their corresponding fiducial values, in both the G and GS cases for $3\times 2pt$, GCph and WL. For WL, we show the results in the case where the multiplicative shear biases are either varied or fixed, in other words, whether we marginalise over all nuisance parameters or only over the IA ones.

including SSC and this is even more true when these nuisance parameters are simply multiplicative such as b_i and m_i . This is why the \mathcal{R} values drop down to values close to unity in contrast to what we have found up to now. Moreover, introducing more nuisance parameters degenerate with the amplitude of the signal dilutes the SSC effect in a larger error budget; because of this, it is the relative rather than the absolute impact of SSC that decreases. Indeed, marginalising over nuisance parameters is formally equivalent to having additional covariance.

Note that this does not mean that adding nuisance parameters improves the constraints. Indeed, the marginalised uncertainties on all parameters increase (hence the FoM decreases) with respect to the case when the multiplicative shear bias is fixed. The degradation is, however, the same with and without SSC so the $\mathcal{R}(\theta)$ values stay close to unity.

On the contrary, the results for the $3\times 2pt$ case show that the SSC still matters. The additional information carried by the GCph and XC data allows the partial breaking of the mathematical degeneracy among $(m_i, \Omega_{m,0}, \sigma_8)$ hence making again the scale-dependent increase of the uncertainties due to the inclusion of SSC important. However, the larger number of nuisance parameters (from 13 to 23) still introduces additional degeneracies with the cosmological ones hence alleviating the impact of SSC. The overall effect is, however, small with the \mathcal{R} values being close to the ones in Table 5.2. In particular, the FoM degradation is essentially the same in both the pessimistic and optimistic cases. Overall, these results suggest a dependence of the SSC significance on both the number and type of parameters

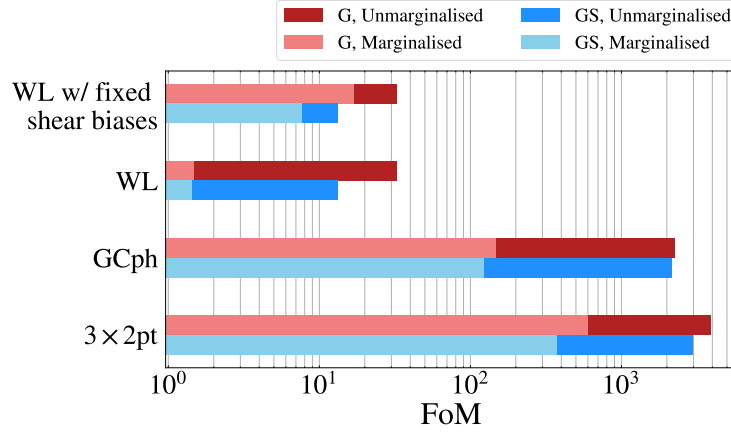


Figure 5.8. Dark energy FoM for marginalised and unmarginalised constraints in both the G and GS cases, 3×2 pt, GCph, WL, and WL with fixed multiplicative shear biases.

to be constrained. Qualitatively, we can argue that SSC is more or less important depending on whether the additional parameters (with respect to the reference case of a flat model with fixed shear bias) introduce degeneracies which are or not scale-dependent and how strong is the degeneracy between these parameters and the amplitude of the power spectrum. In future works lens magnification effects should be included in the analysis as it was shown to have a significant impact on cosmological constraints (Unruh et al., 2020). However, from our results, we can anticipate that the inclusion of magnification-related nuisance parameters will further dilute the impact of SSC.

5.3.4 Dependence on redshift binning

The results summarised in Tables 5.1–5.3 have been obtained for a fixed choice of number and type of redshift bins. We investigate here how they depend on these settings given that we expect both the G and GS constraints to change as we vary the number and type of bins. We will consider the case of non-flat models, fixing the multiplicative shear bias parameters in order to better highlight the impact of SSC. For this same reason, we will only consider the WL and 3×2 pt cases, since SSC has always a modest impact on GCph. Let us first consider changing the number of redshift bins \mathcal{N}_b . We show the scaling of $\mathcal{R}(\theta)$ as a function of \mathcal{N}_b for the WL and 3×2 pt probes, respectively, in Fig. 5.9 – for both the pessimistic and optimistic assumptions. The most remarkable result is the weak dependence of $\mathcal{R}(\text{FoM})$ on \mathcal{N}_b as can be inferred from the small range spanned by the curves in the bottom right panel. The scaling of $\mathcal{R}(\theta)$ with \mathcal{N}_b depends, instead, on the parameter and the probe one is looking at. It is quite difficult to explain the observed trends due to the interplay of different contrasting effects. For instance, a larger number of bins implies a smaller number density in each bin, and hence a larger shot noise. As a consequence, the SSC contribution to the total covariance for the diagonal elements will likely be more and more dominated by the Gaussian component because of the larger shot and shape noise terms. However, this effect also depends on the scale so that, should the SSC be the dominant component on the scales to which a parameter

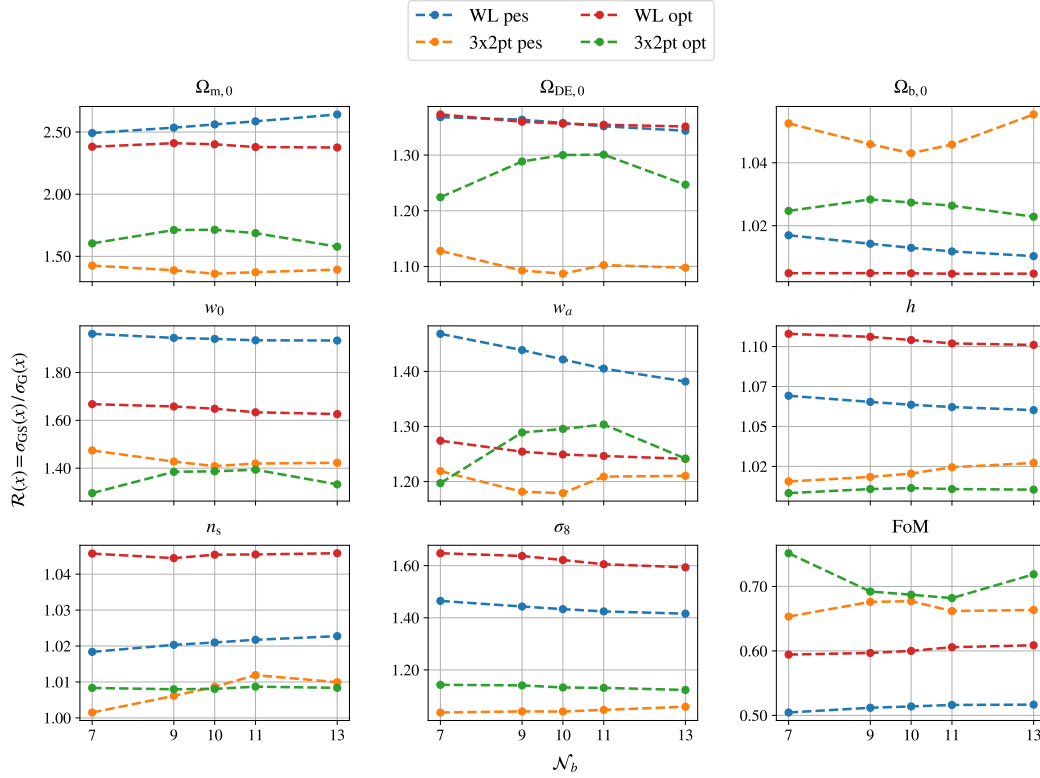


Figure 5.9. Ratio between WL and 3×2 pt marginalised uncertainties computed by including or neglecting the SSC contribution, as a function of the number of redshift bins, for the pessimistic and optimistic cases.

is most sensitive, the impact should still be important. On the other hand, a larger number of bins also comes with a larger number of nuisance parameters, which, as shown above, leads to a reduction of the SSC impact. Quantifying which actor plays the major role is hard, which explains the variety of trends in the different panels.

As a further modification to the reference settings, we can change how the redshift bins are defined. Up to now, we have considered equipopulated (EP) bins so that the central bins cover a smaller range in z , because of the larger source number density. As an alternative, we divide the full redshift range into \mathcal{N}_b bins with equal length (ED) and recompute the FM forecasts with and without SSC. We show the FoM ratio as a function of the number of bins for EP and ED bins considering WL (left) and 3×2 pt (right) probes in the optimistic scenario in Fig. 5.10. Note that finding the exact number and type of redshift bins used to maximize the constraining power of *Euclid* is outside the scope of this paper; this effort is indeed brought forward in the context of the SPV exercise.

In order to qualitatively explain these results, let us first consider the WL case. Given that the bins are no longer equipopulated, the number density of galaxies will typically be larger in the lower redshift bins than in the higher ones. As a consequence, the larger the number of bins, the higher the shape noise in the higher redshift bins, so that the SSC will be subdominant in a larger number of bins, which explains why its impact decreases (i.e. $\mathcal{R}(\text{FoM})$ increases) with \mathcal{N}_b . Nevertheless,

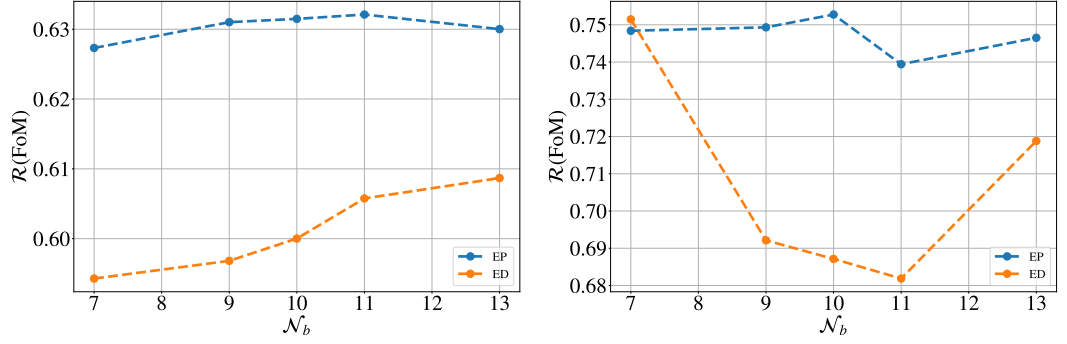


Figure 5.10. FoM ratio vs the number of EP and ED redshift bins for WL (left) and 3×2 pt (right) in the optimistic scenario.

the impact of SSC will be larger than in the EP case since SSC will dominate in the low redshift bins which are the ones with the largest S/N. However, this effect is less important, so although $\mathcal{R}(\text{FoM})$ is smaller for ED bins than for EP bins, the difference is not greater than 3–5%.

When adding GCph and XC into the game, the impact of SSC is determined by a combination of contrasting effects. On the one hand, we can repeat the same qualitative argument made for WL also for GCph, thus pointing to $\mathcal{R}(\text{FoM})$ increasing with \mathcal{N}_b . No shape or shot noise is included in the XC Gaussian covariance, which is then only determined by how much shear and position are correlated. The larger the number of bins, the narrower they are, and the smaller the cross-correlation between them hence the smaller the Gaussian covariance. This in turn increases the number of elements in the data vector whose uncertainty is dominated by the SSC. Should this effect dominate, we would observe a decrease of $\mathcal{R}(\text{FoM})$ with \mathcal{N}_b with the opposite trend if it is the variation of the shape and the noise of the shot that matters the most. This qualitative argument allows us then to roughly explain the non-monotonic behaviour of $\mathcal{R}(\text{FoM})$ we see in the right panel of Fig. 5.10. It is worth remarking, however, that the overall change of $\mathcal{R}(\text{FoM})$ for ED bins over the range in \mathcal{N}_b is smaller than $\sim 12\%$, which is also the typical value of the difference between $\mathcal{R}(\text{FoM})$ values for EP and ED bins once \mathcal{N}_b is fixed.

The analysis in this section, therefore, motivates us to argue that the constraints and FoM degradation due to SSC are quite weakly dependent on the redshift binning.

5.3.5 Requirements on prior information

The results in the previous paragraph show that the SSC may dramatically impact the constraints on the cosmological parameters. As a consequence, the 3×2 pt FoM is reduced by up to $\sim 24\%$ with respect to the case when only the Gaussian term is included in the total covariance. This decrease in the FoM should not be interpreted as a loss of information due to the addition of the SSC. On the contrary, one can qualitatively say that removing SSC from the error budget is the same as adding information that is not actually there. It is nevertheless interesting to ask which additional information must be added to recover the Gaussian FoM, which is usually taken as a reference for gauging the potential of a survey. This information

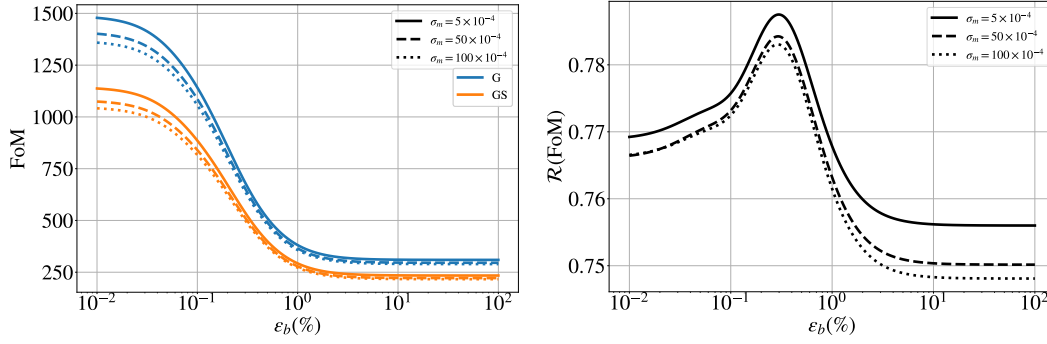


Figure 5.11. *Left.* 3×2 pt FoM in the optimistic scenario with and without SSC as a function of the percentage prior ε_b on the galaxy bias parameters for $\sigma_m = (5, 50, 100) \times 10^{-4}$ (solid, dashed, dotted lines). *Right.* FoM ratio as function of ε_b for the three σ_m values in the left panel.

can come from priors on the nuisance (or cosmological) parameters. In the following section, we will investigate the former option by adding Gaussian priors on the galaxy and multiplicative shear bias parameters. This is easily done in the FM formalism, as explained in Sect. 2.2, by adding $(\sigma_\alpha^p)^{-2}$ to the appropriate diagonal elements of the G and GS FMs (σ_α^p being the value of the prior uncertainty on parameter α).

To this end, we consider the realistic case of a non-flat model plus the galaxy bias and multiplicative shear bias as nuisance parameters. As a simplifying assumption, we will assume that all the \mathcal{N}_b bias values b_i are known with the same percentage uncertainty $\varepsilon_b = \sigma_b/b_{\text{fid}}$, while we put a prior σ_m on all the m_i parameters (having set the fiducial value m_{fid} to 0). We then compute the FoM with and without SSC for the 3×2 pt probe in the optimistic scenario and investigate how the ratio $\mathcal{R}(\text{FoM})$ scales with $(\varepsilon_b, \sigma_m)$ obtaining the results shown in Fig. 5.11.

A prior on the nuisance parameters increases both the Gaussian and Gaussian + SSC FoM so that one could expect their ratio to be independent of the prior itself. This is not exactly the case since the correlation between different multipoles introduced by SSC alters the way the prior changes the FM elements. As a result, we find a non-flat scaling of $\mathcal{R}(\text{FoM})$ as can be seen from the right panel of Fig. 5.11. When a strong prior is set on the galaxy bias (i.e., $\varepsilon_b \ll 1$), there is not much gain in improving the knowledge of the multiplicative shear bias so that the solid, dashed, and dotted lines (corresponding to three σ_m values) are quite close to each other. This is no longer the case for larger ε_b values (i.e., weak or no prior on the bias): lowering σ_m has now a larger impact on $\mathcal{R}(\text{FoM})$. The non-monotonic behaviour of $\mathcal{R}(\text{FoM})$ with ε_b tells us that FoM_{GS} increases with decreasing ε_b faster (slower) than FoM_{G} when the galaxy bias is known with an uncertainty smaller (higher) than the sub-percent level. Another way to interpret it is that the information gained in the FoM saturates faster when SSC is included: better constraints on ε_b do not bring more information as the SSC now dominates the error budget. However, it is worth stressing that, even for a strong prior on the multiplicative shear bias, the FoM ratio can actually be improved by less than a few percent under the (likely unrealistic) assumption of a sub-percent prior on the galaxy bias.

The need for such strong priors comes from the attempt to retrieve the same FoM as a Gaussian case. Alternatively, one can also wonder which additional information must be added through priors to retrieve the idealised FoM value obtained in forecasts that neglect the SSC. In other words, we look for the requirements that must be put on the priors $(\varepsilon_b, \sigma_m)$ in order to make $\text{FoM}_{\text{GS}}/\text{FoM}_{\text{ref}} = 1$, where $\text{FoM}_{\text{ref}} = 295$ is the FoM computed for a non-flat reference case without SSC and with no priors on galaxy bias, but a fiducial prior $\sigma_m = 5 \times 10^{-4}$ on the shear bias. The answer to this question is shown in Fig. 5.12 for the optimistic scenario and 10 equipopulated redshift bins. Some numbers help to better understand how priors can indeed supply the additional information to retrieve the FoM one would obtain in an ideal case where SSC is absent. Solving

$$\text{FoM}_{\text{GS}}(\varepsilon_b, \sigma_m) = f \text{FoM}_{\text{ref}}$$

with respect to ε_b , we get

$$\varepsilon_b = \begin{cases} (2.34, 1.19, 0.86) \% & \text{for } \sigma_m = 0.5 \times 10^{-4} \\ (2.27, 1.18, 0.85) \% & \text{for } \sigma_m = 5 \times 10^{-4} \\ (1.40, 0.93, 0.72) \% & \text{for } \sigma_m = 100 \times 10^{-4} , \end{cases}$$

where the three values refer to $f = (0.8, 0.9, 1.0)$. These numbers (and the contours in Fig. 5.12) show that it is indeed possible to compensate for the degradation due to SSC by adding strong priors on the galaxy bias, which have a much larger impact on the (G and GS) FoM than strong priors on the multiplicative shear bias. However, it is worth noticing that it is actually easier to obtain priors on the multiplicative shear bias provided a sufficient number of realistic image simulations are produced and fed to the shear measurement code to test its performance. It is therefore worth wondering how much the FoM is restored by improving the prior on m for a fixed one on the bias. We find

$$\frac{\text{FoM}_{\text{GS}}}{\text{FoM}_{\text{ref}}} = \begin{cases} (2.87, 2.86, 2.64) & \text{for } \varepsilon_b = 0.1\% \\ (0.95, 0.95, 0.88) & \text{for } \varepsilon_b = 1\% \\ (0.76, 0.76, 0.70) & \text{for } \varepsilon_b = 10\% , \end{cases}$$

with the three values referring to $\sigma_m = (0.5, 5.0, 100) \times 10^{-4}$. As expected, improving the prior on the multiplicative bias with respect to the fiducial one (which, we remind, is included in FoM_{ref}) does not help a lot in recovering the constraining power. However, a 1% prior on the galaxy bias can almost fully recover the reference FoM thanks to the additional information compensating for the presence of SSC.

Investigating whether the priors proposed here can be achieved in practice (e.g., through theoretical bias models tailored to galaxy clustering data or N -body hydrodynamic simulations) is outside the aim of this work. We refer the interested reader to, e.g., Barreira et al. (2021) and Zennaro et al. (2022) for some preliminary results.

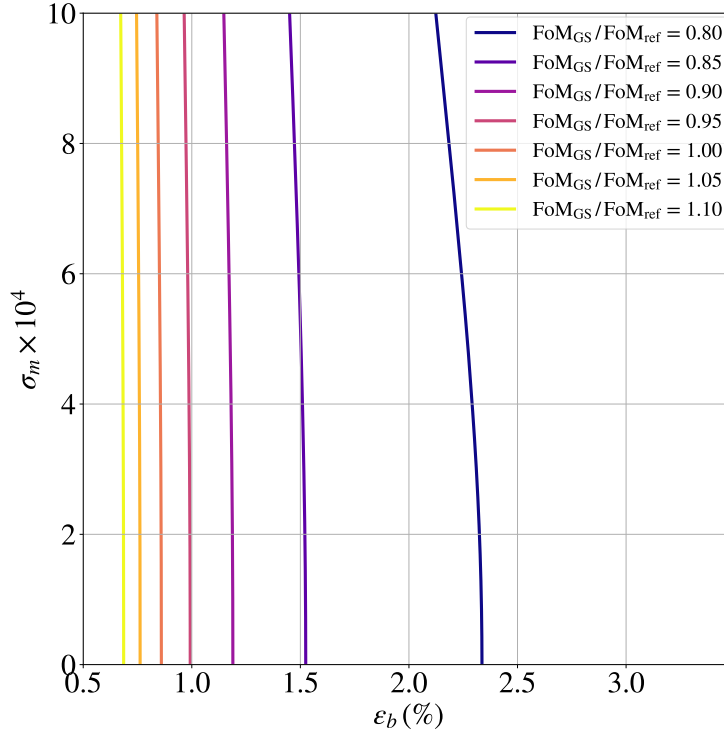


Figure 5.12. FoM_{GS} contours in the $(\varepsilon_b, \sigma_m)$ plane for $\text{FoM}_{\text{GS}}/\text{FoM}_{\text{ref}}$ going from 0.8 to 1.1 in steps of 0.05 (from right to left).

5.4 Summary

Precision cosmology asks for precision computation too: previously neglected theoretical contributions must therefore now be taken into account. Motivated by this consideration, we have here computed and studied the impact of SSC on the *Euclid* photometric survey, exploring how the different probes and their combination are affected by this additional, non-Gaussian term in the covariance matrix. The analysis of the impact of SSC on the spectroscopic survey, which has been shown to be small in [Wadekar et al. \(2020\)](#) for the BOSS data, is left for future work. We employed a FM analysis, producing forecasts of the 1σ marginalised uncertainties on the measurement of the cosmological parameters of the flat and non-flat $w_0w_a\text{CDM}$ cosmological models. We validated two different forecast pipelines against the results of [EC20](#), taking as reference survey the one specified therein, and then updated the galaxy bias and the source redshift distributions according to the most recent versions presented in [Euclid Collaboration: Pocino et al. \(2021\)](#). The SSC was computed relying on the analytical approximations and numerical routines presented in [LG19](#), interfacing the public code PySSC with two distinct forecast pipelines to validate the constraints. As a further step forward, we build upon the work of [LG19](#) by computing the scale and redshift dependence of the response functions of the different probes, starting from the results of [Wagner et al. \(2015b\)](#) and [Barreira et al. \(2018b\)](#).

We find the severity of the impact, quantified by the ratio $\sigma_{\text{GS}}/\sigma_{\text{G}}$ between the

marginalised uncertainties with and without SSC, to vary substantially between different parameters and probes. For both WL and GCph, the most affected parameters are $(\Omega_{m,0}, w_0, \sigma_8)$, while the constraints on $(\Omega_{b,0}, h, n_s)$ are only weakly degraded by SSC. However, there is a great difference between the two probes in how much the constraints worsen because of SSC. In agreement with previous results (Upham et al., 2022; Barreira et al., 2018a), we found the WL case to be dramatically impacted by SSC so that the corresponding FoM is reduced by as much as 55%, while GCph is less affected with the FoM decrease being about 17%. The 3×2 pt case sits in between these two since it receives contributions from both extreme cases. These results are the consequence of a complicated interplay among three factors. First, SSC originates from the uncertainty in the determination of the background mean density when measuring it over a finite region. This prevents determining the overall amplitude of the matter power spectrum hence increasing the uncertainty on those parameters that concur in setting its amplitude, mainly $\Omega_{m,0}$ and σ_8 . Secondly, the elements of the SSC matrix depend on the amplitude of the response functions. Thirdly, the impact depends on how large a contribution the signal receives from the low- z region, where the effective volume probed is smaller, making the variance of the background modes larger. Both the last two factors are more severe for WL than for GCph, hence causing the former probe to be more affected than the latter. Finally, the deviation of a given element of the GS FM from the Gaussian one depends also on its correlations: in other words, the degradation of the constraints on a given parameter can be large if this is strongly correlated with a parameter severely degraded by SSC. Quantifying the impact of SSC on a single parameter is therefore quite hard in general, and must be investigated on a case-by-case basis taking care of the details of the probe and the way it depends on the parameter of interest.

Nuisance parameters to be marginalised over act as a sort of additional contribution to the covariance. As such, the importance of both the Gaussian and SSC contribution to the overall effective covariance becomes less important when the number of nuisance parameters increases. In order to consider cases that mimic the most future *Euclid* data, we have opened up the parameter space by adding $\Omega_{DE,0}$ (i.e., removing the flatness prior), and the multiplicative shear bias. It turns out that, as long as the additional parameters have a scale-independent degeneracy with the most impacted ones, the relative impact of SSC decreases. We stress, however, that this reduction in the SSC impact does not come for free. On the contrary, the marginalised uncertainties on the parameters are definitely worsened, but the degradation is roughly the same whether the SSC is included or not, hence making the ratio σ_{GS}/σ_G closer to unity for all parameters and probes. This result can be taken as a warning against investing too much effort in refining the estimate of the computationally expensive SSC when no approximations are done. For a *Euclid*-like survey, the main concern would indeed be the number of nuisance parameters, which makes less relevant the impact of the SSC itself.

We furthermore note that, in light of the recent theoretical developments presented in Lacasa et al. (2023), it appears feasible to include the effect of SSC in the form of nuisance parameters, which would be the value of the density background δ_b in each redshift bin. This approach is interesting as it would reduce the complexity of the data covariance matrix and would allow for a simpler interpretation of the effect

of SSC and how it is correlated to the other cosmological and nuisance parameters.

Variations in the z binning strategy have contrasting effects: a larger number of bins means a larger number of nuisance parameters (either galaxy bias or multiplicative shear bias for each bin), which leads to a loss of constraining power. Moreover, the larger the number of bins, the larger the Gaussian contribution to the covariance, causing the shot and shape noise to dominate over the SSC for diagonal elements. On the downside, a larger number of bins leads to larger data vectors, thus adding information that can partially compensate for the increase in covariance. The contrasting effects at play conspire in such a way that the degradation of the FoM due to SSC ends up being approximately independent of the number of redshift bins (cf. Fig. 5.10).

An interesting development in this sense is to leverage the SSC dependence on the low- z contribution to investigate whether its impact could be mitigated by the use of the BNT transform (Bernardeau et al., 2014), which transforms redshift bins in such a way as to increase the separation between the WL kernels (see Sect. 6.1).

An alternative strategy is to increase the constraining power by adding information through informative priors, hence recovering the FoM when SSC is incorrectly neglected. We investigate this possibility by quantifying the requirements on the prior information needed to recover the Gaussian FoM. Our results show that the main role is played here by the priors on galaxy bias parameters, while the FoM recovery quickly saturates with the prior on the multiplicative shear bias. However, the galaxy bias must be known to sub-percent level in order to recover $\sim 90\%$ of the Gaussian FoM. Investigating whether this is possible is beyond the scope of this work. We nevertheless note that including such remarkable prior information is the same as stating we are able to model the evolution of the bias with redshift. This is actually quite difficult based on the current knowledge of galaxy formation processes. Alternatively, one could investigate whether an empirical fitting formula can be found as a compromise between the need for strong priors on bias and the number of nuisance parameters.

Although some more work is needed to make the results more robust, we can safely conclude that the effect of including the SSC term in the total covariance matrix of *Euclid* photometric observables is definitely non-negligible, especially for WL and 3×2 pt. However, the degradation of the constraints on cosmological parameters depends on the particular probe and the number and kind of parameters to constrain. The FoM is nevertheless reduced by 32% (25%) for the 3×2 pt probe in the pessimistic (optimistic) scenario in the case where all cosmological (including $\Omega_{\text{DE},0}$) and nuisance (multiplicative shear bias) parameters are left free to vary.

Chapter 6

Scale Cuts

The treatment of SSC for *Euclid* is just a part of the broader effort to characterize the constraining power of the survey. This is an inter-group endeavour, framed in the context of the “Science Performance Verification”. The aim of this exercise is twofold:

- Verifying that the expected performance of *Euclid* is still in line with the core science objectives of the nominal mission.
- Developing and maintaining tools and codes used to make quick assessments of the performances of the mission for different scenarios.

These aims are achieved through the collaboration between teams focusing on virtually all of the scientific aspects of the mission: from the survey strategy to the calibration, to the modelling of the PSF, the choice of the nonlinear model and the binning strategy, just to name a few.

Our work in this activity mainly concerned the optimization of the survey, that is, the search for a reference choice for some of the many ingredients involved in the computation of the final forecasts. In particular, we studied the effect of different prescriptions and codes for the computation of the nonlinear matter PS, the inclusion of systematics such as multiplicative shear bias, the shift in the mean of the redshift distribution, magnification bias, the optimal type and number of redshift bins, and the impact of different magnitude and scale cuts, using as main metric the 3×2 pt FoM.

This Chapter illustrates in detail the last of these. Section 6.1 presents the BNT transform, an essential ingredient to include scale cuts in the harmonic space photometric analysis; Sect. 6.2 shows the procedure used, on the basis of BNT transform, to obtain redshift-dependent *angular* scale cuts, and Sect. 6.3 illustrates the forecast setup and the results obtained. We present our conclusions in Sect. 6.4.

These results, along with the other themes explored in the SPV, will be published once the exercise is concluded.

6.1 Scale cuts and the BNT transform

As stated earlier in this work, the current decades have seen Cosmology rise from the status of “data-starved” (Tegmark et al., 1997) to “data-rich” science. This will

be increasingly the case now that state-of-the-art Stage IV LSS surveys are beginning to come online. In such a scenario, it is actually the theoretical side to have become the limiting factor in some (important) aspects of the analysis. In particular, *Euclid* will be able to probe scales that, at this point in time, are poorly understood. Our analytical models, some of which have been introduced in Sect. 1.4.4, are unable to capture either DM structure formation deeply in the nonlinear regime, or the impact of baryonic (collisional) matter, which introduces a whole new layer of complexity.

A viable option, widely used in the literature, is to resort to magnetohydrodynamic (MHD) numerical simulations (see Chisari et al. 2019b for a review of the most recent simulations, as well as the approximate methods), which however often give different results based on the modelling choices adopted and the numerical implementation. Another possibility is to try to capture baryonic feedback through parameters which are marginalized over or calibrated against simulations.

An alternative, more conservative approach is simply to remove (“cut”) the elements of the data vector corresponding to the poorly understood scales. This approach has already been adopted, for example, in EC20, which as illustrated in Sect. 5.1.6 defined “pessimistic” and “optimistic” scenarios, depending on our ability to exploit the high- ℓ measurements. The cuts hereby defined have two main problems.

Firstly, they are redshift-independent. This means that we assume to be able to model the same maximum angular scale, ℓ_{\max} , without taking into account whether we are considering a close source (which will then correspond to a smaller physical scale, or larger k_{\max}) or a faraway source (for which the opposite will be true).

Secondly, the correspondence between physical scale k and angular scale ℓ is not, in general, well-defined. We have seen that the angular PS is obtained from a radial projection of the three-dimensional PS, weighted by some probe-specific radial kernel: this means that a whole *range* of scales k will contribute to a given ℓ mode. The extension of this range is modulated by the redshift width of the kernels, so that narrow kernels will result in a better consistency between ℓ and k . More specifically (rewriting here Eq. 3.10 for convenience), this correspondence is given by the Limber relation, which tells us how to compute, for a given ℓ value, the k_ℓ entering the $C(\ell)$ integral as a function of redshift: $k_\ell = \frac{\ell+1/2}{\chi(z)}$.

$$C_{ij}^{AB}(\ell) = \frac{c}{H_0} \int_0^{z_{\max}} dz \frac{\mathcal{K}_i^A(z) \mathcal{K}_j^B(z)}{E(z) \chi^2(z)} P_{AB} \left[k_\ell = \frac{\ell+1/2}{\chi(z)}, z \right]. \quad (6.1)$$

Wide kernels will result in a large support for the z integral and a large range of scales contributing to the overall power at the same multipole. This issue is relevant for GCph, because of the broadening of the kernels due to photo- z uncertainties, but much more so for WL, because as discussed the kernel is necessarily very broad, spanning the whole distance between source and observer.

A potential solution to this problem has been proposed in Bernardeau et al. (2014). The main idea outlined in this work is to transform the lensing kernels so as to make them separable in z , by weighting galaxies according to their photometric redshifts. In practice, this means reorganizing the data so that the lensing signal in a given redshift bin becomes only sensitive to a narrow distribution of sources. This

makes the $k - \ell$ relation more precise, and largely reduces the overlap between the kernels.

To illustrate this transformation, we sketch the steps illustrated in the original paper. We begin by writing the projected convergence (but the transform can be applied also to the shear angular PS, the two differing only by an ℓ -dependent prefactor) as:

$$\kappa = \frac{3\Omega_{m,0}H_0^2}{2c^2} \sum_i p_i \int_0^{\chi_i} d\chi \frac{S_k(\chi_i - \chi)S_k(\chi)}{S_k(\chi_i)} \frac{\delta_m(\chi)}{a(\chi)}, \quad (6.2)$$

where $S_k(\chi)$ has been defined in Eq. (1.2) and p_i are dimensionless weight coefficients. We now take three discrete source planes, $i, i-1, i-2$ at comoving distance $\chi_i > \chi_{i-1} > \chi_{i-2}$: the main idea is to find a set of weights p_i such that the contribution to the projected convergence for $\chi < \chi_{i-2}$ vanishes. Being this already true for $\chi > \chi_i$, because background lenses do not contribute to the signal, this would make the signal only sensitive to lenses in the narrow range $[\chi_{i-2}, \chi_i]$.

To do this, we can rewrite Eq. (6.2) in the form

$$\kappa = \frac{3\Omega_{m,0}H_0^2}{2c^2} \int_0^{\chi_H} d\chi \frac{\delta(\chi)}{a(\chi)} w(\chi), \quad (6.3)$$

χ_H being the comoving distance to the horizon and having defined the weight function

$$w(\chi) = \sum_{i, \chi_i > \chi} p_i \frac{S_k(\chi_i - \chi)S_k(\chi)}{S_k(\chi_i)} \quad (6.4)$$

$$= S_k^2(\chi) \left[\frac{1}{g_k(\chi)} \sum_{i, \chi_i > \chi} p_i - \sum_{i, \chi_i > \chi} \frac{p_i}{g_k(\chi_i)} \right], \quad (6.5)$$

with

$$g_k(\chi) \equiv \begin{cases} \frac{\tan(\sqrt{K}\chi)}{\sqrt{K}} & \text{for } K > 0, \\ \chi & \text{for } K = 0, \\ \frac{\tanh(\sqrt{-K}\chi)}{\sqrt{-K}} & \text{for } K < 0; . \end{cases} \quad (6.6)$$

The condition $w(\chi) = 0$ for $\chi \notin [\chi_{i-2}, \chi_i]$ then translates into the system of equations

$$\begin{cases} \sum_{i=1}^3 p_i = 0 \\ \sum_{i=1}^3 \frac{p_i}{g_k(\chi_i)} = 0, \end{cases} \quad (6.7)$$

which has the unique solution

$$\frac{p_2}{p_1} = \frac{c(2, 3, 1)}{c(1, 2, 3)}, \quad \frac{p_3}{p_1} = \frac{c(3, 1, 2)}{c(1, 2, 3)}, \quad (6.8)$$

having defined

$$c(i, j, k) = g_k(\chi_i) [g_k(\chi_j) - g_k(\chi_k)] . \quad (6.9)$$

The generalization to the case of an arbitrary number n of discrete planes κ_j requires taking linear combinations of the solutions (6.8):

$$\tilde{\kappa}_i = \mathcal{M}_{ij} \kappa_j \quad (6.10)$$

where the tilde denotes BNT-transformed quantities and the matrix \mathcal{M} , which we refer to as the BNT matrix (of size $\mathcal{N}_b \times \mathcal{N}_b$), is defined by:

$$\begin{aligned} \mathcal{M}_{ii} &= 1, \\ \mathcal{M}_{i,i-1} &= c(i-1, i-2, i) / c(i-2, i, i-1), \\ \mathcal{M}_{i,i-2} &= c(i-2, i-1, i) / c(i-2, i, i-1) . \end{aligned} \quad (6.11)$$

This gives the solution for $n-2$ of the new maps. To make the transformation invertible, we set

$$\mathcal{M}_{11} = 1, \quad \mathcal{M}_{21} = -1, \quad \mathcal{M}_{22} = 1 , \quad (6.12)$$

so that the first two maps, $\tilde{\kappa}_1$ and $\tilde{\kappa}_2$, are left unchanged. The normalization is set to have the diagonal elements equal to 1.

We can further generalize this result to the case of a continuous distribution $n_i(z)$ instead of a set of planes, by defining (Taylor et al., 2021a) (in the flat case):

$$B_i = \int_0^{z_H} dz' \frac{n_i(z')}{\chi(z')} , \quad (6.13)$$

where z_H is the redshift of the horizon (or the maximum distance available in the survey). In this way, we finally get the system:

$$\begin{cases} \sum_{j=i-2}^i \mathcal{M}_{ij} = 0 \\ \sum_{j=i-2}^i \mathcal{M}_{ij} B_j = 0 . \end{cases} \quad (6.14)$$

which again must be accompanied by the condition $\mathcal{M}_{ii} = 1$. From Eq. (6.13) we see that the BNT matrix is cosmology-dependent, since it involves an integral over the comoving distance; moreover, its computation requires an accurate characterization of the redshift distribution $n_i(z)$. We will nonetheless neglect this cosmology dependence, which Taylor et al. (2021a) found to have little impact on the results. The BNT matrix is shown for the specifics under consideration in this Chapter in Fig. 6.1.

Since the transform is linear, it can be applied to the kernels:

$$\tilde{\mathcal{K}}_i^L = \mathcal{M}_{ij} \mathcal{K}_j^L , \quad (6.15)$$

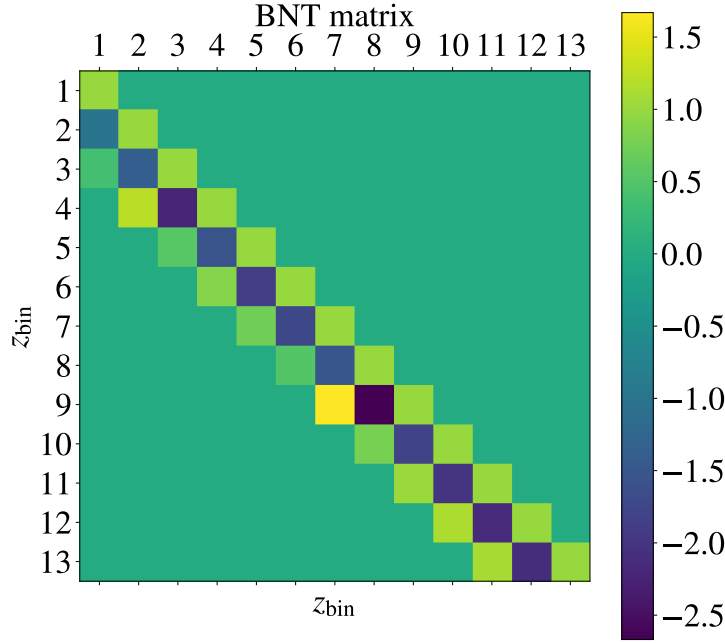


Figure 6.1. BNT matrix from the Flagship 2 N -body simulation.

or to the $C(\ell)$ s. For the 3×2 pt case, since the angular PS contain products of kernels, we have (Taylor et al., 2021b):

$$\begin{aligned}\tilde{C}_{ij}^{\text{LL}}(\ell) &= \mathcal{M}_{im} C_{mn}^{\text{LL}}(\ell) (\mathcal{M}^T)_{nj} \\ \tilde{C}_{ij}^{\text{GL}}(\ell) &= \delta_{im}^{\text{K}} C_{mn}^{\text{GL}}(\ell) (\mathcal{M}^T)_{nj} \\ \tilde{C}_{ij}^{\text{GG}}(\ell) &= \delta_{im}^{\text{K}} C_{mn}^{\text{GG}}(\ell) \delta_{nj}^{\text{K}} = C_{ij}^{\text{GG}}(\ell),\end{aligned}\tag{6.16}$$

where the Kronecker delta reflects the fact that the BNT is not applied to the galaxy kernels (which are already narrow). The angular PS transformed in this way have a very low sensitivity on the matter power spectrum above the chosen k scale, which allows mitigating the potential bias due to incorrect modelling while retaining the large-scale information when cutting the angular scales. Additionally, the $k - \ell$ correspondence can be further improved by taking into account a larger number of z bins (Vazsonyi et al., 2021).

Having defined the BNT matrix, we illustrate the procedure used to test the impact of these well-defined scale cuts, with a particular focus on the 3×2 pt FoM. This has been referred to “ k -cut” analysis in Taylor et al. (2018a).

6.2 Angular scale cuts

The above-mentioned Limber relation between physical and angular scale, after BNT-transforming the radial kernels, can be used as a way to define redshift-dependent angular scale cuts starting from a chosen k_{max} . Inverting the Limber

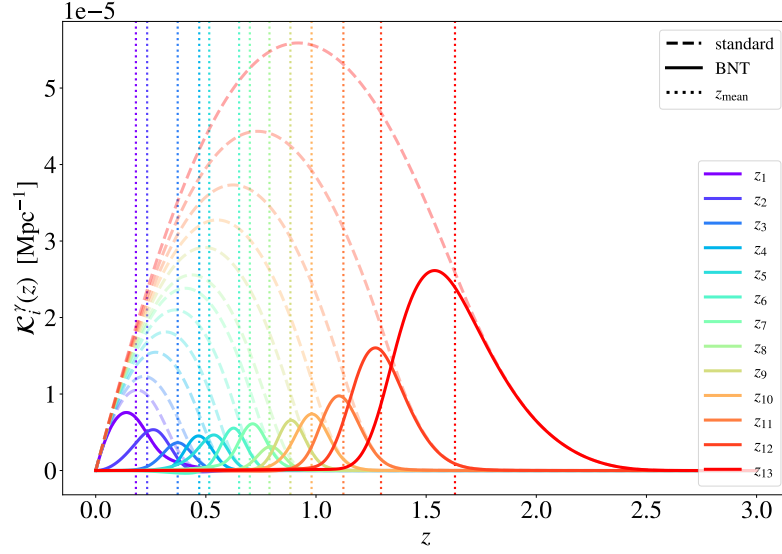


Figure 6.2. Standard (dashed lines) and BNT-transformed (solid lines) γ kernels. The latter have much narrower support and are clearly separated, allowing the typical bin distance $\chi(z_{\text{mean},i})$ (dotted vertical lines) to be well-defined.

relation, the corresponding maximum multipole is

$$\ell_{\text{max},i}^A = k_{\text{max}} \chi(z_i^A) - 1/2. \quad (6.17)$$

The redshift z_i , the “typical distance” to the i -th bin, can be defined as the mean of the kernel (as usual, A indicating the probe under consideration):

$$z_i^A = \frac{\int dz z \tilde{\mathcal{K}}_i^A(z)}{\int dz \tilde{\mathcal{K}}_i^A(z)}. \quad (6.18)$$

Figure 6.2 shows the z_i^L values; note that we compute these from the BNT-transformed γ kernel (Eq 3.77), excluding the IA kernel, which has a different expression (Eq 3.82). This is not optimal, but the contribution of IA is subdominant (Taylor et al., 2021b). From the plot, it’s clear how the BNT transform allows properly defining a typical distance for each kernel.

We can now proceed to compute redshift-dependent ℓ cuts, for each tomographic combination; for the cross-bin and cross-probe case ($z_i \neq z_j$, or $A \neq B$) we choose take the more conservative (lower) ℓ cut (Taylor et al., 2021b):

$$\ell_{\text{max},ij}^{AB} = \min\{k_{\text{max}} \chi(z_i^A) - 1/2, k_{\text{max}} \chi(z_j^B) - 1/2\}. \quad (6.19)$$

We can then proceed to *cut* (remove) the elements of the (BNT-transformed) data vector where $C_{ij}^{AB}(\ell > \ell_{\text{max},ij}^{AB})$. Of course, the same elements have to be removed from the (BNT-transformed) covariance matrix as well.

We can BNT-transform the covariance matrix either by computing it from the BNT-transformed $C(\ell)$ s (remembering to transform the noise spectra $N_{ij}^{AB}(\ell)$ as well), or by applying the BNT matrix to the covariance directly (cf. Appendix A of Vazsonyi et al. 2021):

$$\widetilde{\text{Cov}}_{abcd}^{ABCD}(\ell, \ell') = \mathcal{X}_{aebf}^{AB} \mathcal{X}_{cgdh}^{CD} \text{Cov}_{efgh}^{ABCD}(\ell, \ell'), \quad (6.20)$$

where

$$\chi_{AB}^{aebf} = \begin{cases} \mathcal{M}_{ae}\mathcal{M}_{bf}, & \text{if } AB = \text{LL} \\ \delta_{ae}^{\text{K}}\mathcal{M}_{bf}, & \text{if } AB = \text{GL} \\ \delta_{ae}^{\text{K}}\delta_{bf}^{\text{K}}, & \text{if } AB = \text{GG} \end{cases} \quad (6.21)$$

and the indices from a to h identify the redshift bin. We test that the two methods give consistent results to well below sub-percent agreement. We also validate our computation of the BNT by checking that the constraints from the FM analysis with and without applying the BNT, *when no scale cuts are imposed*, agree to excellent precision. This is because, in the computation of the FM (Eq. 5.13), the BNT matrix transforming the derivatives of the $C(\ell)$ s cancels out with the inverse BNT matrices transforming the covariance matrix: indicating with \mathbf{D} the vector of derivatives and taking as an example the WL probe, we have that

$$\begin{aligned} \tilde{F} &= \tilde{\mathbf{D}}^T \widetilde{\text{Cov}}^{-1} \tilde{\mathbf{D}} \\ &= (\mathcal{M}\mathbf{D})^T (\mathcal{M}^T \text{Cov} \mathcal{M})^{-1} \mathcal{M}\mathbf{D} \\ &= \mathbf{D}^T \mathcal{M}^T (\mathcal{M}^T)^{-1} \text{Cov}^{-1} \mathcal{M}^{-1} \mathcal{M}\mathbf{D} \\ &= \mathbf{D}^T \text{Cov}^{-1} \mathbf{D} = F. \end{aligned} \quad (6.22)$$

In the above equations, we assumed the covariance and the vector of derivatives to have size \mathcal{N}_{b} , but the same relation holds for every combination of multipoles and probes. We also leveraged the fact that the covariance is an invertible matrix and the (approximate) cosmology independence of the BNT matrix, which makes the operations of differentiation and BNT transform commutative. On the other hand, applying scale cuts does *not* commute with the BNT transform: this is the reason why the constraints in the k -cut case can differ from the standard ones.

To summarize, the steps taken for the k -cut procedure are the following:

1. Starting from an $n_i(z)$, solve the system of equations (6.14) to get the BNT matrix.
2. Apply the BNT transform to the γ kernels.
3. Use the (narrow) BNT-transformed kernels to compute the mean redshifts z_i^{L} . For GCph, we do the same using the standard galaxy kernels, to get z_i^{G} .
4. Choose a value for k_{max} .
5. Use the Limber relation through Eq. (6.19) to translate the k_{max} into redshift- and probe-dependent ℓ cuts (see Fig. 6.3).
6. BNT-transform the covariance matrix through Eq. (6.20) and the derivatives of the data vectors (in the same way as we transform the data vectors, i.e., through Eq. 6.16), which are the two ingredients entering the computation of the FM.
7. Cut the elements of the derivatives and covariance with $\ell_{ij}^{AB} > \ell_{\text{max},ij}^{AB}$.
8. Compute the Fisher matrix and the k -cut parameter constraints (and FoM).

The results of this procedure are presented in the next section.

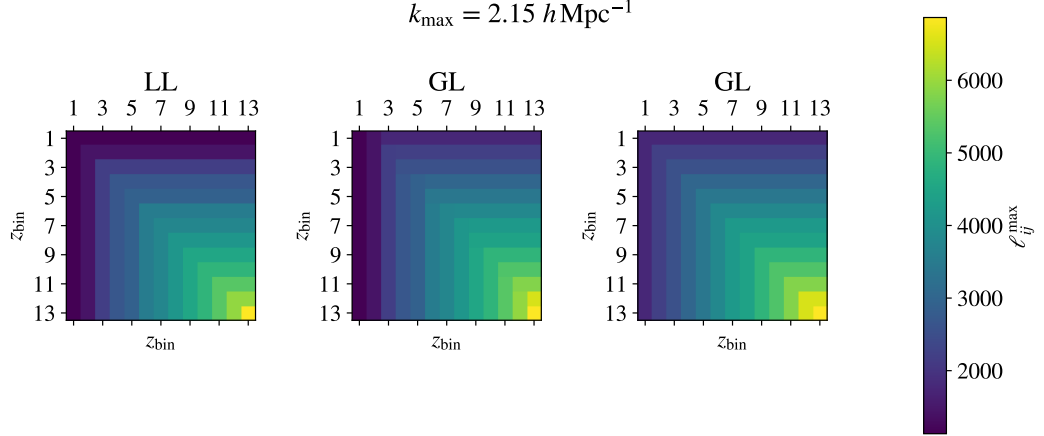


Figure 6.3. Redshift-dependent ℓ cuts for the different probe combinations, for the closest k_{\max} to the threshold found to get a FoM of 400 in the reference case (see text). Note that the GL matrix is not symmetric under the exchange of redshift indices, as can be seen from the definition (Eq. 6.19).

6.3 k -cut forecasts

Having presented the formalism of the BNT transform and the actual algorithm used to derive the redshift- and probe-dependent angular scale cuts, we can proceed to apply it in our FM analysis, using this time the latest ingredients and prescriptions concerning the modelling of the observables and systematics for the *Euclid* mission. As mentioned in the introduction, finding an optimal combination of these parameters is precisely the aim of the SPV exercise. This is necessarily a dynamic process since some of the survey specifications are being updated as the commissioning and performance verification phases of the mission unfold (see Fig. 3.12).

A number of elements differentiate the setup used here and the one described in the previous Chapters; these take into account the evolving specifications, and go in the direction of an increasingly realistic modelling. We list below the most notable changes:

- We update the reference model for the nonlinear PS to a more recent recipe, HMcode2020 (Mead et al., 2021), which amongst the other improvements allows taking into account baryonic effects in the form of gas expulsion by AGN feedback.
- We cut the redshift distribution below $z = 0.2$, due to the saturation of the detectors by luminous close sources.
- We include magnification bias in the GC angular PS (Sect. 3.1.5).
- We fit the linear galaxy bias and magnification bias computed from the Flagship 2 N -body simulation with a third-order polynomial, resulting in 4 free parameters for each of these two systematics instead of \mathcal{N}_b .

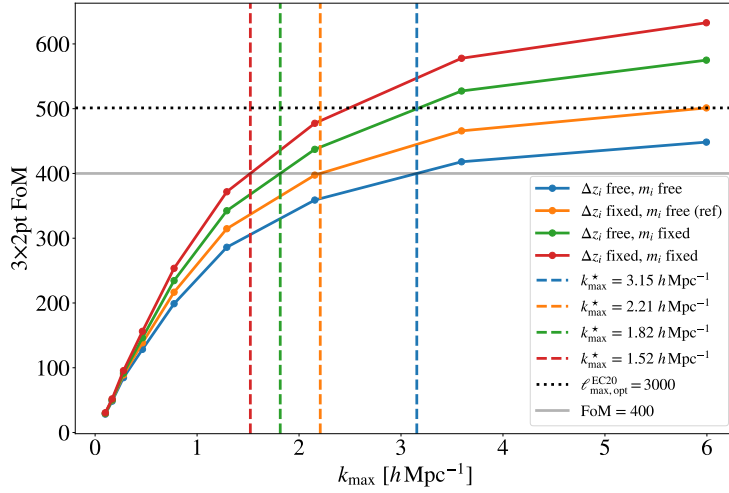


Figure 6.4. FoM vs. k_{\max} for the 3×2 pt case (solid coloured lines), using HMcode2020 with baryon corrections to model the nonlinear matter PS. The Red Book FoM (equals to 400, grey horizontal solid line) and the optimistic-case FoM (equals to 501, black horizontal dotted line) are also shown, allowing finding the minimum required k_{\max} (k_{\max}^* , colored vertical dashed lines) and to check the convergence of the results to the “hard-cut” case, respectively.

- We increase the number of redshift bins from 10 to 13, mainly to allow better tracking of the DE EoS time-dependence (hence a larger FoM). This has some drawbacks, such as a lower number of sources per bin, larger shot noise and number of bin-dependent nuisance parameters (shift in the mean of the redshift distribution Δz_i – Sect. 3.1.3 – and multiplicative shear bias – Sect. 3.2.7).

The forecasts obtained for the k -cut analysis with the reference setting described above are shown in Fig. 6.4 and Fig. 6.5.

In the first, we plot the FoM for the full 3×2 pt case as a function of k_{\max} , in 10 logarithmically-spaced steps from 10^{-1} to $10^1 h \text{ Mpc}^{-1}$; it should be noted that in this analysis we maintain the (optimistic) EC20 redshift-independent ℓ cuts. In fact, while the k -cut analysis allows properly taking into account the maximum scale at which we have reasonable belief in the *modelling*, additional cuts may be imposed in angular space due to other sources of uncertainty, such as the PSF. Therefore, the asymptotic behaviour of the curves is due to the fact that, for increasing k_{\max} values, increasingly more $\ell_{\max, ij}^{AB}$ values are above the redshift-independent, “hard” cut $\ell_{\max} = 3000$, reducing to the optimistic case in the standard analysis (equals to 501, dotted horizontal line, shown only for the reference case). In fact, we do not show the last of the 10 k_{\max} values, since convergence is reached already at $k_{\max} \simeq 6 h \text{ Mpc}^{-1}$. The different curves correspond to increasingly optimistic setups, either fixing or marginalizing over the nuisance parameters Δz_i and/or m_i ; for the latter set of parameters, a Gaussian prior of width $\sigma_m = 5 \times 10^{-5}$ is imposed. Now that the desired k_{\max} is properly accounted for in the harmonic-space analysis, we can find, for example, the minimum scale cut k_{\max}^* for which the target FoM = 400 requirement defined in the *Euclid* Red Book is met (albeit this is for the non-flat case, which we do not consider in this section). This value is shown, for

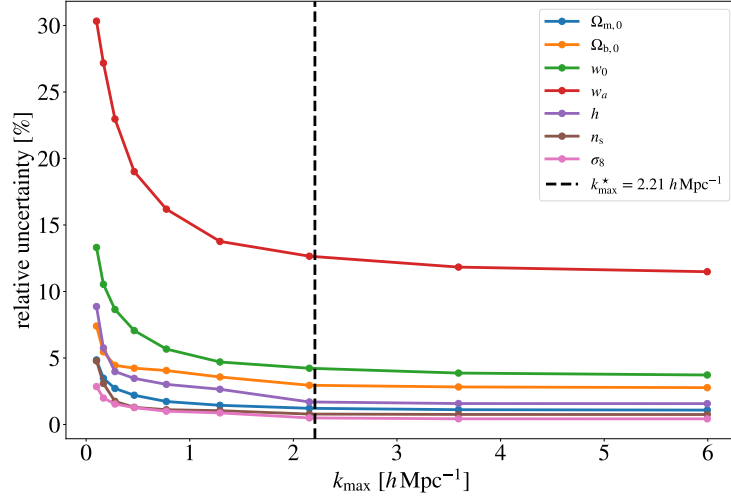


Figure 6.5. Relative 1σ uncertainty of the different cosmological parameters vs. k_{\max} , for the reference case (HMcode2020 with baryonic correction, Δz_i fixed, m_i free). The black vertical dashed line is the threshold cut k_{\max}^* .

the different setups, with colored vertical dashed lines, while the horizontal grey line denotes the target FoM. The reference case in the analysis is shown in orange, i.e., fixing only the mean z shifts parameters, since we expect their prior to be quite narrow. Note that marginalizing over multiplicative shear bias has a larger impact than marginalizing over Δz_i , even when imposing the nominal prior (blue vs. green curves). The dispersion between the different curves increases with k_{\max} , showing how the uncertainty increase caused by marginalization over these nuisance parameters is less important than the one caused by taking aggressive scale cuts.

The whole set of cosmological parameters is shown instead in Fig. 6.5, this time only for the reference case. The k_{\max}^* requirement found for the FoM can be used to obtain the expected relative uncertainties, which apart from w_a all lie in the range $[0.5, 4.2]\%$.

Another interesting possibility is to check the impact of different nonlinear prescriptions on the DE FoM. We explore five different options: the already introduced TakaBird and HMcode2020 (with and without baryonic corrections), plus the emulators Bacco (Aricò et al., 2021) and Euclid Emulator 2 (Euclid Collaboration: Knabenhans et al., 2021). The different results are shown in Fig. 6.6.

This time we gauge the spread between the FoM predicted by the different nonlinear prescriptions, with Δz_i fixed and m_i free, noting again that their difference vanishes for lower values of k_{\max} (because they agree in the linear regime). The measure chosen to quantify this spread is simply the standard deviation σ between the FoM of the different PS, at each k_{\max} . This dispersion is shown in the figure, along with their mean value (μ). We can then find the k_{\max}^* values for which the relative scatter (defined as σ/μ) drops below a certain threshold, in this case, 10%. The resulting wavenumber, $k_{\max}^* = 0.36 h \text{ Mpc}^{-1}$ is shown in light blue (dashed vertical line), and it is significantly lower than the minimum requirement found above to get to FoM = 400 (again, solid grey line). The requirement can be relaxed if we discard the

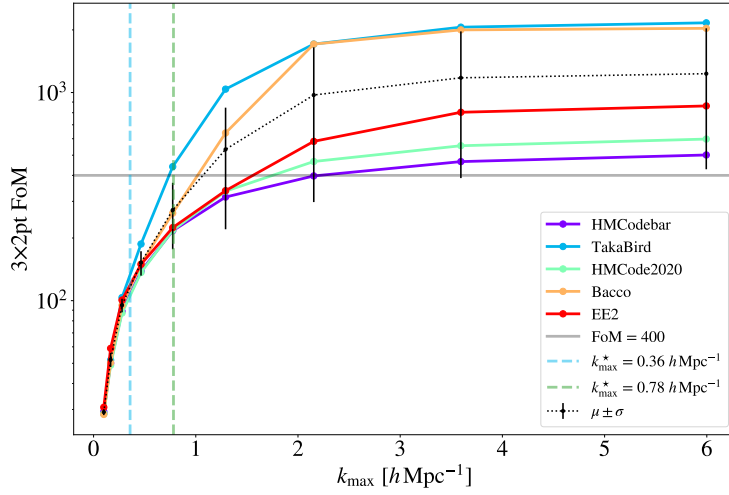


Figure 6.6. 3×2 pt FoM as a function of k_{\max} for the different nonlinear PS considered. The light green and light blue dashed vertical lines denote the maximum k_{\max}^* below which the dispersion between the different nonlinear recipes is lower than 10%, respectively excluding and including the **TakaBird** recipe. The black dotted line is the mean between the different values, with error bars given by the relative standard deviation. Note that these are made anisotropic by the logarithmic scale.

TakaBird recipe, which is the most outdated of the ones considered (see [Smith and Angulo 2019](#) for some recent improvements to the original recipe); removing it from the sample we obtain the less stringent vertical dashed light green line, corresponding to $0.78 h \text{ Mpc}^{-1}$, still too severe to reach the target FoM (for which a FoM of 233 is reached instead).

We note that [Taylor et al. 2021b](#) finds for a similar analysis (albeit using **EC20** specifications) a threshold to reach the Red Book FoM of $k_{\max}^* = 0.7 h \text{ Mpc}^{-1}$, which is in very good agreement with the value found here ($k_{\max}^* = 0.698 h \text{ Mpc}^{-1}$) for the **TakaBird** case, which is supposedly the nonlinear PS used in by the authors – being it the one chosen in **EC20**).

The difference between the curves in the figure is not necessarily representative, in principle, of the discrepancy between the power spectra themselves. Oftentimes the largest disagreement between the PS models and N -body simulations, hence the largest modelling uncertainty, is found precisely for the DE EoS parameters; this is the case for [Mead et al. 2021](#), for example. Moreover, the Figure of Merit also depends on the *correlation* between the different parameters: in fact, to compute it we need to marginalize the FM over *all* parameters but w_0 and w_a – see Eq. (5.20). Different recipes for the matter PS may give similar results as a function of k given the same cosmology while displaying different parameters’ covariance.

Figure 6.7 shows the ratio between the correlation matrices of the cosmological parameters obtained with **HMCode2020** including baryonic corrections and **TakaBird**, without scale cuts (the FMs having a sub-percent agreement with the case $k_{\max} \sim 6 h^{-1} \text{ Mpc}$). The correlation coefficient between w_0 and w_a differs by a factor of two, and many other combinations have larger discrepancies. The correlation between different parameters can be summarized by the figure of correlation (FoC; [Casas](#)

et al. 2017); a larger FoC indicates a higher correlation, which means a weaker constraining power. This can be defined as (EC20):

$$\text{FoC} = \sqrt{\det(\text{Corr}^{-1})} \quad (6.23)$$

A larger FoC will then, in general, correspond to a smaller FoM, and vice versa. The FoC is shown, in the context of the k -cuts analysis, in the left panel of Fig. 6.7; the Takabird nonlinear power spectrum seems to underpredict the parameters' correlation, although, as can be seen from the curve of Bacco, this is not enough to explain for the larger FoM. As seen in Fig. 6.6, the spread between the curves tends to decrease when cutting nonlinear scales, since the recipes agree in the linear regime.

All of these results have been obtained through a FM analysis, hence they allow gauging the differences in *constraining power* for the different cases presented. The other side of the coin is to assess the parameters *bias*. This is most likely also going to decrease when applying k cuts, both because of the larger uncertainties, as shown in Fig. 6.5, and because of the lower disagreement between the models themselves. This requires a full MCMC analysis (see Sect. 2.3) for each of the different scale cuts considered. We foresee this to be extremely numerically demanding, given the size of the data vector, the complexity of the model and the number of nuisance parameters.

Another interesting possibility to retain more information is to use the $\ell_{\text{max},ij}^{AB}$ matrix to redefine the upper edge of the last ℓ bin, instead of cutting it altogether. Then, the PS would have to be recomputed either at that value – i.e., $C_{ij}^{AB}(\ell_{\text{max},ij}^{AB})$, or at the centre of the newly defined, narrower bin. This would also require recomputing the covariance matrix (ideally, just the bins involved). Moreover, carrying out an analysis with a larger number of ℓ bins (or an unbinned one) would help in assessing the validity of taking wide bins, over the range of which large variations of relevant quantities (such as the comoving distance or the galaxy bias) occur.

Lastly, we note the potential of the BNT transform to mitigate the SSC, because the transformation of the highly-impacted lensing signal nulls the low- z support for many of the redshift bins. As discussed in Sect. 5.3.1, in this region the covariance of the background modes increases for $z \rightarrow 0$ because of the decrease in the effective volume. Moreover, removing nonlinear scales lessens the relative importance of non-Gaussian covariance. Preliminary results show this indeed to be the case; however, some numerical instabilities arise from the unstructured sparsity of the BNT-transformed GS covariance matrix. This induces larger uncertainties in its inversion, with the condition number being, e.g., 1.99×10^{18} at $k_{\text{max}} = 2.15h^{-1} \text{ Mpc}$, which results in an estimate for the precision of the matrix inversion of 4.42×10^2 – five orders of magnitude larger than what found in Sect. 5.1.6 for the non-BNT GS covariance.

Investigating potential solutions to this problem, as well as developing the other points listed above, will constitute the next steps of our work.

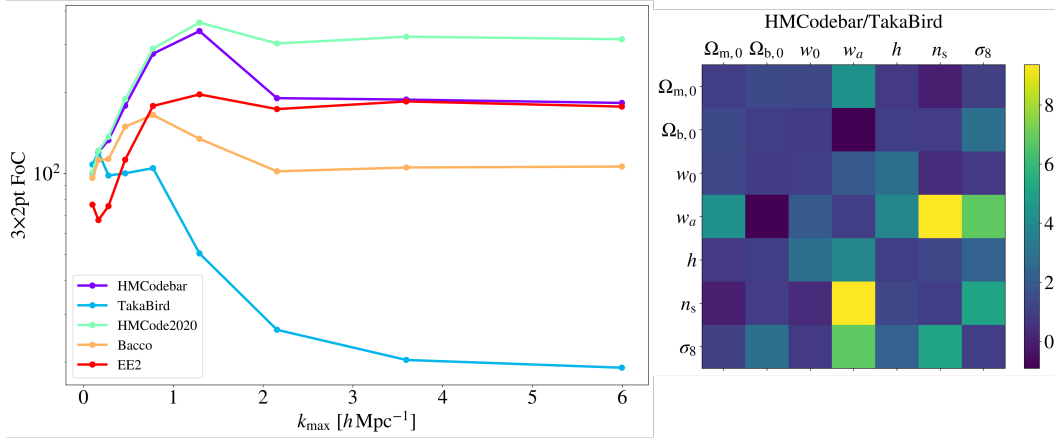


Figure 6.7. Left: Figure of Correlation as a function of k_{\max} for the different nonlinear recipes. As seen above, the results tend to converge for lower values of the k -cut, because the models agree on linear scales. Right: Ratio between the correlation matrices obtained from HMCode2020 including baryonic corrections and TakaBird.

6.4 Summary

The analysis presented in this Chapter, mainly based on the works of [Bernardeau et al. \(2014\)](#) and [Taylor et al. \(2021b\)](#), has shown the impact of the inclusion of scale cuts in the 3×2 pt forecast analysis. The procedure followed allows properly mapping such scale cuts to realistic, redshift- and probe-dependent ℓ cuts through BNT-transforming the cosmic shear signal. Small-scale modelling uncertainties, due to the limited understanding of nonlinear dark matter clustering and baryonic effects, can in this way be mitigated while retaining information from larger scales.

Our k -cut analysis characterized different quantities as a function of the cut k_{\max} : the FoM when fixing different sets of nuisance parameters and the marginalized uncertainties on the cosmological ones, as well as the agreement between nonlinear models and their correlation.

The study takes into account a large set of nuisance parameters (\mathcal{N}_b for multiplicative shear bias and shift in the mean $n_i(z)$, four for galaxy and magnification bias and two for intrinsic alignment, for a total of 36 parameters), a more realistic redshift distribution, a higher number of redshift bins, and more recent models (and tools) for the computation of the nonlinear matter PS. Some of these elements make the requirements on the FoM presented in [Laureijs et al. \(2011\)](#) difficult to meet, unless highly nonlinear scales ($k_{\max} \sim 2 h^{-1} \text{ Mpc}$) are included in the analysis. Our results show that this threshold is significantly above the scale at which the nonlinear models considered display consistent predictions ($k_{\max} \sim 0.4 - 0.8 h^{-1} \text{ Mpc}$ at the 10% level) on the DE FoM. The bias on the best-fit parameters is another potential issue to be explored, and that can again be mitigated through the use of the BNT transform.

The BNT will also be used in the analysis of the soon-to-arrive *Euclid* photometric data thanks to its development, to which I had the opportunity to participate, in the official code of the collaboration, CLOE.

Postface

THE main aim of the work presented in this thesis has been to improve the realism and flexibility of the *Euclid* forecast analysis, which allows propagating the impact of the different choices entering the modelling of the observables and survey specifications to the final uncertainties on the cosmological parameters. This makes it possible to optimize the survey to maximize the constraining power on the most important quantities of interest, such as the DE EoS parameters. Several different possibilities have been explored in this way, mainly within the context of the assessment of the impact of super-sample covariance and scale cuts, with a particular focus on the 3×2 pt analysis, which provides the majority of *Euclid* constraining power.

We find the inclusion of SSC, computed with PySSC with the approximations presented in Chap. 4 to be important for an accurate estimate of the precision of the measurements. We quantify its impact as the ratio between the 1σ FM uncertainties including and neglecting this covariance term, and find it causes significant degradation of the WL constraints and the 3×2 pt FoM (up to 38% in the EC20 optimistic case). GCph is less affected because of the lower probe response and of the reduced contribution that the majority of redshift bins receive from the low- z region, where the effective survey volume decreases and the covariance of the background modes increases. The results are in broad agreement with the recent works of Barreira et al. (2018a) and Upham et al. (2022), which have some differences in the setup.

The impact has been gauged for different survey settings, namely varying the number of redshift and multipole bins and broadening both the cosmological and nuisance parameters space by letting Ω_{DE} and the multiplicative shear bias parameters free to vary. Variations in the redshift binning have almost no effect on the strength of SSC, while marginalization over multiplicative shear bias significantly reduces its importance for WL, at the cost of overall weaker constraints. This is because SSC is degenerate with the amplitude of the signal, as are multiplicative shear and galaxy bias parameters. We also quantified the requirements on the prior information to be added on galaxy bias and multiplicative shear bias to recover the Gaussian FoM, finding them to be quite stringent (at the percent-level on galaxy bias, when applying the fiducial prior with $\sigma_m = 5 \times 10^{-5}$ on the multiplicative shear bias).

The second part of our work focused on the investigation of the BNT transform as a powerful tool to implement scale cuts, and in this way to mitigate modelling uncertainties which would potentially degrade and bias the final measurements. The framework used is flexible and does not introduce significant overhead to the analysis (apart from the necessity to loop over the k_{max} values and to apply the BNT

transform), since the data vectors and covariance matrix are computed once and then cut in different ways. In this way, the requirement on the maximum scale to include in the analysis as a function of the desired FoM, and other interesting points such as the agreement between different nonlinear models, can be investigated. This is likely to become a standard in the analysis of the upcoming photometric data, because of the significant theoretical uncertainties still affecting the modelling of the LSS observables on small scales.

Most of the tools and procedures developed to compute the forecasts presented here are ready to be applied to the analysis of the actual data, allowing us to finally witness the real power of the *Euclid* mission.

Appendix A

High order bias from halo model

As described in Sect. 5.1.4, the second-order bias $b_{(2)}(z)$ has been estimated using the halo model. In the following Appendix, we provide further details on the input quantities, and how we set the relevant parameters.

A key role is played by the halo mass function $\Phi_{\text{MF}}(M, z)$, which we model as

$$\Phi_{\text{MF}}(M, z) = \frac{\bar{\rho}_{\text{m}}}{M} f(\nu) \frac{d \ln \sigma^{-1}}{dM}, \quad (\text{A.1})$$

with M the halo mass, $\bar{\rho}_{\text{m}}$ the mean matter density, $\nu = \delta_c / \sigma(M, z)$, $\delta_c = 1.686$ the critical overdensity for collapse, and $\sigma(M, z)$ the variance of linear perturbation smoothed with a top-hat filter of radius $R = [3M / (4\pi\bar{\rho}_{\text{m}})]^{1/3}$. We follow [Tinker et al. \(2010\)](#), setting

$$f(\nu) = \mathcal{N}_{\text{MF}} \left[1 + (\beta_{\text{MF}} \nu)^{-2\phi_{\text{MF}}} \right] \nu^{2\eta_{\text{MF}}} \exp \left(-\gamma_{\text{MF}} \nu^2 / 2 \right), \quad (\text{A.2})$$

where \mathcal{N}_{MF} is a normalisation constant, and the halo mass function fitting parameters β_{MF} , η_{MF} , γ_{MF} and ϕ_{MF} – not to be confused with $\Phi_{\text{MF}}(M, z)$ – scale with redshift as illustrated in Eqs. (9–13) of the above-mentioned paper.

The other quantity needed is the average number of galaxies hosted by a halo of mass M at redshift z . This is given by

$$\langle N|M \rangle(M) = N_{\text{cen}}(M) [1 + N_{\text{sat}}(M)] , \quad (\text{A.3})$$

where $N_{\text{cen}}(M, z)$ and $N_{\text{sat}}(M, z)$ account for the contributions of central and satellite galaxies, respectively. We model these terms as in [White et al. \(2011\)](#)

$$N_{\text{cen}}(M) = \frac{1}{2} \left\{ 1 + \text{erfc} \left[\frac{\ln(M/M_{\text{cut}})}{\sqrt{2}\sigma_c} \right] \right\} , \quad (\text{A.4})$$

$$N_{\text{sat}}(M) = \begin{cases} 0 & M < \kappa_s M_{\text{cut}} \\ \left(\frac{M - \kappa_s M_{\text{cut}}}{M_1} \right)^{\alpha_s} & M \geq \kappa_s M_{\text{cut}}, \end{cases} \quad (\text{A.5})$$

with fiducial parameter values

$$\{\log_{10}(M_{\text{cut}}/M_{\odot}), \log_{10}(M_1/M_{\odot}), \sigma_c, \kappa_s, \alpha_s\} = 13.04, 14.05, 0.94, 0.93, 0.97 , \quad (\text{A.6})$$

M_{\odot} being the mass of the Sun. These values give the best fit to the clustering of massive galaxies at $z \sim 0.5$ as measured from the first semester of BOSS data. It is, however, expected that they are redshift-dependent although the precise scaling with z also depends on the galaxy population used as a tracer. We, therefore, adjust them so that the predicted galaxy bias matches, at each given redshift, our measured values from the Flagship simulation. Since, for each z , we have a single observable quantity, we can not fit all parameters. On the contrary, we fix all of them but M_{cut} to their fiducial values and use Eq. (5.8) to compute the bias as a function of M_{cut} . We then solve with respect to M_{cut} repeating this procedure for each redshift bin. We then linearly interpolate these values to get M_{cut} as a function of z , and use it to compute $b_{(2)}(z)$. Although quite crude, we have verified that changing the HOD parameter to be adjusted (e.g., using σ_c or M_1) has a negligible impact on the predicted $R^{\text{gm}}(\ell)$ and $R^{\text{gg}}(\ell)$.

Appendix B

Appendix B: Details of the code validation

In the following Appendix, we provide an overview of the steps undertaken to compare and validate the codes used in this work, and some of the lessons learnt in the process.

To compute and validate the results we adopt the scheme sketched in Fig. B.1, which highlights the dependency of each main element of the forecast computation on the others. In particular, we have that:

1. The 1σ constraints are obtained from the FM through Eq. (5.17), and the FM is built in turn from the (inverse) covariance matrix and the derivatives of the angular PS $C_{ij}^{AB}(\ell)$ as indicated in Eq. (5.13).
2. The Gaussian covariance depends on the $C_{ij}^{AB}(\ell)$ through Eq. (5.11) (and the noise PS, Eq. 5.12). The SSC also depends on the $C_{ij}^{AB}(\ell)$, with the added contribution of the $\mathcal{R}_{ij}^{AB}(\ell)$ terms and the output of the PySSC module, the S_{ijkl} matrix – following Eq. (4.97).
3. The $C_{ij}^{AB}(\ell)$ are constructed by convolving the (nonlinear) matter PS with the lensing and galaxy weight functions, as in Eq. (4.91). The S_{ijkl} matrix also depends on the weight functions (see Eq. 4.98), which are in fact the main external input needed by PySSC, and on the *linear* matter PS through the $\sigma^2(z_1, z_2)$ term (Eq. 4.85, modulo the $1/(4\pi)^2$ factor). It is to be noted, however, that PySSC computes this PS internally, needing only the specification of a dictionary of cosmological parameters with which to call the Boltzmann solver CLASS through the Python wrapper `classy`. This means that we also have to make sure that the fiducial value of the parameters used to compute the PS of Eq. (4.91) are the same ones passed to PySSC (this time to compute the linear PS), in order to work with the same cosmology.

While to compute the constraints we follow the scheme from right to left, starting from the basic ingredients to arrive at the final result, the general trend of the validation is the opposite: we begin by comparing the final results, then work our way back whenever we find disagreement.

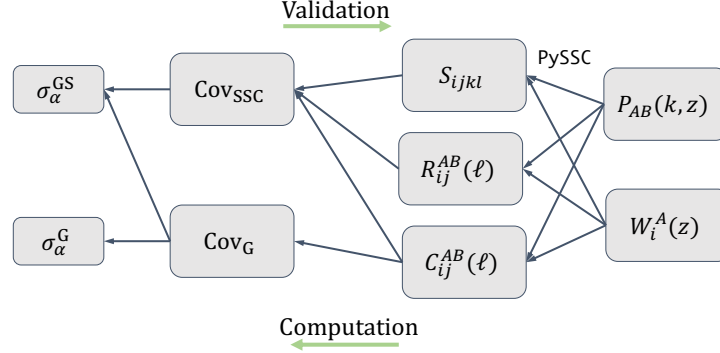


Figure B.1. Some of the most important elements examined in the comparison. The arrows show the ordering followed to produce the parameters constraints, which is opposite to the one followed to validate the code. The derivatives of the PS with respect to the cosmological parameters, entering the final step of the computation, are not shown.

We then start the comparison from the σ_α . If a discrepancy larger than 10% is found, we check the quantities they depend on, which in this case are the covariance matrices (see Eq. 5.13). If these agree, we check the codes directly. If these disagree, we iterate the process by checking the subsequent element in the scheme (in this case the S_{ijkl} matrix and the $C_{ij}^{AB}(\ell)$), until agreement is found. Essentially, this means that the disagreement in the outputs of the codes at each step can either come from the inputs, or from the codes themselves. Once the cause of the discrepancy is found and fixed, the computation is repeated and the process can start again.

The pipelines under comparison are both written in the **Python** language. One of them requires as external inputs the weight functions, the angular PS $C_{ij}^{AB}(\ell)$ and their derivatives with respect to the cosmological parameters; whilst the other produces these through the use of **CosmoSIS**, and hence needs no external inputs but the vectors of fiducial cosmological and nuisance parameters. For the reader wishing to repeat the validation, we list below some of the lessons learnt in the code comparison process.

- **PySSC** needs as input the WL and GCph kernels of Eqs. (3.88) and (3.11), as well as their argument, the redshift values. The code then uses this redshift array to perform the necessary integrals in dV through Simpson's rule. The user is responsible for sampling the kernels on a sufficiently fine z grid ($\mathcal{O}(10^4)$ values have been found to be sufficient in the present case) to make sure these integrals are performed accurately.
- The latest version of **PySSC** accepts a **convention** parameter. This specifies whether the kernels are in the form used in **LG19** (i.e., $K_i^A(z)$; **convention** = 0) or the one prescribed in **EC20** (i.e., $\mathcal{K}_i^A(z)$; **convention** = 1). The two differ by a $1/\chi^2(z)$ factor, as shown in Eq. (5.4). Passing the kernels in the **EC20** form without changing the parameter's value from 0 – the default – to 1 will obviously yield incorrect results.
- The ordering of the S_{ijkl} matrix's elements depends on the ordering chosen when passing the input kernels to **PySSC** – whether $K_i^L(z)$ first and $K_i^G(z)$

second or vice versa. This must be kept in mind when implementing Eq. (4.97).

- The GCph constraints can show a discrepancy greater than 10% for the dark energy equation of state parameters w_0 and w_a even when the corresponding covariance is found to be in good agreement. This discrepancy is due to GCph being less numerically stable because of the lower constraining power compared to the other probes, and because the bias model considered has a strong degeneracy with σ_8 , making the numerical derivatives unstable (see e.g., [Euclid Collaboration: Casas et al., 2023](#)). Since this is a known issue, not coming from the SSC computation, and the covariance matrices and angular PS show good agreement, we choose to overcome the problem by using, for GCph, one code to compute both sets of parameter constraints (that is, we run one FM evaluation code with as input the covariance matrices from both groups).

Appendix C

Slowly varying response approximation for broad kernels

At the time of writing, all of the publicly available codes to compute the SSC term adopt some approximations. On one side, PySSC adopts the slowly varying response approximation, which has been tested, as mentioned in Sect. 4.4, for GCph, obtaining good agreement against the full computation up to small angular scales, as well as for cluster number counts.

The two other codes are the Core Cosmology Library (CCL - Chisari et al. 2019a) and CosmoLike (Krause and Eifler, 2017), both of which implement the recipe given in the latter paper. This also adopts an approximation, dubbed the “KE approximation”: this consists of considering $\sigma^2(z_1, z_2)$ as a Dirac delta function at $z_1 = z_2$, so that the double redshift integral collapses into a single integral; this speeds up the code considerably, although not as much as the LG19 approximation. Lacasa et al. (2018) argued the latter to underestimate the full SSC less than the KE approximation for cluster number counts, and in general for probes with narrow radial kernels. Besides its speed, PySSC was mainly chosen for the full control over the observables and the choice of the probe responses, which allowed us to use the measurements from the separate universe technique.

As mentioned in Sect. 5.3.1, our results are in broad agreement with the ones from Barreira et al. (2018a) and Upham et al. (2022) (computed with CosmoLike), which adopts the closest setup to the *Euclid* settings used in this work. However, significant differences still persist; the use of pseudo- C_ℓ s or of a reduced parameter space, just to name a few. An in-depth comparison between the different codes is currently undergoing: in Fig. C.1 we show the marginalised 1σ uncertainties for the WL probe, for the Gaussian and Gaussian + SSC covariance matrix. The absolute value of the percent discrepancy w.r.t. the mean of the Gauss + SSC constraints computed with the two different codes is shown in red; in general the agreement is quite good, except for σ_8 and $\Omega_{m,0}$. To explore this issue more in detail, we are currently developing a new code to compute the SSC term without any of the above-mentioned approximations, the results of which will be shared in a forthcoming publication.

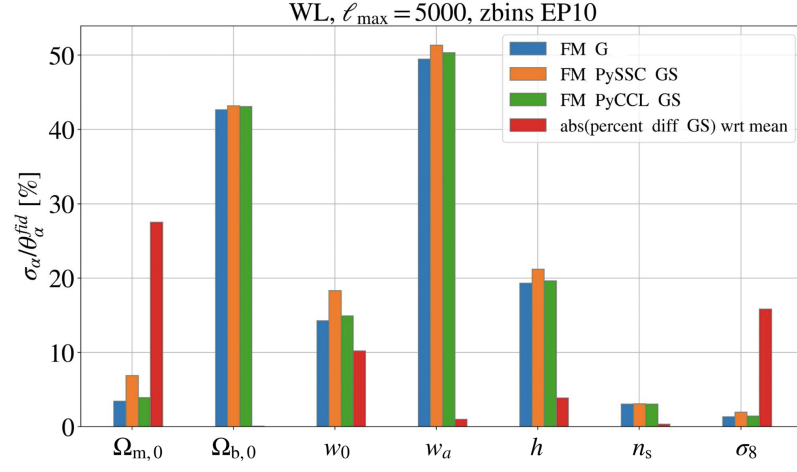


Figure C.1. Gauss + SSC constraints for WL (10 equipopulated redshift bins), computed with PySSC and PyCCL. The percent difference with respect to the mean of the Gauss. + SSC constraints is shown in red; a marginally significant difference (10% being the threshold for agreement considered in this work) is still present on the most affected parameters.

Appendix D

Multipole binning

We bin the ℓ space according to the following procedure: the ℓ_k values, where $k = 1, \dots, \mathcal{N}_\ell$, are the centers of $\mathcal{N}_\ell + 1$ logarithmically equispaced values, λ_k , which act as the edges of the \mathcal{N}_ℓ bins:

$$\ell_k = \text{dex} \left[\left(\lambda_k^- + \lambda_k^+ \right) / 2 \right] , \quad (\text{D.1})$$

with $\text{dex}(x) = 10^x$, $(\lambda_k^-, \lambda_k^+) = (\lambda_k, \lambda_{k+1})$, and

$$\lambda_k = \lambda_{\min}^{\text{XC}} + (k - 1)(\lambda_{\max}^{\text{XC}} - \lambda_{\min}^{\text{XC}}) / \mathcal{N}_\ell , \quad (\text{D.2})$$

being

$$\left\{ \lambda_{\min}^{\text{XC}}, \lambda_{\max}^{\text{XC}} \right\} = \left\{ \log_{10}(\ell_{\min}^{\text{XC}}), \log_{10}(\ell_{\max}^{\text{XC}}) \right\} . \quad (\text{D.3})$$

In order to compute the Gaussian covariance, we also need the width of the bin, which will simply be

$$\Delta \ell_k = \text{dex}(\lambda_{k+1}) - \text{dex}(\lambda_k) , \quad (\text{D.4})$$

so that $\Delta \ell_k$ is not the same for all bins, since the bins are logarithmically – and not linearly – equispaced.

Bibliography

- T. M. C. Abbott, M. Agüena, A. Alarcon, S. Allam, O. Alves, A. Amon, F. Andrade-Oliveira, J. Annis, S. Avila, D. Bacon, E. Baxter, K. Bechtol, M. R. Becker, G. M. Bernstein, S. Bhargava, et al. Dark Energy Survey Year 3 results: Cosmological constraints from galaxy clustering and weak lensing. *Phys. Rev. D*, volume 105(2):023520, 2022. doi:[10.1103/PhysRevD.105.023520](https://doi.org/10.1103/PhysRevD.105.023520).
- H. Aihara, N. Arimoto, R. Armstrong, S. Arnouts, N. A. Bahcall, S. Bickerton, J. Bosch, K. Bundy, P. L. Capak, J. H. H. Chan, M. Chiba, J. Coupon, E. Egami, M. Enoki, F. Finet, et al. The Hyper Suprime-Cam SSP Survey: Overview and survey design. *PASJ*, volume 70:S4, 2018. doi:[10.1093/pasj/psx066](https://doi.org/10.1093/pasj/psx066).
- A. Albrecht, G. Bernstein, R. Cahn, W. L. Freedman, J. Hewitt, W. Hu, J. Huth, M. Kamionkowski, E. W. Kolb, L. Knox, J. C. Mather, S. Staggs, and N. B. Suntzeff. Report of the Dark Energy Task Force. *astro-ph/0609591*, 2006. doi:[10.48550/arXiv.astro-ph/0609591](https://doi.org/10.48550/arXiv.astro-ph/0609591).
- L. Amendola, S. Appleby, A. Avgoustidis, D. Bacon, T. Baker, M. Baldi, N. Bartolo, A. Blanchard, C. Bonvin, S. Borgani, E. Branchini, C. Burrage, S. Camera, C. Carbone, L. Casarini, et al. Cosmology and fundamental physics with the Euclid satellite. *Living Reviews in Relativity*, volume 21(1):2, 2018. doi:[10.1007/s41114-017-0010-3](https://doi.org/10.1007/s41114-017-0010-3).
- G. Aricò, R. E. Angulo, S. Contreras, L. Ondaro-Mallea, M. Pellejero-Ibañez, and M. Zennaro. The BACCO simulation project: a baryonification emulator with neural networks. *MNRAS*, volume 506(3):4070–4082, 2021. doi:[10.1093/mnras/stab1911](https://doi.org/10.1093/mnras/stab1911).
- M. Asgari, A. J. Mead, and C. Heymans. The halo model for cosmology: a pedagogical review. *arXiv e-prints*, arXiv:2303.08752, 2023. doi:[10.48550/arXiv.2303.08752](https://doi.org/10.48550/arXiv.2303.08752).
- B. Audren, J. Lesgourgues, S. Bird, M. G. Haehnelt, and M. Viel. Neutrino masses and cosmological parameters from a Euclid-like survey: Markov Chain Monte Carlo forecasts including theoretical errors. *J. Cosmology Astropart. Phys.*, volume 2013(1):026, 2013. doi:[10.1088/1475-7516/2013/01/026](https://doi.org/10.1088/1475-7516/2013/01/026).
- J. M. Bardeen. Gauge-invariant cosmological perturbations. *Phys. Rev. D*, volume 22(8):1882–1905, 1980. doi:[10.1103/PhysRevD.22.1882](https://doi.org/10.1103/PhysRevD.22.1882).
- A. Barreira, E. Krause, and F. Schmidt. Accurate cosmic shear errors: do we need ensembles of simulations? *J. Cosmology Astropart. Phys.*, volume 2018(10):053, 2018a. doi:[10.1088/1475-7516/2018/10/053](https://doi.org/10.1088/1475-7516/2018/10/053).

- A. Barreira, E. Krause, and F. Schmidt. Complete super-sample lensing covariance in the response approach. *J. Cosmology Astropart. Phys.*, volume 2018(6):015, 2018b. doi:[10.1088/1475-7516/2018/06/015](https://doi.org/10.1088/1475-7516/2018/06/015).
- A. Barreira, T. Lazeyras, and F. Schmidt. Galaxy bias from forward models: linear and second-order bias of IllustrisTNG galaxies. *J. Cosmology Astropart. Phys.*, volume 2021(8):029, 2021. doi:[10.1088/1475-7516/2021/08/029](https://doi.org/10.1088/1475-7516/2021/08/029).
- A. Barreira, D. Nelson, A. Pillepich, V. Springel, F. Schmidt, R. Pakmor, L. Hernquist, and M. Vogelsberger. Separate Universe simulations with IllustrisTNG: baryonic effects on power spectrum responses and higher-order statistics. *MNRAS*, volume 488(2):2079–2092, 2019. doi:[10.1093/mnras/stz1807](https://doi.org/10.1093/mnras/stz1807).
- M. Bartelmann and P. Schneider. Weak gravitational lensing. *Phys. Rep.*, volume 340(4-5):291–472, 2001. doi:[10.1016/S0370-1573\(00\)00082-X](https://doi.org/10.1016/S0370-1573(00)00082-X).
- A. E. Bayer, J. Liu, R. Terasawa, A. Barreira, Y. Zhong, and Y. Feng. Super-sample covariance of the power spectrum, bispectrum, halos, voids, and their cross-covariances. *arXiv:2210.15647*, 2022. doi:[10.48550/arXiv.2210.15647](https://doi.org/10.48550/arXiv.2210.15647).
- J. J. Bennett, G. Buldgen, P. F. de Salas, M. Drewes, S. Gariazzo, S. Pastor, and Y. Y. Y. Wong. Towards a precision calculation of the effective number of neutrinos N_{eff} in the Standard Model. Part II. Neutrino decoupling in the presence of flavour oscillations and finite-temperature QED. *J. Cosmology Astropart. Phys.*, volume 2021(4):073, 2021. doi:[10.1088/1475-7516/2021/04/073](https://doi.org/10.1088/1475-7516/2021/04/073).
- F. Bernardeau, S. Colombi, E. Gaztañaga, and R. Scoccimarro. Large-scale structure of the Universe and cosmological perturbation theory. *Phys. Rep.*, volume 367(1-3):1–248, 2002. doi:[10.1016/S0370-1573\(02\)00135-7](https://doi.org/10.1016/S0370-1573(02)00135-7).
- F. Bernardeau, T. Nishimichi, and A. Taruya. Cosmic shear full nulling: sorting out dynamics, geometry and systematics. *MNRAS*, volume 445(2):1526–1537, 2014. doi:[10.1093/mnras/stu1861](https://doi.org/10.1093/mnras/stu1861).
- S. Bird, M. Viel, and M. G. Haehnelt. Massive neutrinos and the non-linear matter power spectrum. *MNRAS*, volume 420(3):2551–2561, 2012. doi:[10.1111/j.1365-2966.2011.20222.x](https://doi.org/10.1111/j.1365-2966.2011.20222.x).
- D. Blas, J. Lesgourgues, and T. Tram. The Cosmic Linear Anisotropy Solving System (CLASS). Part II: Approximation schemes. *J. Cosmology Astropart. Phys.*, volume 2011(7):034, 2011. doi:[10.1088/1475-7516/2011/07/034](https://doi.org/10.1088/1475-7516/2011/07/034).
- M. Bolzonella, J. M. Miralles, and R. Pelló. Photometric redshifts based on standard SED fitting procedures. *A&A*, volume 363:476–492, 2000. doi:[10.48550/arXiv.astro-ph/0003380](https://doi.org/10.48550/arXiv.astro-ph/0003380).
- J. R. Bond and A. S. Szalay. The collisionless damping of density fluctuations in an expanding universe. *ApJ*, volume 274:443–468, 1983. doi:[10.1086/161460](https://doi.org/10.1086/161460).
- S. Bridle and L. King. Dark energy constraints from cosmic shear power spectra: impact of intrinsic alignments on photometric redshift requirements. *New Journal of Physics*, volume 9(12):444, 2007. doi:[10.1088/1367-2630/9/12/444](https://doi.org/10.1088/1367-2630/9/12/444).

- S. Camera, I. Harrison, A. Bonaldi, and M. L. Brown. SKA weak lensing - III. Added value of multiwavelength synergies for the mitigation of systematics. *MNRAS*, volume 464(4):4747–4760, 2017. doi:[10.1093/mnras/stw2688](https://doi.org/10.1093/mnras/stw2688).
- F. Capozzi, E. Di Valentino, E. Lisi, A. Marrone, A. Melchiorri, and A. Palazzo. The unfinished fabric of the three neutrino paradigm. *arXiv e-prints*, arXiv:2107.00532, 2021. doi:[10.48550/arXiv.2107.00532](https://doi.org/10.48550/arXiv.2107.00532).
- S. Casas, M. Kunz, M. Martinelli, and V. Pettorino. Linear and non-linear Modified Gravity forecasts with future surveys. *Physics of the Dark Universe*, volume 18:73–104, 2017. doi:[10.1016/j.dark.2017.09.009](https://doi.org/10.1016/j.dark.2017.09.009).
- M. Chevallier and D. Polarski. Accelerating Universes with Scaling Dark Matter. *Int. J. Mod. Phys. D*, volume 10(2):213–223, 2001. doi:[10.1142/S0218271801000822](https://doi.org/10.1142/S0218271801000822).
- N. E. Chisari, D. Alonso, E. Krause, C. D. Leonard, P. Bull, J. Neveu, A. S. Villarreal, S. Singh, T. McClintock, J. Ellison, Z. Du, J. Zuntz, A. Mead, S. Joudaki, C. S. Lorenz, et al. Core Cosmology Library: Precision Cosmological Predictions for LSST. *ApJS*, volume 242(1):2, 2019a. doi:[10.3847/1538-4365/ab1658](https://doi.org/10.3847/1538-4365/ab1658).
- N. E. Chisari, A. J. Mead, S. Joudaki, P. G. Ferreira, A. Schneider, J. Mohr, T. Tröster, D. Alonso, I. G. McCarthy, S. Martin-Alvarez, J. Devriendt, A. Slyz, and M. P. van Daalen. Modelling baryonic feedback for survey cosmology. *The Open Journal of Astrophysics*, volume 2(1):4, 2019b. doi:[10.21105/astro.1905.06082](https://doi.org/10.21105/astro.1905.06082).
- N. E. Chisari, M. L. A. Richardson, J. Devriendt, Y. Dubois, A. Schneider, A. M. C. Le Brun, R. S. Beckmann, S. Peirani, A. Slyz, and C. Pichon. The impact of baryons on the matter power spectrum from the Horizon-AGN cosmological hydrodynamical simulation. *MNRAS*, volume 480(3):3962–3977, 2018. doi:[10.1093/mnras/sty2093](https://doi.org/10.1093/mnras/sty2093).
- D. Clowe, M. Bradač, A. H. Gonzalez, M. Markevitch, S. W. Randall, C. Jones, and D. Zaritsky. A Direct Empirical Proof of the Existence of Dark Matter. *ApJ*, volume 648(2):L109–L113, 2006. doi:[10.1086/508162](https://doi.org/10.1086/508162).
- A. Cooray and W. Hu. Power Spectrum Covariance of Weak Gravitational Lensing. *ApJ*, volume 554(1):56–66, 2001. doi:[10.1086/321376](https://doi.org/10.1086/321376).
- C. Cragg, C. A. J. Duncan, L. Miller, and D. Alonso. Propagating spatially varying multiplicative shear bias to cosmological parameter estimation for stage-IV weak-lensing surveys. *MNRAS*, volume 518(4):4909–4920, 2023. doi:[10.1093/mnras/stac3324](https://doi.org/10.1093/mnras/stac3324).
- R. G. Crittenden, P. Natarajan, U.-L. Pen, and T. Theuns. Discriminating Weak Lensing from Intrinsic Spin Correlations Using the Curl-Gradient Decomposition. *ApJ*, volume 568(1):20–27, 2002. doi:[10.1086/338838](https://doi.org/10.1086/338838).
- M. Crocce, A. J. Ross, I. Sevilla-Noarbe, E. Gaztanaga, J. Elvin-Poole, S. Avila, A. Alarcon, K. C. Chan, N. Banik, J. Carretero, E. Sanchez, W. G. Hartley, C. Sánchez, T. Giannantonio, R. Rosenfeld, et al. Dark Energy Survey year 1

- results: galaxy sample for BAO measurement. *MNRAS*, volume 482(2):2807–2822, 2019. doi:[10.1093/mnras/sty2522](https://doi.org/10.1093/mnras/sty2522).
- M. Cropper, S. Pottinger, S. Niemi, R. Azzollini, J. Denniston, M. Szafraniec, S. Awan, Y. Mellier, M. Berthe, J. Martignac, C. Cara, A. M. Di Giorgio, A. Sciortino, E. Bozzo, L. Genolet, et al. VIS: the visible imager for Euclid. In H. A. MacEwen, G. G. Fazio, M. Lystrup, N. Batalha, N. Siegler, and E. C. Tong, editors, *Space Telescopes and Instrumentation 2016: Optical, Infrared, and Millimeter Wave*, volume 9904 of *Society of Photo-Optical Instrumentation Engineers (SPIE) Conference Series*, page 99040Q. 2016. doi:[10.1117/12.2234739](https://doi.org/10.1117/12.2234739).
- K. S. Dawson, J.-P. Kneib, W. J. Percival, S. Alam, F. D. Albareti, S. F. Anderson, E. Armengaud, É. Aubourg, S. Bailey, J. E. Bautista, A. A. Berlind, M. A. Bershadsky, F. Beutler, D. Bizyaev, M. R. Blanton, et al. The SDSS-IV Extended Baryon Oscillation Spectroscopic Survey: Overview and Early Data. *AJ*, volume 151(2):44, 2016. doi:[10.3847/0004-6256/151/2/44](https://doi.org/10.3847/0004-6256/151/2/44).
- J. T. A. de Jong, K. Kuijken, D. Applegate, K. Begeman, A. Belikov, C. Blake, J. Bout, D. Boxhoorn, H. Buddelmeijer, A. Buddendiek, M. Cacciato, M. Capaccioli, A. Choi, O. Cordes, G. Covone, et al. The Kilo-Degree Survey. *The Messenger*, volume 154:44–46, 2013. <https://ui.adsabs.harvard.edu/abs/2013Msngr.154...44D>.
- P. F. de Salas, D. V. Forero, S. Gariazzo, P. Martínez-Miravé, O. Mena, C. A. Ternes, M. Tórtola, and J. W. F. Valle. 2020 global reassessment of the neutrino oscillation picture. *Journal of High Energy Physics*, volume 2021(2):71, 2021. doi:[10.1007/JHEP02\(2021\)071](https://doi.org/10.1007/JHEP02(2021)071).
- J. De Vicente, E. Sánchez, and I. Sevilla-Noarbe. DNF - Galaxy photometric redshift by Directional Neighbourhood Fitting. *MNRAS*, volume 459(3):3078–3088, 2016. doi:[10.1093/mnras/stw857](https://doi.org/10.1093/mnras/stw857).
- V. Desjacques, D. Jeong, and F. Schmidt. Large-scale galaxy bias. *Phys. Rep.*, volume 733:1–193, 2018. doi:[10.1016/j.physrep.2017.12.002](https://doi.org/10.1016/j.physrep.2017.12.002).
- E. Di Valentino, O. Mena, S. Pan, L. Visinelli, W. Yang, A. Melchiorri, D. F. Mota, A. G. Riess, and J. Silk. In the realm of the Hubble tension-a review of solutions. *Classical and Quantum Gravity*, volume 38(15):153001, 2021. doi:[10.1088/1361-6382/ac086d](https://doi.org/10.1088/1361-6382/ac086d).
- M. C. Digman, J. E. McEwen, and C. M. Hirata. Forecasting super-sample covariance in future weak lensing surveys with SuperSCRAM. *J. Cosmology Astropart. Phys.*, volume 2019(10):004, 2019. doi:[10.1088/1475-7516/2019/10/004](https://doi.org/10.1088/1475-7516/2019/10/004).
- S. Dodelson and F. Schmidt. *Modern Cosmology*. 2020. doi:[10.1016/C2017-0-01943-2](https://doi.org/10.1016/C2017-0-01943-2).
- D. J. Eisenstein and W. Hu. Baryonic Features in the Matter Transfer Function. *ApJ*, volume 496(2):605–614, 1998. doi:[10.1086/305424](https://doi.org/10.1086/305424).
- D. J. Eisenstein, I. Zehavi, D. W. Hogg, R. Scoccimarro, M. R. Blanton, R. C. Nichol, R. Scranton, H.-J. Seo, M. Tegmark, Z. Zheng, S. F. Anderson, J. Annis,

- N. Bahcall, J. Brinkmann, S. Burles, et al. Detection of the Baryon Acoustic Peak in the Large-Scale Correlation Function of SDSS Luminous Red Galaxies. *ApJ*, volume 633(2):560–574, 2005. doi:[10.1086/466512](https://doi.org/10.1086/466512).
- I. Esteban, M. C. Gonzalez-Garcia, M. Maltoni, T. Schwetz, and A. Zhou. The fate of hints: updated global analysis of three-flavor neutrino oscillations. *Journal of High Energy Physics*, volume 2020(9):178, 2020. doi:[10.1007/JHEP09\(2020\)178](https://doi.org/10.1007/JHEP09(2020)178).
- V. Euclid Collaboration: Ajani, M. Baldi, A. Barthelemy, A. Boyle, P. Burger, V. F. Cardone, S. Cheng, S. Codis, C. Giocoli, J. Harnois-Déraps, S. Heydenreich, V. Kansal, M. Kilbinger, L. Linke, C. Llinares, et al. Euclid preparation. XXVIII. Forecasts for ten different higher-order weak lensing statistics. *A&A*, volume 675:A120, 2023. doi:[10.1051/0004-6361/202346017](https://doi.org/10.1051/0004-6361/202346017).
- A. Euclid Collaboration: Blanchard, S. Camera, C. Carbone, V. F. Cardone, S. Casas, S. Clesse, S. Ilić, M. Kilbinger, T. Kitching, M. Kunz, F. Lacasa, E. Linder, E. Majerotto, K. Markovič, M. Martinelli, et al. Euclid preparation. VII. Forecast validation for Euclid cosmological probes. *A&A*, volume 642:A191, 2020. doi:[10.1051/0004-6361/202038071](https://doi.org/10.1051/0004-6361/202038071).
- S. Euclid Collaboration: Casas et al. Euclid: Constraints on $f(R)$ cosmologies from the spectroscopic and photometric primary probes. 2023.
- G. Euclid Collaboration: Desprez, S. Paltani, J. Coupon, I. Almosallam, A. Alvarez-Ayllon, V. Amaro, M. Brescia, M. Brodwin, S. Cavioti, J. De Vicente-Albendea, S. Fotopoulou, P. W. Hatfield, W. G. Hartley, O. Ilbert, M. J. Jarvis, et al. Euclid preparation. X. The Euclid photometric-redshift challenge. *A&A*, volume 644:A31, 2020. doi:[10.1051/0004-6361/202039403](https://doi.org/10.1051/0004-6361/202039403).
- M. Euclid Collaboration: Knabenhans, J. Stadel, D. Potter, J. Dakin, S. Hannestad, T. Tram, S. Marelli, A. Schneider, R. Teyssier, P. Fosalba, S. Andreon, N. Auricchio, C. Baccigalupi, A. Balaguera-Antolínez, M. Baldi, et al. Euclid preparation: IX. EuclidEmulator2 - power spectrum emulation with massive neutrinos and self-consistent dark energy perturbations. *MNRAS*, volume 505(2):2840–2869, 2021. doi:[10.1093/mnras/stab1366](https://doi.org/10.1093/mnras/stab1366).
- F. Euclid Collaboration: Lepori, I. Tutusaus, C. Viglione, C. Bonvin, S. Camera, F. J. Castander, R. Durrer, P. Fosalba, G. Jelic-Cizmek, M. Kunz, J. Adamek, S. Casas, M. Martinelli, Z. Sakr, D. Sapone, et al. Euclid preparation. XIX. Impact of magnification on photometric galaxy clustering. *A&A*, volume 662:A93, 2022. doi:[10.1051/0004-6361/202142419](https://doi.org/10.1051/0004-6361/202142419).
- N. Euclid Collaboration: Martinet, T. Schrabback, H. Hoekstra, M. Tewes, R. Herbonnet, P. Schneider, B. Hernandez-Martin, A. N. Taylor, J. Brinchmann, C. S. Carvalho, M. Castellano, G. Congedo, B. R. Gillis, E. Jullo, M. Kümmel, et al. Euclid preparation. IV. Impact of undetected galaxies on weak-lensing shear measurements. *A&A*, volume 627:A59, 2019. doi:[10.1051/0004-6361/201935187](https://doi.org/10.1051/0004-6361/201935187).
- A. Euclid Collaboration: Pocino, I. Tutusaus, F. J. Castander, P. Fosalba, M. Crocce, A. Porredon, S. Camera, V. Cardone, S. Casas, T. Kitching, F. Lacasa, M. Mar-

- tinelli, A. Pourtsidou, Z. Sakr, S. Andreon, et al. Euclid preparation. XII. Optimizing the photometric sample of the Euclid survey for galaxy clustering and galaxy-galaxy lensing analyses. *A&A*, volume 655:A44, 2021. doi:[10.1051/0004-6361/202141061](https://doi.org/10.1051/0004-6361/202141061).
- R. Euclid Collaboration: Scaramella, J. Amiaux, Y. Mellier, C. Burigana, C. S. Carvalho, J. C. Cuillandre, A. Da Silva, A. Derosa, J. Dinis, E. Maiorano, M. Maris, I. Tereno, R. Laureijs, T. Boenke, G. Buenadicha, et al. Euclid preparation. I. The Euclid Wide Survey. *A&A*, volume 662:A112, 2022. doi:[10.1051/0004-6361/202141938](https://doi.org/10.1051/0004-6361/202141938).
- M. Euclid Collaboration: Schirmer, K. Jahnke, G. Seidel, H. Aussel, C. Bodendorf, F. Grupp, F. Hormuth, S. Wachter, P. N. Appleton, R. Barbier, J. Brinchmann, J. M. Carrasco, F. J. Castander, J. Coupon, F. De Paolis, et al. Euclid preparation. XVIII. The NISP photometric system. *A&A*, volume 662:A92, 2022. doi:[10.1051/0004-6361/202142897](https://doi.org/10.1051/0004-6361/202142897).
- D. Euclid Collaboration: Sciotti, S. G. Beauchamps, V. F. Cardone, S. Camera, I. Tutusaus, F. Lacasa, A. Barreira, A. Gorce, M. Aubert, P. Baratta, R. E. Upham, M. Bonici, C. Carbone, S. Casas, S. Ilić, et al. Euclid preparation. tbd. forecast impact of super-sample covariance on 3x2pt analysis with euclid. 2023.
- R. A. Fisher. The Logic of Inductive Inference. *Journal of the Royal Statistical Society*, volume 98(1):39–54, 1935. ISSN 0952-8385. doi:[10.1111/j.2397-2335.1935.tb04208.x](https://doi.org/10.1111/j.2397-2335.1935.tb04208.x).
- O. Friedrich, F. Andrade-Oliveira, H. Camacho, O. Alves, R. Rosenfeld, J. Sanchez, X. Fang, T. F. Eifler, E. Krause, C. Chang, Y. Omori, A. Amon, E. Baxter, J. Elvin-Poole, D. Huterer, et al. Dark Energy Survey year 3 results: covariance modelling and its impact on parameter estimation and quality of fit. *MNRAS*, volume 508(3):3125–3165, 2021. doi:[10.1093/mnras/stab2384](https://doi.org/10.1093/mnras/stab2384).
- Gaia Collaboration, T. Prusti, J. H. J. de Bruijne, A. G. A. Brown, A. Vallenari, C. Babusiaux, C. A. L. Bailer-Jones, U. Bastian, M. Biermann, D. W. Evans, L. Eyer, F. Jansen, C. Jordi, S. A. Klioner, U. Lammers, et al. The Gaia mission. *A&A*, volume 595:A1, 2016. doi:[10.1051/0004-6361/201629272](https://doi.org/10.1051/0004-6361/201629272).
- A. Gelman and D. B. Rubin. Inference from iterative simulation using multiple sequences. *Statistical Science*, volume 7(4):457–472, 1992. ISSN 08834237. <http://www.jstor.org/stable/2246093>.
- S. Gouyou Beauchamps, F. Lacasa, I. Tutusaus, M. Aubert, P. Baratta, A. Gorce, and Z. Sakr. Impact of survey geometry and super-sample covariance on future photometric galaxy surveys. *A&A*, volume 659:A128, 2022. doi:[10.1051/0004-6361/202142052](https://doi.org/10.1051/0004-6361/202142052).
- P. Gurri, E. N. Taylor, and C. J. Fluke. Shape noise and dispersion in precision weak lensing. *MNRAS*, volume 502(4):5612–5621, 2021. doi:[10.1093/mnras/stab423](https://doi.org/10.1093/mnras/stab423).
- A. H. Guth. Inflationary universe: A possible solution to the horizon and flatness problems. *Phys. Rev. D*, volume 23(2):347–356, 1981. doi:[10.1103/PhysRevD.23.347](https://doi.org/10.1103/PhysRevD.23.347).

- A. Hall. Cosmology from weak lensing alone and implications for the Hubble tension. *MNRAS*, volume 505(4):4935–4955, 2021. doi:[10.1093/mnras/stab1563](https://doi.org/10.1093/mnras/stab1563).
- A. J. S. Hamilton, C. D. Rimes, and R. Scoccimarro. On measuring the covariance matrix of the non-linear power spectrum from simulations. *MNRAS*, volume 371(3):1188–1204, 2006. doi:[10.1111/j.1365-2966.2006.10709.x](https://doi.org/10.1111/j.1365-2966.2006.10709.x).
- W. K. Hastings. Monte carlo sampling methods using markov chains and their applications. *Biometrika*, volume 57(1):97–109, 1970. ISSN 00063444. <http://www.jstor.org/stable/2334940>.
- S. R. Hinton. ChainConsumer. *The Journal of Open Source Software*, volume 1:00045, 2016. doi:[10.21105/joss.00045](https://doi.org/10.21105/joss.00045).
- D. W. Hogg. Distance measures in cosmology. *arXiv e-prints*, astro-ph/9905116, 1999. doi:[10.48550/arXiv.astro-ph/9905116](https://doi.org/10.48550/arXiv.astro-ph/9905116).
- B. Hoyle, D. Gruen, G. M. Bernstein, M. M. Rau, J. De Vicente, W. G. Hartley, E. Gaztanaga, J. DeRose, M. A. Troxel, C. Davis, A. Alarcon, N. MacCrann, J. Prat, C. Sánchez, E. Sheldon, et al. Dark Energy Survey Year 1 Results: redshift distributions of the weak-lensing source galaxies. *MNRAS*, volume 478(1):592–610, 2018. doi:[10.1093/mnras/sty957](https://doi.org/10.1093/mnras/sty957).
- W. Hu and A. V. Kravtsov. Sample Variance Considerations for Cluster Surveys. *ApJ*, volume 584:702–715, 2003. doi:[10.1086/345846](https://doi.org/10.1086/345846).
- Ž. Ivezić, S. M. Kahn, J. A. Tyson, B. Abel, E. Acosta, R. Allsman, D. Alonso, Y. AlSayyad, S. F. Anderson, J. Andrew, J. R. P. Angel, G. Z. Angeli, R. Ansari, P. Antilogus, C. Araujo, et al. LSST: From Science Drivers to Reference Design and Anticipated Data Products. *ApJ*, volume 873(2):111, 2019. doi:[10.3847/1538-4357/ab042c](https://doi.org/10.3847/1538-4357/ab042c).
- E. Jennings, J. Zuntz, M. Paterno, D. Rudd, A. Manzotti, S. Dodelson, S. Bridle, S. Sehrish, and J. Kowalkowski. CosmoSIS: modular cosmological parameter estimation. In T. Jenness, T. Robitaille, E. Tollerud, S. Mumford, and K. Cruz, editors, *Python in Astronomy 2016*, page 14. 2016. doi:[10.5281/zenodo.48183](https://doi.org/10.5281/zenodo.48183).
- B. Joachimi, M. Cacciato, T. D. Kitching, A. Leonard, R. Mandelbaum, B. M. Schäfer, C. Sifón, H. Hoekstra, A. Kiessling, D. Kirk, and A. Rassat. Galaxy Alignments: An Overview. *Space Sci. Rev.*, volume 193(1-4):1–65, 2015. doi:[10.1007/s11214-015-0177-4](https://doi.org/10.1007/s11214-015-0177-4).
- B. Joachimi, C. A. Lin, M. Asgari, T. Tröster, C. Heymans, H. Hildebrandt, F. Köhlinger, A. G. Sánchez, A. H. Wright, M. Bilicki, C. Blake, J. L. van den Busch, M. Crocce, A. Dvornik, T. Erben, et al. KiDS-1000 methodology: Modelling and inference for joint weak gravitational lensing and spectroscopic galaxy clustering analysis. *A&A*, volume 646:A129, 2021. doi:[10.1051/0004-6361/202038831](https://doi.org/10.1051/0004-6361/202038831).
- G. Jungman, M. Kamionkowski, and K. Griest. Supersymmetric dark matter. *Phys. Rep.*, volume 267:195–373, 1996. doi:[10.1016/0370-1573\(95\)00058-5](https://doi.org/10.1016/0370-1573(95)00058-5).

- N. Kaiser. Clustering in real space and in redshift space. *MNRAS*, volume 227:1–21, 1987. doi:[10.1093/mnras/227.1.1](https://doi.org/10.1093/mnras/227.1.1).
- N. Kaiser. Weak Lensing and Cosmology. *ApJ*, volume 498(1):26–42, 1998. doi:[10.1086/305515](https://doi.org/10.1086/305515).
- M. Kerscher and J. Weller. On model selection in cosmology. *SciPost Physics Lecture Notes*, volume 9, 2019. doi:[10.21468/SciPostPhysLectNotes.9](https://doi.org/10.21468/SciPostPhysLectNotes.9).
- M. Kilbinger, C. Heymans, M. Asgari, S. Joudaki, P. Schneider, P. Simon, L. Van Waerbeke, J. Harnois-Déraps, H. Hildebrandt, F. Köhlinger, K. Kuijken, and M. Viola. Precision calculations of the cosmic shear power spectrum projection. *MNRAS*, volume 472(2):2126–2141, 2017. doi:[10.1093/mnras/stx2082](https://doi.org/10.1093/mnras/stx2082).
- T. D. Kitching, J. Alsing, A. F. Heavens, R. Jimenez, J. D. McEwen, and L. Verde. The limits of cosmic shear. *MNRAS*, volume 469(3):2737–2749, 2017. doi:[10.1093/mnras/stx1039](https://doi.org/10.1093/mnras/stx1039).
- E. Krause and T. Eifler. cosmolike - cosmological likelihood analyses for photometric galaxy surveys. *MNRAS*, volume 470(2):2100–2112, 2017. doi:[10.1093/mnras/stx1261](https://doi.org/10.1093/mnras/stx1261).
- E. Krause, X. Fang, S. Pandey, L. F. Secco, O. Alves, H. Huang, J. Blazek, J. Prat, J. Zuntz, T. F. Eifler, N. MacCrann, J. DeRose, M. Crocce, A. Porredon, B. Jain, et al. Dark Energy Survey Year 3 Results: Multi-Probe Modeling Strategy and Validation. arXiv:2105.13548, 2021. <https://ui.adsabs.harvard.edu/abs/2021arXiv210513548K>.
- F. Lacasa. The impact of braiding covariance and in-survey covariance on next-generation galaxy surveys. *A&A*, volume 634:A74, 2020. doi:[10.1051/0004-6361/201936683](https://doi.org/10.1051/0004-6361/201936683).
- F. Lacasa, M. Aubert, P. Baratta, J. Carron, A. Gorce, S. Gouyou Beauchamps, L. Legrand, A. Moradinezhad Dizgah, and I. Tutusaus. Efficient computation of the super-sample covariance for stage IV galaxy surveys. *A&A*, volume 671:A115, 2023. doi:[10.1051/0004-6361/202245148](https://doi.org/10.1051/0004-6361/202245148).
- F. Lacasa and J. Grain. Fast and easy super-sample covariance of large-scale structure observables. *A&A*, volume 624:A61, 2019. doi:[10.1051/0004-6361/201834343](https://doi.org/10.1051/0004-6361/201834343).
- F. Lacasa, M. Lima, and M. Agüena. Super-sample covariance approximations and partial sky coverage. *A&A*, volume 611:A83, 2018. doi:[10.1051/0004-6361/201630281](https://doi.org/10.1051/0004-6361/201630281).
- F. Lacasa and R. Rosenfeld. Combining cluster number counts and galaxy clustering. *J. Cosmology Astropart. Phys.*, volume 2016(8):005, 2016. doi:[10.1088/1475-7516/2016/08/005](https://doi.org/10.1088/1475-7516/2016/08/005).
- O. Lahav, P. B. Lilje, J. R. Primack, and M. J. Rees. Dynamical effects of the cosmological constant. *MNRAS*, volume 251:128–136, 1991. doi:[10.1093/mnras/251.1.128](https://doi.org/10.1093/mnras/251.1.128).

- R. Laureijs, J. Amiaux, S. Arduini, J. L. Auguères, J. Brinchmann, R. Cole, M. Cropper, C. Dabin, L. Duvet, A. Ealet, B. Garilli, P. Gondoin, L. Guzzo, J. Hoar, H. Hoekstra, et al. Euclid Definition Study Report. *arXiv:1110.3193*, 2011. doi:[10.48550/arXiv.1110.3193](https://doi.org/10.48550/arXiv.1110.3193).
- T. Lazeyras, C. Wagner, T. Baldauf, and F. Schmidt. Precision measurement of the local bias of dark matter halos. *J. Cosmology Astropart. Phys.*, volume 2016(2):018–018, 2016. doi:[10.1088/1475-7516/2016/02/018](https://doi.org/10.1088/1475-7516/2016/02/018).
- P. Lemos, A. Challinor, and G. Efstathiou. The effect of Limber and flat-sky approximations on galaxy weak lensing. *J. Cosmology Astropart. Phys.*, volume 2017(5):014, 2017. doi:[10.1088/1475-7516/2017/05/014](https://doi.org/10.1088/1475-7516/2017/05/014).
- C. D. Leonard, T. Ferreira, X. Fang, R. Reischke, N. Schoeneberg, T. Tröster, D. Alonso, J.-E. Campagne, F. Lanusse, A. Slosar, and M. Ishak. The N5K Challenge: Non-Limber Integration for LSST Cosmology. *The Open Journal of Astrophysics*, volume 6:8, 2023. doi:[10.21105/astro.2212.04291](https://doi.org/10.21105/astro.2212.04291).
- J. Lesgourgues and S. Pastor. Neutrino mass from Cosmology. *arXiv e-prints*, arXiv:1212.6154, 2012. doi:[10.48550/arXiv.1212.6154](https://doi.org/10.48550/arXiv.1212.6154).
- A. Lewis, A. Challinor, and A. Lasenby. Efficient Computation of Cosmic Microwave Background Anisotropies in Closed Friedmann-Robertson-Walker Models. *ApJ*, volume 538(2):473–476, 2000. doi:[10.1086/309179](https://doi.org/10.1086/309179).
- Y. Li, W. Hu, and M. Takada. Super-sample covariance in simulations. *Phys. Rev. D*, volume 89(8):083519, 2014. doi:[10.1103/PhysRevD.89.083519](https://doi.org/10.1103/PhysRevD.89.083519).
- Y. Li, W. Hu, and M. Takada. Separate universe consistency relation and calibration of halo bias. *Phys. Rev. D*, volume 93(6):063507, 2016. doi:[10.1103/PhysRevD.93.063507](https://doi.org/10.1103/PhysRevD.93.063507).
- E. M. Lifshitz. On the gravitational stability of the expanding universe. *Zhurnal Eksperimentalnoi i Teoreticheskoi Fiziki*, volume 16:587–602, 1946. <https://ui.adsabs.harvard.edu/abs/1946ZhETF..16..587L>.
- D. N. Limber. The Analysis of Counts of the Extragalactic Nebulae in Terms of a Fluctuating Density Field. *ApJ*, volume 117:134, 1953. doi:[10.1086/145672](https://doi.org/10.1086/145672).
- E. V. Linder. Cosmic growth history and expansion history. *Phys. Rev. D*, volume 72(4):043529, 2005. doi:[10.1103/PhysRevD.72.043529](https://doi.org/10.1103/PhysRevD.72.043529).
- L. Linke, P. A. Burger, S. Heydenreich, L. Porth, and P. Schneider. What is the super-sample covariance? A fresh perspective for second-order shear statistics. *arXiv e-prints*, arXiv:2302.12277, 2023. doi:[10.48550/arXiv.2302.12277](https://doi.org/10.48550/arXiv.2302.12277).
- C.-P. Ma and E. Bertschinger. Cosmological Perturbation Theory in the Synchronous and Conformal Newtonian Gauges. *ApJ*, volume 455:7, 1995. doi:[10.1086/176550](https://doi.org/10.1086/176550).
- C.-P. Ma and J. N. Fry. Deriving the Nonlinear Cosmological Power Spectrum and Bispectrum from Analytic Dark Matter Halo Profiles and Mass Functions. *ApJ*, volume 543(2):503–513, 2000. doi:[10.1086/317146](https://doi.org/10.1086/317146).

- A. J. Mead, S. Brieden, T. Tröster, and C. Heymans. HMCODE-2020: improved modelling of non-linear cosmological power spectra with baryonic feedback. *MNRAS*, volume 502(1):1401–1422, 2021. doi:[10.1093/mnras/stab082](https://doi.org/10.1093/mnras/stab082).
- M. Meneghetti. *Introduction to Gravitational Lensing: With Python Examples*. 2022. <https://ui.adsabs.harvard.edu/abs/2022iglp.book.....M>.
- G. Montani, M. V. Battisti, R. Benini, and G. Imponente. *Primordial Cosmology*. 2011. doi:[10.1142/7235](https://doi.org/10.1142/7235).
- V. F. Mukhanov, H. A. Feldman, and R. H. Brandenberger. Theory of cosmological perturbations. *Phys. Rep.*, volume 215(5-6):203–333, 1992. doi:[10.1016/0370-1573\(92\)90044-Z](https://doi.org/10.1016/0370-1573(92)90044-Z).
- J. F. Navarro, C. S. Frenk, and S. D. M. White. The Structure of Cold Dark Matter Halos. *ApJ*, volume 462:563, 1996. doi:[10.1086/177173](https://doi.org/10.1086/177173).
- S. Pandey, E. Krause, J. DeRose, N. MacCrann, B. Jain, M. Crocce, J. Blazek, A. Choi, H. Huang, C. To, X. Fang, J. Elvin-Poole, J. Prat, A. Porredon, L. F. Secco, et al. Dark Energy Survey year 3 results: Constraints on cosmological parameters and galaxy-bias models from galaxy clustering and galaxy-galaxy lensing using the redMaGiC sample. *Phys. Rev. D*, volume 106(4):043520, 2022. doi:[10.1103/PhysRevD.106.043520](https://doi.org/10.1103/PhysRevD.106.043520).
- J. A. Peacock. Large-scale surveys and cosmic structure. *arXiv e-prints*, astro-ph/0309240, 2003. doi:[10.48550/arXiv.astro-ph/0309240](https://doi.org/10.48550/arXiv.astro-ph/0309240).
- J. A. Peacock and S. J. Dodds. Reconstructing the Linear Power Spectrum of Cosmological Mass Fluctuations. *MNRAS*, volume 267:1020, 1994. doi:[10.1093/mnras/267.4.1020](https://doi.org/10.1093/mnras/267.4.1020).
- J. A. Peacock and R. E. Smith. Halo occupation numbers and galaxy bias. *MNRAS*, volume 318(4):1144–1156, 2000. doi:[10.1046/j.1365-8711.2000.03779.x](https://doi.org/10.1046/j.1365-8711.2000.03779.x).
- P. J. E. Peebles. *Principles of Physical Cosmology*. 1993. doi:[10.1515/9780691206721](https://doi.org/10.1515/9780691206721).
- P. J. E. Peebles and J. T. Yu. Primeval Adiabatic Perturbation in an Expanding Universe. *ApJ*, volume 162:815, 1970. doi:[10.1086/150713](https://doi.org/10.1086/150713).
- S. Perlmutter, G. Aldering, G. Goldhaber, R. A. Knop, P. Nugent, P. G. Castro, S. Deustua, S. Fabbro, A. Goobar, D. E. Groom, I. M. Hook, A. G. Kim, M. Y. Kim, J. C. Lee, N. J. Nunes, et al. Measurements of Ω and Λ from 42 High-Redshift Supernovae. *ApJ*, volume 517(2):565–586, 1999. doi:[10.1086/307221](https://doi.org/10.1086/307221).
- O. F. Piattella. Lecture Notes in Cosmology. *arXiv e-prints*, arXiv:1803.00070, 2018. doi:[10.48550/arXiv.1803.00070](https://doi.org/10.48550/arXiv.1803.00070).
- Planck Collaboration, P. A. R. Ade, N. Aghanim, C. Armitage-Caplan, M. Arnaud, M. Ashdown, F. Atrio-Barandela, J. Aumont, C. Baccigalupi, A. J. Banday, R. B. Barreiro, J. G. Bartlett, E. Battaner, K. Benabed, A. Benoît, et al.

- Planck 2013 results. XVI. Cosmological parameters. *A&A*, volume 571:A16, 2014. doi:[10.1051/0004-6361/201321591](https://doi.org/10.1051/0004-6361/201321591).
- Planck Collaboration, P. A. R. Ade, N. Aghanim, M. Arnaud, M. Ashdown, J. Aumont, C. Baccigalupi, A. J. Banday, R. B. Barreiro, N. Bartolo, E. Battaner, R. Battye, K. Benabed, A. Benoît, A. Benoit-Lévy, et al. Planck 2015 results. XIV. Dark energy and modified gravity. *A&A*, volume 594:A14, 2016. doi:[10.1051/0004-6361/201525814](https://doi.org/10.1051/0004-6361/201525814).
- Planck Collaboration, N. Aghanim, Y. Akrami, M. Ashdown, J. Aumont, C. Baccigalupi, M. Ballardini, A. J. Banday, R. B. Barreiro, N. Bartolo, S. Basak, R. Battye, K. Benabed, J. P. Bernard, M. Bersanelli, et al. Planck 2018 results. VI. Cosmological parameters. *A&A*, volume 641:A6, 2020a. doi:[10.1051/0004-6361/201833910](https://doi.org/10.1051/0004-6361/201833910).
- Planck Collaboration, N. Aghanim, Y. Akrami, M. Ashdown, J. Aumont, C. Baccigalupi, M. Ballardini, A. J. Banday, R. B. Barreiro, N. Bartolo, S. Basak, R. Battye, K. Benabed, J. P. Bernard, M. Bersanelli, et al. Planck 2018 results. VI. Cosmological parameters. *A&A*, volume 641:A6, 2020b. doi:[10.1051/0004-6361/201833910](https://doi.org/10.1051/0004-6361/201833910).
- Planck Collaboration, Y. Akrami, F. Arroja, M. Ashdown, J. Aumont, C. Baccigalupi, M. Ballardini, A. J. Banday, R. B. Barreiro, N. Bartolo, S. Basak, K. Benabed, J. P. Bernard, M. Bersanelli, P. Bielewicz, et al. Planck 2018 results. X. Constraints on inflation. *A&A*, volume 641:A10, 2020c. doi:[10.1051/0004-6361/201833887](https://doi.org/10.1051/0004-6361/201833887).
- D. Potter, J. Stadel, and R. Teyssier. PKDGRAV3: beyond trillion particle cosmological simulations for the next era of galaxy surveys. *Computational Astrophysics and Cosmology*, volume 4(1):2, 2017. doi:[10.1186/s40668-017-0021-1](https://doi.org/10.1186/s40668-017-0021-1).
- T. Poutanen, D. Maino, H. Kurki-Suonio, E. Keihänen, and E. Hivon. Cosmic microwave background power spectrum estimation with the destripping technique. *MNRAS*, volume 353(1):43–58, 2004. doi:[10.1111/j.1365-2966.2004.08043.x](https://doi.org/10.1111/j.1365-2966.2004.08043.x).
- W. H. Press and P. Schechter. Formation of Galaxies and Clusters of Galaxies by Self-Similar Gravitational Condensation. *ApJ*, volume 187:425–438, 1974. doi:[10.1086/152650](https://doi.org/10.1086/152650).
- P. Ramond. Neutrinos: a glimpse beyond the Standard Model. *Nuclear Physics B Proceedings Supplements*, volume 77(1):3–9, 1999. doi:[10.1016/S0920-5632\(99\)00382-5](https://doi.org/10.1016/S0920-5632(99)00382-5).
- R. Reischke. Propagating photo- z uncertainties: a functional derivative approach. *arXiv e-prints*, arXiv:2301.04085, 2023. doi:[10.48550/arXiv.2301.04085](https://doi.org/10.48550/arXiv.2301.04085).
- A. G. Riess, A. V. Filippenko, P. Challis, A. Clocchiatti, A. Diercks, P. M. Garnavich, R. L. Gilliland, C. J. Hogan, S. Jha, R. P. Kirshner, B. Leibundgut, M. M. Phillips, D. Reiss, B. P. Schmidt, R. A. Schommer, et al. Observational Evidence from Supernovae for an Accelerating Universe and a Cosmological Constant. *AJ*, volume 116(3):1009–1038, 1998. doi:[10.1086/300499](https://doi.org/10.1086/300499).

- C. D. Rimes and A. J. S. Hamilton. Information content of the non-linear power spectrum: the effect of beat-coupling to large scales. *MNRAS*, volume 371(3):1205–1215, 2006. doi:[10.1111/j.1365-2966.2006.10710.x](https://doi.org/10.1111/j.1365-2966.2006.10710.x).
- M. Rizzato, K. Benabed, F. Bernardeau, and F. Lacasa. Tomographic weak lensing bispectrum: a thorough analysis towards the next generation of galaxy surveys. *MNRAS*, volume 490(4):4688–4714, 2019. doi:[10.1093/mnras/stz2862](https://doi.org/10.1093/mnras/stz2862).
- V. C. Rubin, N. T. Thonnard, and J. Ford, W. K. NGC 3067: additional evidence for nonluminous matter ? *AJ*, volume 87:477–485, 1982. doi:[10.1086/113120](https://doi.org/10.1086/113120).
- R. Scoccimarro, M. Zaldarriaga, and L. Hui. Power Spectrum Correlations Induced by Nonlinear Clustering. *ApJ*, volume 527(1):1–15, 1999. doi:[10.1086/308059](https://doi.org/10.1086/308059).
- U. Seljak. Analytic model for galaxy and dark matter clustering. *MNRAS*, volume 318(1):203–213, 2000. doi:[10.1046/j.1365-8711.2000.03715.x](https://doi.org/10.1046/j.1365-8711.2000.03715.x).
- I. Smail, R. S. Ellis, and M. J. Fitchett. Gravitational lensing of distant field galaxies by rich clusters - I. Faint galaxy redshift distributions. *MNRAS*, volume 270:245–270, 1994. doi:[10.1093/mnras/270.2.245](https://doi.org/10.1093/mnras/270.2.245).
- R. E. Smith and R. E. Angulo. Precision modelling of the matter power spectrum in a Planck-like Universe. *MNRAS*, volume 486(1):1448–1479, 2019. doi:[10.1093/mnras/stz890](https://doi.org/10.1093/mnras/stz890).
- R. E. Smith, J. A. Peacock, A. Jenkins, S. D. M. White, C. S. Frenk, F. R. Pearce, P. A. Thomas, G. Efsthathiou, and H. M. P. Couchman. Stable clustering, the halo model and non-linear cosmological power spectra. *MNRAS*, volume 341(4):1311–1332, 2003. doi:[10.1046/j.1365-8711.2003.06503.x](https://doi.org/10.1046/j.1365-8711.2003.06503.x).
- D. Spergel, N. Gehrels, C. Baltay, D. Bennett, J. Breckinridge, M. Donahue, A. Dressler, B. S. Gaudi, T. Greene, O. Guyon, C. Hirata, J. Kalirai, N. J. Kasdin, B. Macintosh, W. Moos, et al. Wide-Field Infrared Survey Telescope-Astrophysics Focused Telescope Assets WFIRST-AFTA 2015 Report. arXiv:1503.03757, 2015. doi:[10.48550/arXiv.1503.03757](https://doi.org/10.48550/arXiv.1503.03757).
- V. Springel. The cosmological simulation code GADGET-2. *MNRAS*, volume 364(4):1105–1134, 2005. doi:[10.1111/j.1365-2966.2005.09655.x](https://doi.org/10.1111/j.1365-2966.2005.09655.x).
- A. A. Starobinsky. A new type of isotropic cosmological models without singularity. *Physics Letters B*, volume 91(1):99–102, 1980. doi:[10.1016/0370-2693\(80\)90670-X](https://doi.org/10.1016/0370-2693(80)90670-X).
- S. Sugiyama, H. Miyatake, S. More, X. Li, M. Shirasaki, M. Takada, Y. Kobayashi, R. Takahashi, T. Nishimichi, A. J. Nishizawa, M. M. Rau, T. Zhang, R. Dalal, R. Mandelbaum, M. A. Strauss, et al. Hyper Suprime-Cam Year 3 Results: Cosmology from Galaxy Clustering and Weak Lensing with HSC and SDSS using the Minimal Bias Model. *arXiv e-prints*, arXiv:2304.00705, 2023. doi:[10.48550/arXiv.2304.00705](https://doi.org/10.48550/arXiv.2304.00705).
- M. Takada and W. Hu. Power spectrum super-sample covariance. *Phys. Rev. D*, volume 87(12):123504, 2013. doi:[10.1103/PhysRevD.87.123504](https://doi.org/10.1103/PhysRevD.87.123504).

- R. Takahashi, M. Sato, T. Nishimichi, A. Taruya, and M. Oguri. Revising the Halofit Model for the Nonlinear Matter Power Spectrum. *ApJ*, volume 761(2):152, 2012. doi:[10.1088/0004-637X/761/2/152](https://doi.org/10.1088/0004-637X/761/2/152).
- P. L. Taylor, F. Bernardeau, and E. Huff. x-cut Cosmic shear: Optimally removing sensitivity to baryonic and nonlinear physics with an application to the Dark Energy Survey year 1 shear data. *Phys. Rev. D*, volume 103(4):043531, 2021a. doi:[10.1103/PhysRevD.103.043531](https://doi.org/10.1103/PhysRevD.103.043531).
- P. L. Taylor, F. Bernardeau, and T. D. Kitching. k-cut cosmic shear: Tunable power spectrum sensitivity to test gravity. *Phys. Rev. D*, volume 98(8):083514, 2018a. doi:[10.1103/PhysRevD.98.083514](https://doi.org/10.1103/PhysRevD.98.083514).
- P. L. Taylor, T. Kitching, V. F. Cardone, A. Fert  , E. M. Huff, F. Bernardeau, J. Rhodes, A. C. Deshpande, I. Tutusaus, A. Pourtsidou, S. Camera, C. Carbone, S. Casas, M. Martinelli, V. Pettorino, et al. Euclid: Forecasts for k-cut 3 \times 2 Point Statistics. *The Open Journal of Astrophysics*, volume 4(1):6, 2021b. doi:[10.21105/astro.2012.04672](https://doi.org/10.21105/astro.2012.04672).
- P. L. Taylor, T. D. Kitching, J. D. McEwen, and T. Tram. Testing the cosmic shear spatially-flat universe approximation with generalized lensing and shear spectra. *Physical Review D*, volume 98(2):023522, 2018b. doi:[10.1103/PhysRevD.98.023522](https://doi.org/10.1103/PhysRevD.98.023522).
- P. L. Taylor and K. Markovi  . Covariance of photometric and spectroscopic two-point statistics: Implications for cosmological parameter inference. *Phys. Rev. D*, volume 106(6):063536, 2022. doi:[10.1103/PhysRevD.106.063536](https://doi.org/10.1103/PhysRevD.106.063536).
- M. Tegmark, A. N. Taylor, and A. F. Heavens. Karhunen-Lo  ve Eigenvalue Problems in Cosmology: How Should We Tackle Large Data Sets? *ApJ*, volume 480(1):22–35, 1997. doi:[10.1086/303939](https://doi.org/10.1086/303939).
- The Dark Energy Survey Collaboration. The Dark Energy Survey. *arXiv e-prints*, astro-ph/0510346, 2005. doi:[10.48550/arXiv.astro-ph/0510346](https://doi.org/10.48550/arXiv.astro-ph/0510346).
- J. L. Tinker, B. E. Robertson, A. V. Kravtsov, A. Klypin, M. S. Warren, G. Yepes, and S. Gottl  ber. The Large-scale Bias of Dark Matter Halos: Numerical Calibration and Model Tests. *ApJ*, volume 724(2):878–886, 2010. doi:[10.1088/0004-637X/724/2/878](https://doi.org/10.1088/0004-637X/724/2/878).
- M. A. Troxel and M. Ishak. The intrinsic alignment of galaxies and its impact on weak gravitational lensing in an era of precision cosmology. *Phys. Rep.*, volume 558:1–59, 2015. doi:[10.1016/j.physrep.2014.11.001](https://doi.org/10.1016/j.physrep.2014.11.001).
- I. Tutusaus, M. Martinelli, V. F. Cardone, S. Camera, S. Yahia-Cherif, S. Casas, A. Blanchard, M. Kilbinger, F. Lacasa, Z. Sakr, S. Ili  , M. Kunz, C. Carbone, F. J. Castander, F. Dournac, et al. Euclid: The importance of galaxy clustering and weak lensing cross-correlations within the photometric Euclid survey. *A&A*, volume 643:A70, 2020. doi:[10.1051/0004-6361/202038313](https://doi.org/10.1051/0004-6361/202038313).

- S. Unruh, P. Schneider, S. Hilbert, P. Simon, S. Martin, and J. C. Puertas. The importance of magnification effects in galaxy-galaxy lensing. *A&A*, volume 638:A96, 2020. doi:[10.1051/0004-6361/201936915](https://doi.org/10.1051/0004-6361/201936915).
- R. E. Upham, M. L. Brown, and L. Whittaker. Sufficiency of a Gaussian power spectrum likelihood for accurate cosmology from upcoming weak lensing surveys. *MNRAS*, volume 503(2):1999–2013, 2021. doi:[10.1093/mnras/stab522](https://doi.org/10.1093/mnras/stab522).
- R. E. Upham, M. L. Brown, L. Whittaker, A. Amara, N. Auricchio, D. Bonino, E. Branchini, M. Brescia, J. Brinchmann, V. Capobianco, C. Carbone, J. Carretero, M. Castellano, S. Cavauoti, A. Cimatti, et al. Euclid: Covariance of weak lensing pseudo- C_ℓ estimates. Calculation, comparison to simulations, and dependence on survey geometry. *A&A*, volume 660:A114, 2022. doi:[10.1051/0004-6361/202142908](https://doi.org/10.1051/0004-6361/202142908).
- L. Vazsonyi, P. L. Taylor, G. Valogiannis, N. S. Ramachandra, A. Ferté, and J. Rhodes. Constraining $f(R)$ gravity with a k -cut cosmic shear analysis of the Hyper Suprime-Cam first-year data. *Phys. Rev. D*, volume 104(8):083527, 2021. doi:[10.1103/PhysRevD.104.083527](https://doi.org/10.1103/PhysRevD.104.083527).
- L. Verde. Statistical Methods in Cosmology. In G. Wolschin, editor, *Lecture Notes in Physics*, Berlin Springer Verlag, volume 800, pages 147–177. 2010. doi:[10.1007/978-3-642-10598-2_4](https://doi.org/10.1007/978-3-642-10598-2_4).
- R. Voivodic and A. Barreira. Responses of Halo Occupation Distributions: a new ingredient in the halo model & the impact on galaxy bias. *J. Cosmology Astropart. Phys.*, volume 2021(5):069, 2021. doi:[10.1088/1475-7516/2021/05/069](https://doi.org/10.1088/1475-7516/2021/05/069).
- D. Wadekar, M. M. Ivanov, and R. Scoccimarro. Cosmological constraints from BOSS with analytic covariance matrices. *Phys. Rev. D*, volume 102(12):123521, 2020. doi:[10.1103/PhysRevD.102.123521](https://doi.org/10.1103/PhysRevD.102.123521).
- C. Wagner, F. Schmidt, C. T. Chiang, and E. Komatsu. Separate universe simulations. *MNRAS*, volume 448:L11–L15, 2015a. doi:[10.1093/mnrasl/slu187](https://doi.org/10.1093/mnrasl/slu187).
- C. Wagner, F. Schmidt, C.-T. Chiang, and E. Komatsu. The angle-averaged squeezed limit of nonlinear matter N -point functions. *J. Cosmology Astropart. Phys.*, volume 2015(8):042–042, 2015b. doi:[10.1088/1475-7516/2015/08/042](https://doi.org/10.1088/1475-7516/2015/08/042).
- D. H. Weinberg, M. J. Mortonson, D. J. Eisenstein, C. Hirata, A. G. Riess, and E. Rozo. Observational probes of cosmic acceleration. *Phys. Rep.*, volume 530(2):87–255, 2013. doi:[10.1016/j.physrep.2013.05.001](https://doi.org/10.1016/j.physrep.2013.05.001).
- M. White, M. Blanton, A. Bolton, D. Schlegel, J. Tinker, A. Berlind, L. da Costa, E. Kazin, Y. T. Lin, M. Maia, C. K. McBride, N. Padmanabhan, J. Parejko, W. Percival, F. Prada, et al. The Clustering of Massive Galaxies at $z \sim 0.5$ from the First Semester of BOSS Data. *ApJ*, volume 728(2):126, 2011. doi:[10.1088/0004-637X/728/2/126](https://doi.org/10.1088/0004-637X/728/2/126).
- L. Wolz, M. Kilbinger, J. Weller, and T. Giannantonio. On the validity of cosmological Fisher matrix forecasts. *J. Cosmology Astropart. Phys.*, volume 2012(9):009, 2012. doi:[10.1088/1475-7516/2012/09/009](https://doi.org/10.1088/1475-7516/2012/09/009).

- J. Yao, H. Shan, R. Li, Y. Xu, D. Fan, D. Liu, P. Zhang, Y. Yu, B. Hu, N. Li, Z. Fan, H. Xu, and W. Guo. CSST forecast: impact from non-Gaussian covariances and requirements on systematics-control. [arXiv e-prints](#), arXiv:2304.04489, 2023. doi:[10.48550/arXiv.2304.04489](#).
- M. Zennaro, R. E. Angulo, S. Contreras, M. Pellejero-Ibáñez, and F. Maion. Priors on Lagrangian bias parameters from galaxy formation modelling. [MNRAS](#), volume 514(4):5443–5456, 2022. doi:[10.1093/mnras/stac1673](#).